UNIVERSITÀ DEGLI STUDI DI PAVIA
DOTTORATO DI RICERCA IN FISICA – XXXII CICLO

Effects of magnetic nanoparticles correlation times and aspect ratio on hyperthermic and relaxometric properties

Matteo Avolio

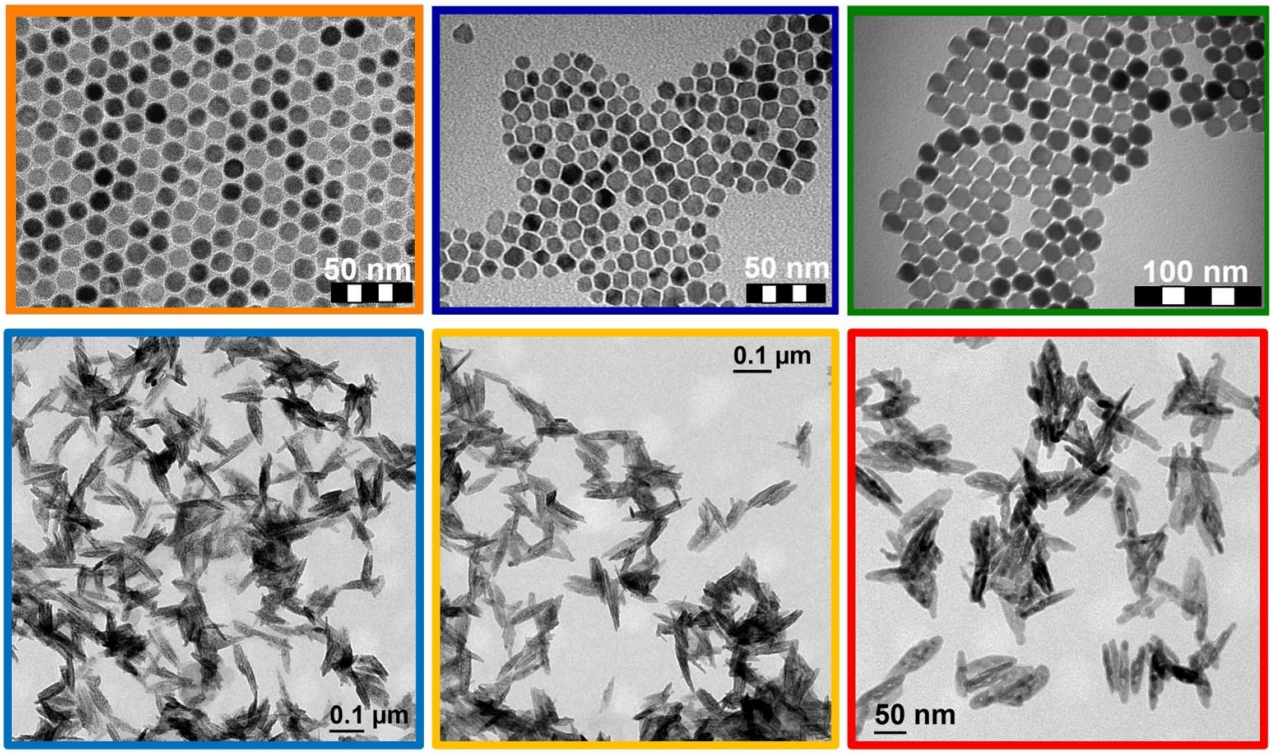

Tesi per il conseguimento del titolo

Università degli Studi di Pavia
Dipartimento di Fisica

DOTTORATO DI RICERCA IN FISICA – XXXII CICLO

Effects of magnetic nanoparticles correlation times and aspect ratio on hyperthermic and relaxometric properties

Matteo Avolio

Submitted to the Graduate School of Physics in partial fulfillment of the requirements for the degree of

DOTTORE DI RICERCA IN FISICA

DOCTOR OF PHILOSOPHY IN PHYSICS

at the

University of Pavia

Supervisors: Prof. Alessandro Lascialfari, Dr. Manuel Mariani

Cover: collection of TEM pictures of Magnetic Nanoparticles from the thesis.

Effects of magnetic nanoparticles correlation times and aspect ratio on hyperthermic and relaxometric properties

Matteo Avolio
PhD thesis - University of Pavia
Pavia, Italy, September 2019

A mia madre e a mio padre,
che mi hanno insegnato tutto quello che,
di importante, conosco.

Contents

Overview

In the recent years, great interest was born for the research field regarding magnetic nanoparticles (MNPs). MNPs are nanosized objects (generally from few nanometers to $\sim$ 100 nm) with powerful and tunable magnetic properties, which can be employed for several applications ranging from magnetic memories to both therapy and diagnostics in clinics. In particular, the latter field is the one within which this thesis is developed.

To be employed in *in-vivo* applications, MNPs have to be small enough to minimize the risk of aggregation due to magnetic interactions, and organic coatings have to be used to make them biocompatible, to stabilize the particles in solutions and to minimize inter-particles interactions.

The small size of MNPs allows a favourable interaction with the cells and the biological structures, a property that can be exploited for different applications. Moreover, it is possible to functionalize the particles with drugs attached to the external coating, or embedded within pores or cavities, to carry these substances to specific targets of the body with therapeutics aim. This goal can be achieved using both magnetic or non-magnetic particles, although MNPs could allow a magnetic delivery by means of external magnets. However, the targeting of MNPs within the body, particularly into deep organs, is an open problem that several research groups around the world are facing, since without an effective targeting strategy most of the MNPs potentials are destined to remain unexpressed.

The magnetic properties of MNPs allow their usage with theranostic purposes and not only as simple carriers. In particular, iron oxide MNPs, showing a strong magnetization and a superparamagnetic behaviour, can be exploited as contrast agents (CAs) for Magnetic Resonance Imaging (MRI) and heating mediators for Magnetic Fluid Hyperthermia (MFH). Magnetite (Fe_3O_4) or maghemite ($\gamma - Fe_2O_3$) MNPs are commonly preferred for these applications, due to their low toxicity for the body, which has its own metabolic pathways for the iron absorption and disposal.

The fluctuations of the hyperfine interaction between the particles magnetization and the ^1H nuclear magnetization strongly affect the nuclear relaxation times, determining a change of the intensity of the signal coming from the

region where MNPs accumulate (generally, a lesion) and allowing its better detection in the MR image.

MNPs can also be used with therapeutic purposes: if an alternating magnetic field is applied with a frequency of some hundreds of kHz and an amplitude of tens of mT, the interaction between the field and the MNPs magnetization causes a strong heating of the magnetic cores and, by induction, of the surrounding tissues. In tissues heated up to about 42°C (mild-hyperthermia), the denaturation of proteins and DNA, an increased oxidative stress, etc., weaken the cells and make them more susceptible to combined treatments as radiotherapy or chemotherapy, easily inducing apoptosis.

To date, MNPs are already used as CAs for MRI (for example the withdrawn commercial product "Endorem") or for the therapeutic treatment of glioblastoma, prostate cancer and some other poor-prognosis tumours with MFH (see www.Magforce.com). However, in particular MFH treatments are far to be optimized, since large amounts of particles have to be injected into the tumour to reach the therapeutic goal. Many improvements are therefore necessary before reaching a wide usage of MNPs in clinics, and a strong research in collaboration between physicists, chemists, biologists, engineers, physicians, etc., is mandatory.

To cite some of the open questions in the MNPs field, it is still unknown which are (i) the best material, (ii) the best size and (iii) the best shape of the magnetic core that optimize the magnetic properties and the MRI and MFH efficiencies. Better coatings must be developed (iv) to optimize the colloidal stability and (v) the targeting capabilities of MNPs, and (vi) to increase the cellular uptake. To date, (vii) few synthetic routes exist that allow reproducing systematically the synthesis of MNPs with same and tunable features. Finally, (viii) no definitive answer has been given to the problem of the MNPs toxicity.

This thesis focuses on the physical characterization of samples of MNPs with different features, trying to investigate on some of the previously listed open questions in the MNPs field. In particular, three main topics are investigated: (i) the effects of the size of spherical MNPs on their hyperthermic and relaxometric efficiencies; (ii) the role of the Brownian motion on the Specific Absorption Rate (SAR) of MNPs; (iii) the possibility of exploiting elongated shapes and porous structures to tune the magnetic properties of MNPs and to increase their performances in MFH and MRI.

As regard the effect of the core size of MNPs on SAR and nuclear relaxivity, systematic measurements of these properties were carried out in water colloidal solutions of 10 nm, 14 nm and 20 nm maghemite MNPs. This work started during author's Master degree thesis and led to two publications that worked as a basis for the development of the actual PhD project. It is shown that both SAR and nuclear relaxivity increase with the particle diameter, being maximum for the 20 nm sample (SAR $\simeq$ 120 W/g at 110 kHz and 19 kA/m, $r_2 \simeq 610\,\mathrm{s^{-1}mM^{-1}}$ at 1.41 T) compared to the 14 nm (SAR $\simeq$ 40 W/g at 110 kHz and 19 kA/m, $r_2 \simeq 250\,\mathrm{s^{-1}mM^{-1}}$ at 1.41 T) and 10 nm (SAR $\simeq$ 15 W/g

at 110 kHz and 19 kA/m, $r_2 \simeq 250\,\mathrm{s}^{-1}\mathrm{mM}^{-1}$ at 1.41 T) samples.

Moreover, theoretical models of MFH and Nuclear Magnetic Resonance (NMR) are applied to deepen the knowledge about the investigated systems. A strong dependence of the SAR on the particles size is experimentally demonstrated, although only the heating efficiency of small superparamagnetic particles (10 nm sample) results to be correctly explained by the available models of MFH as the Linear Response Theory (LRT). The Nuclear Magnetic Resonance Dispersion (NMRD) profiles, i.e. the longitudinal (r_1) and transversal (r_2) relaxivities as a function of the magnetic field 0.2 mT $< \mu_0 H_0 <$ 1.41 T, are investigated by applying heuristic models available in the literature, which succeed only in describing the longitudinal profiles (r_1 vs H_0), probably due to the lack of some physical mechanisms in the theory explaining r_2 *vs* H_0.

The effect of the viscosity of the dispersant medium on the efficiency of MNPs for MFH is investigated by employing three samples of magnetite MNPs with different sizes, and water and agarose gel phantoms as tissue-mimicking materials. Commonly, SAR is measured in water solutions, which have rheological properties far from those of the biological medium. In particular, literature reports that MNPs internalized by cells (in the viscous cytoplasm) or attached to the cell membrane are essentially immobilized and, contrarily to water, the Brownian relaxation (one of the most important heating mechanisms of MNPs in MFH) is suppressed. This occurrence could lead to a drop of the heating efficiency of MNPs when injected into the body, and the SAR measured in water solutions may result useless and even misleading.

MFH measurements on 10 nm, 14 nm and 18 nm MNPs in water and agarose gel show a clear effect of the particles immobilization on the SAR depending on the particles size. For particles with $d = 10$ nm the SAR does not change in the different media, due to the dominant role of the Néel relaxation. On the contrary, for larger particles ($d = 14$ nm and $d = 18$ nm) the SAR decreases up to the 70% when MNPs are immobilized within the gels. For example, at $f = 109.8$ kHz and $H = 16.2$ kA/m the SAR decreases from 113 W/g to 54 W/g for the 14 nm sample, and from 67 W/g to 25 W/g for the 18 nm sample. These results are supported by kinetic Monte Carlo simulations appositely implemented to describe systems involving only the Néel relaxation or both the Néel and Brown relaxation, and to allow *in-silico* measurements of the SAR. The latter step was realized thanks to the fundamental help of Prof. Julian Carrey at the Laboratoire de Physique et Chimie des Nano-objets, at INSA Touluse (France), where the thesis' author spent two months for a training on numerical simulations in the field of MFH, with financial support of the COST Action TD1402 *Radiomag*.

In conclusion, both experimental and computational results demonstrate that SAR of MNPs aimed to be used in clinics must be characterized in media other than water, since the physical mechanisms involved in the heating process strongly depend on the medium properties.

As regard the role of the particles shape in MFH and MRI, it must be noted

that spherical MNPs are commonly preferred because of their easier synthesis strategies and their isotropic shape, which allows an easier modelling of the physical phenomena involved in the heating and in the nuclear relaxation, respectively. However, particle shapes other than spherical have attracted a strong interest, since different shapes determine different cellular uptake, different circulation-time within the blood or the lymphatic vessels, and tunable magnetic properties exploiting the shape anisotropy of the particles.

Thanks to the availability of Prof. Maria del Puerto Morales, the thesis' author had the possibility to spend three months at the Institute of Materials Science of Madrid (ICMM) for the synthesis and the characterization of elongated magnetic nanoparticles (e-MNPs) with ellipsoidal shape ($\sim 100 \times 25$ nm) and tunable magnetic properties, arising from both a porous structure and a mixed composition of hematite and magnetite.

Poor data are available in literature about the MFH and MRI efficiencies of similar materials, that were systematically characterized to find the best solution for future applications and to highlight the chemico-physical relationships between the e-MNPs morphological properties, their magnetic properties, their SAR and nuclear relaxivities.

Results clearly show that these samples are promising candidates for MRI and eventually MFH applications, and that the porosity of the particles affects both the SAR and the nuclear relaxivity. In particular, the sample with the largest pores and size of the magnetite crystals within the MNPs volume shows the best magnetic properties (saturation magnetization near to the value of bulk magnetite) and consequently the highest SAR (SAR $\simeq$ 370 W/g at 109 kHz and 55 mT) and transversal relaxivity ($r_2 \simeq 343\,\mathrm{mM^{-1}s^{-1}}$ at 1.33 T) values. Although the heating efficiency needs to be improved at the clinical fields of MFH (SAR $\simeq$ 20 W/g at 109 kHz and 15-20 mT) to be more attractive compared to the strong performances of other particles reported in literature, the transversal relaxivity results to be much higher than that of Endorem (r_2(Endorem) $\simeq 100\,\mathrm{mM^{-1}s^{-1}}$ at 1.33 T), attesting promising properties of these samples already at this initial stage.

Finally, author has been involved in the *Hadromag* project funded by the Italian National Institute for Nuclear Physics (INFN), which focuses on the investigation of the combined efficiency of MFH and Hadron therapy (HT), a new form of radiotherapy employing heavy charged particles as protons or carbon ions to kill cancer cells. The project aims to find a new therapy to defeat pancreatic cancer, a poor-prognosis tumour with the current clinical trials, and it is developed in collaboration between several Italian Universities and exploiting the facilities (a syncrotron accelerating both protons and carbon ions) of the National Center for Oncological Hadrontherapy (CNAO) in Pavia.

Author was involved in this project for all that concerns MFH, i.e. the development and optimization of an experimental setup for *in-vitro* MFH treatments on cells samples, the measurements of the SAR of the ferrofluids used in the project and the MFH experiments on cells. This project was carried out in

parallel with author's main PhD activities and it is still going on. Therefore, only preliminary results, which seem to indicate a promising *in-vitro* combined efficiency of HT and MFH against pancreatic cancer, are shown.

Chapter 1

Nanoparticles Magnetism

In this chapter, the physical laws governing magnetism in magnetic nanoparticles (MNPs) are presented. A first section is dedicated to a recall of the basis of magnetism in bulk materials, since it makes easier the subsequent translation to the nanoscale. Relevant attention is then dedicated to the description of the superparamagnetic regime and to the magnetic anisotropy of MNPs.

1.1 Magnetism in the bulk domain

Interactions between atomic magnetic moments in a material can lead to long-distance effects and ordering, determining the appearance of macroscopic magnetic properties and, sometimes, a net magnetization M [1].

The main interaction responsible of a magnetic ordering is the exchange interaction, which arises from the quantum mechanical nature of electrons, and it describes the overlapping of the charge distributions (wave functions) of two close atoms, whose energy competes with the thermal energy for the reversal of the magnetic moments. In a multi-atoms system, according to the Heisenberg model, it can be described by the hamiltonian:

$$\mathcal{H} = -2 \sum_{i>j} \mathrm{J}_{ij} \vec{S_i} \cdot \vec{S_j}, \tag{1.1}$$

where $\vec{S_i}$ and $\vec{S_j}$ are atomic spins at neighboring sites and J_{ij} is the exchange integral, which determines the type of magnetic ordering in the material [2]. When $\mathrm{J}_{ij} > 0$, a parallel alignment of the spins is favoured, and it leads to a ferromagnetic ordering. Oppositely, if $\mathrm{J}_{ij} < 0$ the magnetic ordering of the system is realized through an antiparallel orientation of the spins. In the latter case, if the system is made by identical spins then an antiferromagnetic ordering is observed, and the total magnetization results to be zero; otherwise, if two sublattice with different spins are chain-linked in the systems, a ferrimagnetic ordering is realized and the global magnetization is greater than zero. The ferrimagnetic ordering is of particular interest, since iron-oxides like magnetite

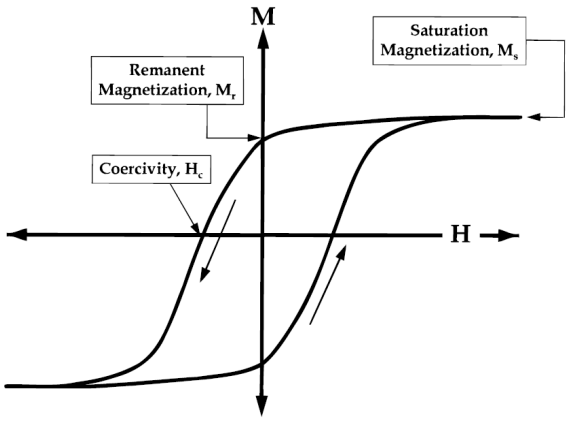

Figure 1.1: Hysteresis loop of a ferrimagnetic or ferromagnetic material. Arrows indicate the saturation magnetization M_S at high fields, the remanent magnetization M_r and the coercive field H_c. Image from Ref. [6].

(Fe_3O_4) and maghemite ($\gamma - Fe_2O_3$), commonly used for MNPs preparation, present a ferrimagnetic structure, which leads to magnetic properties exploited for several applications.

It is important to note that any type of magnetic ordering is highly susceptible to thermal agitation of the spins induced by increasing temperatures, which may cause transitions to the paramagnetic regime. In particular, a critical temperature is defined that determines the disappearance of the magnetic ordering, namely the Curie temperature (T_C) for ferromagnets and the Néel temperature (T_N) for antiferromagnets.

Magnetically ordered bulk materials commonly present a multidomain structure (each one made by $10^{12} - 10^{18}$ atoms, up to 10 μm in size) with different spin orientations [3], such that they result macroscopically non-magnetic. The magnetic ordering produced by the exchange interaction is in fact dominated over long ranges by the demagnetization field, which act to reduce the net magnetization.

Hovewer, it is possible to change the magnetization of a bulk material by applying an external magnetic field H. When even small fields are applied, the magnetic domains favourably oriented to the field increase in size thanks to the movement of their surrounding domain walls. If the field is particularly strong, then also the spins in magnetic domains unfavourably oriented turn their orientation through the field direction, determining a progressive increment of the magnetization of the material up to saturation (M_S). For ferromagnets or ferrimagnets, even if the field H is removed, the material continues to present a remanent magnetization (M_r), which can be cancelled only by forcing the movement of the domain walls by applying a coercive field (H_C) in a direction opposite to that of H (as described by the hysteresis loop in Fig. 1.1). The domain walls motion is in fact hindered by impurities or defects (like dislocations in the crystallographic structure) commonly present within the crystal structure of a ferromagnet, which cause the so called domain wall pinning.

Magnetocrystalline anisotropy

The spins orientation in a magnetic domain is mainly determined by the magnetocrystalline anisotropy, which arises from the spin-orbit interaction and determines the existence of one or more energetically convenient orientations, called *easy axes* [2, 4].

In the simplest case of uniaxial anisotropy, an additional term must be added to the hamiltonian of Eq.1.1:

$$\mathcal{H} = -2\sum_{i>j} \mathrm{J}_{ij}\vec{S_i}\cdot\vec{S_j} - K_{mc}\sum_i (S_{zi})^2 \tag{1.2}$$

where K_{mc} is the magnetocrystalline anisotropy constant and the easy axis has been assumed parallel to $\hat{z}$ [7]. Moreover, the anisotropy energy can be written as a series of expansions of cosines of the angle θ between the *easy axis* and the magnetization, leading to the simplified expression $E_{uniaxial} \approx K\sin^2\theta$. Therefore, the anisotropy energy is minimized when $\theta = 0$ or $\theta = \pi$, i.e. when the magnetization lies along the *easy axis*.

1.2 Single domain magnetic nanoparticles

Due to the small size of MNPs, their magnetic properties are slightly different from those of bulk materials. In particular, in a nanometric object the energy required for the formation of a magnetic domain wall overcomes the energy of the demagnetization field, leading to the formation of a single domain structure. The critical radius for a spherical particle that signs the transition from a multidomain to a single domain configuration is

$$R_c = \frac{6\sqrt{AK}}{\mu_0 M_S^2} \tag{1.3}$$

where A is the exchange stiffness, i.e. a parameter related to the critical temperature for the magnetic ordering of the material, K is the magnetic anisotropy constant, μ_0 is the vacuum magnetic permeability and M_S the saturation magnetization [5–7]. For magnetite (Fe_3O_4) $R_C \simeq 64$ nm; for maghemite ($\gamma - Fe_2O_3$) $R_C \simeq 83$ nm [6].

The sum of all the electronic spins oriented parallel to each other in a single domain magnetic nanoparticle is generally referred to as *superspin*. When an external field is applied, the magnetization process of a single domain MNP can be simply described by the coherent rotation of the spins through the direction of the field. However, when the size of a single domain MNP decreases down to the order of some tens of nanometers, its magnetic behaviour cannot be described anymore by the laws of ferromagnets: the thermal energy indeed strongly influences the superspin orientation, determining its fluctuations in characteristic relaxation times and the transition to the superparamagnetic regime.

Magnetic anisotropy in nanoparticles

The magnetic anisotropy of MNPs is commonly assumed as uniaxial, and the anisotropy energy is defined as:

$$E(\theta) = KV \sin^2 \theta \tag{1.4}$$

where K is the anisotropy constant, V the MNP volume and θ the angle between the easy axis and the superspin (Fig. 1.2a) [7].

As shown in Fig. 1.2b, the potential energy has two minima for $\theta = 0$ and $\theta = \pi$, i.e. it is energetically convenient for the magnetization to lie along the easy axis, in one or the opposite direction. These two minima are separated by an energy barrier $\Delta E = KV$, and a reversal of the magnetization from one direction to the other is possible only when the thermal energy overcomes the energy barrier, i.e. $k_B T > KV$, where T is the temperature and k_B the Boltzmann constant. In this case, thermal excitations allow the magnetization reversal in a characteristic Néel relaxation time [7,8], defined by the Arrhenius law

$$\tau_N = \tau_0 \exp \frac{KV}{k_B T}, \tag{1.5}$$

where τ_0 is a typical attempt time for magnetization reversal, different for each material and generally assumed as $\tau_0 \simeq 10^{-9} \div 10^{-12}$ s.

Obviously, when an external magnetic field H is applied at a random angle α relative to the easy axis (Fig.1.2a), a competitive interaction for the alignment of the magnetization along both the easy axis and the direction of the field modifies Eq. 1.4 to:

$$E(\alpha, \theta) = KV \sin^2 \theta - \mu_0 M_S V H \cos(\alpha - \theta). \tag{1.6}$$

As shown in Fig. 1.2b for the simplest case when H is applied in parallel to the easy axis but in the opposite direction ($\alpha = 180°$), the energy degeneracy of the wells disappears and the energy barrier decreases, making more favourable for M_S the alignment along the same orientation of H. The particular case when $\alpha = 180°$ is treated by the Stoner-Wohlfarth theory, which predicts an evolution of the energy barrier E_B with the amplitude of the field H according to the law:

$$E_B = KV\Big(1 - \frac{H}{H_K}\Big)^2 \tag{1.7}$$

where $H_K = 2K/(\mu_0 M_S)$ is the *anisotropy field* [4,9].

Shape and surface anisotropy

Due to the small size of MNPs, the shape and the surface anisotropy play an important role in addition to the magnetocrystalline anisotropy previously described for bulk materials.

The shape anisotropy is always zero for spherical particles (for symmetry reasons), but it becomes relevant for anisotropic particles. For example, a

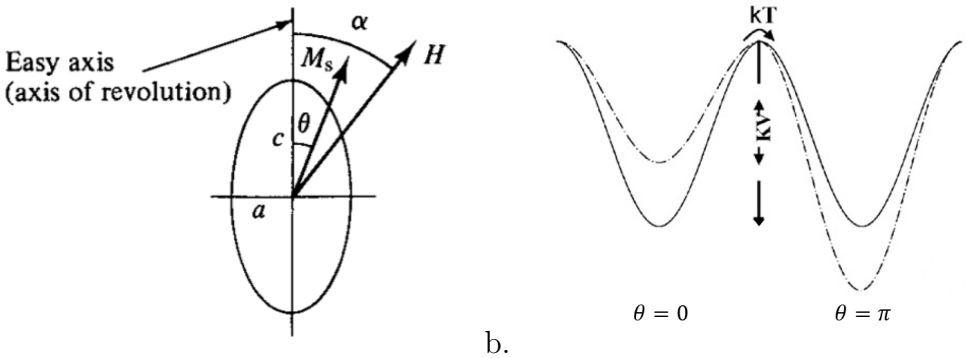

a. b.

Figure 1.2: (a) Schematic representation of an ellipsoidal MNP with uniaxial anisotropy along its major axis. An external magnetic field H is applied at an angle α relative to the easy axis, causing the magnetization M_S to orientate at a compromise angle θ that minimize the energy of the system. Image from Ref. [4]. (b) Magnetic potential energy as a function of the angle θ in the absence of external magnetic fields (solid line) and in the special case when an external field is applied at $\alpha = 180°$, parallel to the easy axis (dashed line). Image from Ref. [7].

spheroidal particle with elliptical section has an easy axis aligned with its major axis, due to the minor energy demand for the magnetic field produced around the particle. For particles with aspect ratio (i.e. the ratio between the size of the major and minor axes) greater than 1.1, the shape anisotropy dominates over the magnetocrystalline anisotropy [4].

Another contribution comes from the surface anisotropy. What happens at the surface strongly influences the properties at the nanoscale, since the surface to volume ratio quickly rises while diminishing the MNPs size. The crystal structure is abruptly interrupted at the particle surface, causing lattice distortion (vacancies, broken bonds, etc.) and trapping the spins in non-equilibrium states. The atomic disorder and spin frustration on the surface destabilizes the collinear spin arrangement predicted by the Stoner Wohlfarth theory (Fig 1.3a), and produce disordered spin structures that differentiate from those of the highly crystalline core (Fig 1.3b) [7]. Spin structures on the surface result also to be magnetically harder than those of the core.

Considering the high surface to volume ratio of MNPs, the surface anisotropy results to be up to two orders of magnitude higher than the magnetocrystalline anisotropy of the core [10, 11]. Indicating with K_B the bulk anisotropy of the core, with K_S the surface anisotropy and with d the particle diameter, an effective anisotropy constant is generally defined [12–14] as:

$$K_{eff} = K_B + \frac{6}{d} K_S. \tag{1.8}$$

Both K_B and K_S are assumed as uniaxial, and the surface anisotropy rescale with d^{-1}, becoming more and more relevant while decreasing the particle size.

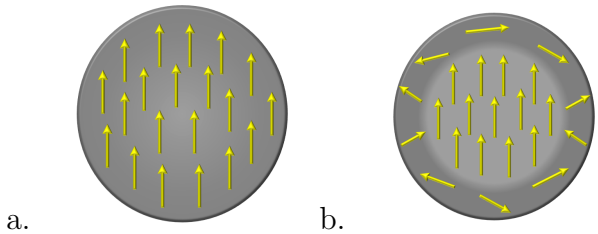

Figure 1.3: (a) Schematic representation of a MNP according to the Stoner Wohlfarth model: the magnetization is uniformly defined by collinear spins that rotate simultaneously. (b) When surface anisotropy is considered, atomic disorder and spin frustration are observed at the MNP surface, where the crystal structure is abruptly interrupted. Images inspired from Ref. [7].

1.3 Superparamagnetism

With reference to Fig. 1.4a, it is observed that when the size of a single domain MNP is decreased down to some tens of nanometers, its coercive field decreases to zero. This behaviour characterizes the superparamagnetic regime. As it has been described in Sec. 1.2, for very small particles the thermal energy overcomes the anisotropy barrier ($\Delta E = KV \leq k_B T$) causing quick and random fluctuations of the superspins (Fig. 1.5a), whose frequency increases with the temperature. The characteristic time of the superspin fluctuations is the Néel relaxation time τ_N, presented in Eq. 1.5, which indeed exponentially depends on the inverse of the temperature.

The collective behaviour of the superspins of a MNPs system could be described as that of single magnetic moments in a paramagnet. When an external magnetic field is applied, superspins progressively align up to saturation (M_S), as described by the Langevin function:

$$M(H,T) = M_S\, L\Big(\frac{\mu H}{k_B T}\Big) = M_S \left[\coth\Big(\frac{\mu H}{k_B T}\Big) - \frac{k_B T}{\mu H} \right] \tag{1.9}$$

where μ indicates the superspin of each particle and not a single magnetic moment. As shown in Fig. 1.4c, the hysteresis loop of a superparamagnet is very similar to that of a paramagnet: the loop is closed ($H_C = 0$), but the saturation magnetization is much higher due to the stronger value of the magnetic moments entering Eq. 1.9 [3, 15].

However, superparamagnetism is not an absolute property of a material: it strongly depends on the experimental technique used to measure the system, and particularly on its characteristic measurement time (τ_m). If the measurement is performed in a shorter time than that required for the magnetization to reverse its orientation, i.e. $\tau_m < \tau_N$, then the superspins appear to be blocked during the measurement (Fig. 1.5b). This situation is referred to as the *blocked state*, which allows studying the quasi-static behaviour of the system, likely showing magnetic hysteresis ($H_C \neq 0$).

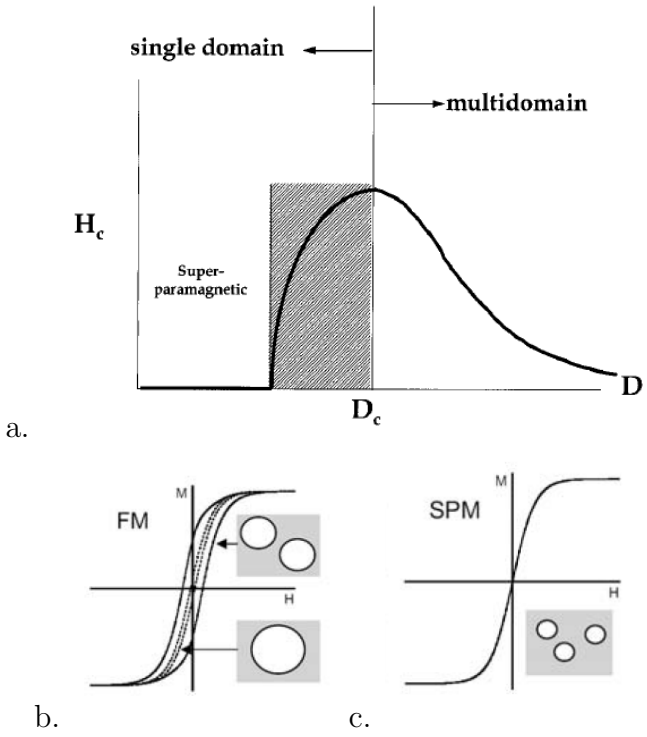

Figure 1.4: (a) Coercive field H_C dependence on the MNPs diameter D in the multidomain and single domain ferromagnetic regimes, and in the superparamagnetic regime. (b) For ferromagnetic multidomain MNPs the coercive field increases while decreasing the diameter, up to a maximum occurring at the critical diameter D_C that determines the transition to the single domain regime. In the single domain regime, H_C progressively decreases until it becomes zero (c) in the superparamagnetic regime, where the hysteresis loop is closed. Images from Refs. [7] and [3].

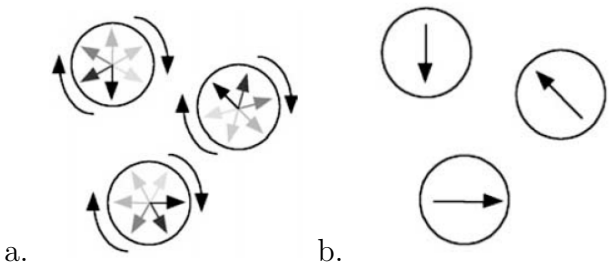

Figure 1.5: Schematic representation of three spherical nanoparticles and their superspins in the superparamagnetic regime (a) and in the blocked state (b), in zero field. In (a) the temperature overcomes the blocking temperature T_B causing quick thermal reversals of the particles magnetization. In (b) $T < T_B$ and the superpins are blocked during the measurement; although the net magnetization could still be equal to zero, due to the random orientation of the particles, in this case the system likely shows magnetic hysteresis. Images from Ref. [3].

For particles of a given volume V, the transition from the superparamagnetic regime to the blocked state happens at the *blocking temperature* T_B,

defined from the condition $\tau_m = \tau_N$:

$$T_B = \frac{KV}{k_B \ln(\frac{\tau_m}{\tau_0})}. \tag{1.10}$$

The value of T_B is commonly extracted from the *Zero-Field-Cooled* (ZFC) curve, showing a maximum at a temperature T_{max} that is commonly assumed as a good estimation of T_B (although a proportionality constant β, depending on the size distribution of the particles, is often considered between the two temperatures, i.e. $T_B \propto \beta T_{max}$) [7, 16].

If an external magnetic field is applied, the blocking temperature decreases with increasing field amplitude according to the law:

$$T_B(H) = T_B(0)\Big(1 - \frac{H}{H_c}\Big)^k \tag{1.11}$$

where $T_B(0)$ is the blocking temperature in zero-field, $H_c = 2K/M_S$ and k is a parameter equal to 2 at low fields, and 2/3 at high fields [15]. If the external magnetic field oscillates with a given frequency f (as it is in the case of Magnetic Fluid Hyperthermia experiments), then the period $\tau_m = 1/f$ could be assumed as the measurement time, and a *blocking frequency* f_B determines the transition from the superparamagnetic regime to the blocked state.

1.4 Nanoparticles hysteresis loop

The opening of the hysteresis loop of MNPs, as showed in Fig.1.4a, strongly depends on the size of the particles. For large multidomain ferromagnetic nanoparticles the coercive field is low, since it results easy to move the domain walls when a magnetic field is applied. Decreasing the particles size, the movement of the domain walls becomes progressively more energetically demanding, and the coercive field increases (Fig.1.4b) up to a maximum that is achieved at the critical diameter determining the transition from the multidomain to the single domain ferromagnetic regime. A further decrease of the particle size determines a drop of the coercive field, down to zero in the superparamagnetic regime, where the hysteresis loop shows the characteristic shape of sigmoid functions (Fig.1.4c), as for paramagnets [3, 6].

From experimental measurements, the dependence of the coercive field from the particles size has been derived to be:

$$H_C(D) = H_M \cdot \Big(\frac{D}{D_1}\Big)^{-0.6} \cdot \Big[1 - \exp\Big(-\frac{D}{D_1}\Big)^5\Big] \tag{1.12}$$

where D_1 is the critical diameter determining the transition from the single domain ferromagnetic regime to the superparamagnetic regime. For maghemite, $D_1 \approx 18$ nm [17].

The description of the coercive field dependence from the particles size in a sample of MNPs is complicated by the MNPs size distribution. In the previous

discussion the size of the particles has always been considered as a constant. However, polydispersions of MNPs are always experimentally observed, and described by a log-normal function:

$$g(R)\mathrm{d}R = \frac{1}{\sqrt{2\pi}\sigma R}\exp\Big[-\frac{(\ln(R/R_0))^2}{2\sigma^2}\Big] \tag{1.13}$$

where σ is the standard deviation on $\ln R$ and $\ln R_0$ is the mean value [8]. The mean particle radius is therefore given by

$$\mu = R_0\exp(\sigma^2/2), \tag{1.14}$$

and the width of the distribution is:

$$\sigma_\mu = R_0\sqrt{\mathrm{e}^{\sigma^2}\cdot(\mathrm{e}^{\sigma^2}-1)}. \tag{1.15}$$

Additional variables should be considered for their effect on H_C when working with colloidal suspensions of MNPs: the dipolar interactions; the concentration of the ferrofluid (i.e. the mean distance between the particles, which influences the dipolar interactions); the anisotropy constant distribution within the sample; the orientation of the particles relative to an external magnetic field; the frequency of the latter field, if oscillating. Some of these aspects will be discussed in Chapter 2 with regard to MFH applications; other details are reported in Refs. [4, 17–21].

1.5 Iron oxide nanoparticles

MNPs for biomedical applications, which will be presented in Chapter 2, are typically made of iron oxides like magnetite (Fe_3O_4) or maghemite ($\gamma{-}Fe_2O_3$). These materials are chosen due to (a) their good biocompatibility and low toxicity, since the body owns metabolic pathways for the iron disposal, and (b) for the strong magnetization occurring from their ferrimagnetic structure.

Magnetite (Fe_3O_4) is organized in an inverse spinel structure with a face-centered cubic unit cell, schematized in Fig. 1.6a [22]. Differently from most of the other iron oxides, magnetite contains both divalent (Fe^{2+}) and trivalent (Fe^{3+}) iron ions. The ferrimagnetic nature of magnetite is due to the interactions among the Fe^{3+} and Fe^{2+} ions on the tetrahedral and octahedral sites. In particular, Fe^{3+} and Fe^{2+} ions, both occupying the octahedral sites, are subject to a double exchange interaction, causing a ferromagnetic coupling. Oppositely, Fe^{3+} ions on the tetrahedral sites interact antiferromagnetically with the Fe^{3+} ions on the octahedral sites. The latter interaction is mediated by the oxygen ions and it is responsible of a zero net magnetization in the Fe^{3+} sublattice [22]. The magnetization of magnetite therefore arises from the unpaired spins of Fe^{2+} ions on the octahedral sites.

Maghemite ($\gamma - Fe_2O_3$), similarly to magnetite, is also organized in a cubic spinel structure, represented in Fig. 1.6b [22]. The two iron oxides are

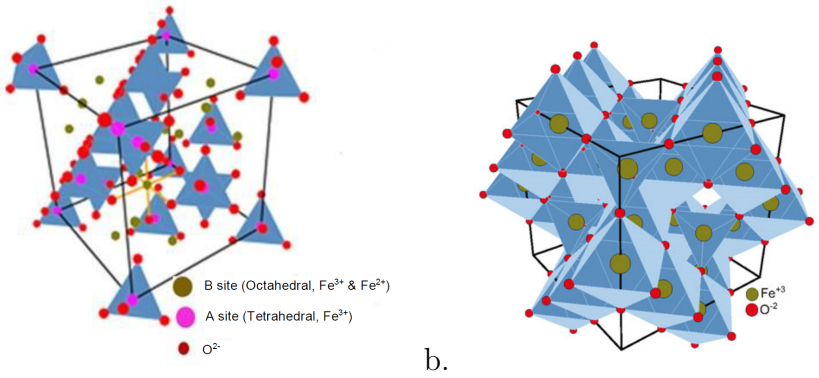

a. b.

Figure 1.6: (a) Magnetite (Fe_3O_4) inverse spinel structure with a face-centered cubic unit cell, with tetrahedral sites occupied only by Fe^{3+} ions and octahedral sites occupied by both Fe^{3+} and Fe^{2+} ions. (b) Maghemite ($\gamma - Fe_2O_3$) cubic spinel structure, similar to that of magnetite, embedding only Fe^{3+} cations which occupy both tetrahedral and octahedral sites (the latter together with vacancies). Images from Ref. [22].

so similar that very few differences are generally observed performing X-Ray diffraction analysis (XRD) on the two materials. However, differently from magnetite, maghemite contains only trivalent iron ions (Fe^{3+}), and the oxidation of Fe^{2+} ions is compensated by cation vacancies. Analogously to magnetite, the Fe^{3+} ions on the octahedral and tetrahedral sites interact via the oxygen ions in an antiferromagnetic coupling, therefore the net magnetization of maghemite is given only by the unpaired spins of the Fe^{3+} ions on the octahedral sites.

Similarities between magnetite and maghemite are not only limited to the crystal structure; the magnetic properties are in fact also quite similar. The saturation magnetization, for example, is $M_S(Fe_3O_4) \simeq 90$ emu/g for magnetite and $M_S(\gamma - Fe_2O_3) \simeq 84$ emu/g for maghemite [24]. The Curie temperature is instead $T_C(Fe_3O_4) \simeq 858$ K for magnetite and $T_C(\gamma - Fe_2O_3) \simeq 893$ K for maghemite.

To distinguish between the two materials, one method consists in looking at the ZFC curve. At $T_V \simeq 115K$, indeed, magnetite undergoes a structural transition known as the Verwey transition [25], which is easily recognizable as a peak in the ZFC curve [26]. The exact temperature depends on the particles size, since T_V translates to lower temperatures while decreasing the MNPs diameter [27]. However, this transition does not occur in the case of maghemite [25, 26].

Chapter 2

Biomedical applications of Magnetic Nanoparticles

In the latest years magnetic nanoparticles (MNPs) are widely spread in the biomedical field as promising tools for increasing the efficiency of both diagnostics and cancer therapy, both techniques already using MNPs in clinics [28–30, 32–38, 57].

In particular, MNPs allow to obtain clearer diagnostic information through a higher image contrast and a better tissue highlighting when utilized as contrast agents for Magnetic Resonance Imaging (MRI) [39–44]. MNPs can indeed be administered to the patient and, in the regions where they accumulate, they shorten the nuclear relaxation times of the ^1H nuclei, whose magnetization produces a signal that can be collected and used to produce an image with diagnostic purposes.

For cancer therapy, MNPs possess the property to release heat when exposed to alternating magnetic fields (AMFs), due to the interactions between their magnetic moments and the field itself. The local heat release in the region where the particles accumulate (commonly they are directly injected into the tumour) allows to weak or kill the tumour cells [8,17,19,45–49]. This treatment is known as Magnetic Fluid Hyperthermia (MFH), and it is already applied for the treatment of poor-prognosis tumours as the glioblastoma multiforme [50].

In this chapter, the physical mechanisms of MFH and MRI with magnetic nanoparticles will be presented. Particular attention will be also given to the theoretical models available to date in literature for describing the Specific Absorption Rate SAR(H, f) trend as a function of the MNPs and field parameters, and the nuclear relaxivity as a function of the proton Larmor frequency in the presence of superparamagnetic centers.

2.1 Advantages and limits of a theranostic approach

Biomedical applications of MNPs commonly exploit iron oxides, which are the preferred materials due to their low toxicity and high biocompatibility. Small MNPs (up to 100 nm) could pass through blood vessels (even capillaries) and their walls, and interacts favorably with the cells of the body, whose average size varies from 10 to 100 μm. Superparamagnetic nanoparticles showing zero remanent magnetization are particularly appreciated in the clinics, since they minimize the risk of aggregation compared to larger particles (large aggregates could indeed cause blood vessels occlusions [19]).

To reduce inter-particle interactions and to increase the colloidal stability, the magnetic core of MNPs is covered with organic moieties, like sugars or other polymers. The coating function is exploited through a both steric and electrostatic repulsion, i.e. thanks to the volume and the charge of its molecules, which increase the distance among neighbouring particles. The coating is also necessary for achieving biocompatibility of the particles, a fundamental condition for injection into the body. Without the coating, the magnetic cores would be immediately recognized as foreign objects by the Reticulo-Endothelial System (RES), and eliminated by macrophages.

A schematic representation of a spherical MNP for clinical applications is presented in Fig. 2.1. It is worth noting that anisotropic particles have been reported to interact more favorably with the biological medium compared to spheres (a literature overview about the effects of the MNPs shape will be reported in Chapter 5) [54, 179–182, 184]. However, spherical particles are commonly preferred, also for theoretical models, thanks to their isotropic properties that allow a simpler description and modelling of the system. For the aims of this Chapter, the attention will be limited to spherical particles.

Fig. 2.1 shows some of the possible applications of MNPs in the biomedical field. In addition to the already cited MFH (therapy) and MRI (diagnostics), which would allow the so-called theranostic approach, Fig. 2.1 introduces the possibility to functionalize the particles with other molecules, embedded within or attached to the coating. These molecules could be (i) targeting agents (for example, antibodies), that allow to target a specific organ or tissue within the body [56]; (ii) fluorophores, i.e. fluorescent molecules to localize MNPs within the body thanks to their light emission; (iii) therapeutic drugs, to be specifically sent to malignant cells using MNPs as carriers. As regard the latter possibility, it is worth noting that it would be possible to exploit the magnetism of MNPs for a magnetic delivery using external magnets [57].

Although MNPs potentials in the biomedical field are promising, several questions still need to be answered before MNPs could reach a wide approval from physicians and from the companies that invest in the pharmaceutical research. In particular, it is still unknown which is the best material, the best size and the best shape of the magnetic core to optimize the MNPs efficiency in

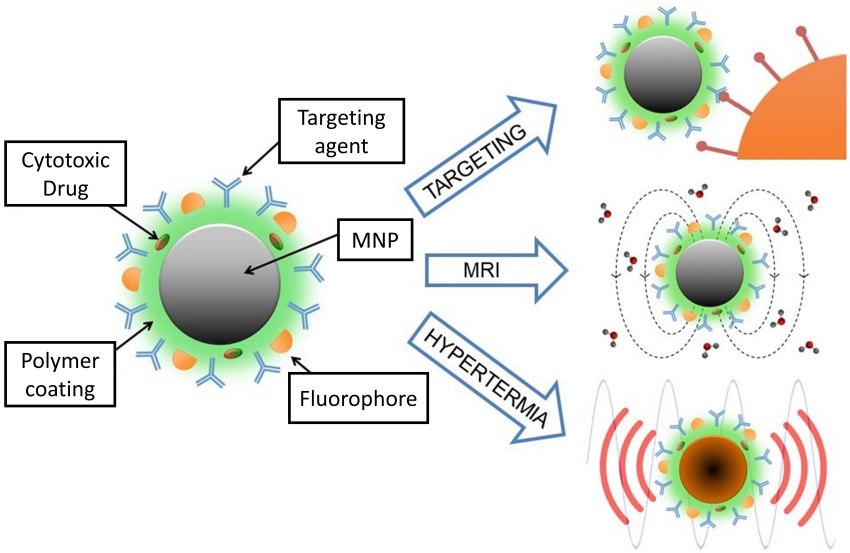

Figure 2.1: Schematic representation of a multifunctional magnetic nanoparticle with its main components: the magnetic core, the organic coating and, possibly, targeting agents, drugs and fluorophores embedded within or attached to the coating. Some of the most interesting applications of MNPs in the biomedical field are also exemplified: targeting of malignant cells within the body, Magnetic Resonance Imaging (MRI) and Magnetic Fluid Hyperthermia. Figure inspired from Ref. [56].

the applications previously listed. New or better coatings have to be developed to optimize the targeting properties cited above and to increase the cellular uptake of MNPs. To date, few synthetic routes exist that allow reproducible synthesis of MNPs with well-defined and tunable features (the problem of standardization is the one the scientific community is facing more seriously, since it must be solved quickly). Finally, no definitive answer has been given to the problem of the MNPs toxicity after they have been administered to the patient.

2.2 Magnetic Fluid Hyperthermia (MFH)

Heat to defeat cancer

Hyperthermia is an antitumoral therapy consisting in a temperature rise up to $42 - 43°C$, with the aim of damaging cancer cells [19, 45]. A mild heating may cause damages to fundamental structures of the cells, like the external membrane, the organelles, the enzymes and the DNA, inducing apoptosis (an organized cell death). If the temperature rises up to higher temperature (i.e. about 45°C), cells damages become so serious to cause necrosis, a totally messy process of cell death (the tissue is burnt) followed by an inflammatory response and systemic effects, that should be possibly avoided.

It has been demonstrated that between 40°C and 44°C a *therapeutic window*

exists [45], since in this temperature range cancer cells stop their growth and result to be more susceptible to chemotherapy and radiotherapy. The latter treatments may be combined with hyperthermia, whose efficiency is not enough to cause the patient complete recovery.

The high susceptibility to temperature of cancer cells compared to healthy cells is mainly due to the disordered vascular network typically characterizing a tumour, being carcinogenesis accompanied by angiogenesis. Consequently, wide regions of the tumours are frequently poor oxygenated and ill-supplied of chemotherapeutic drugs, which reach the tumour passing through the blood vessels [45]. This occurrence lowers also the efficiency of radiotherapy, which arises principally from the indirect interaction between X-rays and Oxygen molecules, producing free-radicals species highly toxic for the cells.

During the hyperthermia treatment, the blood flow within the tumour increases, since blood works also as coolant for the body (although with poor results within the tumour, due to its irregular vascular network). Blood brings more oxygen and eventually drugs to the tumour, increasing the efficiency of both radiotherapy and chemotherapy. Indeed, at high temperatures the DNA repair enzymes denaturate, and their capability to repair DNA damages as those produced by X-Rays decreases.

In addition to the temperature reached during the hyperthermia treatment, its duration is another parameter to be considered, in order to administer the proper thermal dose to the tumour and to avoid over-heating of the surrounding healthy tissues. At $42 - 43$°C, the optimal time length is about 30 minutes [58, 59].

Magnetic Fluid Hyperthermia

A recent alternative method to perform hyperthermia is to employ magnetic nanoparticles exposed to alternating magnetic fields (AMFs). Magnetic Fluid Hyperthermia (MFH), whose physical mechanisms will be widely described in the following section, is already applied in clinics: the german company $MagForce^{©}$ has indeed developed apposite instruments and treatment plans to perform MFH in the hospitals. To date, MFH is performed on patients only in Germany and in the USA, particularly for the treatment of radio-resistant and poor-prognosis tumours like the glioblastoma multiforme and the prostate cancer [50, 60].

In Fig. 2.2 the main steps of the MFH treatment in clinics, according to $MagForce^{©}$ parameters [60], are described. MNPs made of magnetite, with an average diameter of about 12 nm, and suspended in water, at concentration of about 112 mg/mL, are directly injected into the tumour (Fig.2.2a), where they spread in the inter-cellular space (Fig.2.2b) and are subsequently incorporated by cells (Fig.2.2c). MNPs could also remain in the intercellular space or attached to the cell membrane. An average volume of 0.3 mL of ferrofluid per cm^3 of target volume is administered to the patient.

Subsequently, the region to be treated is exposed to an AMF at $f = 100$

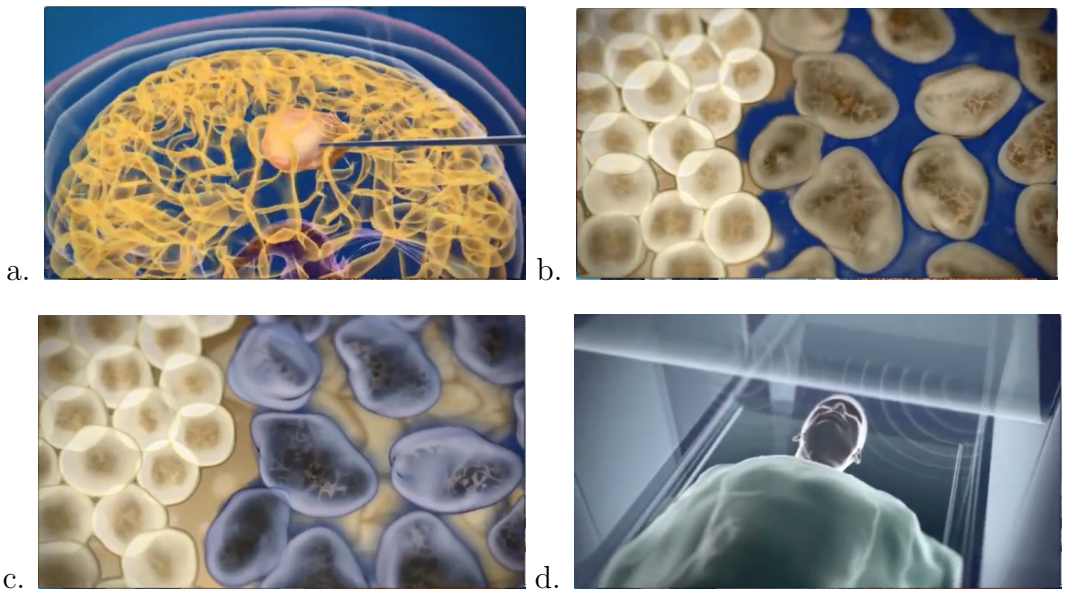

Figure 2.2: Schematic representation of the main steps in a Magnetic Fluid Hyperthermia treatment in clinics. (a) MNPs are directly injected into the tumour (in the picture, a glioblastoma multiforme is considered). (b) MNPs spread in the inter-cellular space between the cancer cells, but not in the surrounding healthy tissues. (c) MNPs are internalized by the cells, or they attach to the cell membrane (*uptake*). (d) The patient is exposed to an alternating magnetic field (AMF) with suitable frequency and amplitude to avoid side effects; the interactions between the MNPs and the AMF is responsible of the heating. Images from a video available on the *MagForce*© company website [60].

kHz and $H = 15$ kA/m. These field parameters are mainly chosen to avoid side effects as eddy currents into the patient body, which may interfere with the nervous system. The safety limit for the application of AMFs to human bodies has been firstly determined experimentally by Brezovich in 1988, who exposed several patients to increasing fields until they felt discomfort [61]. In particular, Brezovich determined an upper limit for the product of the field amplitude and frequency:

$$H \cdot f < 4.85 \cdot 10^8 \,\mathrm{A\,m^{-1}\,s^{-1}}. \tag{2.1}$$

However, this limit is currently under discussion in the scientific community, because side effects depend also on the size of the coils used to apply the field and on the region to be treated (different parts of the body have different electrical conductivity).

The treatment performed by *MagForce*© lasts for 1 hour, during which the temperature is constantly monitored using fiber-optic sensors positioned within the tumour, and it is repeated 2 times a week for 3 weeks. A big advantage of MFH is indeed that MNPs, once injected, remain into the tumour for times long enough to allow the repetition of the treatment [50]. However, the problem of the MNPs disposal and toxicity over long times after the end of the treatment is an open question in the MFH field, that needs to be answered.

2.2.1 Physical mechanisms of heating with MNPs

Heating with MNPs is realized thanks to the interactions between their magnetic moments, or superspins, and the applied alternating magnetic field. Commonly, the physical mechanisms responsible of the heating are classified in two categories: relaxation losses and hysteretic losses. The first ones regard the transfer of energy from the AMF to the particles due to the magnetization reversal in superparamagnetic MNPs, occurring through the Néel and Brown relaxation mechanisms. The second ones refer instead to the heating caused by the domain walls motion in ferromagnetic MNPs, which show an open hysteresis loop. However, although this description allows to distinguish between the heating mechanisms in superparamagnetic and ferromagnetic nanoparticles, it is misleading. All the types of losses are indeed hysteretic losses, also the ones occurring in superparamagnetic particles [47], and the power released by an assembly of MNPs is always proportional to the area of the hysteresis loop:

$$P = A \cdot f \tag{2.2}$$

where f is the frequency of the AMF, whose maximum amplitude is $\mu_0 H_{max}$, and

$$A = \int_{-\mu_0 H_{max}}^{+\mu_0 H_{max}} \mu_0 M(H) \mathrm{d}H. \tag{2.3}$$

Since most of MNPs used for clinical application are superparamagnetic, the most interesting mechanisms to be analysed are those regarding the relaxation losses. In Chapter 1.2 it has already been presented the Néel relaxation, which describes the magnetization reversal towards the anisotropy barrier thanks to the thermal energy in a characteristic relaxation time τ_N (Eq. 1.5). When working with ferrofluids, however, another mechanism is responsible of the reorientation of the MNPs superspin: the Brown relaxation.

Brown relaxation

The Brownian motion of a MNP suspended in a fluid is essentially due to the random collisions between the molecules of the solvent and the particle itself. The torque produced by the sum of the overall contributions determines the rotation of the particles and of its superspin. Assuming the superspin fixed in one position, typically along the easy axis, the reversal of the magnetization happens due to the physical rotation of the particle. The time required for this rotation depends on several parameters of both the MNP and the solvent: the solvent viscosity η, the hydrodynamic volume of the particle V_h, and the temperature T. In particular, V_h account for the total volume of the particle, i.e. the magnetic core (V_M), the thickness of the coating and also the solvent molecules coordinated to the particle surface. It can be expressed by the equation [8]:

$$V_h = \left(1 + \frac{\delta}{R}\right)^3 \cdot V_M \tag{2.4}$$

where δ is the thickness of the sorbed surfactant layer.

The temperature (T) is also an important factor for the Brownian motion, since the higher T, the higher the frequency of the collisions responsible of the rotation, due to the thermal agitation of the molecules of the solvent. Considering all the contributions, the characteristic Brown relaxation time for the magnetization reversal is:

$$\tau_B = \frac{3\,\eta\,V_h}{k_B\,T}. \tag{2.5}$$

The Brownian motion could be responsible of the heating in MFH due to the friction between the particles and the molecules of the solvent. Moreover, changing the orientation of the superspin, the Brownian motion also influences the Néel relaxation time, particularly when an external magnetic field is applied, as for MFH experiments. Brownian rotation may indeed determine a progressive alignment of the easy axes of the particles along the direction of the field, increasing the heating produced by the Néel relaxation (this topic will be discussed in Chapter 4.2). For this reason, to achieve high heating rates, the two mechanisms of Néel and Brown should preferentially have comparable relaxation times, and the Néel relaxation should not be dominant [8].

Heating with superparamagnetic nanoparticles

To account for both the Néel and Brown relaxation times, an effective relaxation time τ is commonly defined:

$$\frac{1}{\tau} = \frac{1}{\tau_B} + \frac{1}{\tau_N}. \tag{2.6}$$

As shown in Fig. 2.3a, τ_N increases exponentially with the core volume, while τ_B increases linearly with the hydrodynamic volume. Consequently, for very small particles τ_N results dominant ($\tau \approx \tau_N$), being 2-3 orders of magnitude faster than τ_B. For large particles, the fastest relaxation time is instead τ_B, and $\tau \approx \tau_B$. For spherical particles, the critical diameter for which $\tau_N = \tau_B$ was approximately determined by Shliomis [4] as:

$$D_S = \sqrt[3]{\frac{24\,k_B\,T}{\pi\,K}}. \tag{2.7}$$

where K is the anisotropy constant.

The capability of the superspin to follow the oscillations of the AMF applied for MFH mainly depends on two parameters: (i) the effective relaxation time τ and (ii) the frequency f of the AMF (i.e. the period T of one oscillation). The way these two parameters are related determines the efficiency of the heating. Indeed, under the action of the AMF a dephasing between the particles superspin and the field is realized, which cause the opening of the hysteresis loop otherwise closed for superparamagnets and, according to Eq.

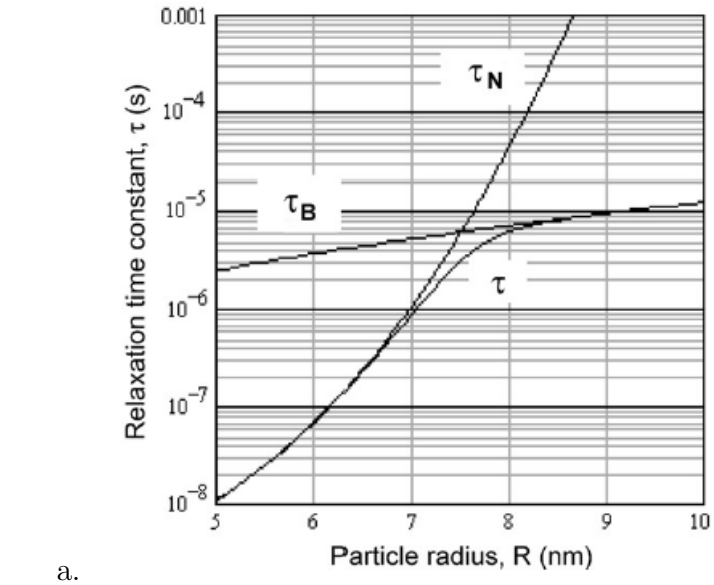

a.

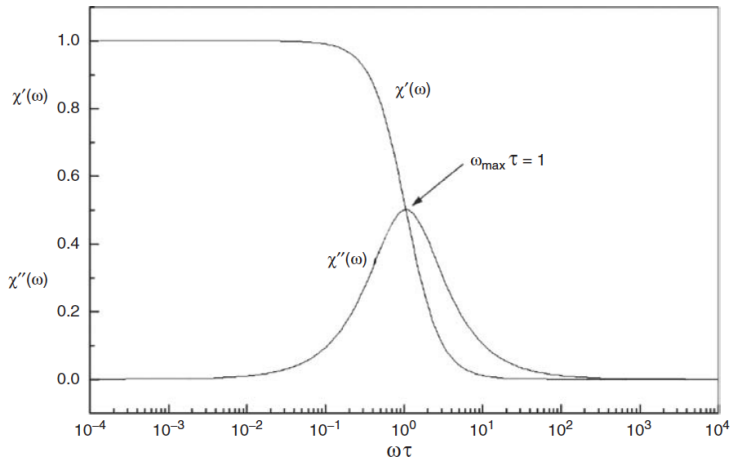

b.

Figure 2.3: (a) Relaxation times (Brown τ_B, Néel τ_N and the effective one τ) simulated for maghemite nanoparticles as a function of the particle radius R. Image from Ref. [8]. (b) Real (dispersion) and imaginary (adsorption) magnetic susceptibility trends as a function of $\omega = 2\pi f$, i.e. of the frequency f of the alternating magnetic field, accordingly to the Debye's theory. Image from Ref. [3].

2.2, the heating. The heating is maximized when a maximum opening of the hysteresis loop (i.e. a maximum dephasing between the superspins and the field) is achieved.

Due to the dephasing between the superspins and the field, the magnetic susceptibility of a MNPs assembly can be expressed as a complex quantity: $\chi = \chi' + i\chi''$, where χ' quantifies the energy dispersion and χ'' the energy adsorption. The magnetic susceptibility strongly depends on the frequency f of the field; introducing $\omega = 2\pi f$ and applying the Debye's theory [3], the

complete expression of $\chi(\omega)$ can be written as:

$$\chi(\omega) = \chi_\infty + \frac{\chi_0 - \chi_\infty}{1 + i\omega\tau} \tag{2.8}$$

where χ_0 is the static susceptibility and χ_∞ the susceptibility at very high frequencies ($f \to \infty$).

For MFH applications, the main interest concerns the adsorption term:

$$\chi''(\omega) = \chi_0 \frac{\omega\,\tau}{1 + (\omega\,\tau)^2} = \chi_0 \frac{2\,\pi\,f\,\tau}{1 + (2\,\pi\,f\,\tau)^2} \tag{2.9}$$

which describes a curve with a maximum at $2\pi f_{max}\tau = \omega_{max}\tau = 1$, as shown in Fig. 2.3b. In Eq. 2.9, the static susceptibility is:

$$\chi_0 = \frac{\mu_0\,M_S^2\,V}{a\,k_B\,T}, \tag{2.10}$$

where M_S is the saturation magnetization of the particles, V the volume of the magnetic core, and a a parameter whose value depends on the shape of the magnetization curve and on the anisotropy. For negligible anisotropy values, it applies $M = M_S L(\xi)$, where $L(\xi)$ is the Langevin function, $\xi = \mu_0 M_S V H_{max}/k_B T$, and $a = 3$. For high anisotropy values, it applies $M = M_S \tanh(\xi)$ and $a = 1$ [47].

As a consequence, samples of MNPs with an effective relaxation time τ that satisfies the condition $2\pi f\tau = 1$ for a given frequency f result to be the most effective ones in terms of heating.

Heating with ferromagnetic nanoparticles

As regards ferromagnetic nanoparticles, a maximum heating in MFH experiments is obtained when the amplitude H_{max} of the applied AMF overcomes the not-null coercive field H_C. Moreover, in multidomain MNPs the heating is essentially due to the movement of the domain walls: the energy provided by the field is transferred to the system to allow the domain walls to overcome the resistance of the domain walls pinning.

For single domain ferromagnetic nanoparticles, the description of the mechanisms responsible of the heating is everything but straightforward. Hergt et al. [17] described the occurrence of particular spin states in these particles, known as *flower* or *vortex* states, and correlated the heating mechanisms in single domain MNPs to those of multidomain MNPs (so-called *pseudo single domain MNPs*). However, as will be discussed in the following sections, the transition region between the single domain and the multidomain ferromagnetic regimes suffers of a lack of models for the theoretical description of the physical mechanisms responsible of the heating.

2.2.2 Specific Absorption Rate (SAR): definition and models

Stoner-Wohlfarth model

To introduce the Specific Absorption Rate (SAR), the first model to be considered is the one proposed by Stoner and Wohlfarth [4,9]. They considered an ensemble of non-interacting ellipsoidal MNPs with a single magnetic domain configuration and uniaxial anisotropy, and assumed the easy axes aligned along the same direction. As discussed in Chapter 1.2, when an alternating magnetic field $H(t)$ is applied, the anisotropy energy of a MNP depends on the angle α between the easy axis and the field, and on the angle θ between the magnetization of the particle and its easy axis. Introducing the quantities

$$\sigma = \frac{K_{eff}V}{k_BT} \tag{2.11}$$

and

$$\xi = \frac{\mu_0 M_S V H_{max}}{k_BT}, \tag{2.12}$$

it is possible to rewrite Eq. 1.6 as:

$$\frac{E(\theta,\phi)}{k_BT} = \sigma \sin^2\theta - \xi\cos(\theta-\phi). \tag{2.13}$$

The dependence of the anisotropy energy on the angle α is directly transferred to the hysteresis loop area, as it is shown in Fig. 2.4. For $\alpha = 0°$, the magnetic field is aligned with the easy axis and, if the maximum amplitude of the applied field overcomes the anisotropy field, i.e. $H_{max} > H_K$ where $H_K = (2K_{eff})/(\mu_0 M_S)$, then the coercive field $H_C = H_K$ and the area of the hysteresis loop is maximized:

$$A = 4\mu_0 H_C M_S = 4\mu_0 H_K M_S = 8K_{eff}. \tag{2.14}$$

In this case the SAR can be simply computed as

$$\mathrm{SAR} = \frac{A\cdot f}{\rho} \tag{2.15}$$

where f is the frequency of the AMF and ρ the MNPs concentration.

When the field is tilted even of a small angle related to the easy axis orientation, the area of the hysteresis loop suddenly decreases, as shown in Fig.2.4, until it becomes equal to zero when the field is applied perpendicularly to the easy axis.

It is worth noting that the situation considered first by Stoner and Wohlfarth is not the more general case. Indeed, ensembles of randomly oriented MNPs would be more realistic, with α changing for each particle. Averaging over the hysteresis loops computed of each particle with its own orientation,

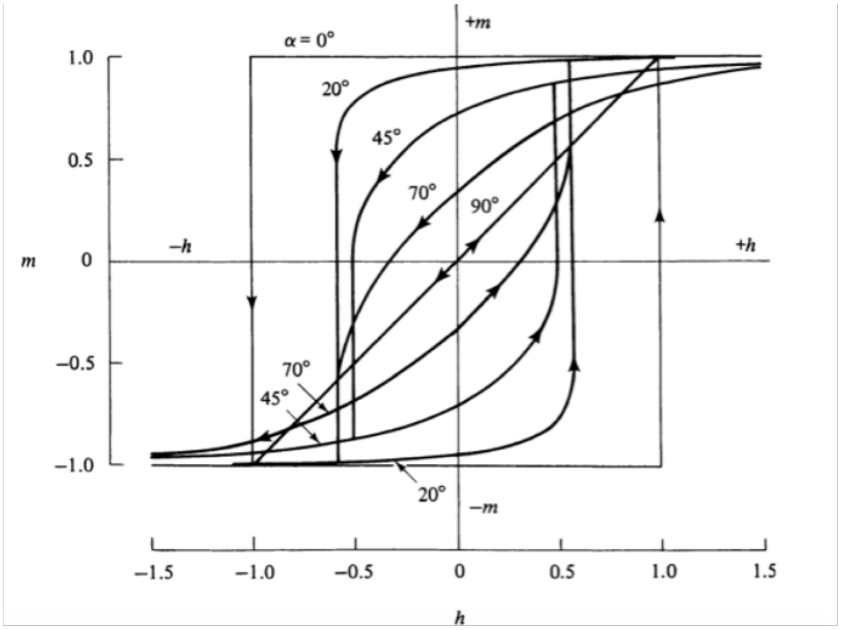

Figure 2.4: Hysteresis loop for single domain MNPs in the Stoner-Wohlfarth model, as a function of the angle α between the easy axis and the external field. On the axes, $h = H/H_K$, where H_K is the anisotropy field, and the normalized magnetization $m = M/M_S$, where M_S is the saturation magnetization. Figure from Ref. [4].

it is found that the system has a remanent magnetization $M_r = 0.5M_S$, and a coercive field $H_C = 0.48H_K$ [47]. The area of the hysteresis loop changes accordingly:

$$A = 4\mu_0 H_C M_R = 4\mu_0 \cdot (0.48H_K) \cdot (0.5M_S) = 0.96\mu_0 H_K M_S = 1.92\, K_{eff} \quad (2.16)$$

giving lower values of SAR.

As it has been shown, the Stoner-Wohlfarth model provides an easy way to compute the SAR for single domain MNPs, but some assumptions must be satisfied. In particular, one condition limits the applicability of this model: the maximum amplitude of the applied field must overcome the coercive field of the system, i.e. $\mu_0 H_{max} > \mu_0 H_C$ when the particles are aligned and $\alpha = 0°$, or $\mu_0 H_{max} > 2\mu_0 H_C$ for randomly oriented MNPs. Only when this condition is satisfied, the maximum opening of the loop is achieved and the previous formulas can be applied.

Moreover, when the size of the particles is so small to determine the transition to superparamagnetism, the thermal reversal of the magnetization described by the Néel relaxation requires a different approach to the problem, due to the progressive reduction of the coercive field.

Linear Response Theory

As reported by Carrey et al. [47], the response of an ensemble of MNPs to an oscillating magnetic field with frequency f is a magnetization

$$M(t) = |\chi| H_{max} \cos(\omega t + \varphi) \tag{2.17}$$

where $\omega = 2\pi f$, $|\chi|$ is the magnitude of the complex susceptibility and φ the dephasing between the field and the magnetization. Consequently, the hysteresis loop described in the plane (H, M) has elliptical shape, with area:

$$A_{ellipse} = \pi H_{max}^2 |\chi| \sin\varphi. \tag{2.18}$$

By rewriting $|\chi| \sin\varphi$ as the imaginary part of the complex susceptibility, it results

$$A_{ellipse} = \pi H_{max}^2 \chi_0 \frac{\omega\tau}{1+\omega^2\tau^2}, \tag{2.19}$$

where χ_0 is the static susceptibility and τ the Néel-Brown relaxation time. Here it must be remembered that, according to Eq. 2.10, the value of χ_0 depends on the high ($\sigma \gg 1$) or low ($\sigma \ll 1$) anisotropy of the MNPs, a factor 3 separating the two cases. $A_{ellipse}$ can be used to compute the SAR according to Eq. 2.15; moreover, using Eq. 2.9 for the imaginary part of the magnetic susceptibility, it follows:

$$\mathrm{SAR} = \mu_0 \, \pi \, f \, \chi''(f) \, \frac{H_{max}^2}{\rho}. \tag{2.20}$$

Eq. 2.20 is the common expression of the SAR in the frame of the *Linear Response Theory* (LRT), which holds if the Langevin function can be approximated as linear, i.e. until $\xi < 1$, that means the thermal energy $k_B T$ overcomes the magnetic energy $\mu_0 M_S H_{max} V$.

The same result of Eq.2.20 can be obtained also through a thermodynamic approach, i.e. by computing the energy transferred from the field to the system [8]. The power released by the MNPs per unit volume is

$$\mathrm{P} = \mu_0 \, \pi \, f \, \chi''(f) \, H_{max}^2, \tag{2.21}$$

therefore $\mathrm{SAR} = P/\rho$.

It must be noted that the LRT applies only to small superparamagnetic nanoparticles, when the Néel and Brown relaxation mechanisms are responsible of the heating. The validity condition $\xi < 1$ implies that, for increasing particle diameter, the maximum field that can be applied to the system in the frame of the LRT decreases quickly:

$$H < \frac{(3)\, k_B \, T}{\mu_0 \, M_S \, V} \tag{2.22}$$

where the factor 3 is present only for low anisotropy MNPs. Hergt et al. [62] represented this limit for magnetite MNPs with anisotropy constant $K =$

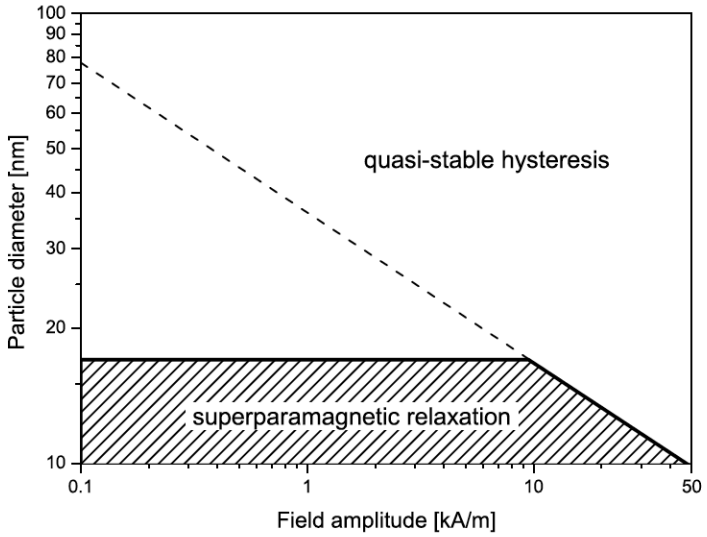

Figure 2.5: Validity limits of the Linear Response Theory (LRT) for magnetite nanoparticles at 400 kHz. Figure from Ref. [62].

$10^4\,\mathrm{J\,m^{-3}}$ at $f = 400$ kHz in Fig. 2.5 (dashed line). Moreover, the continuous horizontal line in Fig. 2.5 represents the critical diameter beyond which the particles stop to be superparamagnetic. Consequently, only the dashed region in the figure can be described by the LRT.

A further consideration on Eq. 2.20: the SAR inherits the frequency dependence of $\chi''(f)$, being maximum when $\tau = 1/(2\,\pi\,f)$, i.e. when a maximum dephasing between the superspins and the field occurs. Looking at Eq. 2.9, it is immediately observed that at low frequencies, i.e. for $f\,\tau \ll 1$, the SAR depends on the square of the field frequency (SAR $\propto f^2$), while at high frequencies, i.e. for $f\,\tau \gg 1$, the SAR saturates to the value $\mu_0\,\chi_0\,H^2/(2\,\tau\,\rho)$.

In the previous discussion, the polydispersity of the MNPs has not be considered. However, the power released by the particles should be integrated over the Log-Normal distribution of Eq. 1.13, giving:

$$\bar{P} = \int_0^\infty P\,g(R)\,\mathrm{d}R. \tag{2.23}$$

As it has been shown by Rosensweig et al. [8], the SAR of highly polydisperse samples of MNPs results to be much lower than that of monodisperse samples. This occurrence is mainly due to the large distribution of the MNPs relaxation times in samples with MNPs with different volumes.

Intrinsic Loss Power - ILP

In the scientific community, a different parameter is often preferred to the SAR to quantify the heating efficiency of MNPs, i.e. the *Intrinsic Loss Power*

(ILP), defined as:

$$\mathrm{ILP} = \frac{\mathrm{SAR}}{f\, H_{max}^2}. \tag{2.24}$$

The main reason of the success of this parameter is that it pretends to eliminate the SAR dependence on the extrinsic parameters of the applied AMF, i.e. its frequency f and its maximum amplitude H_{max}. Indeed, a big problem found in the literature regarding MFH is that, most of the times, SAR values reported by different groups are measured at different field amplitudes and frequencies, an occurrence that does not allow a direct comparison between them. Considering the clear "competition" between different groups to declare the highest values as possible for the SAR of their samples, from hundreds to thousands of W/g, the necessity of a more objective parameter than the SAR to evaluate the heating efficiency, as the ILP should be, is commonly recognized as a priority.

However, it is author's opinion that the ILP is not the best parameter to address this concern, and it could also be misleading. Indeed, it must be cleared first that the ILP completely loses its meaning out of the validity limits of the LRT, for example for ferromagnetic nanoparticles, since the SAR dependence on the amplitude of the field could be higher than quadratic. Moreover, it is not completely true that the ILP is a field-independent parameter: as it has been shown, $\chi''(f)$ entering Eq. 2.20 also depends on the field frequency, therefore it could be wrong to assume a linear dependence of the SAR *vs* f, as it is done by the ILP. For these reasons, the ILP will not be computed in this thesis.

Rayleigh model

When the size of the MNPs increases out of superparamagnetism, the hysteretic losses typical of ferromagnets must be considered. In large ferromagnetic nanoparticles, with a multidomain configuration, the hysteresis losses are due to the movement of the magnetic domain walls, and are also called *Rayleigh losses*. For low magnetic field amplitudes, these losses result to be proportional to the third power of the maximum amplitude of the AMF [63].

Similar hysteretic losses were observed by Hergt et al. [17] for single domain ferromagnetic nanoparticles, where exotic spin configurations may describe the system. However, the dynamic behaviour of these structures is still not completely understood, and Hergt et al. [17] developed a semi-empirical approach to describe the Rayleigh losses. In particular, the coercive field dependence by the particles diameter D of Eq.1.12 was introduced in the formula of the SAR:

$$\mathrm{SAR}(H, D) = \begin{cases} \alpha \cdot D \cdot f \cdot H^3 & \text{if } H \leq H_C \\ \frac{4\, B_r \cdot H_C(D)}{\rho} \cdot f \cdot \left(1 - \left(\frac{H_C(D)}{H}\right)^5\right) & \text{if } H > H_C \end{cases}$$

where α is a parameter that quantifies the contribution of the Rayleigh losses, and $B_r = \mu_0 M_r$, with M_r the remanent magnetization.

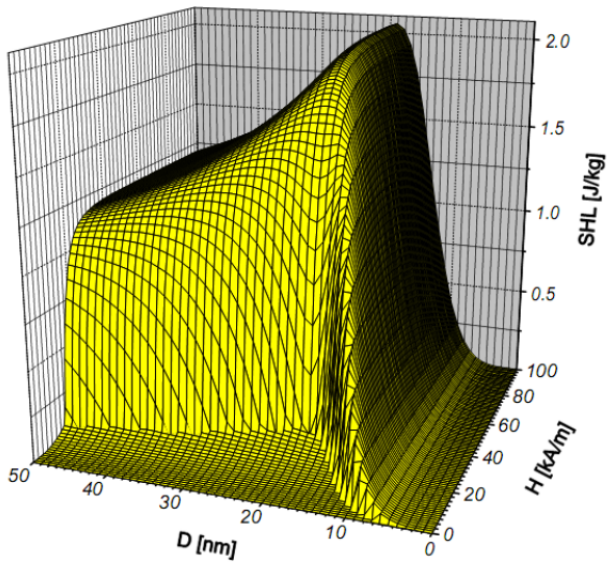

Figure 2.6: *Specific Hysteresis Loss* (SHL) dependence from the MNPs diameter D and the maximum amplitude H of the applied magnetic field. A sharp increase is observed at the critical diameter determining the transition from the superparamagnetic regime to the single domain ferromagnetic regime, and at $H = H_C(D)$. Figure from Ref. [17].

This system of equations allows studying the heating efficiency of MNPs as a function of their diameter D and of the maximum amplitude H of the applied magnetic field. Fig. 2.6 reports the *Specific Hysteresis losses* (SHL), i.e. SHL = SAR$/f$, for maghemite nanoparticles as computed by Hergt et al. [17]. It is immediately observed that for small superparamagnetic nanoparticles the hysteretic losses of the Rayleigh type are almost negligible, while they suddenly increase up to a maximum at the transition diameter from the superparamagnetic regime to the single domain ferromagnetic regime. A further increase in the particle diameter determines a reduction of the SHL due to the progressive closing of the hysteresis loop; in this regard, the trend of the SHL as a function of the particles diameter is strictly connected to the trend of the coercive field $H_C(D)$ reported in Fig.1.4. As regards the trend of the SHL as a function of the field amplitude, a sharp increase up to saturation is observed when H overcomes the coercive field H_C, i.e. when the maximum opening of the hysteresis loop is achieved.

General overview of the models of MFH

Fig. 2.7 reports all the empirical models currently available to describe the SAR as a function of the MNPs size and magnetic properties.

In summary, the Linear Response Theory applies to superparamagnetic nanoparticles, provided that the thermal energy overcomes the magnetic energy, i.e. $\xi < 1$. In the frame of the LRT, an increment of the SAR with the square of the maximum amplitude of the field (H_{max}) is expected. While

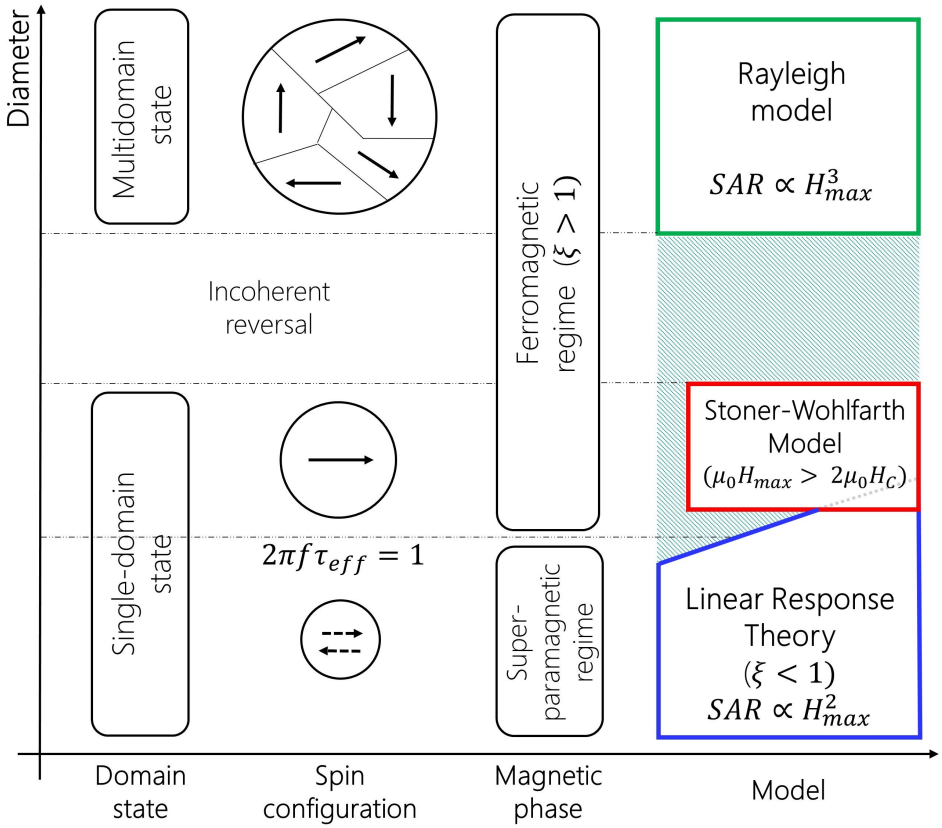

Figure 2.7: Schematic representation of the existing empirical models for the SAR of MNPs in their intervals of validity, as a function of the MNPs diameter and magnetic configuration (single domain/multidomain; superparamagnetic/ferromagnetic). The quantity ξ depends on both intrinsic (V, M_S) and extrinsic (H, T) parameters. The frequency-dependent condition $2\pi f\tau_{eff} = 1$ signs the transition from the superparamagnetic (or unblocked) to the ferromagnetic (or blocked) regime. Image from Ref. [64], inspired from Ref. [47].

increasing the particles diameter, the LRT gradually loses its validity, with the exception of MNPs exposed to progressively lower field amplitudes (oblique blue line in Fig. 2.7).

In the blocked state, i.e. for $2\pi f\tau_{eff} > 1$, where $\tau_{eff} = (\tau_N\,\tau_B)/(\tau_N + \tau_B)$, a ferromagnetic behaviour is observed, even in the single domain state. In this region, the Stoner-Wohlfarth model could be applied to compute the SAR if H_{max} overcomes two times the coercive field H_C of the system (for randomly oriented MNPs) causing a maximum opening of the hysteresis loop. However, it should be stressed that at the fields commonly used for MFH this condition is rarely satisfied.

As well evidenced in Fig. 2.7, a lack of models characterizes the transition region between the superparamagnetic and the ferromagnetic multidomain states. Here incoherent reversal of the magnetization of the particles is commonly observed, and theoretical or empirical descriptions of the physical mechanisms occurring in this region and responsible of the heating in MFH are far from being formulated. Accordingly, an exponent x for the law SAR $\propto H^x$

could not be determined in this region.

Finally, for ferromagnetic nanoparticles the hysteretic losses are responsible of the heating. Since the magnetic fields applied for MFH experiments commonly do not exceed the coercive field H_C of large ferromagnetic nanoparticles, the SAR can be described considering only the so-called Rayleigh losses, which describe an increment of the SAR with the third power of the maximum amplitude of the applied field.

2.3 Magnetic Resonance Imaging (MRI)

Nuclear Magnetic Resonance (NMR) is a powerful technique that exploits the possibility to manipulate the time evolution of the nuclear magnetization by applying simple radiofrequency (RF) pulse sequences [65, 66]. The RF field slightly perturbs the system without changing its properties, producing a resonance signal that provides multiple information about the system. The type of information depends on the characteristic of the RF pulse sequence used for the acquisition, which must be accurately designed [67–69].

NMR is widely applied in several disciplines [70–73], but it is in the medical field that it has found its most successful application with diagnostic purposes in *Magnetic Resonance Imaging* (MRI), being highly appreciated thanks to its low invasiveness and high versatility [74–77]. Clinical MRI is generally exploited by collecting the signal of hydrogen ^{1}H nuclei, which are characterized by a very strong gyromagnetic ratio ($\gamma_{^1\mathrm{H}} = 2\pi \cdot 42.5756$ MHz/T) and a high concentration in soft tissues rich of water, giving therefore a strong RF signal. All the NMR measurements presented in this thesis are performed in water solution, collecting the signal of the protons, therefore the following discussion will be referred only to ^{1}H nuclei.

In this section, a brief recall of the physical basis of NMR is followed by a detailed analysis of MNPs applications in MRI, where they can be used as contrast agents (CAs) to increase the readability of the MR images. To date, paramagnetic molecules (for example Gadolinium-based CAs) are typically used to this aim [78], but a strong interest about MNPs has been developed, since they would allow to combine both diagnosis (MRI) and therapy (MFH) [58].

2.3.1 Basics of Nuclear Magnetic Resonance (NMR)

When an external static magnetic field H_0 is applied to a population of nuclei, with $\vec{H_0}$ typically oriented along $\hat{z}$, a *Zeeman* splitting of the nuclear energy levels occurs, determining the emergence of a net nuclear magnetization $\vec{M}$ (a difference in the population of the two levels of about 1 nucleus over 200000 nuclei is responsible of the NMR signal).

From a classical point of view, the application of the field induces the precession of the nuclear magnetization around $\hat{z}$ with Larmor frequency $\vec{\omega_0} =$

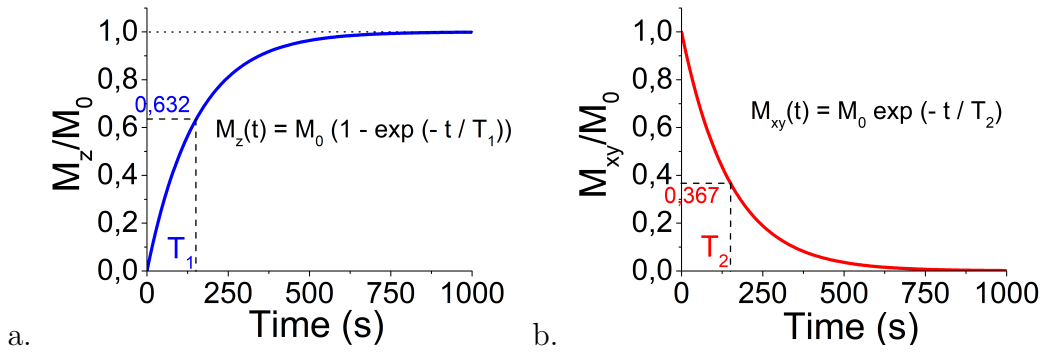

Figure 2.8: (a) Recovery of the nuclear magnetization along $\hat{z}$ with a characteristic longitudinal relaxation time T_1. (b) Decay of the transversal magnetization in the plane $x-y$ with a characteristic transversal relaxation time T_2.

$2\pi\vec{\nu_0} = -\gamma_I \vec{H}_0$, i.e. $\mathrm{d}\vec{M}/\mathrm{d}t = \gamma_I \vec{M} \times \vec{H}_0$, and a rotating frame S' at frequency ω_0 with $\hat{z'} = \hat{z}$ is commonly considered for simplicity.

For NMR experiments, the field H_0 reaches values up to some tesla (T). Around the sample, a small coil oriented along the $\hat{x}$ axis is used to produce radiofrequency (RF) pulses and to collect the resonant signal coming from the nuclei. In particular, each RF pulse consists of a static weak field H_1 in S' (rotating at ω_0 in S), of the order of some mT, which turns the nuclear magnetization $\vec{M}$ according to the equation $\mathrm{d}\vec{M}/\mathrm{d}t = \gamma_I \vec{M} \times \vec{H}_1$. Assuming $\vec{M}$ initially oriented along $\hat{z}$, the amplitude of the *flip angle* depends on the time length δt of the RF pulse, i.e. $\alpha = \gamma_I \, H_1 \delta t$. In NMR sequences, two types of RF pulses are commonly applied: $\pi/2$ pulses, which flip the magnetization of an angle $\alpha = 90°$, i.e. in the plane $x-y$; and π pulses, which flip the magnetization of an angle $\alpha = 180°$, i.e. along $-\hat{z}$.

After a $\pi/2$ pulse, the nuclear magnetization recovers along its equilibrium position $\hat{z}$ (Fig. 2.8a) according to the law:

$$M_z(t) = M_0\left(1 - \mathrm{e}^{-\frac{t}{T_1}}\right), \tag{2.25}$$

while the magnetization in the plane $x-y$ (Fig. 2.8b) decays as described by the equation:

$$M_\perp(t) = M_0 \mathrm{e}^{-\frac{t}{T_2}}. \tag{2.26}$$

In the laboratory frame S, the same time evolution of the nuclear magnetization is described by the *Bloch equations*:

$$\begin{cases} \frac{\mathrm{d}\vec{M}_z}{\mathrm{d}t} = \gamma_I (\vec{M} \times \vec{H}_0)_z + \frac{M_0 - M_z}{T_1} \\ \frac{\mathrm{d}\vec{M}_{x,y}}{\mathrm{d}t} = \gamma_I (\vec{M} \times \vec{H}_0)_{x,y} - \frac{M_{x,y}}{T_2}. \end{cases}$$

As shown, the time evolutions of the longitudinal and transversal magnetizations are defined by two different characteristic relaxation times: T_1 and T_2, respectively. T_1 is called longitudinal relaxation time, or spin-lattice relaxation

time, and it quantifies the time needed to recover the 63% of the magnetization along the direction $\hat{z}$ of the field $\vec{H}_0$. T_2 is instead called transversal relaxation time, or spin-spin relaxation time, and it is due not only to the recovery of the magnetization along $\hat{z}$, but mainly to the different local fields experienced by the nuclei because of the interactions between neighbouring spins. For this reason $T_2 \leq T_1$.

Both the longitudinal and transversal relaxation of the nuclear magnetization produce a variation of the magnetic flux through the coil used to apply the RF pulse, which consequently induce an electromotive force (emf) of some μV that is called *Free Induction Decay* (FID) signal: $S(t) = -\mathrm{d}\Phi_M(t)/\mathrm{d}t$, and that is the actual NMR signal. Being the coil aligned along $\hat{x}$, the FID decays as the transversal magnetization, but with a faster relaxation time called $T_2^\star$, due to the inhomogeneities of the field H_0 and the diffusive motions of the nuclei.

For the measurements of the longitudinal relaxation time T_1, two sequences are commonly applied: the *saturation recovery* sequence or the *inversion recovery* sequence. For the measurements of the transversal relaxation time T_2, instead, the simplest sequence is the *Hahn echo* sequence, but, especially in liquids, it does not allow to compensate for the diffusion effects of the nuclei, therefore resulting in a measurement of $T_2^\star$. For this reason, a *Carr-Purcell-Meiboom-Gill* (CPMG) sequence is commonly preferred for the measurement of T_2 [69].

Fast-Field-Cycling technique

The commercially available spectrometers allow to perform measurements at Larmor frequencies ranging from some kHz ($\mu_0 H_0 < 1$ mT) up to some hundreds of MHz ($\mu_0 H_0 \leq 7$ T, typically). For the measurements at low fields, the *Fast-Field-Cycling* technique is commonly applied [79]. As it can be understood from its name, this technique consists in applying different fields in succession to the sample, switching from one field to another in a very short time, of about 2-3 ms. In particular, three fields are exploited for the measurements: a *polarization field* B_{POL}, a *relaxation field* B_{RLX} and an *acquisition field* B_{ACQ}. All the fields are applied along the same direction, commonly assumed as $\hat{z}$. The switches between the different fields are guided electronically by modulating the current that circulates into the coil that generates the field itself. Unfortunately, the time required for the switch determines a lower limit for the measurement of the relaxation times, since it is not possible to measure T_1 or T_2 faster than the dead time of the instrument.

The *polarization field* B_{POL}, of about 8 mT for the *Stelar SMARTracer* relaxometer used for the measurements of this thesis, is applied first to prepolarize (PP) the sample along the direction of the field, in order to have a stronger signal during the measurement. Hopefully, the magnetization of the sample grows up to saturation; to increase the likelihood of this occurrence, B_{POL} is applied for a time $T_{POL} \simeq 4T_1$. However, for sufficiently high

relaxation fields (B_{RLX}) it is preferable to perform not-pre-polarized (NP) acquisitions (B_{POL} is set to zero), since in a PP sequence the signal is collected by looking at the evolution of the magnetization between B_{POL} and B_{RLX}. Indeed, B_{RLX} is the actual field where the measurement of the relaxation time T_1 (or T_2, although the FFC technique is thought only for T_1 measurements, but it could be adapted also for T_2) is performed. The Larmor frequency of the proton during the relaxation is indeed $\omega_L = \gamma_I B_{RLX}$. Finally, the field is rapidly switched to the higher *acquisition field* B_{ACQ}, that makes the magnetization observable and allows to collect the FID signal.

2.3.2 Proton relaxation induced by superparamagnetic MNPs

Relaxivity and contrast efficiency

When superparamagnetic MNPs, or SPIONs, i.e. *Superparamagnetic Iron Oxide Nanoparticles*, are suspended in a solvent, for example water, their magnetization strongly influences the relaxation times of protons. In particular, T_1 and T_2 of ^{1}H nuclei in the presence of SPIONs (indicated with $T_{i_{obs}}$, with $i = 1, 2$) become shorter than those of protons in the pure solvent (indicated with $T_{i_{diam}}$, with $i = 1, 2$). This fact is exploited for imaging purposes, being the particles able to change the intensity of the NMR signal in the region where they accumulate, allowing for a better tissue highlighting.

The capability of SPIONs (as well as other superparamagnetic or paramagnetic compounds) to work efficiently as MRI contrast agent is evaluated by means of two parameters called the *longitudinal relaxivity*, r_1, and the *transversal relaxivity*, r_2, defined as:

$$r_i = \frac{1}{C}\Big(\frac{1}{T_{i_{obs}}} - \frac{1}{T_{i_{diam}}}\Big) \tag{2.27}$$

where $i = 1, 2$ and C is the molar concentration of the magnetic ions within the solution, expressed in mM (mmol/L). In the case of SPIONs, C commonly refers to the iron molar concentration ([Fe]) within the sample [80].

The way contrast agents (CAs) affect the contrast of a MR image is immediatly understood looking at the dependence from the relaxation times T_1 and T_2 of the signal collected in a typical MRI experiment performed with a classical spin-echo sequence:

$$S(t) \propto \rho(^1H)\, \mathrm{e}^{-\frac{TE}{T_2}} \left(1 - \mathrm{e}^{-\frac{TR}{T_1}}\right) \mathrm{e}^{-bD} \tag{2.28}$$

where $\rho(^1H)$ is the proton density, D the diffusion coefficient, b a constant, TE the echo time and TR the repetition time. The latters are user-defined parameters that allow to design the sequence. If the contrast agent shortens T_1 more than T_2, then there is an increase of the signal intensity in the region where the CA accumulates; this is the case of the so-called *positive* CAs. On

the contrary, if the contrast agent shortens T_2 more than T_1, as is typically the case of SPIONs, the signal intensity decreases in the region where the CA accumulates, and it is marked as *negative*.

Theory of relaxation induced by paramagnetic compounds

The theoretical models for the description of the proton relaxation induced by SPIONs arise from those of paramagnetic compounds, i.e. CAs made by paramagnetic ions (for example Gadolinium). For these compounds, two main contributions are considered for the relaxation, commonly referred to as the *inner-sphere* and *outer-sphere* mechanisms [30, 80]. For the sake of simplicity, these mechanisms will be treated in the case of a vessel (for example a blood vessel), assuming water as the solvent, and only from a classical point of view, although a rigorous quantum theory could be also used to treat rigorously the problem.

The *inner-sphere* contribution, schematized in Fig. 2.9a, describes the dipolar interactions between the paramagnetic compound and the water molecules in the first coordination sphere (on its surface). These interactions fluctuate because of three main mechanisms with well-defined characteristic times: (i) the rotation of the molecule in a time τ_R; (ii) the exchange between the water molecules in the first coordination sphere and those in the bulk water, with a residency time on the compound surface equal to τ_M; (iii) the electronic spin relaxation of the paramagnetic molecule, in characteristic relaxation times τ_{S_1} and τ_{S_2}.

As a result, for the *inner-sphere* contribution two correlation times τ_{C_1} and τ_{C_2} are defined, according to the law:

$$\frac{1}{\tau_{Ci}} = \frac{1}{\tau_R} + \frac{1}{\tau_M} + \frac{1}{\tau_{Si}} \tag{2.29}$$

where $i = 1, 2$.

The *outer-sphere* contribution, schematized in Fig. 2.9b, is instead due to the free bulk diffusion of the protons into the field inhomogeneities produced by the paramagnetic compound, here simply assumed as a single giant spin. This diffusion causes the fluctuation of the hyperfine (dipolar) interactions between the spins of the hydrogen nuclei of the solvent and the electron spins of the contrast agent, with a characteristic diffusion time:

$$\tau_D = \frac{r_d^2}{D} \tag{2.30}$$

where D is the diffusion coefficient (that depends on the solvent) and r_d is the minimum approach distance between the water molecules and the paramagnetic center (a spherical symmetry is assumed).

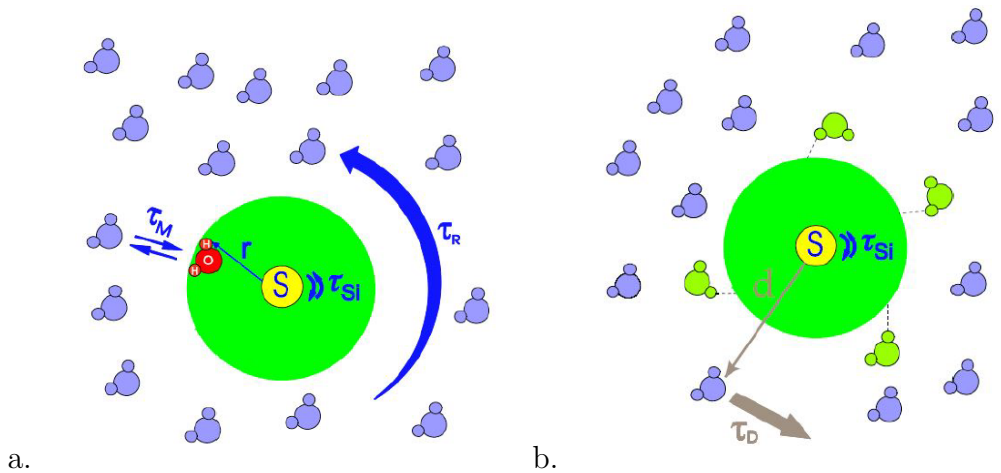

a. b.

Figure 2.9: Schematization of the (a) *inner-shpere* and (b) *outer-sphere* contributions for the proton relaxation induced by paramagnetic compounds. In the figure, S is the paramagnetic ion embedded within a larger molecule (green sphere). The main correlation times are reported: τ_M, i.e. the water molecules residency time in the first coordination sphere (radius r); τ_R, for the rotation of the compound; τ_{S_i}, for the electron spin fluctuations; and τ_D, for the water diffusion [78].

Theory of relaxation induced by SPIONs

In the case of SPIONs, or more generally superparamagnetic MNPs, it was found out that the proton relaxation can be described simply with the same *outer-sphere* model of paramagnetic compounds [81]. The diffusion of the water molecules in the local inhomogeneous field produced by the MNPs is in this case known as *Curie relaxation* [82]. However, in addition to the diffusion, also the Néel and Brown relaxation mechanisms have to be considered.

In the case of USPIOs, i.e. *Ultra Small Particles of Iron Oxides*, only the Néel relaxation is considered, since $\tau_N \ll \tau_B$ due to the small size of the particles. To date, this is the only case that has been theoretically modelled, and the Brown relaxation is commonly neglected. Consequently, the total correlation time is given by:

$$\frac{1}{\tau_C} = \frac{1}{\tau_D} + \frac{1}{\tau_N}. \tag{2.31}$$

The way τ_C correlates with the Larmor frequency ω_I of the nuclear spins determines the efficiency of the fluctuations of the dipolar coupling in inducing the proton relaxation. The maximum efficiency occurs when the condition $\omega_I \tau_C = 1$ is satisfied [80].

Roch's model for proton relaxation induced by SPIONs

The theory of the proton relaxation induced by superparamagnetic nanoparticles has been developed in 1999 by Roch, Muller and Gillis [82]. Since that

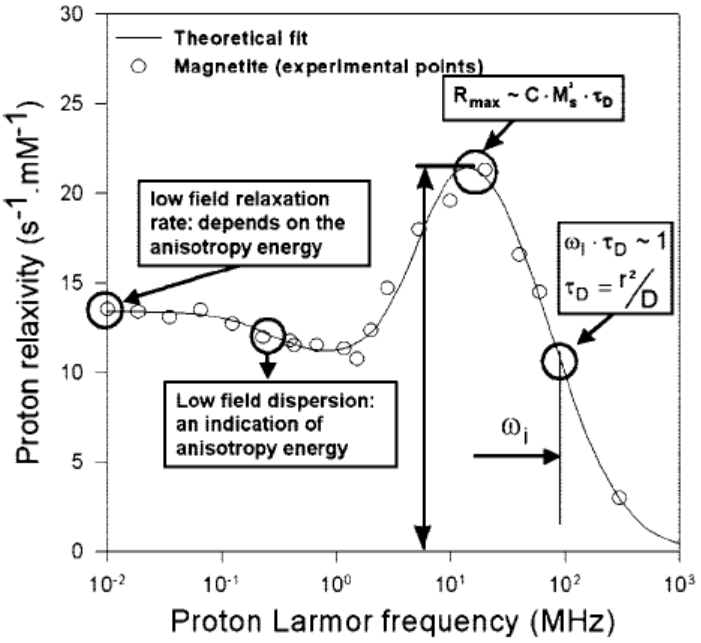

Figure 2.10: Longitudinal NMRD profile for the proton relaxation in the case of a colloidal solution of superparamagnetic MNPs in water. Both experimental data on magnetite MNPs and the fitting curve predicted by the Roch's theory are reported [82]. The main features of the curve and their dependence are also reported on the figure. Image from Ref. [30].

time, other models have been proposed, for example by Levy et al. [83], but their validity was often limited to the case of high anisotropy SPIONs, since the theory failed to fit experimental data of low anisotropy MNPs [81].

The theory developed by Roch aims to explain the shape of the *Nuclear Magnetic Resonance Dispersion* (NMRD) profiles. Indeed, the characterization of the relaxation properties of SPIONs requires the study of the evolution of the longitudinal (r_1) and transversal (r_2) relaxivities as a function of the Larmor frequency, i.e. at different static magnetic fields H_0, ranging from some kHz to hundredths of MHz. A typical longitudinal NMRD profile (r_1) of SPIONs is shown in Fig. 2.10, where the model proposed by Roch is fitted to experimental data [82]. The NMRD profile at high Larmor frequencies (i.e. $\nu_L > 1 - 10$ MHz) is explained by the theory of the Curie relaxation, while the relaxivity at low frequencies is mainly accounted for by the Néel relaxation.

As for paramagnetic compounds, also the NMRD profiles of superparamagnetic MNPs present an inflection point at low frequencies that strongly depends on the magnetic anisotropy of the particles. The inflection point is indeed located at the field H_0 that satisfies the condition $E \cdot \tau_C = \hbar$, where τ_C is the correlation time of Eq. 2.31 and $E = E_Z + E_A$ is total energy of the system, i.e. the sum of the Zeeman energy (E_Z) and the anisotropy energy (E_A). However, differently from the NMRD profiles of paramagnetic compounds, the low field dispersion in SPIONs is commonly attenuated even for very small particles, with a dominant contribution coming from the Zeeman energy, while

it completely vanishes for large particles, with a dominant contribution coming from the anisotropy (in this case $E_A \cdot \tau_C \gg \hbar$) [82]. For this reason, as indicated in Fig. 2.10, the presence of a low field dispersion in the NMRD profile of SPIONs (particles with a mean diameter $d \geq 15$ nm) or USPIOs ($d < 15$ nm) is an evidence of low anisotropy energy. Generally, it is observed only for USPIOs.

The theory proposed by Roch [82] introduces the anisotropy energy as a quantitative parameter of the problem, and it is the only theory to date that is able to fit experimental data of both high and low anisotropy SPIONs. The superparamagnetic nanoparticles are assumed as uniaxial systems, i.e. with a single easy axis determined by the anisotropy. Moreover, three main assumptions are initially formulated for the development of the theory:

(1) The exchange interaction is the largest energy term in the hamiltonian describing superparamagnetic crystals, which includes also the Zeeman term $\mathcal{H}_Z = -\gamma_I \hbar I_z H_0$ and the anisotropy term $\mathcal{H}_A = -E_A(\vec{1_S} \cdot \vec{1_A})$, where $\vec{1_S}$ is the unitary vector aligned with the particle superspin $\vec{S}$ and $\vec{1_A}$ is the unitary vector aligned with the easy axis. The exchange interaction determines the alignment of all the electronic spins within the crystal, whose sum constitutes the superspin.

It is worth noting that this assumption dictates a strong limitation on the MNPs size, since it neglects the existence of *spin waves* into the system (i.e., a collective excitation of the ground spin state of the system, propagating through the crystal lattice as a magnetic wave). Since the energy of spin waves depends on the particle diameter as $E_{SW} \propto d^{-1}$, the first assumption of the Roch's theory limits its validity to small MNPs.

(2) The Néel relaxation time τ_N must be much shorter than the rotational correlation time τ_R, i.e. the time required for the relaxation of the magnetization of the particle must be much shorter than the time required to the particle to rotate (and, particularly, the time required to align the easy axis along the direction of the external field $\vec{B_0}$). As a result, the angle between the easy axis and the external field is assumed as a constant for each MNP, and the relaxation is computed by averaging over the random orientations of the particles.

Since τ_N depends exponentially on the particles volume V (Eq. 1.5), while τ_R (which is related to the Brown relaxation time τ_B) depends only linearly on V (Eq. 2.5), also the second assumption of the theory limits its validity to small particles, in particular with $d < 20$ nm for magnetite MNPs [82].

(3) The Néel relaxation time τ_N is assumed to be the same for all the electronic spin energy levels. This assumption is recognized by Roch et al. [82] as the most questionable one, since it would be correct only if all the spin states had the same occupation probability. Again, this assumption is more likely to be true for small MNPs, i.e. for low anisotropy energy MNPs.

Once fixed these three main assumptions and their consequences, the Roch's model is developed similarly to the *outer-sphere* theory of paramagnets, i.e.

by describing the relaxation as a mechanism induced by the fluctuation of the dipolar interactions between the SPIONs and the hydrogen nuclei. For a complete discussion of the theory, the reader can refer to Ref. [82]. For the aims of this thesis, the two expressions obtained by Roch et al. [82] for the evaluation of the longitudinal and transversal relaxation rates are reported below. In particular, the following equations are not the exact expressions of the relaxation rates, as obtained by the theory, but the result of a further heuristic approach to the problem developed by Roch et al. [82] to overcome computational time constraints.

$$\begin{aligned}\frac{1}{T_1} =& \frac{32\pi}{135000}\mu_{SP}^{\star 2}\gamma_I^2\left(\frac{N_a C}{r_d D}\right)\Bigg\{7P\frac{L(x)}{x}J^F(\Omega(\omega_S,\omega_0),\tau_D,\tau_N)+\Bigg[7Q\frac{L(x)}{x}+\\ &+3(P+Q)\left(1-L^2(x)-2\frac{L(x)}{x}\right)\Bigg]J^F(\omega_I,\tau_D,\tau_N)+3L^2(x)J^A(\sqrt{2\omega_I\tau_D})\Bigg\}\end{aligned} \tag{2.32}$$

$$\begin{aligned}\frac{1}{T_2} =& \frac{16\pi}{135000}\mu_{SP}^{\star 2}\gamma_I^2\left(\frac{N_a C}{r_d D}\right)\Bigg\{13P\frac{L(x)}{x}J^F(\Omega(\omega_S,\omega_0),\tau_D,\tau_N)+\\ &+7Q\frac{L(x)}{x}J^F(\omega_I,\tau_D,\tau_N)+6Q\frac{L(x)}{x}J^F(0,\tau_D,\tau_N)+\left(1-L^2(x)-2\frac{L(x)}{x}\right)\cdot\\ &\cdot\Big[3J^F(\omega_I,\tau_D,\tau_N)+4J^F(0,\tau_D,\tau_N)\Big]+L^2(x)\Big[3J^A(\sqrt{2\omega_I\tau_D})+4J^A(0)\Big]\Bigg\}\end{aligned} \tag{2.33}$$

In Eqs. 2.32 and 2.33:

- $\mu_{SP}^{\star}$ is the effective magnetic moment of the MNPs experienced by the hydrogen nuclei;
- γ_I is the proton (or nuclear, in general) gyromagnetic ratio;
- N_a is the Avogadro number;
- C is the (iron) molar concentration of MNPs;
- r_d is the minimum approach distance between the protons and the MNPs;
- D is the diffusion coefficient of the medium (water);
- $L(x) = \coth x - 1/x$ is the Langevin function, with $x = \mu_{SP}^{\star} B_0/k_B T$;
- τ_D is the diffusion time (Eq. 2.30);

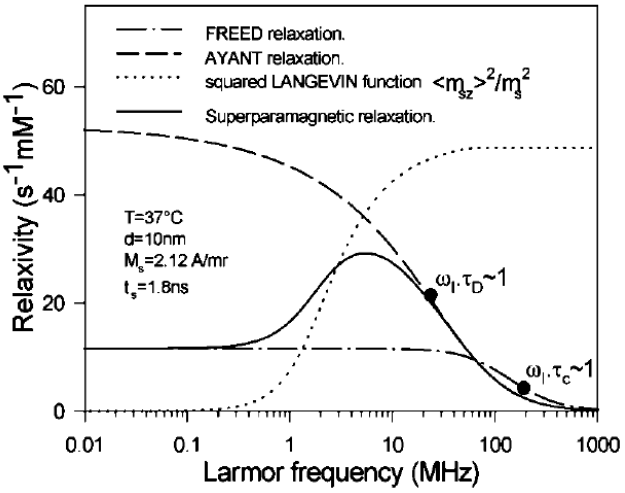

Figure 2.11: Simulated longitudinal NMRD profile for the proton relaxation in the limit of high anisotropy energy (there is no dispersion at low fields) in the case of a superparamagnetic nanoparticle, according to the Roch's theory. The main contribution to the NMRD profile are reported: the Ayant spectral density function describes the high field part of the curve, where the only mechanisms responsible of the relaxation are those of the Curie relaxation; at low fields, the Néel relaxation also contributes and the curve is described by the Freed spectral density function [30].

- τ_N is the Néel relaxation time (Eq. 1.5);
- ω_I and ω_S are the proton and electron Larmor angular frequencies, respectively;
- $\Omega(\omega_S, \omega_0) = (\omega_S^{1/4} - \omega_0^{1/4})^4$ if $\omega_S > \omega_0$, otherwise $\Omega(\omega_S, \omega_0) = 0$;
- ω_0 is an adjustable parameter, with $\omega_0 = 0$ for $E_A = 0$, and it increases proportionally with the anisotropy energy E_A;
- P and Q are two parameters that quantify the Zeeman coupling relative to the anisotropy energy, and are therefore related to the magnetic anisotropy of the system. In particular, P and Q weight the linear combination between the spectral density functions J^F and J^A. For very high anisotropy energy $P = 0$ and $Q = 1$, while $P = 1$ and $Q = 0$ for an anisotropy energy equal to zero. Generally, $P + Q \leq 1$, and the difference $1 - (P + Q)$ quantifies the magnetization fraction that does not contribute to the relaxation, since its precession is too fast [82].
- J^A is the *Ayant spectral density function*, that arises from the Curie relaxation, i.e. from the hydrogen nuclei diffusion through the local inhomogeneous magnetic field produced by the MNPs magnetic moments. It accounts for the case when the Néel relaxation is suppressed, for example due to a strong value of the magnetic field B_0. Consequently, it

describes the right part of the NMRD profile, i.e. at $\nu_L > 1 - 10$ MHz, as shown in Fig. 2.11. J^A is defined as:

$$J_A(z) = \frac{1 + \frac{5z}{8} + \frac{z^2}{8}}{1 + z + \frac{z^2}{2} + \frac{Z^3}{6} + \frac{4z^4}{81} + \frac{z^5}{81} + \frac{z^6}{648}} \tag{2.34}$$

and it shows an inflection point at $\omega_I \tau_D \sim 1$;

- J_F is the *Freed spectral density function*, that accounts for both the Curie and Néel relaxation, therefore it describes the NMRD profile at low fields ($\nu_L \leq 1 - 10$ MHz), as shown in Fig.2.11. It is defined as

$$J_F(\omega_I, \tau_D, \tau_N) = \mathrm{Re}\left(\frac{1 + \frac{1}{4}\Omega^{1/2}}{1 + \Omega^{1/2} + \frac{4}{9}\Omega + \frac{1}{9}\Omega^{3/2}} \right) \tag{2.35}$$

where

$$\Omega = i\omega_I \tau_D + \frac{\tau_D}{\tau_N}, \tag{2.36}$$

and it shows an inflection point at $\omega_I \tau_D \sim 1$.

The validity of the Roch's model has been tested several times in the literature over the last years [81, 84–88]. Great ability of Eq. 2.32 to reproduce the experimental data of the longitudinal relaxivity of superparamagnetic compounds has been verified. On the contrary, poor accordance between the theory of transversal relaxation (Eq. 2.33) and the experimental data has been observed, therefore further efforts will be necessary to implement this part of the model.

Chapter 3

The role of the MNPs size in MFH and MRI

The role of the MNPs size in determining their magnetic behaviour, i.e. superparamagnetic or ferromagnetic, and the features of the hysteresis loop related to the particles diameter have been described in Chapter 1.

The effects of the MNPs size on both the heating efficiency in Magnetic Fluid Hyperthermia (MFH), i.e. on the Specific Absorption Rate (SAR), and on the nuclear relaxivity in Nuclear Magnetic Resonance (NMR) with imaging purposes (MRI), have been instead cited in Chapter 2. In particular, the MNPs size has been introduced as a fundamental parameter in all the theoretical and heuristic models describing the SAR and the relaxivity.

In this Chapter, two experimental studies are presented, which were aimed to test the models of Chapter 2 on experimental data.

The first section of the Chapter focuses on the MNPs size effects in MFH. The study was performed on three samples of maghemite MNPs with different sizes and results were published in:

- Cobianchi, M., Guerrini, A., **Avolio, M.**, Innocenti, C., Corti, M., Arosio, P., Orsini, F., Sangregorio, C., Lascialfari, A., *Experimental determination of the frequency and field dependence of Specific Loss Power in Magnetic Fluid Hyperthermia*, Journal of Magnetism and Magnetic Materials, 444, 154-160 (2017).

The work focuses on the systematic study of the function SAR(H, f), i.e. on the characterization of the SAR dependence on the amplitude H and frequency f of the applied alternating magnetic field (AMF), as a function of the MNPs size.

The same three samples of MNPs were used to study both the longitudinal and transversal Nuclear Magnetic Resonance Dispersion (NMRD) profiles of MNPs as a function of the particles size, and this experimental investigation is presented in the second section of the Chapter. The Roch's model described

in Chapter 2.3 was tested on the experimental relaxivity curves, highlighting some limitations of the theory, in particular when used to fit $r_2(\nu_L)$. Results were published in:

- Basini, M., Guerrini, A., Cobianchi, M., Orsini, F., Bettega, D., **Avolio, M.**, Innocenti, C., Sangregorio, C., Lascialfari, A., Arosio, P., *Tailoring the magnetic core of organic-coated iron oxides nanoparticles to influence their contrast efficiency for Magnetic Resonance Imaging*, Journal of Alloys and Compounds, 770, 58-66 (2018).

In summary, this Chapter presents the main results of the cited papers, which constituted a starting point for the experimental studies of author's PhD project (indeed, measurements were carried out for author's Master Degree Thesis), that will be presented in Chapters 4 and 5.

3.1 Core size effects on SAR

Introduction

This section summarises the work published by Cobianchi et al. [64], which experimentally investigated the SAR dependence on the amplitude and frequency of the applied AMF as a function of the MNPs size. In this paper, SAR is referred to as *Specific Loss Power* (SLP), which is exactly the same parameter although emphasising the energy transfer from the particles to the surrounding medium as an energy *loss* instead of an energy absorption from the AMF.

Particular attention is dedicated to the theoretical models of MFH described in Chapter 2.2.2 and summarised in Fig. 2.7. Data reported in literature often ignore the validity limits of the *Linear Response Theory* (LRT), which is applied without verifying if the condition regarding the magneto-thermal parameter $\xi = (\mu_0 M_S V H_{max})/(k_B T) < 1$ is satisfied. This occurrence is probably due to the lack of models about the physical mechanisms of the magnetic heating in the transition region between the superparamagnetic and ferromagnetic regimes.

A similar study was performed by Mehdaoui et al. [49], which was aimed to determine the optimal MNPs size for obtaining the maximum SAR values. This work was developed both experimentally and theoretically, focusing on the hysteresis loop dependence on the particle size, and exploiting numerical simulations to investigate further on the topic. Authors showed for the first time experimental proofs of theoretical predictions as: (i) the increase of the coercive field with the MNPs size, in the range from 5.5 to 27.5 nm; (ii) a direct correlation between the opening of the hysteresis loop and the SAR; and finally they concluded that (iii) the optimum MNPs size depends on the amplitude of the magnetic field. The latter point has been widely discussed in Chapter 2.2.1.

Table 3.1: Mean diameters of the three MNPs samples as obtained from statistical analysis of TEM and AFM images; saturation magnetization M_S at low ($T = 2.5$ K) and high ($T = 300$ K) temperature; coercive field $\mu_0 H_C$ at low temperature, according to the magnetic characterization of the samples [64].

Sample	d_{TEM} (nm)	d_{AFM} (nm)	M_S at 2.5 K ($\mathrm{A \cdot m^2/kg}$)	$\mu_0 H_C$ (mT)	M_S at 300 K ($\mathrm{A \cdot m^2/kg}$)
A	10.2 ± 1.1	11.4 ± 0.9	62.4 ± 3.4	26.5 ± 1.3	54.6 ± 3.0
B	14.6 ± 1.8	15.6 ± 0.8	67.2 ± 3.7	23.9 ± 1.5	58.3 ± 3.2
C	19.7 ± 1.7	20.5 ± 0.8	69.3 ± 3.8	36.0 ± 1.2	60.9 ± 3.3

Samples

The study performed by Cobianchi et al. [64] investigates further on the above topic by collecting a complete set of SAR(H, f) experimental data on three samples of maghemite ($\gamma - Fe_2O_3$) MNPs with mean core diameters $d = 10.2$ nm, 14.6 nm and 19.7 nm. Detailed information about the particles size are reported in Table 3.1, where results of both the analyses performed with a Transmission Electron Microscope (TEM) and an Atomic Force Microscope (AFM) are shown. TEM allows to measure the size of the inorganic core of the particles; AFM gently touches the external surface of the particles, seeing also the thickness of the organic layer used for the coating and therefore giving an estimation of the hydrodynamic size.

MNPs were synthesized through a thermal decomposition method, starting from metal-organic precursors, and finally coated with PolyAcrylic Acid (PAA) to stabilize them in water solution.

The magnetic characterization of the samples, performed with a SQUID Quantum Design MPMS magnetometer, evidenced differences in the magnetic properties of the samples (Fig. 3.1). In particular, the largest sample (C, with $d = 19.7$ nm) presented the highest values of saturation magnetization M_S and coercive field $\mu_0 H_C$, as listed in Table 3.1, while the intermediate (B, with d =14.6 nm) and smallest (A, with d =10.2 nm) samples showed intermediate and the lowest values of M_S, respectively.

Broad maxima were observed in the ZFC-FC curves of the samples A and B collected in the range $2 \leq T \leq 300$ K at $\mu_0 H = 5$ mT, suggesting a broad distribution of the MNPs sizes. No maxima were detected in the ZFC curve of sample D, evidencing a blocked state even at room temperature.

MFH measurements and results

The SLP (or SAR) of the three samples was evaluated systematically as a function the frequency f and amplitude H of the applied AMF, working at room temperature on 1 mL of MNPs suspensions in water at mean concentration of about 3.5 mg($\gamma - Fe_2O_3$)/mL. Measurements were performed using a

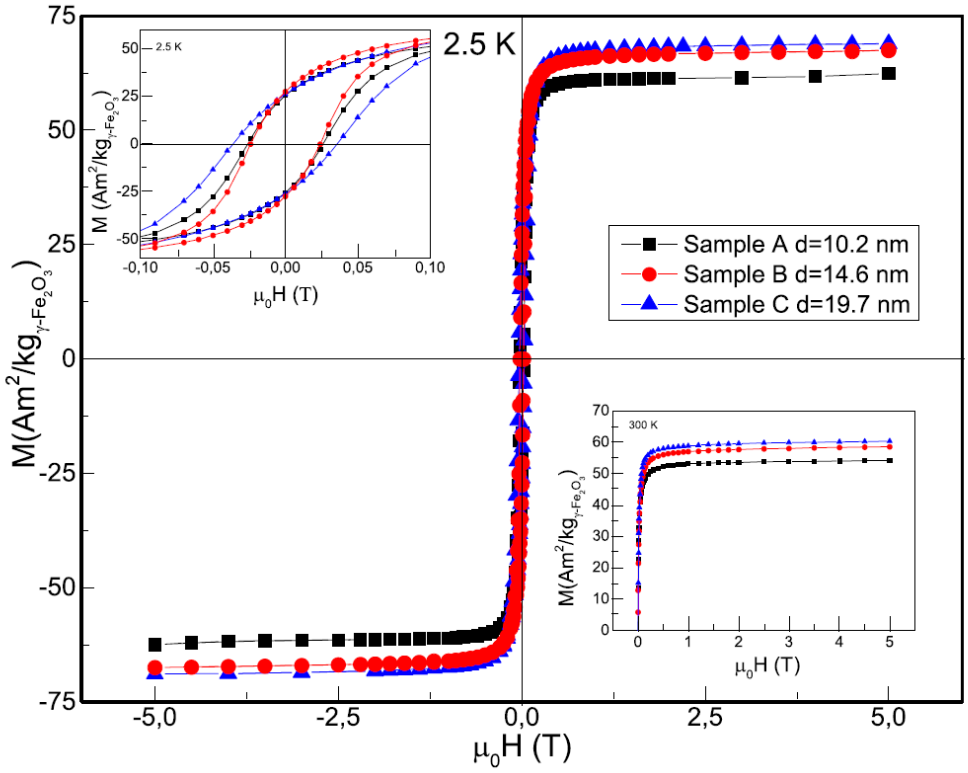

Figure 3.1: Hysteresis loops of three samples of MNPs with different core sizes (diameter d), measured at T = 2.5 K. The left inset highlights the coercive field, while the right inset the first magnetization curves at 300 K [64].

nanoTherics MagneTherm^{TM} setup (for details, see Appendix A.2), working in the frequency range 100 kHz $< f <$ 1 MHz and with amplitude values H from 3 kA/m to 17 kA/m. An Optocon^{TM} fiber-optic temperature probe was used to measure the temperature of the sample.

The SAR of the samples was computed measuring the temperature increment rate $\Delta T/\Delta t$, and multiplying this value for the specific heat of the ferrofluid (details on the measurements of the SAR performed with the same experimental setup will be given in Chapter 4). Results are shown in Fig. 3.2.

As can be immediately seen from Fig. 3.2, the SAR of sample C is the highest one at all the investigated amplitudes and frequencies of the AMF, while samples A and B present similar SAR values, being slightly larger those of sample B. These results mean that the SAR increases with the particles size, at least up to 20 nm, i.e. up to the transition from the superparamagnetic to the single domain ferromagnetic regime. This behaviour could be explained considering an increasing opening of the hysteresis loop (area A), being the SLP proportional to its area (SLP $= f \cdot A/\rho$). Furthermore, the SAR increases with the amplitude H of the AMF, with a power law that has been widely studied in comparison with the predictions of the theory.

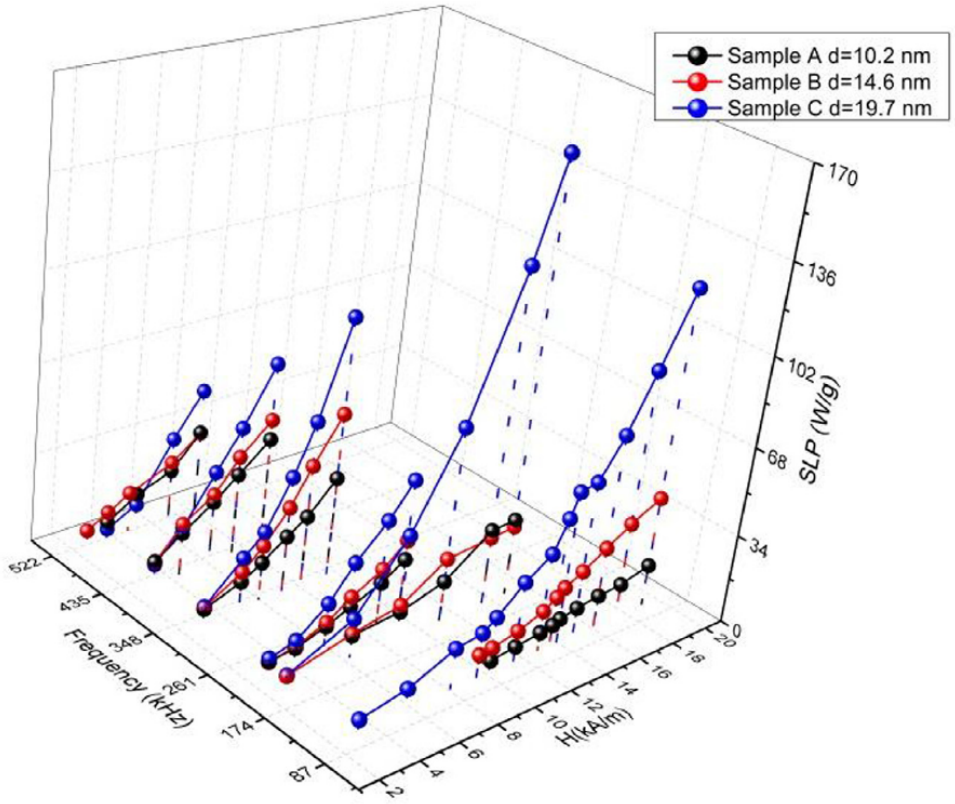

Figure 3.2: Specific Loss Power (SLP) or SAR of three samples of maghemite MNPs with different sizes measured for different frequencies and amplitudes of the alternating magnetic field [64].

Fitting heuristic models to experimental data

The LRT predicts SLP $\propto H^2$ (Eq. 2.20) [8], although its validity is limited to the case $\xi = (\mu_0 M_S V H_{max})/(k_B T) < 1$ [47]. From the latter condition, a maximum field amplitude for the applicability of the LRT can be easily determined by Eq. 2.22. According to this limit, LRT applies only to sample A: coloured shadowed zones in Fig. 3.3 indeed evidences the values of H_{max} for each sample.

At $f = 110$ kHz the LRT was fitted to the SAR experimental data of all the samples, describing correctly only the SAR of sample A. For the other two samples, a fit performed with a free-exponent power law, i.e. $SLP \propto H^x$, described a SAR dependence on H greater than quadratic (LRT), but smaller than cubic (Rayleigh model). All the values of the exponents x from best fits are reported in Table 3.2.

As expected, for sample A it resulted $x \simeq 2$ at all the investigated frequencies, in good agreement with the LRT predictions. On the other hand, for samples B and C the larger values of x (even increasing with the field frequency) could be explained by the progressive tendency towards the blocked

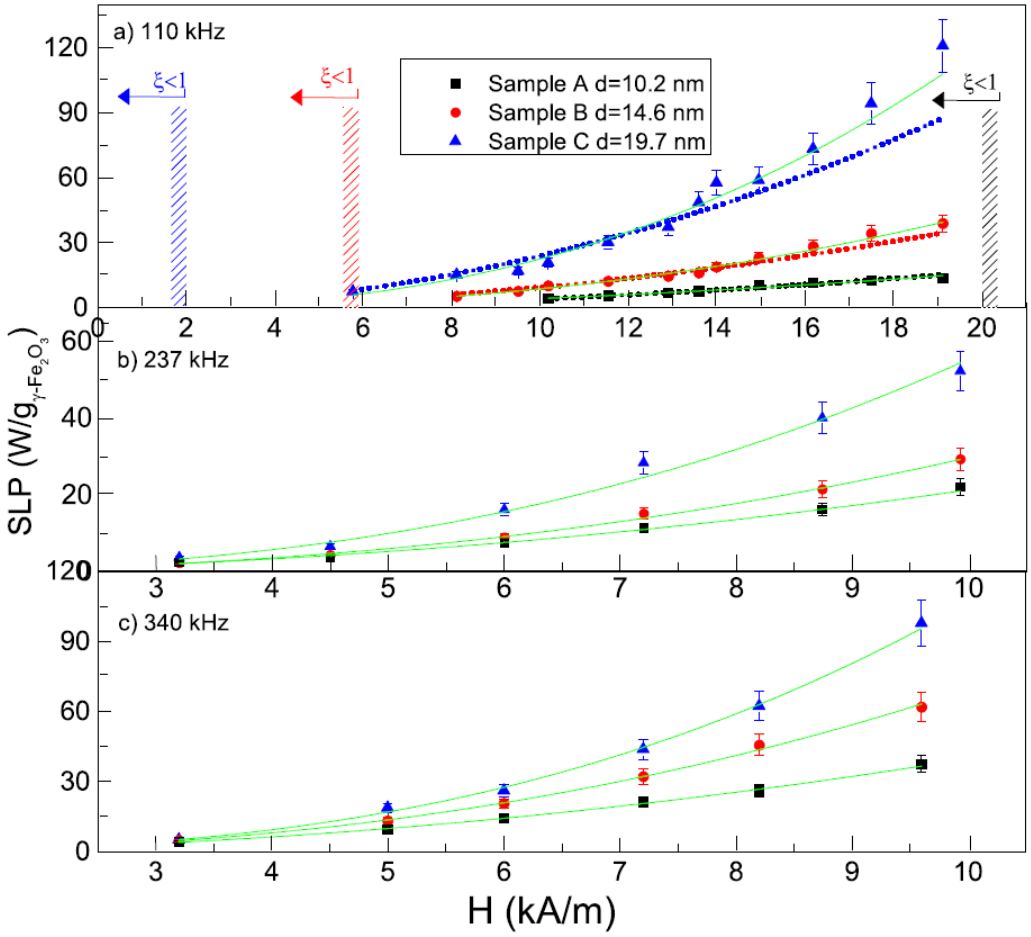

Figure 3.3: Specific Loss Power (SLP) as a function of the amplitude of the applied AMF for three samples of maghemite MNPs with different sizes, at $f = 110$ kHz (a), $f = 237$ kHz (b) and $f = 340$ kHz (c). The maximum field for the applicability of the LRT ($\xi < 1$) is evidenced for each sample by a shadowed coloured zone. Fits with the LRT (SLP $\propto H^2$) are represented by dotted lines. Fits with a free-exponent power law (SLP $\propto H^x$) are represented by continuous green lines. Sample A shows a good agreement with the predictions of the LRT, while for samples B and C it results $2 < x < 3$. Error bars on the SLP were fixed at the 10% of the value [64].

ferromagnetic regime of these samples, occurring at $2\pi f \tau_{eff} = 1$ (Fig. 2.7). Similar results were indeed also reported by Wijaya et al. [89] on Fe-doped gold nanoparticles.

Estimation of the relaxation times

The effective relaxation time τ_{eff} can be easily estimated for sample A, by inverting Eq. 2.20 and using the parameter α obtained from the best-fit of the LRT (function SLP $= \alpha H^2$) to the experimental SAR(H) data. Indeed, it results

$$\alpha = \frac{\mu_0 \, \pi \, f \, \chi''(f)}{\rho} \tag{3.1}$$

Table 3.2: Values of the free-exponent x obtained from the fits of the SLP(H) experimental data at three different frequencies with the power-law SLP $\propto H^x$ [64].

Sample	x at 110 kHz	x at 237 kHz	x at 340 kHz
A	2.0 ± 0.1	2.03 ± 0.01	2.09 ± 0.09
B	2.23 ± 0.08	2.30 ± 0.02	2.34 ± 0.03
C	2.3 ± 0.1	2.47 ± 0.09	2.64 ± 0.06

and

$$\chi''(f) = \frac{\rho}{\mu_0 \pi f}\alpha. \tag{3.2}$$

From Eq. 2.9 it is known that

$$\chi''(f) = \frac{\mu_0 \phi M_S^2 V}{3k_B T} \frac{2\pi f \tau_{eff}}{1 + (2\pi f \tau_{eff})^2} \tag{3.3}$$

where the factor 3 is introduced due to the random MNPs orientation [47], and

$$\phi = \frac{M_{\gamma-Fe_2O_3}}{\rho_{\gamma-Fe_2O_3}} \cdot \frac{1}{V_f} \tag{3.4}$$

is the mass fraction of maghemite within the ferrofluid, being $M_{\gamma-Fe_2O_3}$ the mass of maghemite within the sample, $\rho_{\gamma-Fe_2O_3}$ the maghemite density (4.9 g/cm^3), and V_f the total volume of the sample.

V and M_S in Eq. 3.3 can be replaced by the values determined by the TEM and magnetic characterization, and Eqs. 3.2 and 3.3 can be solved to determine the only unknown variable τ_{eff}. For sample A, it results $\tau_{eff} = 19.5 \pm 2.3$ ns.

The latter value can be compared to the value obtained by applying directly the formulas for τ_N (Eq. 1.5) and τ_B (Eq. 2.5), reminding that $1/\tau_{eff} = 1/\tau_N + 1/\tau_B$. The anisotropy constant entering τ_N can be computed from the hysteresis measurements at low temperature by reversing the approximated formula

$$\mu_0 H_C = 0.96 \frac{K}{M_S}\left[1 - \left(\frac{T}{T_B}\right)^{0.77}\right], \tag{3.5}$$

obtaining $K = 1.8 \cdot 10^4$ J/m^3. The hydrodynamic volume V_h entering τ_B can be computed using the diameter seen by AFM (Table 3.1). It results $\tau_N = 17.6 \pm 2.5$ ns and $\tau_B = 890 \pm 20$ ns, therefore $\tau_{eff} \simeq \tau_N$ [64]. This result is compatible with the value of τ_{eff} obtained from the fit with the LRT, despite the many approximations done for the computation.

Conclusions

In conclusion, the systematic investigation of the heating performances of maghemite MNPs with different mean diameters showed that their SLP (or

SAR) increases with the particle diameter up to 20 nm, having an H-dependence that strongly depends on the particles size. The LRT only applies to small superparamagnetic nanoparticles (sample A), while it fails to describe the SAR of large MNPs at the transition region from the superparamagnetic and the ferromagnetic regimes. In its validity region, the LRT allows to estimate the effective relaxation time of the particles, being almost equal to the Néel relaxation time in the case of small MNPs.

3.2 Core size effects on nuclear relaxivity

This section summarises the work published by Basini et al. [86], which experimentally studied the NMRD profiles of MNPs with different size, trying to fit the heuristic model proposed by Roch [82] to the experimental data.

Samples

The samples of MNPs used for this study were the same used for the work presented in Chapter 3.1, with mean diameter $d = 10.2$ nm (NP_10), $d = 14.6$ nm (NP_14) and $d = 19.7$ nm (NP_19). The local spin dynamics and the contrast efficiency of these maghemite nanoparticles for MRI were probed by means of proton (^{1}H) nuclear magnetic resonance (NMR) relaxation measurements in a wide Larmor frequency range, i.e. 10 kHz $\leq \nu_L \leq$ 60 MHz.

NMR measurements

To collect the NMRD profiles, the longitudinal and transversal relaxation times T_1 and T_2 were measured at room temperature using a Stelar SMARtracer relaxometer at $\nu_L \leq 9.5$ MHz, which make use of the fast-field-cycling technique, and a Stelar Spinmaster Fourier Transform nuclear magnetic resonance spectrometer (FT-NMR) at $\nu_L \geq 9.5$ MHz. T_1 measurements were performed using not-prepolarized Saturation Recovery (SR) pulse sequences at $\nu_L \geq 7.2$ MHz, and pre-polarized SR sequences at $\nu_L \leq 7.2$ MHz. T_2 measurements were instead performed by means of not-prepolarized CPMG pulse sequences at $\nu_L \geq 7.2$ MHz, and pre-polarized spin-echo sequences at $\nu_L \leq 7.2$ MHz (controlling the magnetic field homogeneity) [86].

Results

The obtained experimental NMRD profiles are shown in Fig. 3.4. In green, the relaxivity values of ENDOREM, a commercial nanoparticles-based MRI contrast agent (dismissed from the market due to few costumers), are reported for comparison. Differently from the MNPs of the present study, ENDOREM is made by nanoparticles of about 4.8 – 5.6 nm [90], coated with Dextran, with mean total size ranging from 50 to 180 nm.

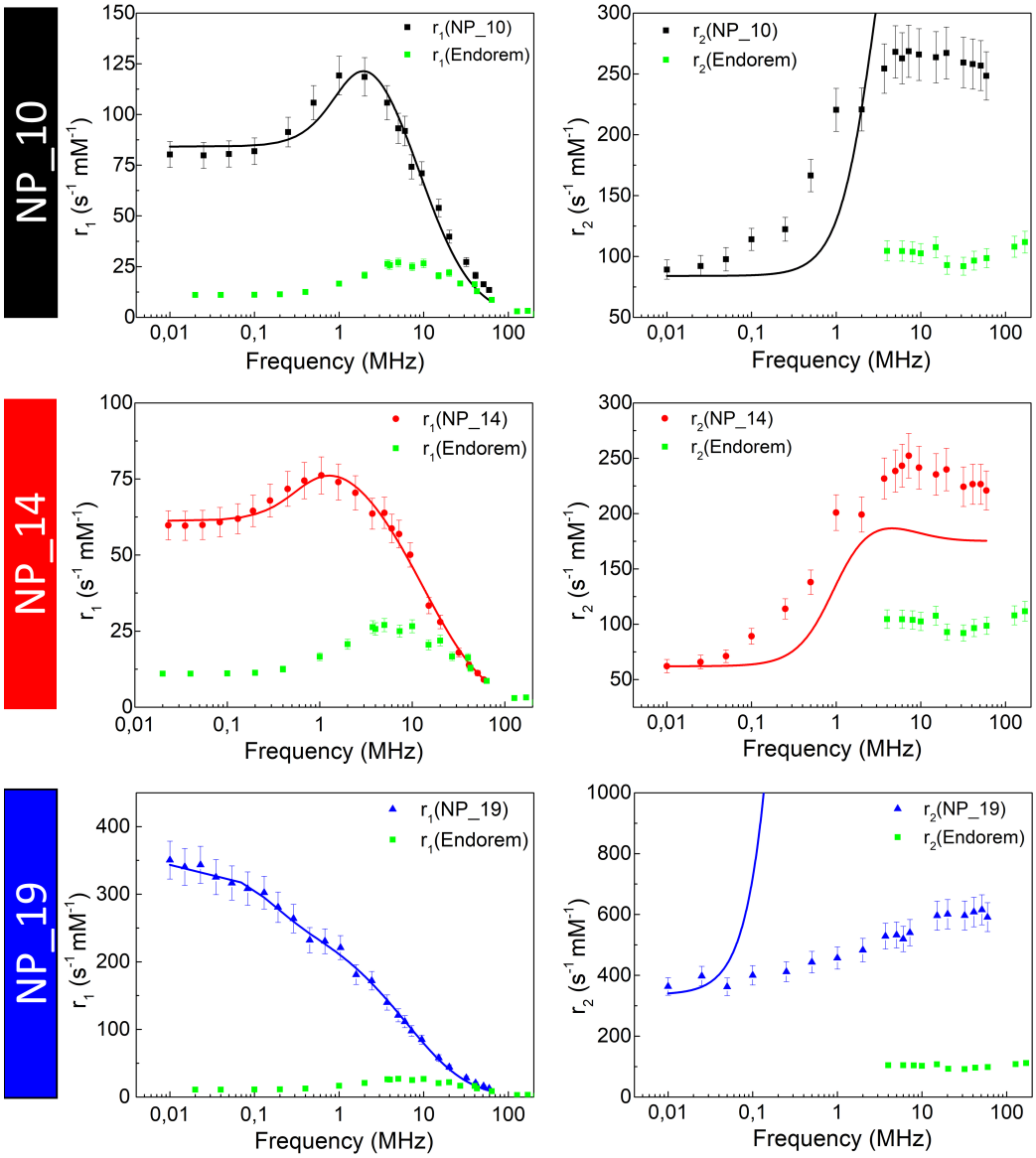

Figure 3.4: NMRD profiles of three samples of maghemite MNPs with different sizes: d = 10.2 nm (label NP_10), d = 14.6 nm (label NP_14) and d = 19.7 nm (label NP_19). The longitudinal (r_1) and transversal (r_2) relaxivity values collected at room temperature in the frequency range 10 kHz $\leq \nu_L \leq$ 60 MHz are reported in the graphs on the left and on the right, respectively. Error bars are set to the 8% of each value. For r_1, the solid lines represent the best-fit curves of the Roch's heuristic model (see text) to the experimental data. For r_2, the best-fit parameters found for r_1 were introduced in Eq. 2.33 to obtain the simulated NMRD profiles according to the Roch's heuristic model for r_2 (solid lines). The longitudinal and transversal relaxivity values of ENDOREM (a commercial nanoparticle based contrast agent for MRI) are reported as green symbols for comparison. [86].

Looking at Fig. 3.4, the first consideration regards the shape of the NMRD profiles, in particular those of r_1 (graphs on the left). Samples named NP_10 and NP_14 show very similar longitudinal NMRD curves, with the typical behaviour of iron oxides nanoparticles with core diameter above 9 nm but

smaller than 16-18 nm: (i) a flattening is recorded at low Larmor frequencies, (ii) a maximum is observed at $\nu_L \simeq 1$ MHz, and finally (iii) a drop occurs in r_1 at $\nu_L \geq 10 - 20$ MHz (depending on the particle diameter). These features are correctly predicted by the theory [82], as well as the disappearance of the maximum in the NMRD profile of MNPs larger than 16-18 nm [30, 81, 83, 91], as it is the case of sample NP_19.

Regarding the values of r_1, the three samples of MNPs (and in particular NP_10) have much higher longitudinal relaxivity values than ENDOREM, and these results may induce the conclusion that they could be suitable as T_1-contrast agents. However, magnetic nanoparticles, even included ENDOREM, are commonly used as T_2 (i.e. negative) contrast agents, because of their much higher values of r_2 compared to r_1 at the clinically most relevant Larmor frequencies (i.e. 63 MHz, 21.2 MHz and 8.5 MHz for ^{1}H-NMR, corresponding to magnetic fields of 1.5, 0.5 and 0.2 T, respectively). As a result, the very high loss of signal caused by the transversal relaxation makes MNPs not suitable as T_1 (i.e. positive) contrast agents for MRI.

The three graphs on the right of Fig. 3.4 evidence the just discussed occurrence, i.e. the three samples show very high values of r_2, which result to be much higher than r_1 at high Larmor frequencies, although a flattening and a convergence of the r_1 and r_2 values is observed at low ν_L as predicted by the theory [82]. Samples NP_10 and NP_14 show again very similar transversal NMRD profiles, having $r_2 \simeq 250\,\mathrm{s^{-1}mM^{-1}}$ at $\mu_0 H \simeq 1.41$ T. Sample NP_19 results to be the most efficient one, having $r_2 \simeq 610\,\mathrm{s^{-1}mM^{-1}}$ at the same field. However, all the three samples result to be much more efficient than ENDOREM, the compound here assumed as main reference of good (transversal) contrast efficiency.

Fitting $r_1(\nu_L)$ and $r_2(\nu_L)$ with the Roch's heuristic model

In addition to the previous qualitative interpretation of the NMRD profiles of Fig. 3.4, it is possible to use the graphs in the figure to test the heuristic model for the longitudinal (Eq. 2.32) and transversal (Eq. 2.33) relaxation rates developed by Roch et al. [82], presented in Chapter 2.3.2. It is worth noting that Eqs. 2.32 and 2.33 must be implemented in Eq. 2.27 to obtain the nuclear relaxivity instead of $1/T_1$ and $1/T_2$. Best-fits of the model to the experimental data are shown in Fig. 3.4 as continuous lines.

As described in Chapter 2.3.2, the Roch's model explain the nuclear relaxation as a phenomenon that arises from the hyperfine interactions between the nuclear magnetic moments of the hydrogen nuclei of the solvents and the MNPs magnetic moments. In particular, MNPs create a local inhomogeneous magnetic field that causes the fluctuation of the hyperfine (dipolar) interaction due to (i) the superspin reversal along the particles easy axis (Néel relaxation), and (ii) the diffusion of protons into this field (Curie relaxation).

Eq. 2.32, obtained from an heuristic approach, fits very well experimental r_1 data reported in Fig. 3.4 (graphs on the left). The fitting procedure of the

r_1 NMRD profiles was realized using the parameters P and Q (which quantify the anisotropy energy of the system) and the Néel relaxation time τ_N as the only free parameters of the model, fixing all the other parameters entering Eq. 2.32. In particular:

- r, i.e. the magnetic core radius, was fixed according to TEM measurements;
- $\mu^{\star}_{SP}$, i.e. the effective MNPs magnetic moment, was obtained from the magnetic measurements (M_S) and TEM measurements (r), implementing $\mu^{\star}_{SP} = M_S \cdot m_{\gamma-Fe_2O_3} = M_S \cdot \rho_{\gamma-Fe_2O_3} \cdot V$ into the fitting code, where $V = 4/3\,\pi\, r^3$.
- C, i.e. the iron molar concentration of MNPs (C_{Fe}), was fixes as $C_{Fe} =$ 1 mM from ICP-MS (Inductively Coupled Plasma Mass Spectrometry) measurements;
- D, i.e. the diffusion coefficient of the solvent (water), was fixed as $D = 1.92 \cdot 10^{-9}\,\mathrm{m^2 s^{-1}}$ as obtained from NMR spectroscopic measurements performed by means of ^{1}H pulsed gradient spin echo sequences.
- T, i.e. the temperature of the system, was kept constant at the room temperature value $T = 300$ K.
- r_d, i.e. the minimum approach distance between the protons and the MNPs, was constrained to vary within a limited range going from the core radius seen by TEM to the hydrodynamic radius seen by AFM measurements.

It is worth noting that the diffusion time τ_D entering Eq. 2.32 is immediately derived from the parameters r_d and D, being defined (and implemented) as $\tau_D = r_d^2/D$ (Eq. 2.30). Moreover, it was discussed in Chapter 2.3.2 that the Roch's model is based on three main assumptions that limit its validity to small MNPs, with diameter $d < 20$ nm. Despite this limit, the model fits successfully also the NMRD profile of the largest MNPs of sample NP_19, returning acceptable physical parameters from the fit.

The values of the free parameters returned by the best-fit procedure applied to all the three samples are reported in Table 3.3. As expected, the Néel relaxation time increases with the particle size (i.e. the spin dynamics - the superspin reversal rate along the easy axis - slow down), assuming reasonable values as $\tau_N \propto 10^{-8} - 10^{-9}$ s for the two samples NP_10 and NP_14. For the sample NP_19 (sample D in the previous section) it was already observed from the ZFC measurements discussed in Chapter 3.1 that this sample is dynamically blocked at room temperature, therefore it is not surprising to have obtained a very long τ_N compared to the other samples.

Table 3.3: Values of the free parameters τ_N (Néel relaxation time), P (related to the anisotropy energy of the system) and r_d (minimum approach distance) as obtained from the best-fits of the r_1 experimental NMRD profiles (Fig. 3.4, upper graphs) with the Roch's heuristic model of Eq. 2.32. [86].

Sample	NP_10	NP_14	NP_19
τ_N (s)	$(1.9 \pm 0.4) \cdot 10^{-9}$	$(2.73 \pm 0.01) \cdot 10^{-8}$	> 10
P	0.7 ± 0.1	0.1 ± 0.1	0 ± 0.1
r_d (nm)	16.0 ± 4.0	15.2 ± 0.6	21.2 ± 1.8

Table 3.4: Values of the MNPs mean volume V computed using the diameter reported in Table 3.1, the anisotropy constant K obtained from the magnetic measurements at low temperature reported in Table 3.1 and by applying Eq. 3.5, and the parameter P (related to the anisotropy energy of the system) from Table 3.3.

Sample	V (m^3)	K (J/m^3)	P
NP_10	$(5.6 \pm 1.8) \cdot 10^{-25}$	8.2 ± 0.4	0.7 ± 0.1
NP_14	$(1.6 \pm 0.6) \cdot 10^{-24}$	7.9 ± 0.5	0.1 ± 0.1
NP_19	$(4.1 \pm 1.0) \cdot 10^{-24}$	12.7 ± 0.5	0 ± 0.1

The parameter P quantifies the magnetic anisotropy energy of the system, being $P \simeq 0$ characteristic of highly anisotropic systems and $P \simeq 1$ characteristic of not anisotropic systems. Values of P reported in Table 3.3 describe an increasing magnetic anisotropy with the particles size, in accordance with the theory.

To further discuss the latter observation, the values of the parameters P obtained from the fits are reported in Table 3.4 near to the mean volume of a single nanoparticle in each sample and the corresponding anisotropy constant K. The values of K were obtained from the magnetic measurements (the coercive field $\mu_0 H_C$ and the saturation magnetization M_S) by applying the approximated formula in Eq. 3.5, which holds at temperatures much lower than the MNPs blocking temperature ($T \ll T_B$). In particular, the values of $\mu_0 H_C$ and M_S evaluated at low temperature ($T = 2.5$ K) and reported in Table 3.1 were used.

Results reported in Table 3.4 show that the highest value of the anisotropy constant is obtained for the largest sample NP_19, coherently with the lowest value of the parameter P obtained from the fits with the Roch's model. This occurrence is reasonably ascribed to a dominant contribution of the volume anisotropy, being the core material the same for the MNPs of the three samples.

Finally, the values of r_d in Table 3.3 could be used to determine whether the MNPs coating made of PAA is permeable or not to the molecules of the solvent (i.e. water molecules in the present case). This information can be ex-

tracted by comparing the r_d values in Table 3.3 with the hydrodynamic radius r_{AFM} measured by AFM and the core radius r_{TEM} measured by TEM, both reported (the diameters) in Table 3.1. If $r_{\mathrm{TEM}} \leq r_d \leq r_{\mathrm{AFM}}$, the coating is fully or partially permeable to water molecules; if $r_d \geq r_{\mathrm{AFM}}$, the coating is completely impermeable. For samples NP_10, NP_14 and NP_19, r_d is approximately compatible with r_{AFM} within the experimental errors; this suggests an impermeability of the PAA coating.

As regards the fit of the r_2 NMRD profiles reported in the graphs on the right of Fig. 3.4, best-fit curves were obtained by applying the heuristic model of Eq. 2.33, where all the parameters were fixed accordingly to the values obtained from the best-fits of r_1. As it could be immediately observed from the graphs, the model fails completely in reproducing the experimental data. It is possible to speculate on the reasons of such difference, looking at the physical mechanisms that are not considered within the model, such as:

- the water molecules exchange between a first coordination sphere and the bulk;
- the Brownian motion of MNPs and the corresponding Brown relaxation time;
- the spins motion on the MNPs surface;
- the magnetic interactions between MNPs, which could affect the transversal relaxation (r_2) much more than the longitudinal one (r_1).
- multi-axial anisotropy (the model assumes a single easy axis).

Universal scaling law for T_2

In addition to the previous considerations, that would necessitate a deeper theoretical study to implement the listed mechanisms into the Roch's model, results of r_2 were compared to the *universal scaling law* proposed by Vuong et al. [92]. The cited law consists in an approximate model that applies to MNPs in the so-called *Motional Averaging Regime* (MAR), i.e. MNPs that satisfy the Redfield condition $\Delta\omega\tau_D < 1$, where τ_D is the diffusion time, $\Delta\omega = \gamma\mu_0 M_V/3$, and M_V is the volumetric saturation magnetization [93, 94]. In particular, $\Delta\omega$ represents the angular Larmor frequency shift at the equator of the MNPs as experienced by the ^1H nuclei. Under this condition, protons diffuse freely around the particles and they experience all the possible values of the inhomogeneous magnetic field produced by the effective electronic magnetic moment $\mu^{\star}_{SP}$.

Introducing the volume fraction of magnetic material ϕ_{intra} for the cases of aggregates or clusters, Vuong et al. [92] determined an empirical law that correlates r_2 to the MNPs size (their diameter d) in the MAR (when $\Delta\omega\tau_D <$

1) and that correctly reproduces most of the experimental data reported in literature:

$$\frac{r_2 \times \phi_{intra}}{M_V^2} = a_{exp} d^2 = 11.6 \times 10^{-12} d^2. \tag{3.6}$$

It is worth noting that a_{exp} is an empirical parameter, which slightly differs from the parameter $a_{theo} = 5.9 \times 10^{-12}$ predicted by the theory [81].

Results reported in this work [86] were shown to be in very good accordance with the universal scaling law of Eq. 3.6, in particular at high Larmor frequencies ($\nu_L \simeq 60$ MHz) where the Roch's model was proved to be not able to properly describe the transversal relaxation.

Conclusions

The role of the size of MNPs in affecting the proton nuclear relaxation properties has been studied: large magnetic nanoparticles ($d > 14$ nm) show higher longitudinal and transversal relaxivity values than small MNPs ($d \leq 14$ nm), at least in the investigated size range from 10 to 20 nm. This occurrence is reasonably due to the higher magnetic moment (i.e. superspin) of large magnetic nanoparticles, which locally affects the hyperfine dipolar interactions between each particle and the surrounding protons, making the nuclear relaxation faster.

Moreover, also the shape of the NMRD profile is strongly affected by the particles size, having large nanoparticles a dominant contribution coming from the magnetic anisotropy that causes the disappearing of both the flattening of r_1 at low ν_L and the maximum of r_1 at $\nu_L \simeq 1$ MHz.

The Roch's heuristic model [82] has been fitted successfully to the longitudinal NMRD profiles of the three samples of MNPs with different sizes, obtaining interesting and physically reasonable information about the microscopic properties of the MNPs from the best-fits procedure. The expression for the transversal relaxivity has been instead proved to fail in describing the transversal NMRD profiles, probably due to the lack of some important physical mechanism for r_2 in the theory.

Finally, the good accordance observed between the experimental data and the *universal scaling law* proposed by Vuong et al. [92] allowed to conclude that, at least for MNPs with core diameters up to 20 nm, the largest the particles the higher the contrast efficiency (r_2) for MRI.

Chapter 4

Role of the Brownian motion in MFH

In Chapter 2 the different contributions of the Néel and Brown relaxation to the heating in Magnetic Fluid Hyperthermia (MFH) have been discussed, focusing the attention on the size dependence of τ_N and τ_B (Fig. 2.3a). However, in addition to the dependence on the size of the particles, the Brown relaxation presents also a linear dependence on the viscosity η of the medium, i.e. $\tau_B \propto \eta$ (Eq. 2.5), which has a strong impact in MFH.

The capability of MNPs (i) to move freely in the dispersant medium and (ii) to rotate in their position (Brown relaxation) are important phenomena with relevant consequences on their heating efficiency. Indeed, as regards point (i), MNPs free to move in space could form chain-like structures that have been proved both experimentally [95] and theoretically [96] to enhance the Specific Absorption Rate (SAR) thanks to their advantageous dipolar interactions. As regards point (ii), the rotation of the particles could allow their alignment (of their easy axes) along the direction of the external magnetic field applied for MFH.

In this Chapter, the role of the Brownian motion of MNPs on their heating efficiency is widely studied exploiting both experimental measurements in viscous media (section 2.1) and kinetic Monte Carlo simulations (section 2.2). Results of section 2.1 have been published in:

- **Avolio, M.**, Guerrini, A., Brero, F., Innocenti, C., Sangregorio, C., Cobianchi, M., Mariani, M., Orsini, F., Arosio, P., Lascialfari, A., *In-gel study of the effect of magnetic nanoparticles immobilization on their heating efficiency for application in Magnetic Fluid Hyperthermia*, Journal of Magnetism and Magnetic Materials, 471, 504-512 (2019).

Numerical simulations of Section 2.2 have been performed during a two-months research period at the *Laboratoire de Physique et Chimie des Nano-Objets*, Institut National des Sciences Appliquées (INSA) de Toulouse, in

Toulouse (France), with the precious help of Prof. Julian Carrey, who kindly allowed the author of this thesis to further elaborate on a Monte Carlo code previously developed in his research group [47, 104].

4.1 Experimental study of SAR of MNPs in water and in agarose-gels dispersions

Numerous literature studies report on the MNPs immobilization within the cells [97–100] or, more in general, into the tumour tissues [101]. Moreover, experimental measurements have been performed in viscous media modelling the *in-vitro* condition [102, 103], showing a general decrease of the MNPs heating efficiency that has been attributed to the suppression of the Brownian motion. Despite these evidences, most of experimental measurements of the SAR reported in literature are performed in aqueous colloidal solutions, where also the Brownian relaxation plays an important role.

It can be immediately understood that the research for the most efficient MNPs, i.e. MNPs with outstanding SAR values that would allow performing MFH treatments in clinics with a minor injection of magnetic material into the body of the patient, could be strongly affected by the SAR dependence on the viscosity of the medium. Indeed, the SAR measured in water could be much higher than the SAR really occurring in tumour tissues if MNPs are immobilized within the cytoplasm, on the cell membrane, or aggregate within the cells (for example when they are stored at high concentration into lysosomes) [104–112]. As a consequence, in-water characterization of the MNPs heating efficiency could lead to misleading conclusions about the actual characteristics of the most efficient systems for *in-vivo* MFH [113, 114].

To investigate this effect, a systematic study of the SAR of colloidal suspensions of magnetite nanoparticles in water and in agarose gels has been performed. In particular, agarose gels with different mass fractions (0.5% and 2%) were prepared to simulate the tumour environment, which present different viscosities depending on the nature of the tissue (for example soft tissues or bones).

Experimental findings highlight that, for a translation of the SAR values to the clinical cases of human tissues, the evaluation of the MFH efficiency of MNPs in media other than water is mandatory.

4.1.1 Introduction

In this section a brief overview of the literature reporting on the effects of the suppression of the Brownian motion on the SAR is reported.

The comprehensive study of the SAR in cellular conditions by Di Corato et al.

One of the most comprehensive study on the topic is with no doubts the one reported by Di Corato et al. [97]. Authors studied systematically the SAR of different types of MNPs in water and in cell environments, reporting a systematic decrease of the heating efficiency when nanoparticles were immobilized in cellular conditions, due to the inhibition of the Brownian relaxation. In particular, authors performed the study on human adenocarcinoma cells, (i) pelletizing the cells at high concentration (20 millions of cells in 150 μL of culture medium), (ii) adding enough MNPs to reach iron concentrations of 50 or 25 mM within the samples, and (iii) applying AMFs with frequency ranging from 300 kHz to 1.1 MHz and amplitudes up to 24 kA/m. Maghemite spherical nanoparticles (d = 10 nm), MNPs (d = 10 nm) embedded within liposomes, cobalt ferrite nanoparticles (d = 9.2 nm), iron oxide-gold dimers (d = 14 nm), iron oxide nanocubes (d = 18 nm) and iron oxide nanoflowers (d = 22 nm) were tested.

Depending on their properties, MNPs resulted to attach to the cell membranes (few pg of iron per cell) or to be internalized by the cells (from 6 to 20 pg of iron per cell) after 2 hours incubation. In all cases, a drop in the Specific Loss Power (SLP) was observed in cellular conditions, whether the particles were internalized within vesicles or attached to the cell membrane. Depending on the particles type, the drop of the SLP resulted more or less marked but always greater than the 50%. An example of the SLP values measured in water and in cellular conditions for spherical maghemite nanoparticles is reported in Fig. 4.1a.

Authors tested the same particles also in highly viscous glycerol, observing a drop in the SLP values compared to water, but without a direct correlation with that observed in cellular conditions. Magnetic measurements (in particular hysteresis loops and ZFC-FC curves) performed on cell samples containing magnetic nanoparticles at the transition from the superparamagnetic regime to the ferromagnetic regime gave a clear evidence of the particles immobilization in the cellular environment. The results reported by Di Corato et al. [97] lead authors to ask the following questions to the reader: "*are the targeted nanoparticles, which can only reach low concentrations in their target cells, really suitable for therapeutic magnetic hyperthermia? Or should efforts be restricted to intratumoral injection of hydrophobic nanoparticles, which do not interact with cells and thus remain in the liquid phase of the extracellular tumor environment?*". These questions are still unanswered, but precisely highlight one of the most important open issue in the field of MFH.

The AC susceptometry study by Soukop et al.

Soukop et al. [98] applied AC susceptometry to study *in situ* the magnetic response of superparamagnetic (d = 10.5 nm) and blocked (d = 23.8 nm)

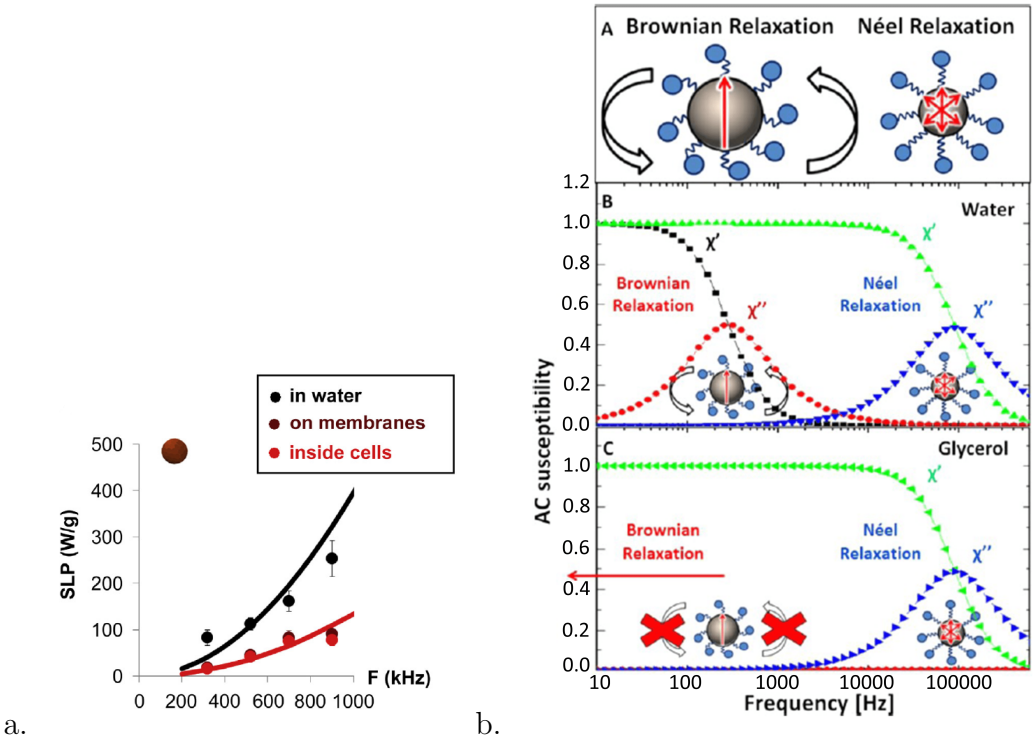

a. b.

Figure 4.1: (a) Specific Loss Power (SLP) of maghemite spherical nanoparticles (d = 10 nm) dispersed in water and in cellular conditions, showing a drop in the SLP when MNPs are immobilized (attached on the cell membrane or internalized by the cells) [97]. (b) Schematic representation of the Néel and Brown relaxation mechanisms of MNPs (A) and their AC susceptibility curves (in-phase χ' and out-of-phase χ'' components) in water solutions (B), showing two dispersions due to the Néel and Brown relaxation, and in glycerol (C), showing only the dispersion due to the Néel relaxation because of the high viscosity of glycerol [98].

nanoparticles after cellular internalization, using osteosarcoma cells. Interestingly, authors observed an AC susceptibility signal (a maximum in the out-of-phase component of the magnetic susceptibility χ'') arising only from the Néel relaxation, attesting the particles immobilization within the cells (Fig. 4.1b). An AC susceptibility signal arising from the Brown relaxation was instead restored only after cells lysis. Results presented by Soukop et al. [98] have two main implications: (i) they proof the MNPs immobilization in cellular conditions and (ii) they demonstrate that the particles immobilization within the cells is a reversible phenomenon, i.e. the nanoparticles integrity is preserved into the cells. The latter occurrence suggests that MNPs could be reused after the first hyperthermia treatment if it leads to cells destruction, since MNPs could be reabsorbed afterwards by other viable cells, allowing for a repetition of the therapeutic procedure.

In-vivo evidences of MNPs immobilization in tumour tissues by Dutz et al.

A different *in-vivo* study of the MNPs immobilization in living tissues was performed by Dutz et al. [19]. Authors employed maghemite multicore nanoparticles (MCNPs), or clusters, with mean diameter between 40 and 60 nm, injected into tumours that were grown in immunodeficient mice through subcutaneous injection of human adenocarcinoma cells.

Upon sacrifice, tissues were analysed and particles were observed to distribute homogenously into spots within the tumours. *Ex-vivo* tissues were subjected to magnetic measurements (hysteresis loops) and results were compared to those acquired both on magnetic nanoparticles suspended in water (i.e. free to move) and immobilized in gelatin.

Besides small differences in the remanence and coercivity, probably due to partial MCNPs aggregation during their immobilization in gelatin, a very good agreement was registered between the measurements performed on the tumour and those performed on the gelatin sample, while large differences were observed for the loop measured in water. Consequently, the behaviour of MCNPs in living tissues was concluded to be more similar to the behaviour of MCNPs in gelatin than that in water, which attests the immobilization of the particles into the tumour.

As a result, Dutz et al. [19] proved the suppression of the Brownian relaxation mechanism into the tumour, whose contribution to the heating in *in-vivo* MFH treatments is therefore negligible. Moreover, authors highlighted the necessity to evaluate the heating efficiency of MNPs in media other than water, otherwise it would be a common mistake to overestimate the real SAR of MNPs once injected into the tumour.

In-water and in-gel measurements of the SAR by De la Presa et al.

Unfortunately, not all the groups performing research in the field of MFH have the possibility to access *in-vitro* and *in-vivo* studies, and this is probably the main reason for the large abundance of papers characterizing the SAR of MNPs only in water. However, easy and cheap solutions could be implemented to model the behaviour of MNPs in living tissues, for example exploiting phantoms of tissue mimicking materials like gels.

An example is reported in literature by De la Presa et al. [102], which characterized systematically the SAR of maghemite nanoparticles with different sizes, ranging from 6 to 14 nm, at different values of the applied AMF (f = 522.7 kHz and amplitude H up to 7.5 kA/m), both in water solutions and in agar (at 1 wt%) phantoms. Agar is indeed typically used as tissue mimicking material in different fields of science [115], and could be exploited to immobilize efficiently the MNPs, modelling an *in-vivo* condition. However, temperature of the agar samples was not allowed to exceed 50°C, otherwise a partial melting of agar could lead to a higher mobility of the particles.

Interestingly, the SAR values measured in water and in agar for MNPs with sizes up to 11 nm perfectly overlapped at all the analysed field amplitudes, while a drop in the SAR values of the larger magnetic nanoparticles was observed when they were immobilized in agar, compared to water. Again, this result is reasonably explained with the Brownian motion suppression in agar, whose viscosity was valuated to be at least 20 times larger than that of water.

Computing τ_N and τ_B by means of Eqs. 1.5 and 2.5, respectively, and exploiting the physical parameters obtained from the particles characterization, it was observed by De la Presa et al. [102] that for $d < 11$ nm it resulted $\tau_N \ll \tau_B$, i.e. the Néel relaxation mechanism dominated over the Brown relaxation and it was the only one responsible for the heating. This explains why the SAR did not change when the Brownian relaxation was suppressed in agar. On the contrary, for the largest particles (i.e. 11 nm $< d <$ 14 nm) $\tau_N \simeq \tau_B$ and the Brownian relaxation contributed actively to the heating. Consequently, if the particles were immobilized in gel the SAR decreased consistently.

Despite the different behaviour of the MNPs in water and in agar, De la Presa et al. [102] observed that both the SAR measured in water and in agar slightly increased with the particle size up to 14 nm. As a result, they suggested that the best compromise for efficient MFH treatments would be to use particles with intermediate diameter of about 12 nm, i.e. particles that combine a quite high heating efficiency with the SAR independence from the viscous properties of the medium. The latter is indeed a parameter not easily controlled when particles are injected into the tumour for the clinical practice.

SAR measurements in gelatine gels by Piñeiro et al.

A similar study to that of De la Presa et al. [102] was performed by Piñeiro et al. [114]. In this case authors employed magnetite nanoparticles with two different sizes ($d = 10$ nm and $d = 20$ nm), preparing several dispersions of MNPs in gelatine gels with different weight concentrations, from 2 wt% to 20 wt%. SAR was measured for all the samples by applying only one AMF, with $f = 293$ kHz and $\mu_0 H = 30$ mT. Results showed that SAR decreases up to the 50% in the gelatin samples with the lowest w/w%, and up to the 80% in the gelatin samples with the highest w/w%, compared to water samples. This difference was again explained by the particles immobilization in gelatin, with the Brownian relaxation suppression that resulted to be more efficient in the gelatin samples with the highest viscosities.

SAR of size-sorted magnetic nanoparticles in liquid carriers with different viscosity by Fortin et al.

One of the first systematic studies about the role of the Néel and Brown relaxation in MFH is the one reported in 2007 by Fortin et al. [116]. In this work the authors considered both maghemite and cobalt ferrite nanoparticles with different sizes in the range from 5 to 20 nm. MNPs were dispersed in aqueous

suspensions with different viscosities (η varying over 3 orders of magnitude) thanks to the addition of increasing percentages of glycerol. SAR measurements were performed by varying both the amplitude (up to 27 kA/m) and the frequency (from 300 kHz to 1.1 MHz) of the applied alternating magnetic field.

The large number of samples and field parameters allowed authors to investigate systematically and independently the effects of (i) the MNPs size distribution, (ii) the particle material, (iii) the carrier viscosity and (iv) the AMF amplitude and frequency on the MNPs heating efficiency for MFH. Moreover, theoretical calculations of the SAR were also carried out and compared to the experimental measurements, to highlight the relative contribution of the Néel and Brown relaxation.

Fortin et al. reported a decreasing SAR of both maghemite and cobalt ferrite MNPs with increasing viscosities of the liquid carrier. However, this decrease was described as *slight* (from 135 W/g to 100 W/g) in the case of maghemite MNPs, while it was described as *drastic* (from 420 W/g to 90 W/g) in the case of cobalt ferrite MNPs. This opposite occurrence was due to the different magnetic anisotropy of the two materials, which was about two orders of magnitude higher for cobalt ferrite compared to maghemite.

The large gap between the values of K of maghemite and cobalt ferrite determines a different contribution of the Néel and Brown relaxation mechanisms on the heating of the two materials. In particular, being τ_N exponentially related to the anisotropy constant (Eq. 1.5), it becomes quickly much slower than the frequency of the AMF in the case of cobalt ferrite MNPs, determining a dominant contribution of the Brown relaxation. As a consequence, increasing viscosities (η) of the liquid carriers lengthen also τ_B (Eq. 2.5), causing a quick drop of the SAR. Oppositely, for maghemite MNPs the low magnetic anisotropy makes the Néel relaxation dominating with respect to the Brown one, in particular for the smallest particles, with a less marked effect of the τ_B increase (i.e., the viscosity) on the SAR.

Aims of the work presented in this thesis

In addition to the previous works selected from literature, several other authors further investigated on the role of the Brownian relaxation in MFH, as for example Moise et al. [99], Kalambur et al. [100] and Salas et al. [113].

In the frame of this wide literature studies, this thesis complement the current knowledge by investigating the heating efficiency of magnetite nanoparticles with different core sizes (d = 10 nm, d= 14 nm and d= 18 nm), prepared both in aqueous suspensions and in agarose gels with different mass fractions (0.5 wt% and 2 wt%), which can efficiently simulate soft and hard tissues of the human body. In particular, the SAR is systematically measured at five different frequencies of the applied AMF (from 109.8 kHz to 990.5 kHz), changing the amplitude of the field (up to 16.2 kA/m) at each frequency, from the minimum to the maximum value available depending on the experimental

setup.

The three different particles sizes were chosen in order to have both superparamagnetic nanoparticles ($d = 10$ nm), blocked nanoparticles ($d = 18$ nm) and nanoparticles at the transition between the superparamagnetic and the blocked states ($d = 14$ nm), differently from De la Presa et al. [102] who only focused on small MNPs, up to 14 nm. Moreover, De la Presa et al. performed SAR measurements at only one frequency, i.e. 522 kHz, which is much higher than the frequency commonly applied for MFH treatments in clinics, of about 100 kHz [50]. Therefore, results here presented at 109.8 kHz must be considered of fundamental importance, since for the first time the SAR of MNPs with different sizes is systematically reported at field parameters suitable for clinical MFH. Finally, for this investigation three different media were prepared (i.e. water and two agarose gels with different mass fractions), to further investigate on the MNPs behaviour reported by Piñeiro et al. [114] in media with different viscosities, having them observed a decrease of the SAR (measured at only one AMF) with increasing weight concentration of the gelatins used as dispersant media. This aspect was not analysed by De la Presa et al., who only considered one agar gel with concentration 1 wt%. It is also for this reason that two agarose concentrations, one lower (0.5 wt%) and one higher (2 wt%) than those previously reported, were chosen.

In addition, a further novelty of the present work is that the results obtained from the samples characterization have been analysed to derive an experimental determination of the MNPs relaxation times, and the trends of the SAR(H, f) curves have been compared to the theoretical models discussed in Section 2.2.2.

4.1.2 Synthesis and morpho-dimensional characterization of the samples

Synthesis

For this study three samples of magnetite nanoparticles with different sizes were used. Their synthesis was performed by the group of Dr. Claudio Sangregorio at University of Florence, by applying a thermal decomposition procedure, starting from metal-organic precursors in high boiling solvents, in solution with appropriate surfactant. In details, as reported in Ref. [64], Iron(III) acetylacetonate, Oleylamine and Oleic Acid (relative quantities: 2 mmol, 2.5 mmol and 2 mmol, respectively) were dissolved in 40 mL of Benzylether and subsequently underwent a stirring process for 15 minutes at room temperature under nitrogen flow. The temperature of the obtained mixture was increased in two steps: at first up to 200°C for 30 minutes and then up to 300°C for a variable time, depending on the desired MNPs size. Finally, the temperature was decreased again down to room temperature, and the precipitate was magnetically collected and washed with ethanol.

At the end of the previous list of steps, an Oleic Acid (OA) coating assem-

bled around the particles allow to suspend them in toluene, an organic solvent. However, for the aims of this thesis and, in general, for any application of nanoparticles in the biomedical field, a suspension of MNPs in water rather than in organic solvents is strongly recommended. Consequently, a further step aimed to change the coating of the particles was performed, i.e. exchange ligand by reacting 20 mg of MNP@OA suspended in toluene at 5 mg/mL with 10 mg of meso-2,3-dimercaptosuccinic acid (DMSA) solved in 2 mL of Dimethyl sulfoxide (DMSO). Afterwards, (i) the two solutions were mixed with ultrasounds for 1 hour and (ii) held in mechanical agitation for 24 hours; (iii) MNPs were magnetically separated from the supernatant and (iv) washed two times with ethanol and finally with water; (v) the final suspension of MNPs in water at 10 mg/mL was produced by adding some drops of a NaOH solution 0.1 M in order to adjust the pH to 8 (a value assuring a good colloidal stability for DMSA coated nanoparticles in water) [117].

It is worth noting that, in addition to the good colloidal stability guaranteed by DMSA in water, DMSA coatings are widely used for biomedical applications of MNPs. Indeed, by means of *in-vitro* studies it was observed that DMSA allow high MNPs uptake rates by different types of cell lines, thanks to a favourable interaction with the cell membrane [118, 119].

XRD analysis

The nature of the iron oxide obtained at the end of the synthesis was confirmed as magnetite by X-Ray Diffraction (XRD) analysis. Measurements were carried out by means of a Bruker D8 advance diffractometer equipped with a graphite monochromator, using CuKα radiation ($\lambda = 1.54178$ Å) and collecting the pattern in $\theta - 2\theta$ Bragg-Brentano geometry at 40 kV and 40 mA, over the range from 25° to 70°. Results are shown in Fig. 4.2; the peaks of the spectra of the three samples are those characteristics of the face centered cubic (fcc) structure typical of inverse-spinel such as magnetite and maghemite. No traces of other crystalline phases such as hematite or wustite are identified in the spectrum, attesting a good purity of the samples.

The Pawley method refinement [120] was used to evaluate the crystal size and the lattice parameter a of the samples, by setting the structure of the magnetite (Fd-3m) with the T.O.P.A.S.© software [121]. In particular, the crystal size is useful to evaluate the monocrystalline nature of the synthesized particles, while the lattice parameter a quantifies the size of the unit cell of the crystal lattice. Results are reported in Table 4.1; as will be shown in the following section, the crystal size is compatible with the core size (Table 4.2) quantified by Transmission Electron Microscopy (TEM), attesting the monocrystallinity of the particles, while the values of the a parameters are more compatible with that of magnetite ($a = 8.3970$ Å) than with that of maghemite ($a = 8.3515$ Å), confirming the magnetite composition of the samples.

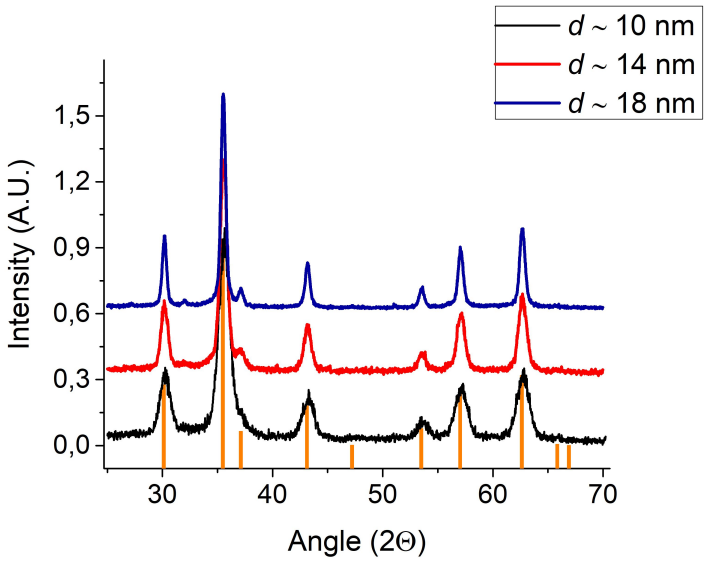

Figure 4.2: XRD patterns of the three samples of MNPs with different sizes ($d = 10$ nm, $d = 14$ nm, $d = 18$ nm); comparison of diffraction peaks with the reference lines (PDF 65-3107) of magnetite (orange bars) confirms the nature of the iron oxide in the magnetic cores [117].

Table 4.1: Values of the crystal size and lattice parameter a of the three samples of MNPs as obtained from the analysis of the XRD patterns with the Pawley method [120] using T.O.P.A.S.© software [117, 121].

Sample	Crystal size (nm)	Lattice parameter a (Å)
10 nm	9.3	8.407(3)
14 nm	13.8	8.391(1)
18 nm	17.2	8.398(1)

TEM

For the measurement of the cores size of the three samples of MNPs, and for a qualitative evaluation of the particles shape, Transmission Electron Microscopy (TEM) was used. In particular, a CM12 Philips TEM was employed, using a LaF_6 source and operating at 100 kV. MNPs in diluted toluene solutions were drop casted onto 200 mesh carbon-coated copper grids and dried for the measurement. The iTEM TEM Imaging Platform software (Olympus) was used for processing the acquired TEM micrographs, and further statistical analysis was performed by means of the FIJI open software on over 600 MNPs.

Exemplary TEM pictures of the three samples and the histograms reporting the distribution of the MNPs sizes according to the statistical analysis are reported in Fig. 4.3. First, all the samples present a polyhedral shape that with a good level of approximation can be assumed as spherical, in particular the sample $d = 14$ nm presenting very regular and symmetrical particles. The

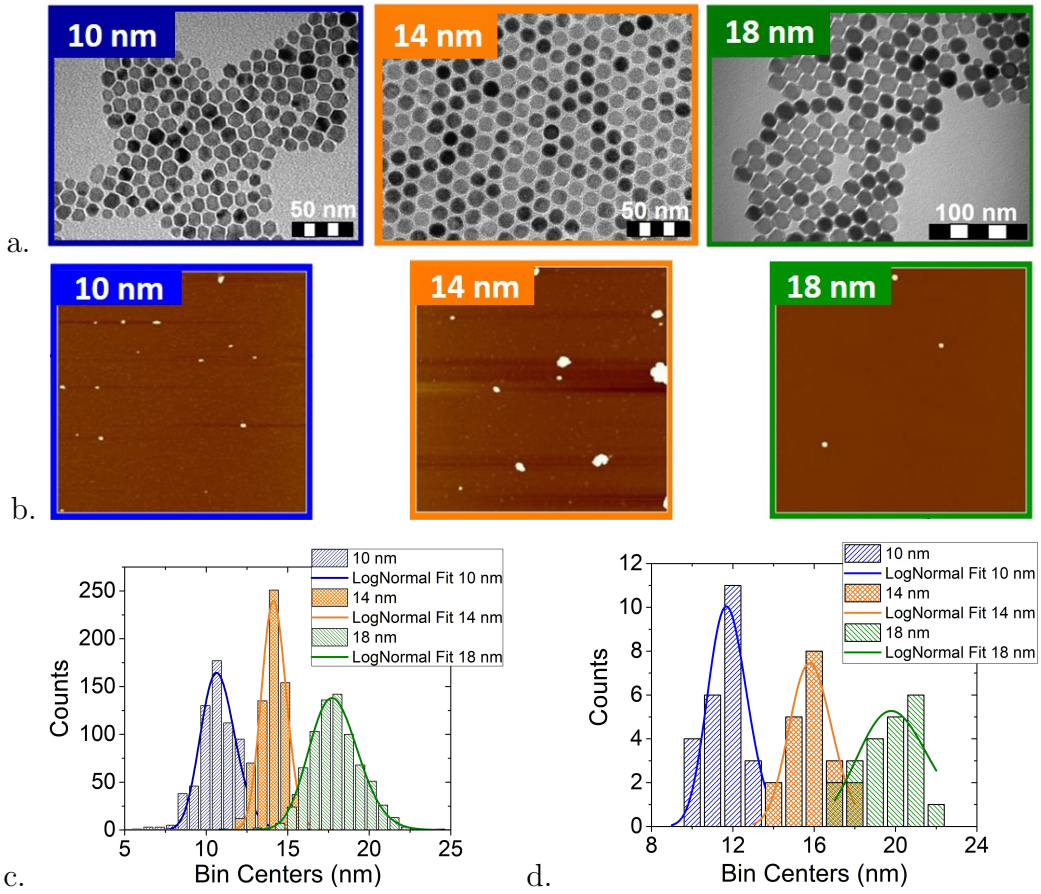

Figure 4.3: (a) TEM and (b) AFM images of three samples of magnetite MNPs with different sizes. AFM images cover a surface of $2 \times 2\,\mu m^2$. Histograms reporting the core size distributions (c) and the hydrodynamic size distributions (d) were obtained by TEM and AFM statistical analysis, respectively. Histograms were fitted in all cases with a Log-Normal function.

distributions were fitted with a Log-normal function, according to Eq. 1.13, giving mean diameters of about 10 nm, 14 nm and 18 nm, which are being used as labels to distinguish among the three samples. Interestingly, the sample with $d = 14$ nm shows the narrowest distribution, while larger polydispersity of the cores size is observed for the samples $d = 10$ nm and d= 18 nm. Mean values and standard deviations of the particles diameters, computed according to the formulas reported by Rosensweig et al. [8], are reported in Table 4.2.

AFM

To evaluate the hydrodynamic size, i.e. the total size of the particles including the thickness of the coating, one possible technique is Atomic Force Microscopy (AFM). For the measurements, samples were prepared by drying a drop of very diluted aqueous suspension of MNPs on a Mica substrate, which is commonly used in AFM because of its almost perfect flatness arising from

Table 4.2: Mean diameter and standard deviations of the size distributions of the three samples of MNPs as obtained from statistical analysis of TEM images (core size), AFM images (hydrodynamic size of dried nanoparticles, i.e. core+coating) and DLS data (hydrodynamic size in solution) [117].

Sample	d_{TEM} (nm)	d_{AFM} (nm)	d_{DLS} [PDI] (nm)
10 nm	10.8 ± 0.8	11.6 ± 1.0	15.8[0.379]
14 nm	14.2 ± 0.5	16.0 ± 1.1	21.4[0.371]
18 nm	17.9 ± 1.5	19.7 ± 1.5	34.1[0.319]

a layered crystalline structure. Measurements were performed by means of a Bruker Nanoscope Multimode IIId AFM system, working in tapping-mode in air with a silicon rectangular cantilever (NSG01, NT_MDT) characterized by the following parameters: 120 μm length, 2.5 N/m spring constant, 130 kHz resonant frequency.

Exemplary AFM pictures are reported in Fig. 4.3b. As it can be immediately seen from the pictures, aggregates of MNPs are sometimes observed on the Mica substrate, probably formed during the drying process of the initial suspension. For this reason, aggregates were always discarded from the analysis, which was performed only on single particles. In particular, statistical analysis of the size distributions were performed over ~ 25 MNPs, fitting the histograms of Fig. 4.3d with a Log-Normal function. Mean values and standard deviations of the three distributions are reported in Table 4.2. As expected, the hydrodynamic size resulted to be slightly larger than the core size measured by TEM, due to the presence of the DMSA coating whose thickness was estimated to be about 1-2 nm.

DLS

Another way to estimate the hydrodynamic size is the Dynamic Light Scattering (DLS) technique. Differently from AFM, measurements were performed in solution, and allowed to estimate the colloidal stability of the samples over time and the formation of aggregates. Moreover, DLS is also susceptible to the first water coordination sphere linked to the MNP surface, therefore it commonly gives larger values of the hydrodynamic size compared to AFM.

DLS measurements were carried out by means of a Malvern Zetasizer ZS, Malvern Instruments Ltd. (UK), working onto 0.5 mg/mL suspensions of the samples. Hydrodynamic sizes with their polydispersity index (PDI) according to DLS are reported in Table 4.2. As expected, they are larger than those measured by AFM, also due to the dynamic nature of the measurements, but small enough to exclude the presence of aggregates within the samples.

Values of the Z-potentials, of about ≈ -20 mV, also confirmed the good colloidal stability of the samples.

4.1.3 Magnetic Measurements

Magnetic characterization of the samples was performed by means of a SQUID Quantum Design MPMS magnetometer on either powder or liquid samples of MNPs. In the case of powder samples, small amounts of MNPs ($\sim 3-5$ mg) were enclosed and pressed in a Teflon-tape holder; in the case of liquid samples, ~ 3 mg/mL suspension of MNPs (Fe_3O_4) in water were sealed in a small capsule of polycarbonate ($\sim 100\,\mu$L) and measurements were performed in frozen solutions at $T \leq 260$ K. In both cases the signal from the empty sample holder was measured and subtracted to the total signal; moreover, in the case of MNPs in water, the diamagnetic contribution of the water was also removed, while in the case of powders the masses were corrected by the thermogravimetric analysis (TGA) to account for the weight of the DMSA coating.

Hysteresis loops were acquired at low temperature ($T = 2$ K or $T = 5$ K) and at high temperature ($T = 300$ K for powders, $T = 260$ K for aqueous samples) in the field range from -5 T to 5 T. Zero-Field-Cooled – Field-Cooled (ZFC – FC) curves were also collected for the samples in solution under a small magnetic field (of about 5 mT) in the range 2 K $\leq T \leq$ 260 K, thus keeping the samples in the frozen state during the acquisition.

The hysteresis loops acquired at low temperature on the three powder samples are reported in Fig. 4.4a, while the ones acquired on MNPs in aqueous frozen solution are shown in Fig. 4.4b. Details of the loops at low fields are shown in the left insets of each figure, allowing an estimation of the coercive field H_C and the remanence M_r. The first-magnetization curves of the three samples at high temperatures are instead displayed in the right insets, showing lower values of M_S due to the greater thermal agitation of the spins.

At high temperatures, hysteresis loops are almost closed (very small values of H_C), suggesting that the three samples are close to the superparamagnetic regime. The Saturation Magnetization M_S of the samples was evaluated by fitting the Langevin function [47] (or its approximated Taylor expansion) to the first magnetization curves, although it is well known from literature [122, 123] that systems near to the blocking temperature (as it is the case of samples $d = 14$ nm and $d = 18$ nm; see the following discussion about the ZFC-FC curves) are not expected to follow the trend of the Langevin function, typical of paramagnetic systems.

Values of the coercive field and of the saturation magnetization for the three samples are listed in Table 4.3 for both powders and aqueous frozen solutions, at low and high temperatures. The 18 nm sample shows the highest value of M_S both in powders and in frozen solution, near to the value of the bulk magnetite (~ 91.7 $(Am^2)/(kg_{Fe_3O_4})$) [124]. The values of M_S rescale with the cores size, accordingly to the expectations due to (i) the larger number of spins that could be aligned along the direction of the field and (ii) the lower contribution of the spins disorder on the particles surface (lower surface to volume ratio) for larger particles [125]. Slightly differences between the

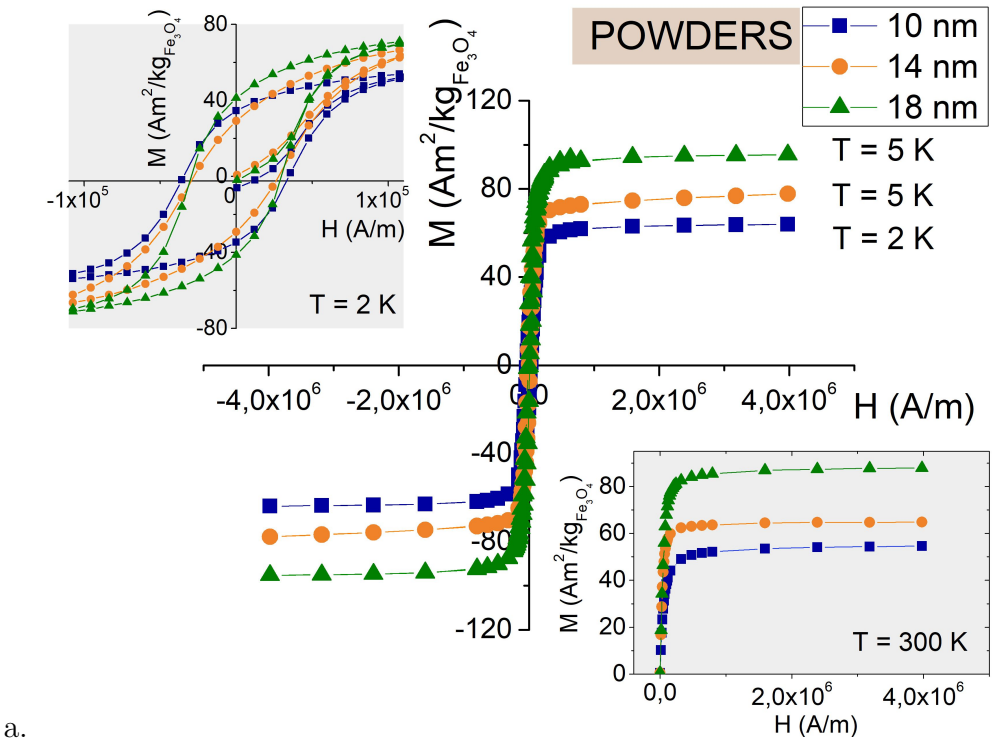

a.

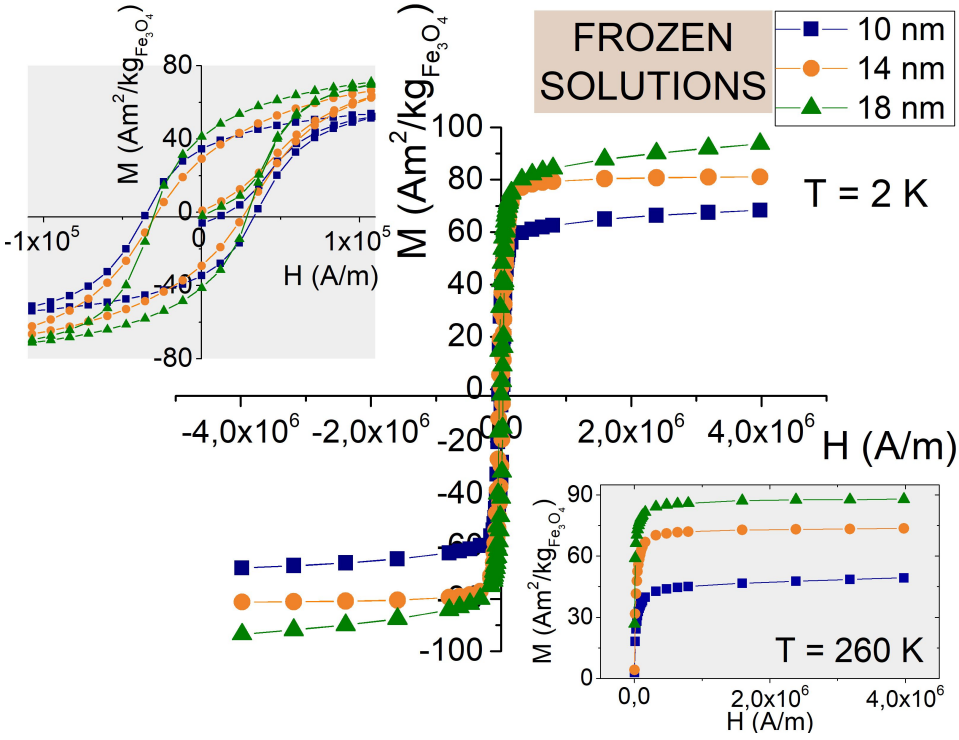

b.

Figure 4.4: Hysteresis loops acquired on the three samples of MNPs in powders (a) and in frozen solutions (b). In the left insets details of the loops at low fields are highlighted, evidencing the coercive field H_C and the remanent magnetization M_r of each sample. In the right insets the first magnetization curves at high temperatures are also reported, allowing to measure M_S [117].

Table 4.3: Saturation Magnetizations (M_S) and Coercive Fields (H_C) of the three samples of magnetite MNPs with different sizes in powders and in frozen solutions at low and high temperatures [117].

POWDERS			
Sample	M_S at low T $Am^2/kg_{Fe_3O_4}$	H_C at low T kA/m	M_S at 300 K $Am^2/kg_{Fe_3O_4}$
10 nm	64.5 ± 3.6 (2K)	34.1 ± 1.7 (2K)	55.4 ± 3.1
14 nm	80.5 ± 4.4 (5K)	19.2 ± 1.0 (5K)	65.4 ± 3.6
18 nm	96.3 ± 5.3 (5K)	10.5 ± 0.5 (5K)	88.6 ± 4.9

FROZEN SOLUTIONS			
Sample	M_S at 2 K $Am^2/kg_{Fe_3O_4}$	H_C at 2 K kA/m	M_S at 260 K $Am^2/kg_{Fe_3O_4}$
10 nm	69.3 ± 3.8	34.6 ± 1.7	51.1 ± 2.8
14 nm	81.6 ± 4.5	27.8 ± 1.4	74.1 ± 4.1
18 nm	96.2 ± 5.2	29.6 ± 1.5	88.3 ± 4.8

values of M_S measured in powders or in frozen solutions could be explained by little interactions between the MNPs, as it is apparently confirmed by the opening of the hysteresis loop (higher values of H_C) in frozen solutions, which is particularly relevant for the 18 nm sample.

ZFC-FC curves

Interesting features characterize the ZFC-FC curves shown in Fig. 4.5 for the three samples in frozen solutions. First, the 10 nm sample presents a maximum in the ZFC curve at $T_{max} = 143$ K, which indicates a clear superparamagnetic behaviour at room temperature since $T_{max} \sim T_B$, i.e. the blocking temperature which signs the transition to the blocked state [126]. The broadness of the peak is probably related to a quite large distribution of the MNPs sizes, as observed from the TEM pictures in Fig. 4.3a. The other two samples don't show any maximum in the ZFC curves, and only the 18 nm sample shows a sharp increase at $T_V \simeq 111$ K probably due to the Verwey transition, a phase transition typical of magnetite. However, it must be noted that the temperature T_V of the Verwey transition is lower than that of stoichiometric magnetite ($T_V^{bulk} \simeq 125$ K), and such decrease could be explained by the presence of impurities in the samples or by a certain degree of non-stoichiometry of the magnetite [26, 127, 128]. Moreover, a decrease of T_V has been already described in literature for particles of decreasing size [27]. The absence of the Verwey transition for the 14 nm sample could be reasonably explained by a partial oxidation to maghemite of the surface layer in water solution.

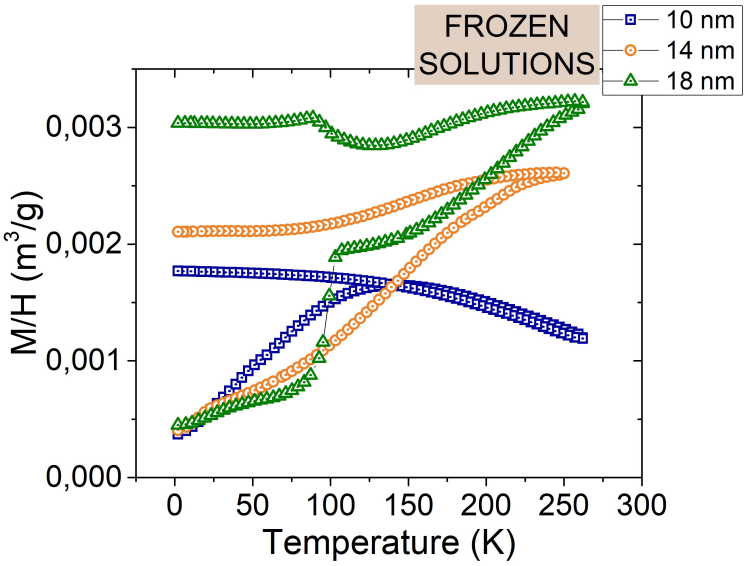

Figure 4.5: Zero-Field-Cooled and Field-Cooled curves acquired for the three samples in solution in frozen state ($T \leq 260$ K) [117].

4.1.4 MNPs in agarose gels

In order to study the role of the Brownian motion on the heating efficiency of MNPs with different sizes, the three samples of MNPs with $d = 10$ nm, $d = 14$ nm and $d = 18$ nm were prepared for hyperthermia measurements both in aqueous suspension and in agarose gel. In particular, two different gels with agarose mass fractions 0.5% and 2% were prepared to evaluate the presence of any effect caused by the agarose concentration and consequently by the medium viscosity. Moreover, the two gels are suitable phantoms materials to simulate soft tissues of the body, with a different level of porosity and hardness [129].

The viscosity of the gels was roughly estimated to be more than 100 times higher than that of water, by using a Brookfield rotational viscometer, as confirmed by literature data [102]. In particular, literature widely reports on the rheological properties of agarose gels [130, 131], whose viscosity is estimated to be at least two order of magnitude higher than the one of pure water. It is also known that the melting temperature of agarose gels is always higher than 75°C and increases with the agarose concentration. For this reason, hyperthermia measurements were performed starting from room temperature and keeping the temperature below 60°C, to avoid partial melting of the agarose structure.

Gels were prepared starting from the same aqueous suspensions used for the measurements in water, at magnetite concentration 10 mg/mL for the 10 nm and 14 nm samples, and 3 mg/mL for the 18 nm sample. Powders of agarose were added in opportune amounts within the solutions, and samples were heated up to the boiling point, while mixing with a pipette. Before gelification, samples were transferred into small Eppendorf ($V \simeq 0.2\,\mu$L) and left at room temperature.

The just described method for the preparation of the gels does not guarantee to completely avoid the formation of small MNPs aggregates (d $<$ 50 nm) within the samples. A powerful method to investigate on this possibility is to perform NMR measurements on all the samples, both in water and in agarose gels. As described in Chapter 2, analysing the NMRD profiles of MNPs the theory predicts a flattening of both longitudinal (r_1) and transversal (r_2) relaxivities at low fields, where $r_1 \simeq r_2$ for perfectly stable and well dispersed MNPs. If aggregation processes occur, it is common to observe a flattening with $r_2 > r_1$ at low Larmor frequencies, i.e. the transversal relaxation becomes much faster than the longitudinal one at low fields. Therefore, NMR measurements performed on gel samples prepared with exactly the same procedure of MFH samples allow to determine if aggregation processes must be taken into account or not.

For this purpose, NMR measurements were performed at room temperature by means of a Stelar Spinmaster Fourier transform nuclear magnetic resonance (FT-NMR) spectrometer at high proton (^{1}H) Larmor frequencies (up to ν_L = 60 MHz), and a Stelar Smartracer relaxometer, which uses a fast-field cycling technique [79], at low Larmor frequencies (from ν_L = 7.2 MHz to ν_L = 0.01 MHz). Both aqueous suspension of MNPs and agarose gels were measured, but investigation was limited to the 18 nm sample, since larger particles are more susceptible of aggregation induced by dipolar interactions.

T_1 measurements were performed by using Saturation Recovery (SR) pulse sequences, pre-polarized at $\nu_L \leq 3.7$ MHz and not pre-polarized at $\nu_L \geq 3.7$ MHz. T_2 measurements were instead carried out by means of CPMG pulse sequences at $\nu_L \geq 3.7$ MHz. At $\nu_L \leq 3.7$ MHz only pre-polarized spin-echo sequences could be used, but because of field inhomogeneities and diffusion effects they often determine erroneous estimation of the transversal relaxation time. This occurrence can be tested by comparing the two values of the transversal relaxation times obtained at $\nu_L = 3.7$ MHz with the not pre-polarized CPMG and the pre-polarized spin-echo sequence.

In the case of agarose gels, a further difficulty complicates NMR measurements. Indeed, as in the case of water, the diamagnetic contribution to the NMR signal coming from the agarose must be subtracted to compute the relaxivity (Eq. 2.27). However, differently from water, the contribution of the agarose to the longitudinal relaxivity at low Larmor frequencies is very relevant, determining a sharp increase of r_1 while decreasing the frequency, as showed by Gossuin et al. [132]. As a result, inaccurate determination of the agarose gels relaxation times at low Larmor frequencies would cause misleading conclusions about the real values of r_1 and r_2 at these frequencies, and consequently about the aggregation phenomena.

The NMR signal coming from pure agarose gels samples was accurately studied in the Larmor frequency range 0.01 MHz $\leq \nu_L \leq$ 60 MHz. Fig. 4.6 shows the inverse of the longitudinal (a) and transversal (b) relaxation times in all the considered range of magnetic fields for agarose gels with different mass

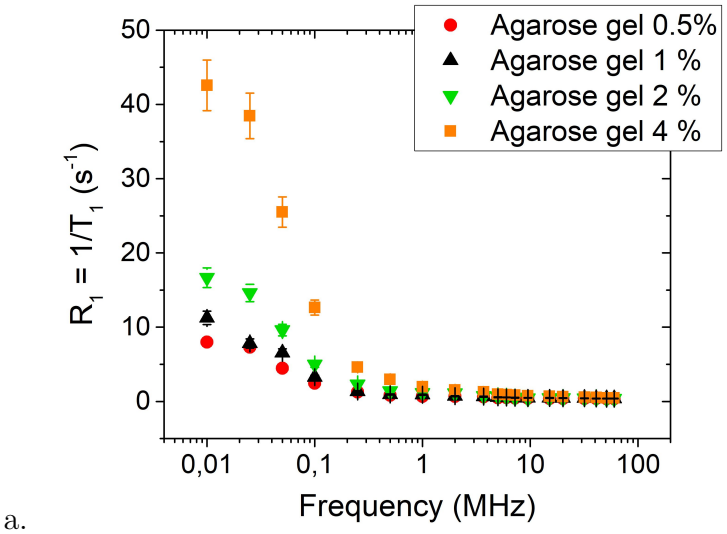

a.

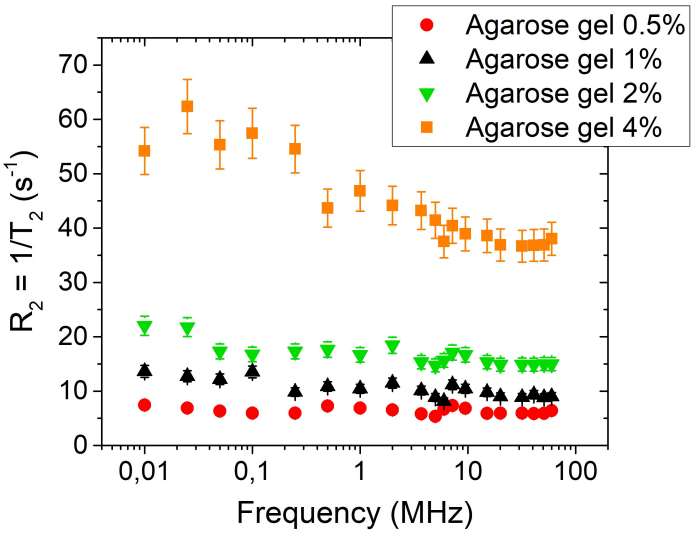

b.

Figure 4.6: (a) Inverse longitudinal relaxation times ($R_1 = 1/T_1$) and (b) inverse transversal relaxation times ($R_2 = 1/T_2$) of pure agarose gel samples as a function of the proton Larmor frequency, determining the diamagnetic contribution to be subtracted to compute the relaxivity of in-gel MNPs samples.

fractions. In accordance with the results reported by Gossuin et al. [132], a sharp increase of $R_1 = 1/T_1$ was observed for $\nu_L \leq 0.3$ MHz, more pronounced for more concentrated gels.

Results of the NMR measurements performed on the 18 nm sample at selected Larmor frequencies in the three dispersant media used for the MFH measurements are reported in Table 4.4. T_2 values obtained at $\nu_L \leq 7.2$ MHz with the Stelar SMARTracer relaxometer (susceptible of larger field inhomogeneities compared to the Stelar Spinmaster) and by applying Spin-echo sequences resulted to differ consistently from those measured with a CPMG

Table 4.4: Longitudinal (r_1) and transversal (r_2) relaxivities of the 18 nm MNPs dispersed in water and in agarose gels with different mass fractions, i.e. 0.5 wt% and 2 wt%, measured at selected proton Larmor frequencies ($\nu_L = \gamma B_0$).

18 nm sample			
r_i at ν_0	Water	Gel 0.5%	Gel 2%
$r_1(s^{-1}mM^{-1})$ at 60 MHz	10.6 ± 0.8	10.8 ± 0.9	11.0 ± 0.9
$r_1(s^{-1}mM^{-1})$ at 7.2 MHz	77.7 ± 6.2	109 ± 9	111 ± 9
$r_1(s^{-1}mM^{-1})$ at 0.01 MHz	418 ± 33	325 ± 26	398 ± 32
$r_2(s^{-1}mM^{-1})$ at 60 MHz	382 ± 31	400 ± 32	415 ± 33
$r_2(s^{-1}mM^{-1})$ at 7.2 MHz	391 ± 31	421 ± 34	425 ± 34

sequence and the Stelar Spinmaster relaxometer at $\nu_L \geq 7.2$ MHz, and were therefore considered unreliable. However, r_2 resulted to be already flattened in the frequency range from 60 MHz to 7.2 MHz, and therefore it can be assumed it remains flat down to 0.01 MHz, where instrumental limitations does not allow to measure r_2.

The absence of relevant aggregation phenomena for the 18 nm sample dispersed in water and in 2% agarose gel can be inferred by comparing the r_1 value at 0.01 MHz with the r_2 value at 7.2 MHz, which results to be compatible (Table 4.4). Conversely, r_1 and r_2 values in the case of the 0.5% gel suggest (probably a small degree of) aggregation. This kind of behaviour for gels cannot be totally explained, because three situations are reasonably predictable: (i) no aggregation neither in the 2% gel nor in the 0.5% gel; (ii) no aggregation in the 0.5% gel but aggregation in the 2% gel (since it is more viscous); (iii) aggregation in both media. No reasonable explanation for aggregation occurring in the 0.5% gel but not in the 2% gel can be easily given in the present discussion. However, results presented in Table 4.4 seems to exclude the possibility aggregates could have a relevant contribution to the effects investigated in this thesis.

4.1.5 Magnetic Hyperthermia measurements

Setup preparation

Magnetic Hyperthermia measurements were performed using a MagneTherm™ setup by NanoTherics. This setup is equipped with one of two possible coils (L, with 9 and 17 turns) and one of five different capacitors (C); the ten combinations LC allow working at ten different frequencies of the AMF, from about 100 kHz to 1 MHz. For each frequency, the field amplitude can be set up to a maximum value, that decreases while increasing the frequency due to power limitations of the system. For the lower frequency, i.e. 109.8 kHz, the maximum amplitude of the AMF is slightly higher than 16 kA/m. Most of the

couples of frequency (f) and amplitude (H) values satisfy the Brezovich criterion $H \cdot f < 4.85 \cdot 10^8\,\mathrm{Am^{-1}s^{-1}}$ for the safe application of a magnetic field to a patient [61], and all of them fulfil the criterion reported by R. Hergt and S. Dutz [133], requiring $H \cdot f < 5 \cdot 10^9\,\mathrm{Am^{-1}s^{-1}}$.

The MagneTherm$^{\mathrm{TM}}$ was equipped with a home-made thermalization system and a polystyrene sample holder, which allow to set the initial temperature of the sample and to keep it isolated from the external environment as much as possible. Details about the home-made implementation of the setup for MFH are given in Appendix A.2.

All hyperthermia measurements were performed starting from a temperature slightly higher than the room temperature, i.e. 25°C, fixed thanks to the thermalization system. Very small amount of MNPs suspensions in water or in gel were used, i.e. $\sim 200\,\mu$L placed inside an Eppendorf PCR Tube and centred in the middle of the coil, obtaining reproducible heating curves for each sample.

An Optocon$^{\mathrm{TM}}$ optical fibre thermometer was used to measure the temperature of the samples. This system is not susceptible to the AMF, allowing reliable measurements of the temperature within the coil thanks to a semiconductor material positioned at the tip of the fiber. It is worth noting that for hyperthermia measurements is of crucial importance the correct and reproducible positioning of the thermometer within the sample, and the positioning of the sample within the coil. It is indeed known that both the shape of the sample holder (particularly if non-symmetrical as in the case of an Eppendorf Tube) and the non-homogeneity of the AMF along the axis of the coil may affect the MFH measurement. Particular attention was therefore given to the correct positioning of the sample and of the temperature probe (for details see Appendix A.2).

Another important parameter that must be evaluated in MFH experiments is the contribution to the temperature rise of the sample coming from the overheating of the coil. This parameter can be easily estimated by measuring the increase of temperature of a test sample made of pure water or gel, while working with the system in the same experimental conditions. For our system, it resulted to be completely negligible. Moreover, for MNPs samples, it was verified that the initial temperature does not affect significantly the rate of the temperature increment (see Appendix A.2).

MFH measurement and computation of the SAR

For the measurements of this thesis, five frequencies covering all the available frequency range were chosen: 109.8 kHz, 329.6 kHz, 524.2 kHz, 741.6 kHz and 990.5 kHz. For each frequency, 5 to 10 values of the amplitude H were chosen in order to study the dependence of SAR on H.

Samples were thermalized within the coil at 25°C, then the AMF was switched on and measurements were performed for 5 or 15 mins at steps of 1 s, depending on the total increment. It is indeed important to not exceed

60°C, for avoiding both damages to the MNPs coating (that would affect the particles stability) and melting of the agarose, in the case of gels. As regards the gels, it is known from literature [134] that the heat conductivity of agarose gels differs slightly from the one of water; in particular, it is about 1.5% lower at 0.5% agarose concentrations, and about 9% lower at 5% agarose concentration, in the temperature range from 303 K to 323 K. It is not easy to include these differences in the formulas for the computation of the SAR; however, at the agarose concentrations used for the preparation of the samples of this thesis, the differences in the heat conductivities of water and agarose gels are so small that they can be considered largely included in the uncertainty assumed for the SAR (10%).

The $T(t)$ curve resulting from a MFH measurement is commonly analysed using the initial-slope method, i.e. by fitting the curve with a linear function in the time interval $\sim 5 \div 20$ s. This interval was chosen (i) to neglect the thermal inertia of the system [46], occurring in the first seconds immediately after the application of the AMF, and (ii) because of the dissipative effects occurring after about 20 seconds in our system, which determine a decrease of the slope of the curve. From the fit the ratio $\Delta T/\Delta t$ was obtained.

At low fields, when the temperature increment was too slow to apply the initial-slope method, also because of the low sensitivity of the fiber-optic system (only 0.1°C), the entire $T(t)$ curves were fitted to the Box-Lucas model $T(t) = A(1-e^{-Bt})$ [136]. As explained by Landi [137], in these cases the ratio $\Delta T/\Delta t$ can be extracted considering the product $A \cdot B$. In boundary cases, when both the initial-slope method and the Box-Lucas model could be applied, both fits returned the same value of the slope $\Delta T/\Delta t$, widely compatible within the error bars.

The SAR of the samples for a given field frequency and amplitude was calculated using the formula [138]:

$$\mathrm{SAR} = \frac{m_{H_2O} c_{H_2O} + m_{Fe_3O_4} c_{Fe_3O_4}}{m_{Fe_3O_4}} \cdot \frac{\Delta T}{\Delta t} \tag{4.1}$$

where m_{H_2O} and $m_{Fe_3O_4}$ are the masses of water and magnetite in the colloidal solutions, respectively, while $c_{H_2O} = 4.18\,\mathrm{JK^{-1}g^{-1}}$ and $c_{Fe_3O_4} = 0.62\,\mathrm{JK^{-1}g^{-1}}$ are their heat capacities. The contribution of the DMSA coating could be neglected because of its small mass fraction compared to water and magnetite. It is worth noting that for MNPs samples in agarose gels it would have been necessary to substitute the heat capacity of water in Eq. 4.1 with the heat capacity of agarose gels. However, literature data on agarose gels report that $c_{agar(1\%)} = (4.18 \pm 0.05)\,\mathrm{JK^{-1}g^{-1}}$ [113], i.e. the heat capacity of agarose gel at mass fraction near to the ones used in this work (0.5% and 2%) is very similar to the heat capacity of water. Consequently, it is not misleading to compute the SAR of the gel samples applying anyway Eq. 4.1.

The uncertainty on the SAR value obtained by Eq. 4.1 was computed by considering the uncertainties on all the parameters entering Eq. 4.1, and propagating them by applying the bootstrap Monte Carlo technique, giving a

standard deviation slightly lower than 10%. Slight inhomogeneous distribution of MNPs inside the gels, if any, would probably lead to small differences in the $\Delta T/\Delta t$ ratios, whose effect could be considered largely included in the 10% standard deviation assumed for the SAR.

Results obtained for all the three samples (10 nm, 14 nm and 18 nm), both in water and in agarose gels (0.5% and 2% w/w), at the five frequencies of the AMF chosen for this study, are reported in Fig. 4.7. Data at 990.5 kHz are not showed for the 10 nm sample because of the limited heating recorded for this sample at the low field amplitudes available at this frequency ($H_{max} = 3.5$ kA/m), which did not allow to reliably quantify the SAR.

A first qualitative analysis of Fig. 4.7 highlights three important indicators of the capability of agarose gels to immobilize MNPs. (i) The SAR measured in the two agarose gels with mass fractions 0.5% and 2% are almost the same at all frequencies for all the samples with different size: this clearly indicates that the viscosity of the gel does not affect the efficiency of MNPs immobilization, which is already realized in the least viscous gel. (ii) No differences are registered for the SAR of the 10 nm sample when measured in water or in agarose gels; this confirms a negligible contribution of the Brownian relaxation compared to the Néel one for particles of small size, as reported by Rosensweig [8] and well discussed in Chapter 2.2.1. (iii) In the case of the 14 nm and 18 nm samples, the SAR measured in the two gels differs consistently from that measured in water, being from 30% to 75% lower. This occurrence can be explained by considering the large influence of the Brown relaxation in the release of heat mechanisms of large MNPs [8], which is suppressed in gel.

Results shown in Fig. 4.7 confirm and extend to a wider range of frequencies and MNPs sizes the observations of De la Presa et al. [102] and Di Corato et al. [97]. However, it is worth noting that Mehdaoui et al. [139] warned other scientists to explain a minor value of SAR of MNPs dispersed in gel compared to the one of MNPs in liquid solution by just considering the suppression of the Brownian motion. In fact, MNPs immobilized in gel are not allowed to self-organize in chain-like structures under the action of the external AMF and thanks to the dipolar interactions between them, as theoretically predicted in water suspensions by Branquinho et al. [95] and experimentally observed by Serantes et al. [96]. However, this effect is described in literature only for low anisotropy MNPs, having an energy barrier induced by the magnetocrystalline anisotropy much lower than the energy of the dipolar interactions [139]. As regards the samples analysed in this Chapter, this occurrence seems unlikely to happen in water samples, since MNPs are characterized by high values of the anisotropy constants K_a (as described in the following of the discussion). It is therefore possible to conclude that the differences observed in the SAR values of the water and gel samples in Fig. 4.7 could be solely attributed to the MNPs immobilization in gel.

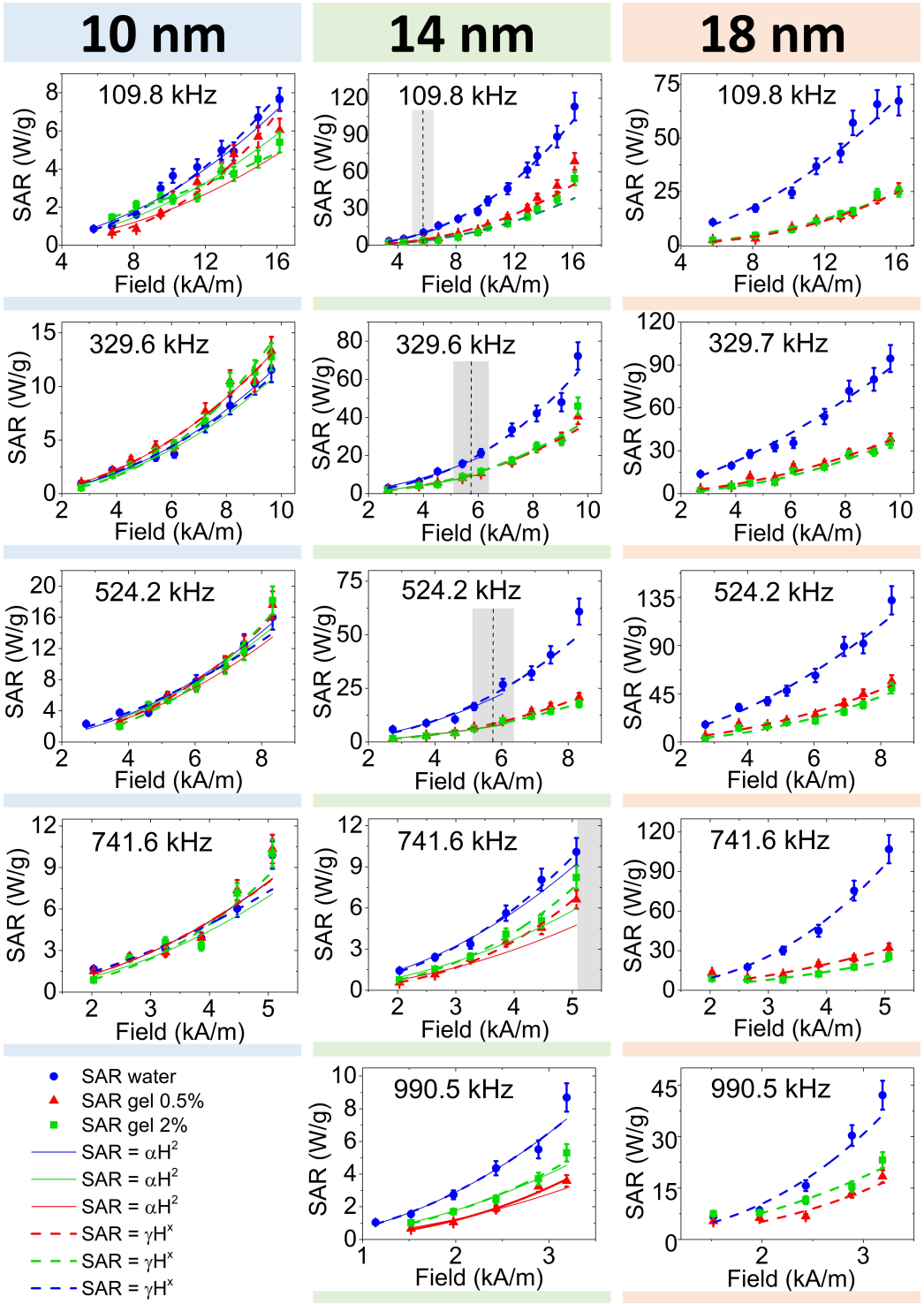

Figure 4.7: SAR values of the 10 nm, 14 nm and 18 nm samples in water and in agarose gels (0.5 wt% and 2 wt%) computed by means of Eq. 4.1, as a function of the amplitude H of the applied AMF at five different frequencies. Fits with theoretical models of MFH are superimposed to experimental data: continuous lines represent the best-fits to the LRT (SAR(H) = αH^2); dotted lines denote the best-fitting curves to the free-exponent function SAR(H) = βH^x. LRT is applied within its validity limits, whose upper limits are evidenced by grey bars (representing the limit $\xi < 1$ with its uncertainty). For the 10 nm sample, LRT is applicable in the whole field range, while it never applies to the 18 nm sample [117].

SAR dependence on the size

Another important information which regards the comparison between the heating efficiencies of the MNPs with different sizes under the action of the same AMF can be obtained from the data reported in Fig. 4.7. In order to make this information more immediately readable, some of the data of Fig. 4.7 are reported again in Fig. 4.8, this time comparing the SAR as a function of the MNPs size in the same medium. In particular, in Fig. 4.8 only the SAR measured in the agarose gel samples with 0.5% mass fraction are reported. This choice is justified by the fact that the graphs that compare the SAR of the samples measured in water and in the 2% w/w gel do not give any additional or different information compared to the graphs of Fig. 4.8.

From the graphs of Fig. 4.8 it can be immediately observed that (i) the 14 nm sample results to be the most efficient sample at $f = 109.8$ kHz, (ii) it has SAR values comparable with those of the 18 nm sample at $f = 329.6$ kHz, and finally (iii) it becomes much less efficient than the 18 nm sample at $f \geq 524.2$ kHz, having heating efficiency comparable with the one of the 10 nm sample. This behaviour of the SAR of the two samples with the frequency is particularly interesting, since only at frequencies higher than 330 kHz it results to be consistent with literature data [46] and with the experimental findings reported in Chapter 3 [64]. It is indeed commonly reported an increase of the SAR with the MNPs core diameter, at least up to d = 20 nm.

However, three main hypothesis can be formulated to explain the highest SAR values of the 14 nm sample at the lowest frequency: (i) the narrower distribution of the MNPs core diameter compared to the other samples, as reported in Table 4.2, due to the "degradative influence of polydispersity" reported by Rosensweig [8]; (ii) the occurrence of a maximum in the out-of-phase component of the magnetic susceptibility ($\chi''(f)$) of the 14 nm sample near to 110 kHz, differently from the 18 nm sample (whose maximum $\chi''(f)$ could be expected at higher frequencies due to the larger size of the MNPs [98]); (iii) most probably, a mix of the hypotheses (i) and (ii). It is indeed important to remind that $\chi''(f)$ presents a maximum when the product $2\pi f\tau = 1$ [98, 140], i.e. when the AMF frequency matches the effective relaxation time of the MNPs, causing a maximum opening of the hysteresis loop and consequently a maximum transfer of energy from the field to the particles (i.e., maximum heating).

4.1.6 SAR models and estimation of the effective relaxation time

Validity of the LRT and Rayleigh models

The most commonly applied model to analyse MFH data is the Linear Response Theory (LRT), described in Chapter 2.2.2. Recalling the most important properties of the model, (i) it predicts an increase of the SAR with the

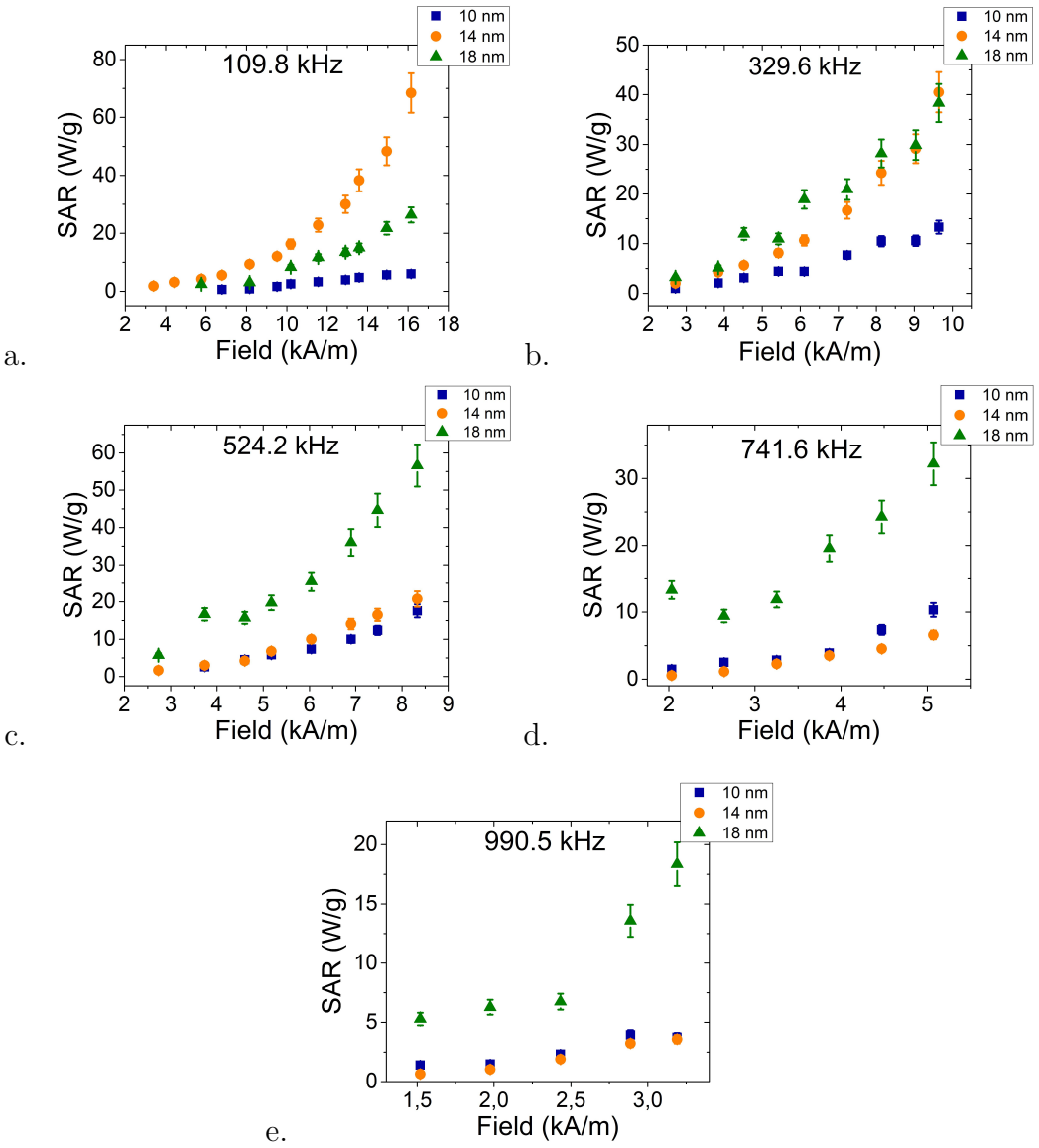

Figure 4.8: SAR values as a function of the amplitude of the applied AMF for the 10 nm, 14 nm and 18 nm samples in agarose gel at 0.5% w/w at (a) $f = 109.8$ kHz, (b) $f = 329.6$ kHz, (c) $f = 524.2$ kHz, (d) $f = 741.6$ kHz and (e) $f = 990.5$ kHz. Comparing the heating efficiency as a function of the MNPs size, a strong dependence on the AMF frequency is observed, being the 14 nm sample the most efficient at $f = 109.8$ kHz, and the 18 nm sample the most efficient at $f > 329.6$ kHz. [117].

square of the maximum amplitude of the applied AMF (Eq. 2.20), and (ii) it can be applied only if the magneto-thermal parameter $\xi = \mu_0 M_S V H_{max}/(k_B T) < 1$.

According to the latter condition (point (ii)), a validity limit for the LRT can be identified as a maximum field $H_{max} = k_B T/(\mu_0 M_S V)$ (Eq. 2.22). The inverse dependence on the particle volume V limits the range of applicability of the LRT to low fields for particles at the transition between the superparamagnetic and the blocked regimes. For the three samples analysed in this Chapter, it was indeed found that the 10 nm and 18 nm samples always and never satisfy the condition $\xi < 1$, respectively, in the range of field amplitudes considered for the measurements. On the contrary, the intermediate size of the 14 nm sample limits the applicability of the LRT to $H_{max} < (5.7 \pm 0.6)$ kA/m, a boundary evidenced in Fig. 4.7 with grey bars.

In order to test the accordance between the SAR(H) trends obtained from the experimental measurements and the LRT, the curves in Fig. 4.7 where fitted to a square law SAR $= \alpha H^2$ in the intervals of validity of the model. Looking at the fits in Fig. 4.7, it can be observed that the LRT sometimes fails to describe correctly the increase of SAR with the amplitude H of the field, particularly at high H values. An example of this behaviour is the SAR of the 14 nm sample at 741.6 kHz.

As a matter of fact, a discrepancy between the LRT predictions and experimental data is not new in literature. It is indeed known that MNPs larger than 10 nm may present an increase of the SAR with the field amplitude H that is better described by a power law greater than 2 [89, 141], particularly at high frequencies. This behaviour is mainly due to the transition from the superparamagnetic regime to the blocked state, which occurs by increasing the particle diameter and/or increasing the frequency [47, 64].

As described in Chapter 2.2.2, however, no models are available to date to describe the SAR(H) trend in the just cited transition region. The Rayleigh model, which predicts SAR $\propto H^3$ and applies to multidomain ferromagnetic nanoparticles, it is also not suitable for describing the SAR of the present samples of MNPs. It is indeed reported in literature that these types of MNPs typically show SAR $\propto H^x$, with $2 < x < 3$ [47, 64].

In order to check this occurrence, the SAR(H) curves were analysed with the same method presented in Chapter 3 while studying the effect of the size of MNPs on their SAR [64]. In details, the SAR(H) curves of all the samples were fitted to a free-exponent power-law model, i.e. SAR$(H) = \beta H^x$, extended to the whole range of amplitudes H used for the measurements. The obtained best-fit curves are shown in Fig. 4.7 in dashed lines: a better agreement between theory and experimental data is clearly observed.

The values of the free-exponents x returned by the best-fits for the three samples, both in water and in agarose gels, are reported in Fig. 4.9. From the graphs it is possible to see that most of the curves are well described by an exponent greater than 2 but lower than 3, in agreement with the previous

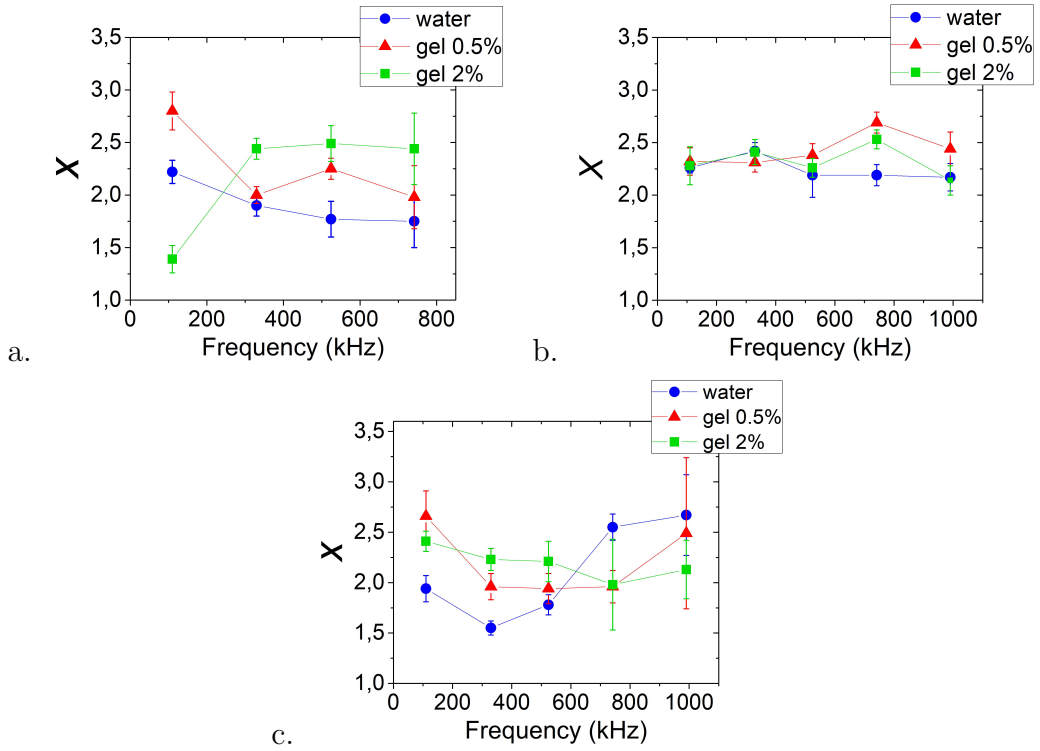

Figure 4.9: Values of the parameter x obtained for the (a) 10 nm, (b) 14 nm and (c) 18 nm samples by fitting the SAR(H) curves shown in Fig. 4.7 with a free-exponent power-law model, in the form SAR(H) = βH^x [64].

discussion. However, it is not observed a clear trend of the exponent neither with the solvent composition, nor with the particles diameter, nor with the frequency f of the AMF ($x(f)$ seems to be quite constant).

Results presented in this section highlight the necessity already mentioned elsewhere [64] to investigate more in depth (also theoretically) the mechanisms responsible for the heat release of MNPs in the transition region between the superparamagnetic regime and the blocked state, when neither the LRT ($\xi < 1$) nor the Rayleigh model are applicable.

LRT model and estimation of the relaxation times

The LRT allows to estimate the effective relaxation time of MNPs when applicable. According to Eq. 2.20, indeed, when fitting the LRT to the SAR(H) data in Fig. 4.7, using a function SAR(H) = αH^2, the best-fit returns a parameter α well defined in the frame of the LRT: $\alpha = \mu_0 \pi f \chi''(f)/\rho$. It is therefore possible to invert the last expression and to estimate the value of $\chi''(f)$ at each of the five frequencies chosen for the measurements:

$$\chi''(f) = \frac{\alpha \rho}{\mu_0 \pi f}. \tag{4.2}$$

Interestingly, this estimation allow to study the experimental trend of $\chi''(f)$ and to compare it with the theoretical expression presented in Eq. 2.9, and shown in Fig. 2.3b. Moreover, by inverting Eq. 2.9, the relaxation time τ of MNPs can also be estimated.

It is worth noting that τ corresponds to the effective relaxation time in the case of water samples, while it equals the Néel relaxation time in the cases of gel samples, because here the Brown relaxation is suppressed. The best fits of the LRT to the SAR(H) curves both in water and in agarose gels allow therefore to estimate all the MNPs relaxation times: τ, τ_N and τ_B. Unfortunately, this analysis applies only to the 14 nm sample, since the SAR is the same in water and in gel for the 10 nm sample (it means $\tau \simeq \tau_N$), while the LRT does not apply to the 18 nm sample.

Experimental values of $\chi''(f)$ as obtained from the just described analysis are shown in Fig. 4.10 for both the 10 nm and 14 nm samples. For the 10 nm sample, $\chi''(f)$ seems to be constant at least in the interval from 329.6 kHz to 741.6 kHz, with the only exception of the point at 109.8 kHz (Fig. 4.10a). These data do not allow to hypothesize any specific trend of $\chi''(f)$, therefore it will be considered as a constant. On the contrary, in the case of the 14 nm sample a clear increase of $\chi''(f)$ when reducing the frequency is observed (Fig. 4.10b) in both the dispersant media (aqueous solution and agarose gels).

The results of the 14 nm sample were tentatively fitted according to Eq. 2.9, using the experimental values of the saturation magnetization M_{S_V} (Table 4.3) and of the core volume V (Table 4.2), and setting the effective relaxation time τ as the only free parameter. Best-fits are shown in dotted lines in Fig. 4.10b, extended to a wider frequency range with the purpose of identifying the position of the maxima. However, it is worth noting that the present discussion is somehow speculative, since fits are extended over a very large interval compared to the experimental data, which are limited to the tail of the curves.

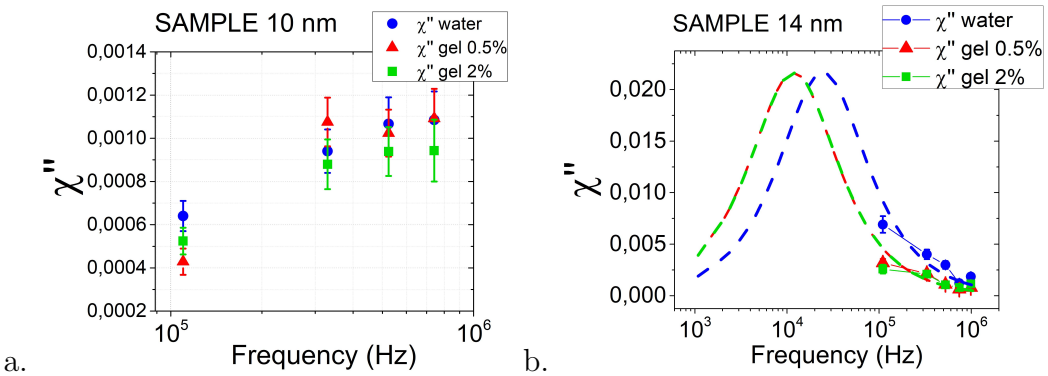

Figure 4.10: Out-of-phase component of the magnetic susceptibility of the 10 nm (a) and 14 nm (b) samples (solid symbols) as obtained by fitting the SAR(H) curves of Fig. 4.7 to the LRT. For the 14 nm sample, data are tentatively fitted (dashed lines) with the theoretical expression of $\chi''(f)$ (see Eq. 2.9).

Table 4.5: Effective relaxation times τ obtained from the best-fit of the $\chi''(f)$ curves of Fig. 4.10, according to Eq. 2.9, for the 10 nm and 14 nm samples in water solution and agarose gels.

Medium	$\tau(s)$ [10 nm sample]	$\tau(s)$ [14 nm sample]
Aqueous solution [τ_{water}]	$(4.0 \pm 1.0) \cdot 10^{-8}$	$(6.5 \pm 1.1) \cdot 10^{-6}$
Agarose gel 0.5% [$\tau_{gel}(0.5\%)$]	$(4.0 \pm 0.9) \cdot 10^{-8}$	$(1.35 \pm 0.21) \cdot 10^{-5}$
Agarose gel 2% [$\tau_{gel}(2\%)$]	$(3.5 \pm 0.9) \cdot 10^{-8}$	$(1.34 \pm 0.30) \cdot 10^{-5}$

From the fits of Fig. 4.10b, the maxima of the $\chi''(f)$ curves in water and agarose gels are shown to occur at 25 kHz for the water sample and at 12 kHz for the gels. These values are lower than those reported in literature for 14 nm MNPs [142, 143], but a direct comparison would be meaningless since $\chi''(f)$ is known to be strongly affected by the polydispersity of the samples.

The effective relaxation times obtained as best-fit parameters in water (τ_{water}) and in agarose gels (τ_{gel}) for both the 10 nm and 14 nm samples are reported in Table 4.5. As expected from the observation of the same SAR values in the two gels with different mass fractions, it results $\tau_{gel}(0.5\%) \simeq \tau_{gel}(2\%)$ for both samples. Moreover, for the 10 nm sample it was observed $\mathrm{SAR}_{water} \simeq SAR_{gel}$, and consistently $\tau_{gel} \simeq \tau_{water}$. On the contrary, τ_{gel} results to be significantly different from τ_{water} in the case of the 14 nm sample.

Considering that MNPs are immobilized in gel (i.e. the Brownian motion is hindered), it can be assumed

$$\tau_{water} \approx \tau = \frac{\tau_N \tau_B}{\tau_N + \tau_B}, \tag{4.3}$$

while $\tau_{gel} \approx \tau_N$. As a consequence, the three relaxation times shown in Table 4.5 for the 10 nm sample are all an estimation of the same Néel relaxation time, which is commonly dominant over the Brown relaxation time for small superparamagnetic nanoparticles. For the 14 nm sample, it is instead possible to assume $\tau_N \approx \tau_{gel}(0.5\%) = (1.35 \pm 0.21) \cdot 10^{-5}$ s, and to estimate the Brown relaxation time by reversing Eq. 4.3, using $\tau \approx \tau_{water} = (6.5 \pm 1.1) \cdot 10^{-6}$. It results $\tau_B = (1.3 \pm 0.4) \cdot 10^{-5}$. Interestingly, for the 14 nm sample $\tau_N \sim \tau_B$, i.e. the two relaxation mechanisms contribute almost equally to the heat release. This result is a direct consequence of the smaller SAR values observed for the 14 nm MNPs in gel compared to water (Fig. 4.7).

However, it is important to stress again that the presented method suffers of several limitations due to the approximations used for estimating both $\chi''(f)$ and τ_N. The information about τ_B obtained using this approach must be intended only as complementary to those reported in literature and obtained by applying more reliable methods [103, 141, 144, 145]. For example, a better estimation of τ_B can be obtained by accurately measuring (i) the physical parameters entering Eq. 2.5 [144] or (ii) the AC magnetically-induced heating

properties of viscous samples [103]; (iii) by modelling of the Brownian relaxation of MNPs in ferrofluids by means of the Fokker–Planck equation [141], or (iv) by means of magnetic spectroscopy of the Brownian motion of MNPs [145].

As regards the nature of the values presented in Table 4.5, the estimated effective relaxation time of the 10 nm MNPs is very similar to other values reported in literature [46,64] for particles of comparable size, while the relaxation times of the 14 nm MNPs are slightly higher than literature data [64, 102]. However, the latter result could be explained by considering a high level of magnetic anisotropy (i.e. a high value of K_a in Eq. 1.5) and/or interactions between the MNPs [21, 49, 137, 146, 147], which would modify Eq.1.5 in the form of the Vogel-Fulcher equation $\tau_{VF} = \tau_0 \exp(KV)/(k_B(T - T_0))$, where T_0 is a temperature factor accounting for the increased energy barrier because of interactions [9].

Estimation of the dipolar coupling

It is interesting to evaluate the strength of the dipolar coupling between the MNPs in the three samples (in water), to further support the initial hypothesis of negligible interactions.

For the 10 nm sample, this evaluation can be easily performed by looking at the FC curve of Fig. 4.5, since this sample is superparamagnetic at room temperature ($T_B \sim 143$ K). Plotting the magnetization of the sample normalized by the amplitude of the applied magnetic field (M_{FC}/H) as a function of the inverse of the temperature ($1/T$), it is indeed immediately observed (Fig. 4.11) that this sample satisfies the Curie-Weiss law in the superparamagnetic regime (red line).

On the contrary, in the case of the 14 nm and 18 nm samples, MNPs are blocked up to 260 K, and the dipolar energy can be estimated only by applying the formula

$$E_{dip} \sim \frac{\mu_w}{4\pi} \cdot \frac{m^2}{\bar{d}^3} \tag{4.4}$$

where $\mu_w \sim 1.256627 \cdot 10^{-6}$ H/m is the magnetic permeability of the water, $m = M_S V \rho_{Fe_3O_4}$ is the magnetic dipole of one particle at T =260 K, $\rho_{Fe_3O_4}$ = 5200 kg/m^3 is the density of magnetite and $\bar{d}$ is the mean interparticle distance (which depends on the concentration of the sample). To obtain the latter value, the total number (# NPs) of nanoparticles in 1 mL of sample was first computed by considering the concentration of each sample and the mass of one particle ($m \simeq V \cdot \rho_{Fe_3O_4}$, where $V = (4/3)\pi(d_{TEM}/2)^3$). The mean interparticle distance was then approximated as $\bar{d} \approx (1/\#NPs)^{1/3}$.

Results of the main parameters computed for each sample for the calculation of E_{dip}, the values of E_{dip} and the ratio between E_{dip} and the thermal energy k_BT (at T = 260 K) are reported in Table 4.6. As can be seen, the ratio E_{dip}/k_BT in water at 260 K is less than $1.2 \cdot 10^{-2}$ for all the samples, i.e. the energy of the dipolar interactions among the particles is less than 1% the thermal energy of the system.

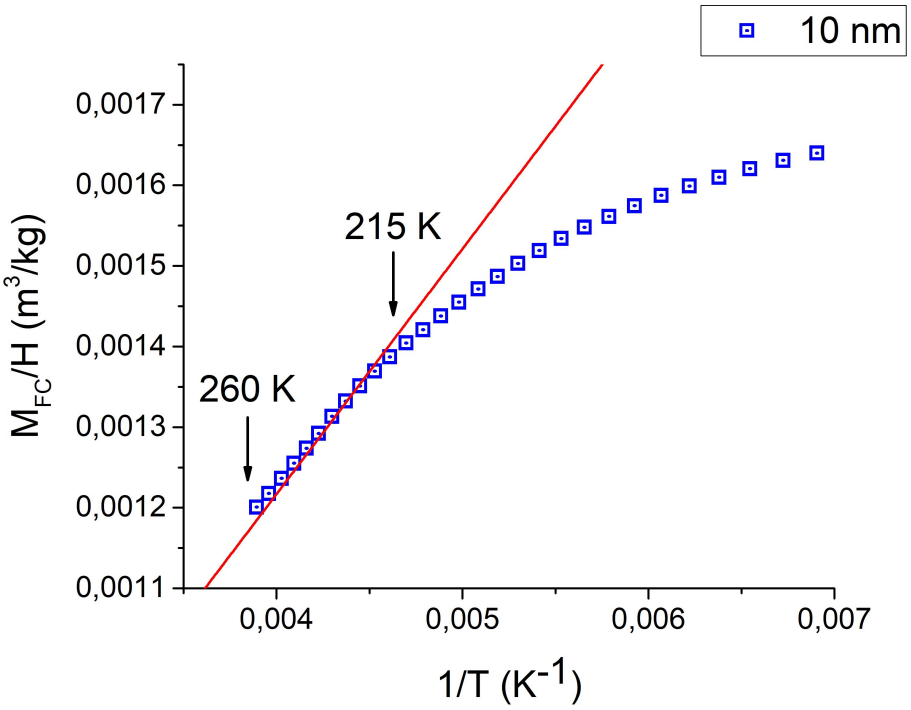

Figure 4.11: Magnetization of the 10 nm sample divided by the amplitude of the applied magnetic field, as a function of the inverse temperature. The linear trend in the temperature interval from 260 K to 215 K is a proof that the sample behaves as predicted by the Curie-Weiss law in the superparamagnetic regime [117].

Table 4.6: From the top to the bottom, for each sample of MNPs: magnetite concentrations into the sample used for MFH measurements; number #NP of MNPs within 1 mL of aqueous solution; mean interparticle distance $\bar{d}$ calculated at the same concentration; mean magnetic moment m of a single MNP; dipolar energy E_{dip} obtained from Eq. 4.4 using the data from the morphological and magnetic characterization of the samples; ratio E_{dip}/k_BT between the dipolar and thermal energies of MNPs [117].

	10 nm sample	14 nm sample	18 nm sample
$[Fe_3O_4]$ (mg/mL)	10	10	3
# NPs per mL	$2.92 \cdot 10^{15}$	$1.28 \cdot 10^{15}$	$1.92 \cdot 10^{14}$
$\bar{d}$ (nm)	70	92	173
m (A·m^2)	$1.75 \cdot 10^{-19}$	$5.78 \cdot 10^{-19}$	$1.38 \cdot 10^{-18}$
E_{dip}(J) in water	$8.96 \cdot 10^{-24}$	$4.28 \cdot 10^{-23}$	$3.65 \cdot 10^{-23}$
$\frac{E_{dip}}{k_BT}$ in water	$2.50 \cdot 10^{-3}$	$1.19 \cdot 10^{-2}$	$1.02 \cdot 10^{-2}$

4.2 Numerical simulations on the Brownian motion effects in MFH

4.2.1 Introduction

Numerical simulations of MFH experiments performed by applying Monte Carlo techniques can provide extremely precious information of what happens to the nanoparticles at the microscopic level, allowing the researcher to reach a deeper understanding of the nature of the heat release. Numerical simulations can be used either as an independent tool to predict the outcome of a MFH experiment, or together with experimental measurements for a direct comparison of the theoretical models developed so far with the actual results. Moreover, most of the times a numerical approach is the only method applicable for deepening the study of MFH at the microscopic level.

In this section, numerical simulations are applied to study *in silico* the role of the Brownian motion in MFH. Simulations were performed with a suitable program written in *C++*, developed by Prof. Julian Carrey and his collaborators for previous studies, as the one of Ref. [47] and Ref. [104]. To summarize briefly the properties of the code (details are given in the cited references), it is capable to simulate an ensemble of magnetic nanoparticles randomly positioned and oriented in the space, and to compute the evolution of the magnetization of the system due to the Néel relaxation when an external alternating magnetic field is applied. All this computation is performed by simulating random numbers with opportune algorithms that must be correctly implemented by the programmer. The main output of the program is a magnetic hysteresis loop, obtained after a proper averaging over multiple repetitions of the same simulation.

In details, the number of MNPs generated by the program, their size, their magnetic properties (M_S and the anisotropy constant K) and the concentration of the sample are all user-defined parameters. However, it is not possible to define a shape different than the spherical one for both the MNPs and the space where they are confined (i.e. a sample holder, a lysosome, etc.). Moreover, the program does not allow to implement the polydispersity of MNPs, and a perfect monodispersion of particles of identical diameters is assumed. As a result, all the MNPs simulated by the Monte Carlo code are exactly the same for both the morphological and the magnetic features.

As regards the MNPs distribution in space, both MNPs and their easy axes are randomly positioned in the space, and they are supposed to remain motionless with their original orientation. However, the program is designed to repeat each simulation tens of times, each time renewing the MNPs position and the easy axes orientation, and finally averaging over the multiple random configurations of the same system.

Dipolar interactions between MNPs are implemented in the program: the dipolar field produced by each particle on all the other particles is carefully

computed taking into account the distance and the relative orientation between each couple of MNPs. Therefore, the fluctuations of each particle magnetic moment according to the Néel relaxation are computed considering the effects of both the external field and the dipolar field produced by the MNPs.

Considering all these contributions, the calculation time of a single hysteresis loop could result to be very long if a large number of MNPs is defined; in particular, it approximately scales with the square of the number of MNPs [104]. Commonly, thousands of nanoparticles are simulated and the evolution of the magnetization of the system (to describe a single complete hysteresis loop) is computed over 2000 steps, requiring $\sim$ 90 minutes calculation time on 32 processors operating in parallel.

The described program has been used by Carrey et al. [47] to study the heating properties of MNPs inside a lysosome, an almost spherical structure of the cells where MNPs seem to be internalized during the uptake process. The heating efficiency of MNPs was studied as a function of their size, concentration, anisotropy constant and saturation magnetization, and as a function of the properties of the applied alternating magnetic field, i.e. its amplitude and frequency. As can be immediately understood, the main advantage of numerical simulations applied to MFH is their capability to allow scientists to study separately the effects of single parameters on the heating efficiency, keeping fixed all the other parameters. This approach is almost impossible to be realized in experimental studies of MFH, due to the intrinsic difficulties in reproducing and in tuning precise characteristics in real samples of MNPs. Therefore, information obtained from numerical simulations are recognized as a fundamental guide to address the development of more powerful MNPs in MFH and the interpretation of the experimental results.

Implementing the Brownian relaxation

The program developed by Carrey et al. (for details on the algorithm the reader is invited to refer to Refs. [47, 104]) does not take into account the Brownian motion: only the Néel relaxation is implemented. Each complete oscillation of the external magnetic field is divided in thousands of steps and, at each step of the simulation, the energy barrier separating the two minima for the superspin orientation is computed, and a probability value is assigned to the reversal of the magnetization. The drawing of a random number determines whether the reversal occurs or not for each particle, the magnetizations of the particles are summed to give the total magnetization of the system, and the simulation proceeds to the next step. At the end, the entire loop is simulated again, with a different initial random position and orientation of each particle, and the loops obtained in the different runs are averaged to give the final result.

To introduce the Brownian motion in the code, some changes to the algorithm are mandatory. First of all, the averaging procedure over multiple generations of ensembles of MNPs randomly positioned and oriented in space must be replaced by a single initial generation of an ensemble of MNPs with

a given orientation, that is subsequently allowed to evolve in time due to a gradual change of the orientation of their easy axes under the action of the external (and eventually the dipolar) field. It is indeed reasonable to assume that the external field may induce a rotation of the particles through the direction of the field itself. The first step to be realized is therefore to implement the possibility for the particles to rotate, i.e. to change their orientation while remaining fixed in their position in the space. The movement of the MNPs in the space (i.e. the possibility to change their position) has not been implemented in the code up to date (it requires high-level computational skills, resources and time).

The problem of the MNPs Brownian motion has already been addressed by several scientists, in different and sometimes contradictory ways. Main references on the topic are Refs. [148–151]. According to these studies, to implement the Brownian motion in a fluid it is necessary to consider all the forces acting on each particle and on its magnetic moment. Assuming the MNPs as rigid and independent dipoles in the space, the following components must be considered:

- The magnetic torque:
$$\tau_m = \vec{m} \times \vec{B}, \tag{4.5}$$
where $m = M_S V$ is the magnetic moment of the single particle and $\vec{B}$ the local field on the particle (the external magnetic field applied to the sample and eventually the dipolar field).

- The torque due to the viscous drag during the rotation:
$$\tau_V = -6\eta V_h \vec{\Omega}, \tag{4.6}$$
where η is the fluid viscosity, V_h the hydrodynamic volume of the particle and $\vec{\Omega}$ the angular velocity of rotation. This expression is obtained from the Stokes-Einstein relation for small Reynolds number particles.

- Thermal effects due to the random collisions between the particle and the molecules of the fluid. These effects can be implemented in the model as a white noise force N, characterized by a flat power spectrum in frequency and therefore δ-autocorrelated in time and space in the Fourier space, with mean value equal to zero [148]:
$$\begin{aligned} &< N(t) >= 0 \\ &< N_i(t) N_j(t') >= 2D\delta_{ij}\delta(t - t'). \end{aligned} \tag{4.7}$$
In the previous expression, $D = 6k_B T \eta V_h$ is the Einstein-Smoluchowski diffusion constant.

The complete balance of the three torques gives:

$$\tau_T = \vec{m} \times \vec{B} - 6\eta V_h \vec{\Omega} + \sqrt{2D}\vec{N}. \tag{4.8}$$

In the inertia-less limit, which can be considered valid having already defined a low Reynolds number for the MNPs, and considering the frictional drag forces as sufficiently intense to prevent inertial rotation, the previous equation can be simplified to obtain the angular velocity of rotation:

$$\vec{\Omega} = \frac{1}{6\eta V}\left(\vec{m} \times \vec{B} + \sqrt{\frac{12\, k_B\, T\, \eta\, V_h}{\Delta t}}\vec{W}\right) \tag{4.9}$$

where $\vec{W}$ is a random vector in the space: each cartesian direction is given by a random gaussian number with zero mean and unit standard deviation. The second term of $\vec{\Omega}$, which is summed to the magnetic torque, can be called *Brownian torque* because of its random properties.

The module of the Brownian torque needs to be rescaled by $\sqrt{\Delta t}$, where Δt is the time covered by each step of the simulation, because of the intrinsic properties of the Brownian motion (given a number of steps and the length of each step, the distance from the initial point to the final point is proportional to the square root of the total space covered by the object during its Brownian motion). To clarify this point, Δt depends on the frequency f of the magnetic field (i.e. on the period T of one single oscillation of the magnetic field) and on the number of steps N chosen by the programmer to describe one hysteresis loop in the simulation: $\Delta t = T/\mathrm{N} = 1/(f\mathrm{N})$.

To compute the movement of the magnetic moment $\vec{m}$ and of the easy axis $\vec{e}$ (a unit vector) of each particle, it is necessary to consider the tangential rate change of both vectors, given by the perpendicular component of their angular velocity, i.e.:

$$\frac{d\vec{m}}{dt} = \vec{\Omega} \times \vec{m} \tag{4.10}$$

and

$$\frac{d\vec{e}}{dt} = \vec{\Omega} \times \vec{e}. \tag{4.11}$$

These equations lead to the final algorithm for the Brownian rotation of the MNPs:

$$\vec{m_{i+1}} = \vec{m_i} + \frac{d\vec{m}}{dt} \cdot \Delta t \tag{4.12}$$

and

$$\vec{e_{i+1}} = \vec{e_i} + \frac{d\vec{e}}{dt} \cdot \Delta t, \tag{4.13}$$

where i is an index numbering the step of the simulation.

This algorithm was implemented into the code developed by Carrey et al. [104]. To date, however, the program works properly only if $|\vec{\Omega}| \cdot \Delta t < \alpha$, where α is an angle small enough to allow the simulation to describe correctly the physics of the system. This limit is indeed caused by the fact that at each step of the simulation the program at first decide if the magnetization reversal occurs or not due to the Néel relaxation, as in the original version of the code, and subsequently rotates rigidly the particles under the action of the total

torque τ_T. The angle of rotation depends on the amplitude of the torque τ_T and on the time length of each step of the simulation, i.e. $\Delta t = T/\mathrm{N}$. However, the interval Δt must be much lower than the Néel relaxation time, otherwise the physics described by the simulation would be wrong. The probability of the Néel relaxation to occur during the Brownian rotation in a single step must indeed be very small, otherwise the amplitude of the Brownian rotation described by the simulation would be larger than the real one. It is therefore necessary to run simulations with a large number of steps (in the present case N=10000) and only with acceptable frequencies; in this way $\Delta t = T/\mathrm{N} \ll \tau_N$.

Tests validating the proper operation of the algorithm

Several tests have been performed to verify the proper functioning of the algorithm.

(1) To verify that the code implements correctly the Brown relaxation time, an ensemble of 1000 MNPs have been simulated. The MNPs core size was fixed to $d = 12$ nm, the coating thickness to $c_t = 2$ nm, the viscosity of the water to $\eta = 0.001\,\mathrm{Pa{\cdot}s}$ and the room temperature to $T = 300$ K. With these parameters, Eq. 2.5 theoretically leads to a Brown relaxation time $\tau_B = 1.554 \cdot 10^{-6}$ s.

As initial conditions of the simulations, all the easy axes and the magnetic moments were set aligned along the z-axis, so the magnetization of the system was saturated to its maximum value. No external fields were applied, and also dipolar interactions were switched off. To suppress Néel relaxation, a very high value for the anisotropy constant ($K = 10^8\,\mathrm{J/m^3}$) was fixed.

In these conditions, during a run of the simulation the system evolves because of the Brownian torque alone, which determines the decay of the magnetization of the system according to the law $M(t) = M(0)e^{-t/\tau_B}$. The program was ran for a time long enough to allow the magnetization of the system to decay, averaging over 10 repetitions of the same simulation. The result is shown in Fig. 4.12 (the program saves the normalized magnetization of the system, therefore $M(0) = 1$), where the curve has been fitted with an exponential function as the one just reported, giving $t_1 = \tau_B = 1.5567 \cdot 10^{-6}$ s. The accordance between the theoretical estimation of τ_B and the one obtained by simulation is therefore highly satisfactory.

(2) A group of simulations was performed considering only one particle, and starting with its magnetic moment parallelly or perpendicularly oriented to the external oscillating magnetic field (always applied along the z-direction). The capability of the particle to rotate and to follow the oscillations of the field was investigated in limit and peculiar cases, analysing the evolution of both the magnetization and the easy axis orientation through all the 10000 steps of one simulation (one loop). For these simulations, the MNP core size was fixed to $d = 15$ nm, the coating thickness to $c_t = 2$ nm, and the saturation magnetization to $M_S = 2 \times 10^5$ A/m. All the other parameters were changed accordingly

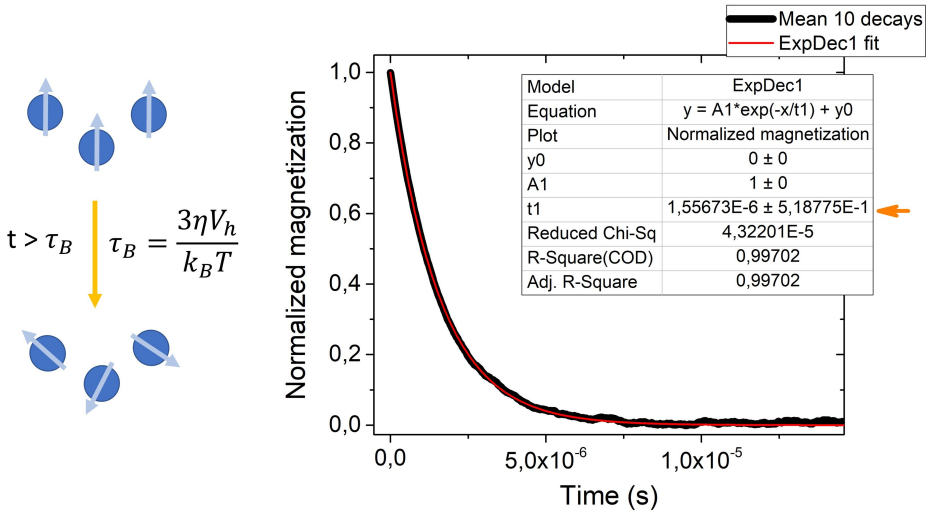

Figure 4.12: Average of 10 simulations of the decay of the magnetization induced by the Brownian torque alone on an ensemble of MNPs initially aligned along the same direction (black line). The red line is the best-fit performed with an exponential function; the orange arrow highligths the estimation of τ_B according to simulations.

to the aim of the simulation, considering that the anisotropy constant K allows to switch on (low values) or switch off (high values) the Néel relaxation, the viscosity η allows to switch off or switch on the Brown relaxation, and the temperature affects both (although linearly for τ_B and exponentially for τ_N).

The reader is invited to look at Figures from Fig. 4.13 to Fig. 4.16, where some of the peculiar cases simulated are presented. Details about the simulations are given in the legends. Graphs on the left (points in 3D space) represent the direction of the vector $\vec{e}$ (the easy axis, centred in (0,0)) at each step of the simulation, with a colour scale associated to the number of steps (1 [blue] < N < 10000 [red]), i.e. with time. Graphs on the right represent the evolution of the particle magnetic moment along the z-axis, and only the first hysteresis loop is reported (no averaging).

These simulations confirmed the ability of the code to correctly describe the Brownian relaxation. Indeed, it was proved that the magnetic torque acts to align the magnetization of the particle along the direction of the oscillating magnetic field (Fig. 4.14), while the Brownian torque appears as a noise in the hysteresis loop due to its random nature (Fig. 4.13). Moreover, the particular cases with the easy axis of the particle fixed perpendicularly (Fig. 4.15) or in parallel (Fig. 4.16) to the direction of the external field gave exactly the results expected from the theory.

(3) To work properly, the program must satisfy the Linear Response Theory within its validity limits with $\tau = \tau_B$ when the Néel relaxation is suppressed. In these conditions, both the magnetic and the Brownian torques introduced in Eq. 4.9 are responsible of the movement of the magnetization, each one

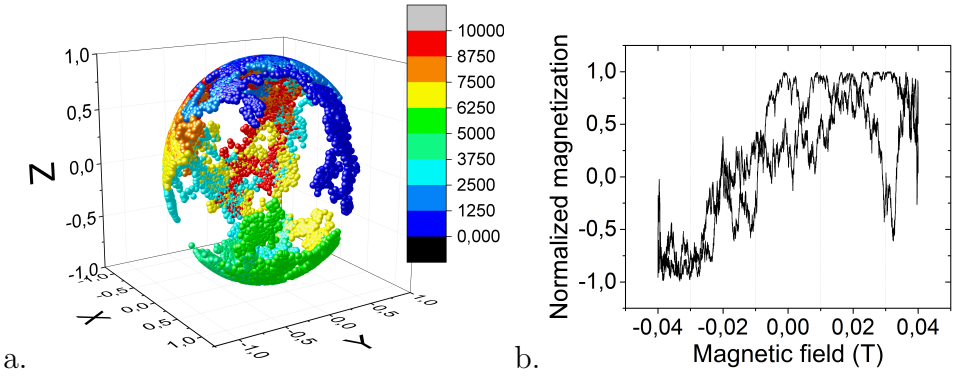

a. b.

Figure 4.13: Simulation parameters: $\vec{m} \perp \vec{B}$, $B = 0.04$ T, $f = 30000$ Hz, $T = 300$ K, $K = 10^8$ J/m^3, $\eta = 0.001$ Pa $\cdot$ s. The Néel relaxation is switched off because of the high K, and the amplitude of the field B is high enough to determine a strong magnetic torque, which tends to align the magnetization to the direction of the alternating magnetic field. However, also the Brownian random torque contributes to the rotation of the easy axis (a) and of the magnetic moment (b), appearing as a noise in the hysteresis loop (b).

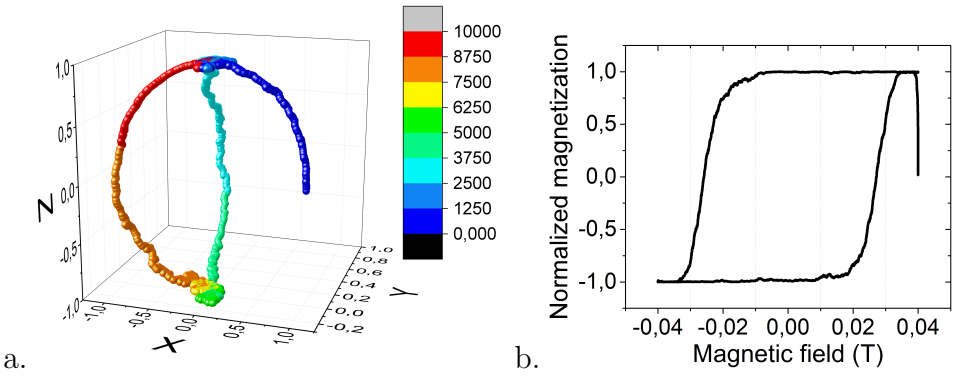

a. b.

Figure 4.14: Simulation parameters: $\vec{m} \perp \vec{B}$, $B = 0.04$ T, $f = 1000$ Hz, $T = 3$ K, $K = 10^8$ J/m^3, $\eta = 0.01$ Pa $\cdot$ s. The Néel relaxation is switched off (high K), the magnetic torque is strong, because of the high field B, and the Brownian torque is almost zeroed (high η and low T). Considering the very low frequency f (long period), the easy axis (a) and the magnetization (b) have time to completely follow the oscillation of the field, i.e. to move towards the z-direction.

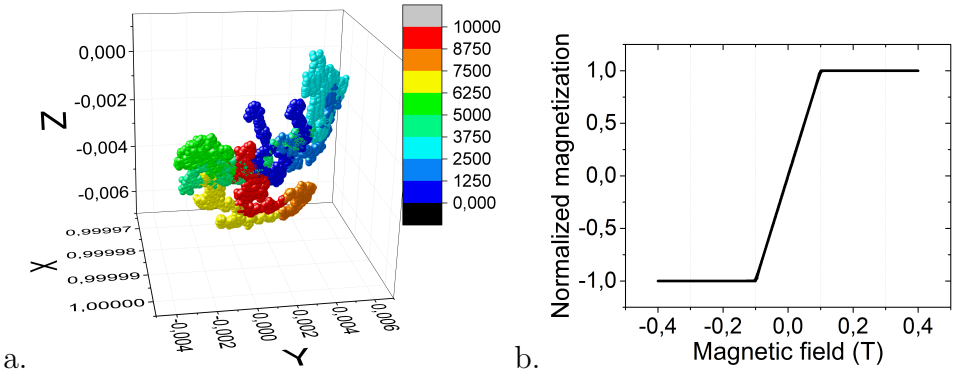

a. b.

Figure 4.15: Simulation parameters: $\vec{m} \perp \vec{B}$, $B = 0.4$ T, $f = 100000$ Hz, $T = 3$ K, $K = 10^4\,\mathrm{J/m^3}$, $\eta = 1$ Pa $\cdot$ s. In these conditions, with very high η and low T, the easy axis remains almost fixed along its initial direction, perpendicular to the field (a), while the magnetization changes its orientation because of the Néel relaxation (low K) and of the high field B. The result is the typical closed hysteresis loop of a MNP with the easy axis fixed perpendicular to the direction of the field (b).

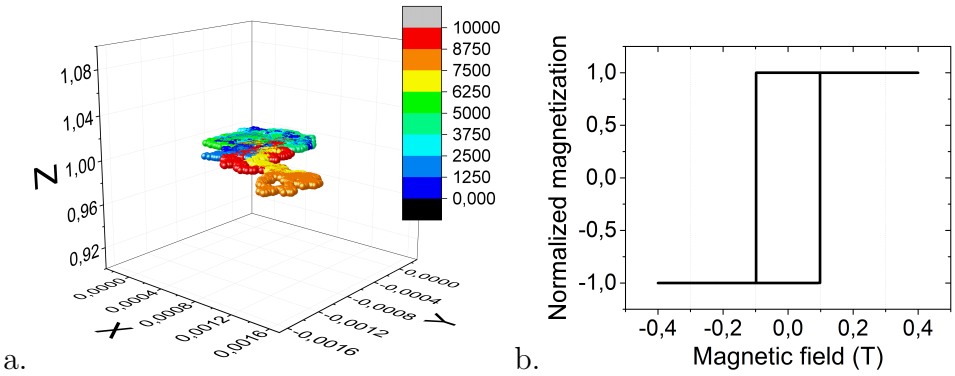

a. b.

Figure 4.16: Simulation parameters: $\vec{m} \parallel \vec{B}$, $B = 0.4$ T, $f = 100000$ Hz, $T = 0.01$ K, $K = 10^4\,\mathrm{J/m^3}$, $\eta = 0.1$ Pa $\cdot$ s. In these conditions, the easy axis remains fixed along the z-direction (a) with the field (high η and low T), the Néel relaxation is switched on (low K), but due to the low temperature T the magnetization reverses only when the field B becomes sufficiently high. The typical square hysteresis loop of a MNP with its easy axis parallel to the direction of the field (b) is obtained, and as expected [47] for the coercive field it results $H_C = 2K/M_S = 0.1$ T.

characterized by an independent characteristic time. As described by Raikher et al. [149], these times are τ_B of Eq. 2.5 for the Brownian torque and

$$\tau_H = \frac{3\eta V_h}{\mu H_0} \tag{4.14}$$

for the magnetic torque, where $\mu = m = M_S V$ and $H_0 = H_{max}$. τ_H can here be defined as a "magnetic relaxation time". As described by Raikher et al. [149], the magnetic relaxation does not follow the LRT, in fact when both the torques move the particle magnetization, the maximum opening of the hysteresis loop is found to occur at $\omega\tau_H \sim 1/\xi_0$, where $\omega = 2\pi f$ and $\xi_0 = mH_0/(k_B T)$, and not at $\omega\tau_H = 1$. For a further clarification of this point, the reader is invited to see test number (4) in the following pages.

In the weak field limit (or high temperatures limit), $\tau_B \ll \tau_H$ and the system should satisfy the LRT [149], with the area of the hysteresis loop equal to:

$$A = \frac{\pi\mu_0^2 H_0^2 M_S^2 V}{3k_B T} \cdot \frac{\omega\tau_B}{1+\omega^2\tau_B^2} \sim \chi''(\omega) H_0^2, \tag{4.15}$$

and the normalized value

$$A \cdot \frac{3k_B T}{\pi\mu_0^2 H_0^2 M_S^2 V} = \frac{\omega\tau_B}{1+\omega^2\tau_B^2} \tag{4.16}$$

having a maximum equal to 0.5 when $\omega\tau_B = 1$. The factor 3 in Eq. 4.15 is introduced because of the random orientation of the easy axes, and it has to be removed when all the MNPs are simulated as aligned. However, since the axis of rotation (due to the magnetic torque) is not defined *a priori*, and the Brownian torque adds a random component to the rotation, the condition with all the easy axes aligned never happens if the Néel reversal of the magnetization is suppressed as in the present case, and the factor 3 must be considered in the formula.

To verify the capability of the program to describe this weak field limit, a set of simulations were ran setting $K = 10^8$ J/m^3, to remove the Néel relaxation, and $\mu_0 H_0 = 0.3$ mT, where $\mu_0 = 4\pi \cdot 10^{-7}$ T·m/A is the vacuum magnetic permeability. Results are shown in Fig. 4.17a. It is worth noting that with the parameters used for the simulation $\tau_B = 1.55 \cdot 10^{-6}$ s and $\tau_H = 1.19 \cdot 10^{-4}$ s, therefore $\tau_B \ll \tau_H$. An averaging procedure over 3000 repetitions of the same hysteresis loop (which required 47 hours of computation time on a 32 processors supercomputer) was necessary to minimize the noise produced by the Brownian torque in the final loops. Despite this, the hysteresis loops simulated at different frequencies resulted to be still very noisy (Fig. 4.17a). However, the normalized area of the loops (Fig. 4.17b) followed exactly the trend predicted by the LRT, showing a maximum equal to 0.5 at $\omega\tau_B = 1$.

(4) If the Brownian torque is zeroed and the Néel relaxation is switched off (for example by setting a very high value of K and $T = 0$ K), only the magnetic

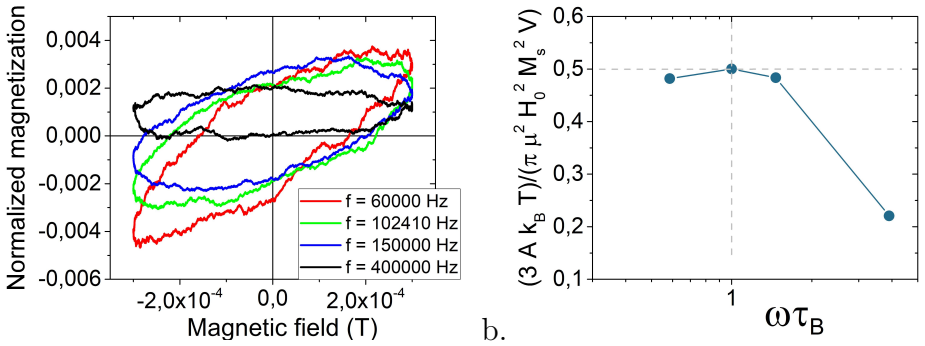

Figure 4.17: (a) Hysteresis loops obtained with the following simulation parameters: 1000 NPs, diameter $d = 12$ nm, coating thickness $c_t = 2$ nm, $K = 10^8$ J/m^3, $M_S = 2 \cdot 10^5$ A/m, $T = 300$ K, $\eta = 0.001$ Pa $\cdot$ s, 1% concentration, $\mu_0 H_0 = 0.0003$ T, frequency $60000 \leq f \leq 400000$ Hz, dipolar interactions switched off, and average over 3000 repetitions of the same hysteresis loop. In these conditions $\tau_B \ll \tau_H$ and the validity of the LRT for the Brownian relaxation could be checked. Simulations with 3000 repetitions required 47 hours of computation time on a 32 processors supercomputer, but were necessary to minimize the noise in the loops as much as possible. (b) Normalized area of the loops, showing a maximum equal to 0.5 at $\omega\tau_B = 1$, as predicted by LRT.

torque acts to rotate the particles through the direction of the field. In this condition, the area of the hysteresis loop should saturate to its maximum value when $\omega\tau_H = 0$ [149].

If the temperature of the system is slightly increased, the Brownian torque starts acting together with the magnetic torque. As a consequence, the normalized dynamic hysteresis loop area A_n presents a maximum at $\omega\tau_H \sim 1/\xi_0$, where $\xi_0 = mH_0/(k_B T)$, and converges to the same value at high frequencies for any ξ_0. Moreover, for any value of ξ_0, the particle rotation may induce the magnetic relaxation, therefore A_n tends to zero at $f = 0$ Hz [149].

The behaviour of A_n as a function of $\omega\tau_H = 2\pi f \tau_H$ for different values of ξ_0 was obtained by Raikher et al. [149] by numerically solving the nonlinear equations describing the magnetodynamics of single-domain MNPs; results are shown in Fig. 4.18a. In this section, the capability of the program to reproduce these results was tested by running a series of simulations with the following parameters: 100 MNPs, diameter $d = 12$ nm, coating thickness $c_t = 2$ nm, $K = 10^8$ J/m^3 (Néel relaxation suppressed), $M_S = 2 \cdot 10^5$ A/m, $\eta = 0.001$ Pa $\cdot$ s, frequency f ranging from 1000 Hz to 400 kHz, and averaging over 20 repetitions of the same hysteresis loop. Five different values of ξ_0 were considered by varying the magnetic field H_0 and the temperature T entering the Brownian torque; these parameters are reported in Table 4.7.

The hysteresis loops obtained from simulations performed at two exemplary values of ξ_0 are shown in Fig. 4.19. For $\xi_0 = \infty$, the area of the loop progressively decreases while increasing the frequency of the AMF (Fig. 4.19a). For $\xi_0 = 10.5$, as well as for the other values of ξ_0, the area of the loop increases up to a maximum and then decreases while increasing the frequency (Fig. 4.19b).

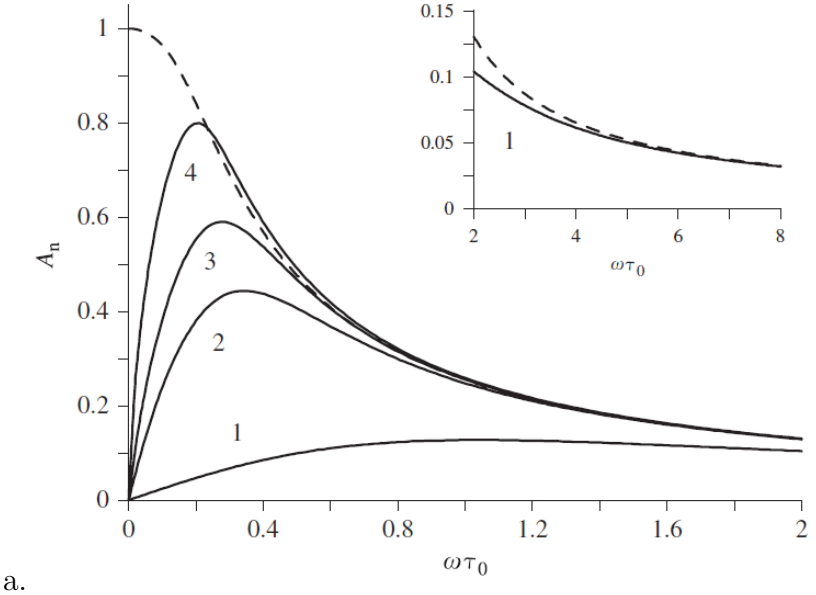

a.

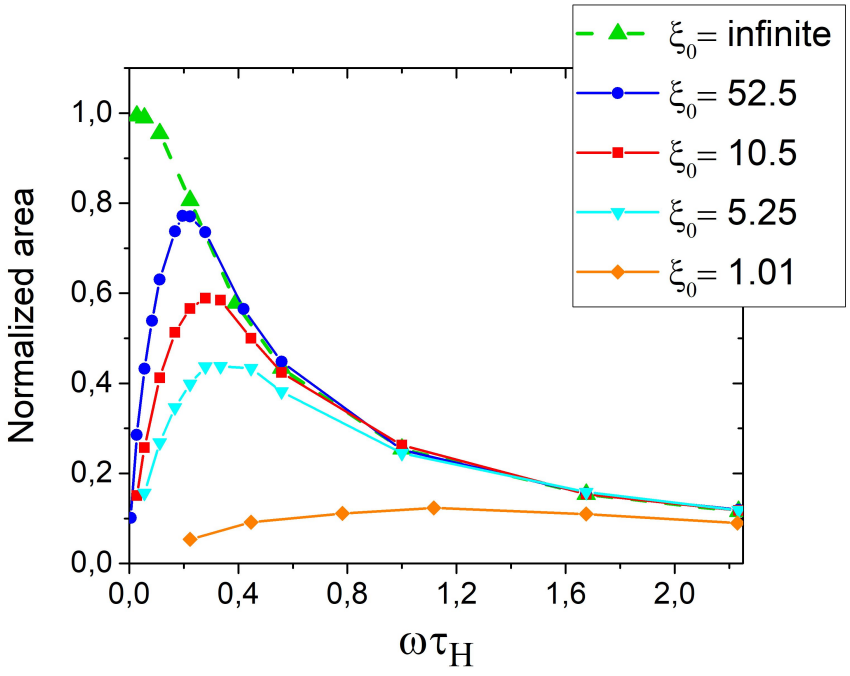

b.

Figure 4.18: (a) Frequency dependence (on the x-axis $\tau_0 = \tau_H$) of the normalized dynamic hysteresis loop area A_n for different values of $\xi_0 = mH_0/(k_BT)$ as reported by Raikher et al. [149] by numerically solving the nonlinear equations describing the magnetodynamics of single-domain MNPs. In particular, $\xi_0 = 1$ (curve 1), $\xi_0 = 5$ (curve 2), $\xi_0 = 10$ (curve 3), $\xi_0 = 50$ (curve 4), and $\xi_0 = \infty$ (dashed line). In the inset, details of the curves 2 and 4 at high frequencies are reported to show the convergence of A_n to the same values for any ξ_0. (b) Frequency dependence of the normalized dynamic hysteresis loop area A_n for similar values of ξ_0 as obtained from kinetic Monte Carlo simulations.

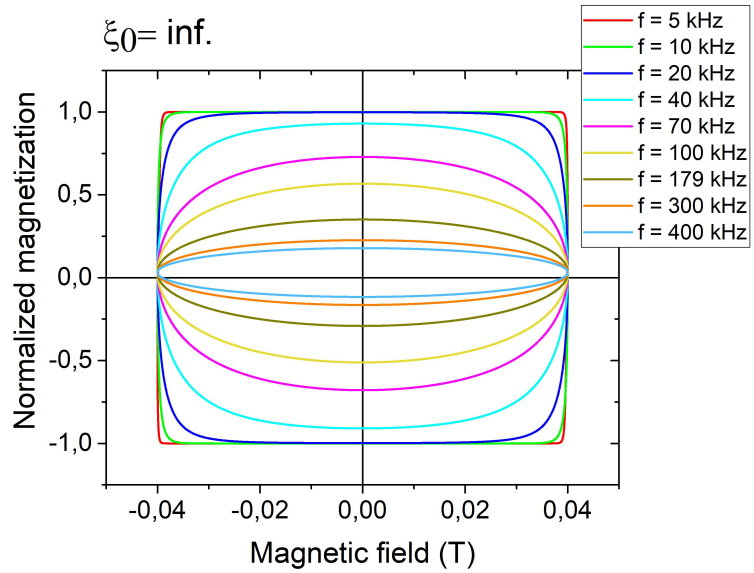

a.

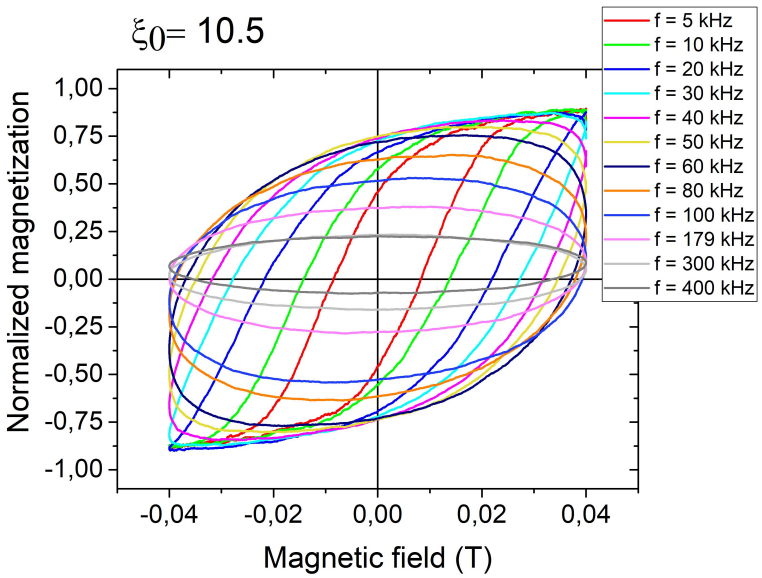

b.

Figure 4.19: Hysteresis loops obtained from Monte Carlo simulations performed for $\xi_0 = \infty$ (a) and $\xi_0 = 10.5$ (b). Details on the parameters used for the simulations are given in the text.

The normalized areas of the loops, describing the behaviour of A_n as a function of $\omega\tau_H$ for different values of ξ_0 according to simulations are reported in Fig. 4.18b.

A perfect agreement between the output of the simulations (Fig. 4.18b) and the results of the theory presented by Raikher et al. [149] (Fig. 4.18a) is observed. This result confirms the correctness of the magnetic torque as implemented in the code, i.e. with the same algorithm used by Mamiya et al. [151], although it was arguably defined as wrong by Usov et al [150].

Table 4.7: Values of the maximum amplitude of the magnetic field $\mu_0 H_0$ and temperature T used for the simulations performed at different values of $\xi_0 = mH_0/(k_B T)$ as reported by Raikher et al. [149].

$\mu_0 H_0$ (T)	T (K)	$\xi_0 = mH_0/(k_B T)$
0.04	0	∞
0.04	10	52.5
0.04	50	10.5
0.04	100	5.25
0.01	130	1.01

4.2.2 Comparison between numerical simulations and experimental results

As it has been shown in the previous section, the outcome of a simulation is a hysteresis loop, the area A of which can be easily computed and used to obtain the SAR of the MNPs with the common equation:

$$SAR = \frac{A \cdot f}{\rho}. \tag{4.17}$$

For the aims of this thesis, the Monte Carlo code developed by Carrey et al. [104], and further implemented to describe the Brownian motion of the MNPs, has been used to study the effect of the Brownian motion and to compare the expected SAR according to simulations with the SAR measured experimentally.

In particular, the new Monte Carlo code allows simulating both the experimental conditions described in Chapter 4.1, i.e. aqueous suspensions of MNPs and MNPs in agarose gel. Indeed, it implements both the Néel and Brown relaxation mechanisms occurring simultaneously in water samples (although the program does not implement the movement of the particles in space). The old version of the code, implementing only the Néel relaxation, is instead suitable to simulate the behaviour of MNPs in agarose gel, where the Brown relaxation is suppressed.

14 nm sample

The most interesting sample, according to the discussion of Chapter 4.1, is undoubtedly the 14 nm sample. To run Monte Carlo simulations on this sample, the core diameter was fixed in the code accordingly to the mean value seen by TEM measurements (14.2 nm, Table 4.3). Similarly, AFM measurements were used to determine the coating thickness (1.8 nm). The frequency ($f = 109800$ Hz) and the amplitude of the field were instead set to the same values used for the experimental measurements reported in Fig. 4.7.

Another important parameter to be fixed in the simulations is the saturation magnetization of the particles at the field values H used for the MFH experiments. To determine this parameter, the general law $M = M_S L(x)$ can be applied (in first approximation), where M_S is the actual saturation magnetization measured by means of a SQUID magnetometer at high fields (Table 4.3), and $L(x)$ is the Langevin function.

Finally, a crucial parameter in the simulations is the anisotropy constant K. To determine this parameter, an inverse approach was used, i.e. starting with an initial standard value of K several simulations were ran using the old version of the program implementing only the Néel relaxation to simulate the gel samples. The value of K was changed until the hysteresis loop obtained from the simulation reproduced exactly the experimental SAR measured in gel at the maximum field. In this way, it was found $K = 35000\,\mathrm{J/m^3}$, a reasonable value for magnetite particles of this size according to literature [7,64,85]. It is worth noting that other methods to experimentally determine the values of K were not applicable, in particular those exploiting the blocking temperature and the energy barrier distribution as obtained from the ZFC-FC measurements, considering the derivative $-d(M_{FC} - M_{ZFC})/dT$. The 14 nm sample, indeed, does not show any maximum in the ZFC-FC curve (Fig. 4.5) and particles are blocked at least up to 260 K.

With the selected value of K, the Néel relaxation time can be computed according to Eq. 1.5, imposing $\tau_0 = 5 \cdot 10^{-11}$ s (a constant in all the simulations of this Chapter); it results $\tau_N = 1.6 \cdot 10^{-5}$ s. Describing each hysteresis loop in N = 10000 steps, and working with $f = 109800$ Hz, each steps lasts $\Delta t = 1/f\mathrm{N}$ $= 9.1 \cdot 10^{-10}$ s, i.e. a time five order of magnitude shorter than τ_N. With these parameters, $\Delta t \ll \tau_N$, and it is therefore possible to run correctly also the new Monte Carlo code implementing both the Néel and Brown relaxation.

The hysteresis loops resulting from the simulations performed with the previous parameters and 4.26 mT $\leq B \leq$ 20.33 mT, averaging over 50 repetitions of the same loop on a sample of 1000 MNPs, are shown in Fig. 4.20. In particular, Fig. 4.20a shows the outputs of the simulations performed with the old Monte Carlo code implementing only the Néel relaxation; while in Fig. 4.20b the outputs of the newer code implementing both the Néel and Brown relaxation are reported. In Fig. 4.20c the loops obtained at the maximum field ($B = 20.33$ mT) with the two codes are superimposed, allowing a better comparison that highlights the effects of the Brownian motion. Indeed, as it can be seen from the figure, when the Brownian relaxation is switched on the MNPs magnetic moments follow more successfully the oscillations of the field, describing a hysteresis loop with higher values of magnetization, minor coercivity and larger area. The shapes of the loops are in both cases ellipsoidal, as expected for superparamagnetic nanoparticles.

Applying Eq. 4.17, the SAR of the sample at the different fields can be computed and compared with the experimental results of Chapter 4.1.5. Both simulated and experimental SAR are reported in Fig. 4.21. It is worth noting

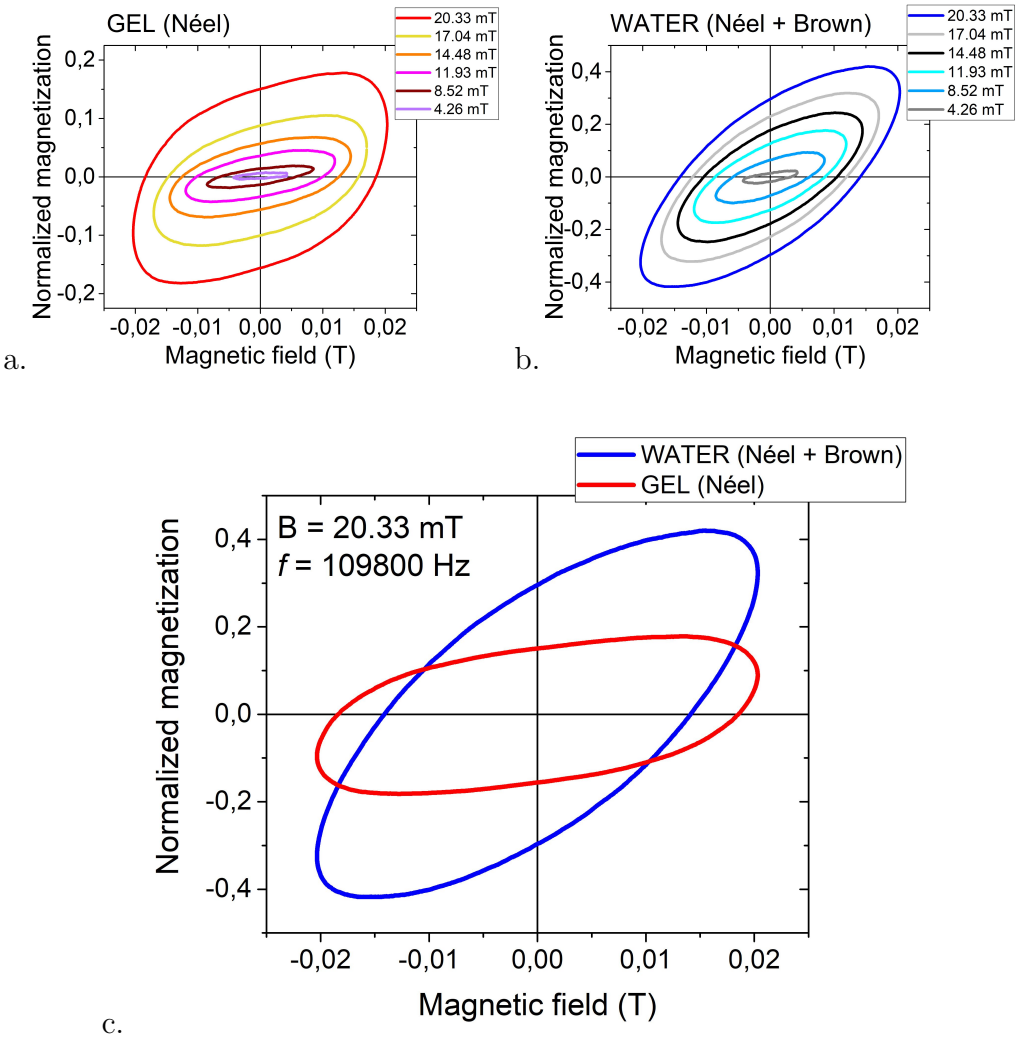

Figure 4.20: Hysteresis loops of 14.2 nm MNPs at $f = 109.8$ kHz obtained from Monte Carlo simulations performed using the parameters from the characterization of the 14 nm sample. (a) Results of the simulations performed with the code implementing only the Néel relaxation ($\sim$ gel samples). (b) Results of the simulations performed with the new version of the code, implementing both the Néel and Brown relaxation ($\sim$ water sample). (c) Direct comparison between the loops at $B = 20.33$ mT obtained with the two versions of the code.

that the perfect matching between the experimental and simulated SAR values in gel at the maximum field ($B = 20.33$ mT) was imposed to determine the value of the anisotropy constant K to be used in the simulations. However, no other constraints were imposed to simulations, so neither the way the SAR rescales with the field amplitude, nor the way the SAR changes when the Brownian relaxation is switched on, are defined or guided by the programmer.

Interestingly, simulations performed with the Brownian motion reproduce with quite very high accuracy the decrease of the SAR measured when MNPs were immobilized in gel. Consequently, this result supports what was supposed and experimentally observed about the role of the Brownian motion in

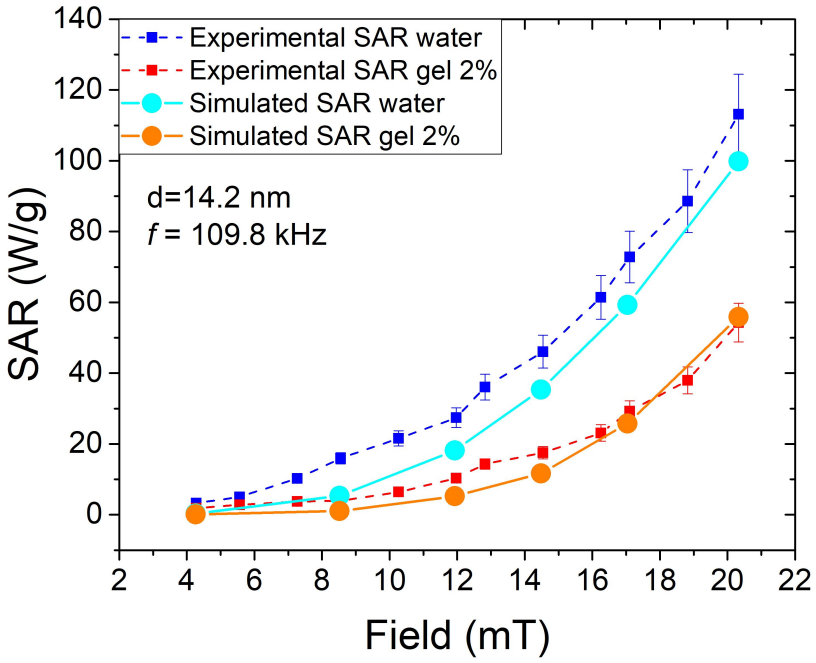

Figure 4.21: Comparison between the experimental SAR values (dotted lines), measured in water (blue points) and in 2 wt% agarose gel (red points) samples, and the simulated SAR values obtained by running a Monte Carlo code implementing the Néel relaxation alone ($\sim$ gel, orange points) or both the Néel and Brown relaxation ($\sim$ water, light blue points). Simulations were performed by setting all the parameters to the values obtained from the sample characterization. The only hypothesis is the perfect matching between the experimental and simulated SAR in gel at the maximum field ($B = 20.33$ mT), which was used to determine the value of the anisotropy constant K.

determining the SAR of MNPs.

10 nm and 18 nm samples

As regards the other two samples analysed in the experimental part of this Chapter, i.e. the 10 nm and 18 nm samples in Chapter 4.1, the same analysis was performed also for these samples to compare simulations and experiments.

For the 10 nm sample, the very small size of the MNPs determines a fast Néel relaxation time, therefore the condition $\Delta t \ll \tau_N$ cannot be easily satisfied. It would be indeed necessary to increase the number of steps (N) of the simulation of each hysteresis loop up to a very high number, that would be difficult to manage (i) in terms of computational time and resources, and (ii) because very small values of Δt would induce computational errors in other parts of the algorithm. Therefore, to date, the algorithm still needs further improvements to handle simultaneously the Néel and Brown relaxation on very small MNPs as those of the 10 nm sample.

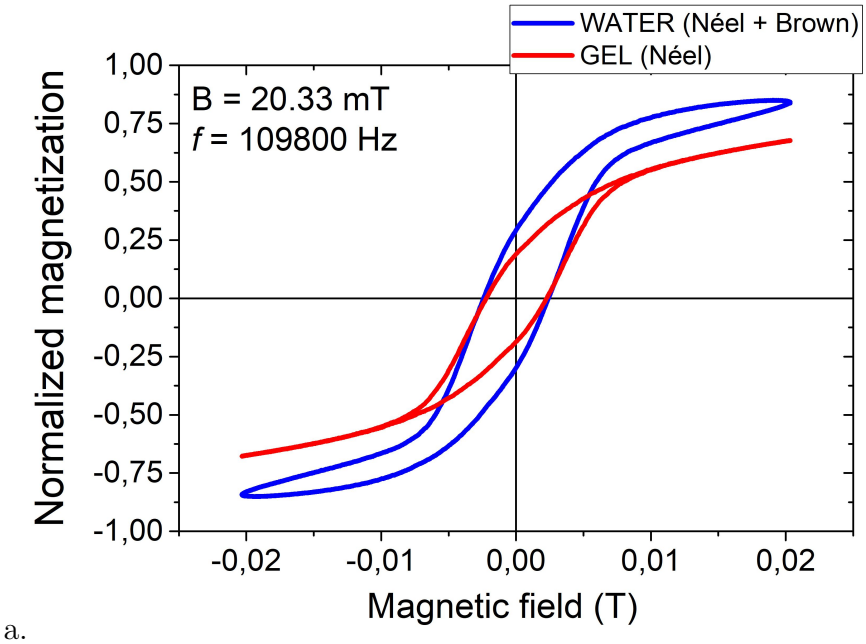

a.

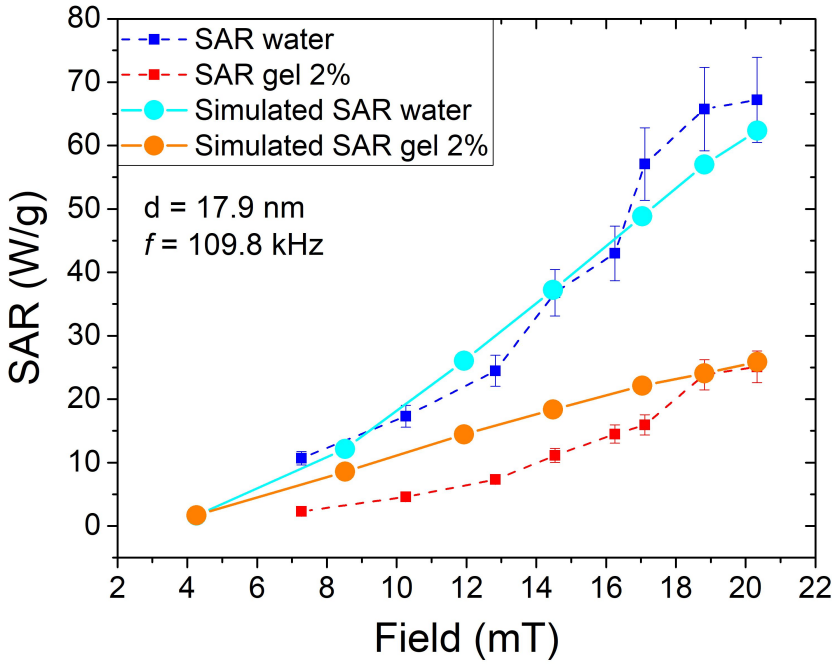

b.

Figure 4.22: (a) Hysteresis loops of 17.9 nm MNPs at $f = 109.8$ kHz and $B = 20.33$ mT as obtained from Monte Carlo simulations performed using the parameters from the characterization of the 18 nm sample. Simulations were performed using both the code implementing the Néel relaxation alone (red line, $\sim$ gel samples) and the new version of the code implementing both the Néel and Brown relaxation (blue line, $\sim$ water sample). (b) Comparison between the experimental SAR values (dotted lines), measured in water (blue points) and in 2 wt% agarose gel (red points) samples, and the simulated SAR values obtained by running a Monte Carlo code implementing the Néel relaxation alone ($\sim$ gel, orange points) or both the Néel and Brown relaxation ($\sim$ water, light blue points).

As regards the 18 nm sample, simulations were performed with the parameters coming from the characterization of this sample, and finding $K = 11900\,\mathrm{J/m^3}$ when simulating the SAR in gel at the higher field ($B = 20.33$ mT). The condition $\Delta t \ll \tau_N$ was satisfied having $\tau_N = 2.80 \cdot 10^{-7}$ s and $\Delta t = 9.1 \cdot 10^{-10}$ s with the chosen parameters.

In Fig. 4.22a the two hysteresis loops obtained by running the two versions of the Monte Carlo code, with and without the Brown relaxation, at $f = 109.8$ kHz and $B = 20.33$ mT are shown. The shape of the hysteresis loops is no longer elliptical, as for superparamagnetic MNPs, but rather similar to the characteristic loop of ferromagnetic materials. This observation is quite coherent with the size of the MNPs, which is close to the transition between the ferromagnetic and superparamagnetic regime. As for the 14 nm sample, the maximum magnetization and the area of the loop are larger when the particles are allowed to rotate (i.e. in water), while the coercive field is similar in the two cases.

The comparison between the experimental SAR at $f = 109.8$ kHz (from Fig. 4.7) and the simulated SAR is shown in Fig. 4.22b. As for the 14 nm sample, the Brownian relaxation results to be responsible of a significant increase of the SAR in comparison to the case when only the Néel relaxation is considered. However, the field dependence of the SAR is calculated to be quite linear in both cases, differently from the experimental results.

4.2.3 Conclusions

In this Chapter, the role of the Brownian relaxation on the heating efficiency of MNPs has been investigated through a double approach: (i) experimental measurements of the SAR of MNPs with different sizes, dispersed in media with different viscosity (water and agarose gels); (ii) numerical simulations of MFH using kinetic Monte Carlo techniques, which allow to study the time evolution of the magnetization of an ensemble of MNPs randomly distributed and oriented in the space.

As regards the experimental study performed in Chapter 4.1, the heating efficiency of magnetite MNPs with mean core sizes 10 nm, 14 nm and 18 nm has been investigated systematically as a function of the frequency f and amplitude H of the applied AMF, both in water and in agarose gels with different mass fractions (0.5% and 2% w/w). It has been shown that the SAR results are completely independent by the mass fraction of the agarose in the two gels, suggesting that if an immobilization of the MNPs in gel occurs, it is already complete in the gel with the lower viscosity. Moreover, the 10 nm sample showed similar SAR values both in water and in agarose gels, while for the 14 nm and 18 nm sample a relevant decrease (up to the 70%) of the SAR in gel compared to water was observed. This behaviour has been explained by the suppression of the Brownian relaxation in gel, which constitutes a relevant heating mechanism, in particular for particles with increasing size.

The results presented in Chapter 4.1 are in good agreement with the predicted role of the Brownian motion in MFH for particles larger than ~ 12 nm, according both to theory [8] and experiments [97, 102]. Considering these outcomes, the core message arising from this study is that the common attitude observed in literature to characterize the heating efficiency of MNPs working only in aqueous solutions should be strongly discouraged. There would indeed be a high probability to derive misleading conclusion about the real heating efficiency of MNPs when transferred to the clinics, since it has been widely hypothesized (and observed [101]) the complete immobilization of MNPs in the tumour environment.

In-gel studies of MNPs could help simulating the *in-vivo* conditions when neither *in-vivo* nor *in-vitro* experiments could be performed. However, further studies are necessary to deepen the knowledge of the effects of the aggregation of MNPs, which have been reported to occur in the biological culture medium [20] and may also occur in *in-vivo* studies or in gel phantoms.

For the 10 nm and 14 nm samples, the LRT has been fitted to SAR(H) curves obtained from the measurements, and the parameters returned by the best-fits have been used to estimate the relaxation times of the MNPs. Moreover, a comparison with the theoretical models of MFH has been performed exploiting a free-exponent function SAR(H) $\propto H^x$. For the 10 nm sample, a good agreement with the predictions of the LRT has been observed. On the contrary, for the 14 nm and 18 nm samples an exponent $2 < x < 3$ has been obtained, attesting that these samples fall in the transition region between the superparamagnetic and the ferromagnetic regimes, where no theoretical models are available to date to describe the SAR of single domain MNPs (apart from the Stoner-Wolfharth model, whose applicability is limited to special cases).

In Chapter 4.2 kinetic Monte Carlo simulations have been exploited to study the effect of the Brownian relaxation in MFH. Most of the work has been dedicated to the implementation of the Brownian relaxation in the Monte Carlo code already developed by Carrey et al. [104] to describe the time evolution of an ensemble of MNPs caused solely by the Néel relaxation. The new algorithm has been validated through numerous tests aimed to compare the capability of the program to reproduce the behaviour of the MNPs under the action of the Brownian and magnetic torques, as described by previous studies available in the literature [148–151].

The new Monte Carlo code has then been used to simulate the time evolution of the magnetization of an ensemble of MNPs with characteristics defined as those of the samples measured in Chapter 4.1. A simulated SAR has been computed from the area of the hysteresis loops returned as outcomes from the simulations. Interestingly, the comparison between the experimental SAR measured in Chapter 4.1 and the simulated SAR here obtained has shown a quite good agreement for the 14 nm and 18 nm samples. In particular, simulations result to be capable of reproducing the differences between the SAR measured in water (with both the Néel and Brown relaxation) and in gel (with only the

Néel relaxation), apparently confirming the important role of the Brownian mechanism on the heating of MNPs larger than $\sim$ 12 nm, as reported by De La Presa et al. [102].

Despite the very positive outcomes of the simulations, it must be emphasized that both (i) the approximations made during the definition of the parameters for the simulations, and (ii) the fact that the code does not describe completely the physics of the system (for example, particles are fixed in the space), do not allow to consider them as a final proof about the role of the Brownian motion in MFH. However, as a matter of fact, to date both experimental measurements and simulations have been showed to converge on the same description of the heating mechanisms in MFH, i.e. they describe an equal and important contribution of the Brownian motion to the SAR of MNPs.

Chapter 5

Relaxometric and hyperthermic efficiency of high aspect ratio nano-needles

In this Chapter an environmentally friendly hydrothermal method to produce magnetic iron oxide elongated nanoparticles (e-MNPs), also called nano-needles, is presented. It is developed in four subsequent steps: (1) an aerial oxidation strategy allows to obtain elongated nanoparticles of goethite; (2) a dehydration process transforms goethite into hematite at high temperatures (T_d); (3) such precursor particles are functionalized with SiO_2, an inorganic shell which has shown to prevent aggregation processes and to preserve the morphology of the particles; (4) a final reduction step in a hydrogen atmosphere for a certain time (t_{red}) leads to $\sim 100 \times 25$ nm magnetite nano-needles.

The synthesis and the morphological and magnetic characterization of these particles have been performed by the author of this thesis thanks to the precious collaboration and availability of the group of Prof. Maria del Puerto Morales, during a mobility period of the three months (from October to December 2017) in her laboratory at the Institute of Materials Science of Madrid (ICMM, member of the Spanish National Research Council - CSIC).

During that period, a systematic study of the dehydration (optimization of T_d values) and reduction (t_{red}) processes allowed to obtain Fe_3O_4 or mixed $\alpha - Fe_2O_3/Fe_3O_4$ magnetic nano-needles with tunable specific surface area, attributed to a different porosity of the samples. Silanol groups present on the silica shells allowed further functionality with dextran, a biocompatible and biodegradable polymer, forming highly stable colloids. Magnetic nano-needles obtained at three different values of T_d (from 250°C to 400°C) and t_{red} were chosen to study the effect of the composition and specific surface area on the Magnetic Fluid Hyperthermia (MFH, by means of the calculations of the Specific Absorption Rate - SAR) and Magnetic Resonance Imaging (MRI, by means of the nuclear relaxivity - r_2) properties, which result very good in

terms of clinical standards. Indeed, in this Chapter it is shown that the specific surface area and/or mixed composition influence both SAR and r_2. Thus, the work presented in this Chapter provides an evaluation of the potential of high-aspect ratio magnetic nano-needles for MFH and MRI, and opens the possibility of using high-aspect ratio nanoparticles for MFH-based and MRI applications. Results have been published in:

- **Avolio, M.**, Gavilán, H., Mazario, E., Brero, F., Arosio, P., Lascialfari, A., Morales, M. P., *Elongated magnetic nanoparticles with high-aspect ratio: a nuclear relaxation and specific absorption rate investigation*, Physical Chemistry Chemical Physics, 2019, 21, 18741-18752.

5.1 Introduction

Several chemico-physical parameters are reported to influence the MNPs efficiency as MRI or MFH agents. The most important ones are (i) the magnetic core composition [85,152–156], (ii) the core size [64,86,117,157], (iii) the hydrodynamic volume, (iv) the coating [125,158] and (v) the core shape. Regarding the latter parameter, that is the main topic of this Chapter, most of the literature about MNPs applications either as MRI contrast agents or MFH agents concern spherical MNPs [27]. The spherical shape is sometimes assumed as approximation for irregular polyhedral MNPs, since synthetic routes to obtain well shaped and monodispersed MNPs are not easy to be realized. However, extensive efforts are being made to standardize the synthesis of MNPs, to obtain well-defined and repeatable MNPs shapes and sizes [159, 160].

In the latest years, a wide interest was born also for particle shapes other than spherical, since from a biological point of view different shapes have been proved to determine (i) different cellular uptake, which is influenced by the way MNPs interact with the receptors on the cell membrane [161–163]; (ii) different circulation-time within the blood or lymphatic vessels, due to the shape-dependent flow resistance of the MNPs [164, 182]; and finally (iii) different residency time within the cytoplasm [165, 166]. Moreover, from the physical perspective, it is well-known the important contribution of the shape anisotropy to the magnetic anisotropy of the particles [128, 167–170]. As a result, depending on the specific problem to be addressed in the biomedical field, cubic MNPs [171], elongated MNPs (e-MNPs) or needles [128, 172, 173], discs [128], nanoclusters [174, 175] or nanoflowers [176, 177] of MNPs can be synthetized (Fig. 5.1), and more and more data are becoming available for the characterization of these particles or with even more exotic shapes.

The specific interest towards elongated shapes, as the one of the MNPs considered in this thesis, has several reasons. Interestingly, they move also far from the simple consideration of a strong shape anisotropy arising from the presence of a geometrical easy-axis along the major axis of the needles, as discussed in Chapter 1, that can be exploited to increase the heating and the relaxometric performances of MNPs.

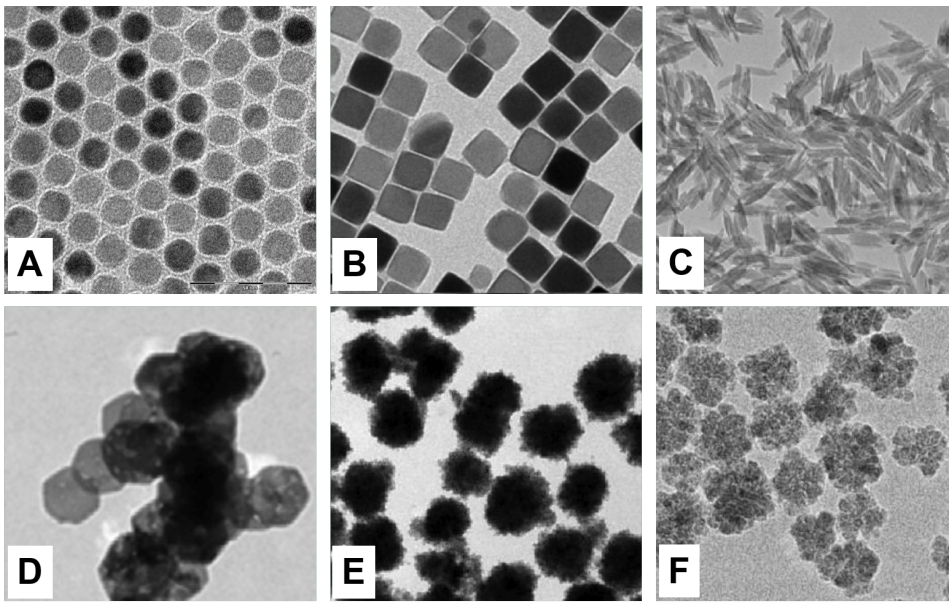

Figure 5.1: Exemplary TEM pictures from literature of MNPs with different shapes: (A) spheres [117], (B) cubes [171], (C) needles [173], (D) discs [128], (E) nanoflowers [176], (F) nanocluster [174].

For example, Simeonidis et al. [178] showed that the orientation of elongated magnetic nanoparticles can be easily controlled in MFH experiments by modulating the AC field parameters and the treatment duration, determining a strong synergy between the e-MNPs orientation and their heating efficiency. The capability of e-MNPs to rotate and to reorientate themselves accordingly to the direction of the AMF would introduce also the possibility of exploiting this behaviour to induce mechanical damages to the cells, combining a mechanical action to the heating typical of MFH.

Interesting considerations regarding elongated nanoparticles (also non magnetic) come from their behaviour in the biological medium, and their interactions with cells. For example, Toy et al. [179] described a favourable uptake of elongated particles by the cells thanks to their larger surface area, that allows multivalent interactions with the receptors of the cell membrane compared to spheres, as schematized in Fig. 5.2a. In the same work, Toy et al. discussed about the different torques and forces acting on the particles when injected into the bloodstream. While in the case of spherical MNPs the isotropic nature of the torques, arising from the spherical symmetry, allows the particles to remain in the center of the flow, in the case of elongated particles (for example, rods) the resultant of the forces acting on the particles determines their drift towards the vessel wall, a phenomenon called margination (Fig. 5.2b). Here the particles may bind to the receptors of the endothelial cells of the vessel wall, or may extravasate through opportune gaps.

A peculiar and favourable flow within the bloodstream of elongated nanoparticles is described also by other authors as Duan et al. [180] and Champion et

a. 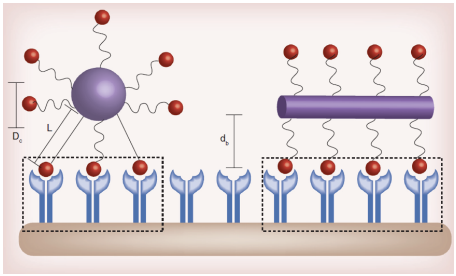 b. 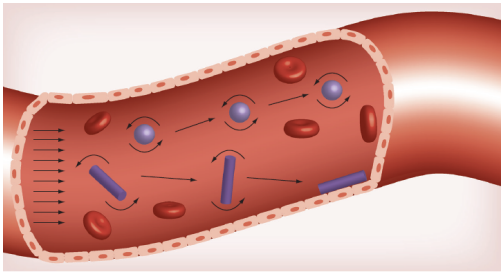

Figure 5.2: (a) Schematic representation of how the particles shape affect their interaction with cells; in particular, elongated particles allow multivalent interactions with the receptors of the cell membrane compared to spheres (d_B is the binding distance nanoparticle-receptor). (b) Representation of the different torques acting within the bloodstream on nanoparticles with different shapes, which allow spherical particles to remain in the centre of the flow while marginating elongated particles to the vessel wall. Images from Ref. [179].

al. [181], the latter studying the possibility of exploiting the particle shape to develop new drug delivery carriers at the nanoscale.

The favourable uptake of elongated nanoparticles by the cells is reported also by Salatin et al. [182] (in a general review on the topic), Gratton et al. [183] and Agarwal et al. [184], the latter works describing shape-specific internalization pathways and uptake mechanisms of HeLa cells and mammalian cells, respectively. Again, the shape of nanoparticles (together with their size) is reported to be a decisive factor for the particles interaction with the receptors of the cell membrane.

Finally, Cheng et al. [185] showed that e-MNPs are suitable for antitumoral treatments aimed at killing cancer cells exploiting the movement of MNPs guided by an external rotating magnetic field. The efficiency of the mechanical action carried out by the particles thanks to the field, which is at the base of the treatment, is indeed maximized when working with e-MNPs compared to other shapes. For example, it was reported that 200 nm × 50 nm Fe_3O_4 rods may induce mechanical disruption of the cell membrane of HeLa cells (and consequently cell death) when exposed to an oscillating magnetic field ($f = 35$ kHz) [186].

In addition to the elongated shape, the work presented in this Chapter investigates also the effect of a porous structure and a mixed composition of magnetite and hematite within the magnetic core of the elongated nanoparticles. These features have been already studied by Rebolledo et al. [173] with e-MNPs made by a porous hematite matrix embedding nanosized clusters of magnetite, doped with Mn, Ni, Cu or Sn and surrounded with an alumina external layer. Samples described in Ref. [173] showed outstanding values of transversal relaxivity ($r_2 \simeq 402\,\mathrm{mM^{-1}s^{-1}}$ for Mn doped e-MNPs) at $B_0 = 1.41$ T thanks to the dipolar field produced by the iron oxide clusters and the decreased proton-cluster distance induced by the porosity (water penetrates within the pores). Contrarily to these samples, the composition of the particles analysed in this thesis is strictly restricted to iron oxides, and the coating

is also different. Therefore, a direct comparison with the compounds reported by Rebolledo et al. [173] is not correct. Moreover, it is important to stress that some dopants like Mn, although being a powerful means of increasing the relaxivity for MRI applications [152], suffers of non-negligible limitations due to their high cellular toxicity [187].

5.2 Synthesis

Samples characterized in this Chapter were synthesized by further developing the synthesis method described in Refs. [188] and [172], similar to that reported by Gavilán et al. [128]. This synthetic route allows to obtain elongated nanoparticles with different compositions (pure magnetite or magnetite in a hematite matrix) and porosities, and is characterized by four main advantages: (i) the high repeatability, (i) it is environmentally friendly, (iii) it is easy to scale-up and, in contrast to other methods that employ organic solvents, (iv) it allows obtaining uniform e-MNPs with tunable magnetic properties.

The final product, i.e. e-MNPs with different porosities and magnetic properties, is obtained after completing four subsequent steps: (i) synthesis of an antiferromagnetic precursor, i.e. goethite ($\alpha-$FeOOH) elongated nanoparticles, by aerial oxidation; (ii) coating of the goethite particles with an inorganic material as silica (SiO_2); (iii) dehydration of goethite to hematite ($\alpha - Fe_2O_3$) at high temperatures; (iv) reduction of hematite nanoparticles to magnetite (Fe_3O_4) nanoparticles in a hydrogen (H_2) atmosphere at high temperature. This sequence of steps is referred to in the text as "Strategy 1" or S1; if the order of steps (ii) and (iii) is reversed, i.e. the silica coating is applied to hematite particles after having dehydrated uncoated goethite particles, the synthesis process is named "Strategy 2" or S2 (Fig. 5.3).

Step (i) was realized accordingly to the strategy described by Pozas et al. [188] and Gavilán et al. [128], but with different reactants ratios. Solutions of Na_2CO_3 0.9 M and Fe(II)SO_4 0.075 M were prepared using distilled water and in an inert atmosphere (achieved by bubbling N_2, in order to avoid Fe(II) oxidation). The molar ratio CO_3^{2-}/Fe(II) = 12 was identified as the best choice for obtaining particles about 100 nm long. The Na_2CO_3 solution was transferred in a glass reaction vessel that allows to bubble nitrogen inside, keeping its temperature at 40°C thanks to a thermal bath. Subsequently, the $FeSO_4$ solution was poured into the reaction vessel, mixing the two solutions thanks to N_2 bubbling and a moderate magnetic stirring (first picture in Fig. 5.4a). The N_2 flux was then replaced overnight by a 2 L/min air flow to form goethite by aerial oxidation. Briefly, Fe(II) cations oxidize on aeration forming a solid phase of a mixture of sulphate and carbonate green-rusts, which decompose as a result of a further oxidation producing goethite (Fig. 5.4a). At the end of the process, the obtained goethite nanoparticles suspension was centrifuged for 10 minutes at 7500 rpm, and the precipitate was washed several times with distilled water and lyophilized.

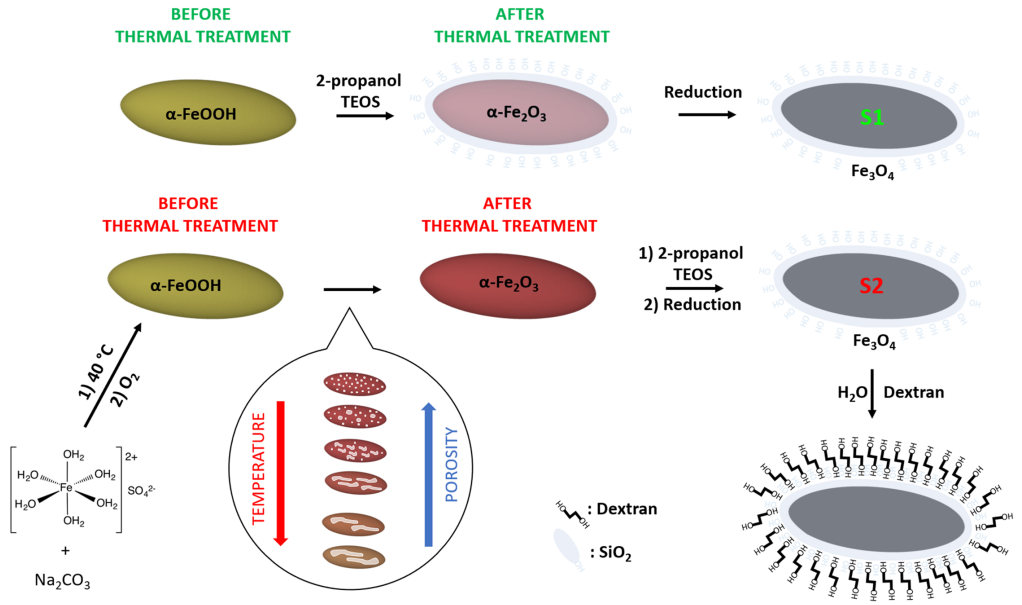

Figure 5.3: Schematic representation of the four main steps of two synthesis strategies applied to obtain e-MNPs with a porous structure. The porosity of the samples is determined by the dehydration temperature (T_d): the higher T_d, the larger the size and the lower the number of the pores.

Step (ii) was realized by applying the Stöber method [189,190] to coat the particles with silica, an inorganic material commonly used for stabilizing the particles in solution and to avoid aggregation thanks to a steric and electrostatic repulsion. In the present case, the silica coating is particularly necessary to avoid nanoparticles sintering during the thermal treatment in the step (iv) of the synthesis. In a 400 mL glass bottle, 100 mg of nanoparticles were added to 200 mL of 2-propanol and 100 mL of distilled water, and sonicated for 15 mins. Then, 20 mL of NH_4OH 28.0-20.0% V/V were added to the solution and mixed using ultrasounds for 5 mins. Finally, 200 μL of tetraethyl orthosilicate (TEOS) were added during sonication and the reaction was allowed to continue for 15 mins. The obtained sample was centrifuged for 45 minutes at 7500 rpm, washed with ethanol several times and lyophilized.

In **step (iii)** powders of goethite nanoparticles (coated with silica in the case of S1, uncoated in S2) were heated at very high temperatures for three hours using an oven, in order to dehydrate goethite to hematite. The temperature at which goethite turns into hematite depends on the goethite crystallinity, but it must always be kept at values lower than 600°C, otherwise a sintering process would occur [23]. During dehydration, water is lost from the particles and cations are rearranged, and the slit-shaped micropores typical of goethite coalesce in larger mesopores in hematite on continued heating. Different dehydration temperatures determine different porous structure in the final particles (Fig. 5.3 in the balloon). For the aims of this thesis, i.e. to study e-MNPs

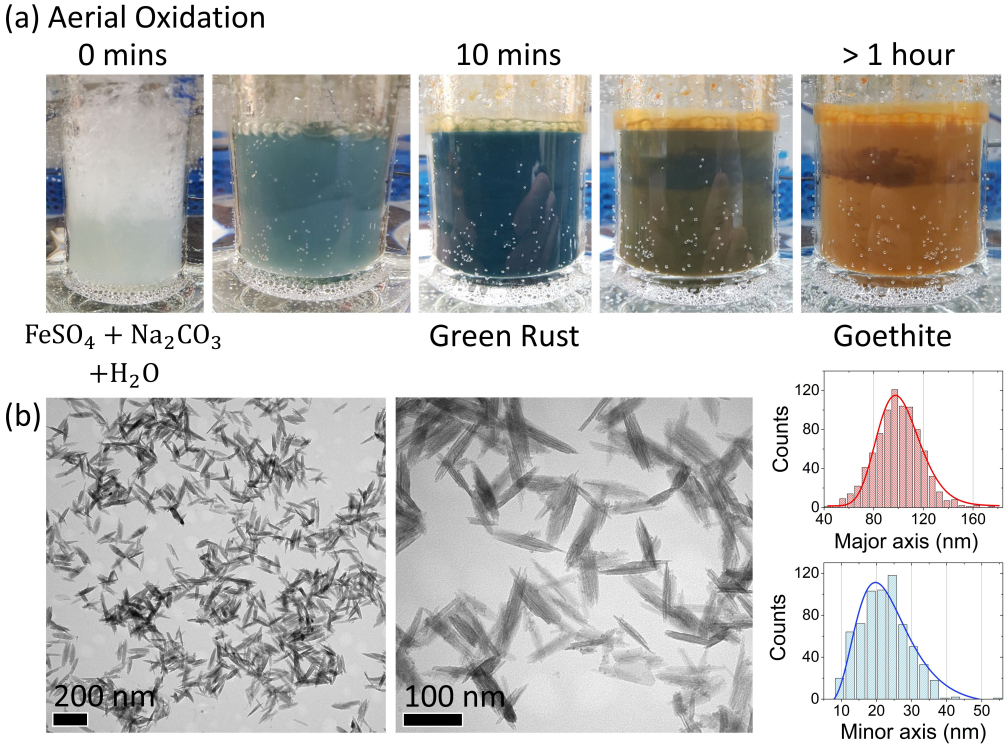

Figure 5.4: (a) Pictures at different times of the aerial oxidation reaction taking place in the reaction vessel, starting from iron sulfate and sodium carbonate in water solution and leading to goethite nanoparticles. (b) TEM pictures and size distributions for the major and minor axes of the elongated nanoparticles of the goethite precursor.

with different porosity, step (iii) was realized at three temperatures (250°C, 300°C and 400°C) on different fractions of the same precursor batch.

Finally, in **step (iv)** the silica coated $\alpha-Fe_2O_3$ elongated hematite nanoparticles were reduced to magnetite in sequential steps as follow: (i) hematite powders were heated at 360°C for 1 hour in a vacuum line; (ii) the line was filled with H_2 at a pressure of 1 atm; (iii) after 3 hours and 30 mins, samples of magnetite nanoparticles were collected (the H_2 atmosphere was renewed after the first hour). These samples will be named in the following of the Chapter as *totally reduced* samples.

If the reduction step is stopped after the first 30 minutes, not all the hematite is allowed to transform to magnetite and a mixed composition of magnetite crystals in a hematite matrix is obtained, similarly to the samples reported by Rebolledo et al. [173]. In order to study the properties of samples with such a mixed composition $\alpha - Fe_2O_3/Fe_3O_4$, a fraction of the three hematite precursors prepared at different T_d was reduced setting a short reduction time. These samples will be referred to as *partially reduced* samples and marked with a P-suffix.

In summary, changing the synthesis strategy (S1 or S2), the dehydration temperature (250°C, 300°C or 400°C) and the reduction time to obtain samples

totally or partially (P) reduced to magnetite, seven different samples were prepared. They will be named as S2-250, S2-300, S2-400, S1-300, S2-250-P, S2-300-P and S2-400-P to allow an easy identification of the strategy, the dehydration temperature and the type of reduction. As can be understood from the list of samples, the effect of the partial or total reduction has been studied at all the temperatures, while the effect of the different synthetic route (S1 or S2) has been studied only at $T = 300°C$.

Coating with Dextran

To increase the particles stability in water solution, a further dextran coating was added on the silica layer, as showed in Fig. 5.3. Dextran is a sugar that allows both steric and electrostatic repulsion among the particles, and it has been chosen because of its several advantages reported in literature. First, dextran coated nano-systems have been already approved by the FDA for clinical practice [191], and this is of fundamental importance if considering perspective biomedical applications of the particles here presented. Moreover, it seems that dextran facilitates nanoparticles binding to the cell membrane [192], probably increasing the uptake rate. Finally, the hydrophilicity of dextran allows (a) long circulation time of the nanoparticles within the bloodstream [193], and (b) slow dissolution rate of the magnetic core into the body. Thanks to the latter property, dextran preserves the MNPs features from degradation, and prevents the amount of free iron into the blood to overcome the level of toxicity after MNPs injection at high dose [194].

To coat the particles with dextran, 0.41 g of NaOH were dissolved in a glass in 20 mL of distilled water to get a 0.5 M solution (A). In another glass, 0.64 g of NaOH ($\geq$ 98% (T), Sigma) were dissolved in 20 mL of distilled water to get a 0.8 M solution (B). 20 mg of dextran 40 kDa (average mol wt 35.000-45.000, Sigma) were dissolved within a vial in 2.5 g of A. In a second vial, 20 mg of dried nanoparticles were dissolved in 1.6 g of B. The solution containing the nanoparticles was then added dropwise (for a total addition time of about 20 mins) on the dextran solution, while mixing with ultrasounds. The final solution was kept under sonication for 6 hours, maintaining constant the temperature of the water in the bath (room temperature). Finally, samples were dialyzed for 24 hours in 10 L of distilled water, using a porous membrane. Water for the dialysis was renewed three times, and samples were maintained under magnetic stirring. The average ligand surface coverage at the end of the process was estimated to be ~ 0.5 ligands/nm^2. Considering the average surface area of each particle (assumed as an ellipsoid), this means the ratio of number of ligands per needle was kept above 1000.

The dextran coating, and in particular the long sonication time required for its formation around the particles, was not expected to affect the silica shell of the e-MNPs. The properties of the inorganic silica layer should indeed be preserved despite the sonication. However, dextran was expected to penetrate into the pores of the silica, probably affecting its permeability to water (and

Table 5.1: Mean values of the major axis (length, L_{TEM}) and minor axis (width, W_{TEM}) of the e-MNPs as obtained from the statistical analysis of TEM images. Measurements are referred to goethite precursors (first line) and hematite precursors. The latter measurements were confirmed after the total or partial reduction to magnetite (step iv). The aspect ratio of the e-MNPs is also reported.

Sample	Major axis $[L_{TEM}]$ (nm)	Minor axis $[W_{TEM}]$ (nm)	Aspect ratio $[L_{TEM}/W_{TEM}]$
α-FeOOH	102 ± 18	24 ± 9	4.3
S2-250	98 ± 14	26 ± 5	3.8
S2-300	97 ± 10	25 ± 4	3.9
S2-400	87 ± 11	16 ± 4	5.4
S1-300	98 ± 11	25 ± 4	3.9

therefore the NMR properties of the particles).

5.3 Morpho-dimensional characterization of the samples

5.3.1 TEM: evaluating the particles size and structure

Transmission Electron Microscopy (TEM) was used to characterize the core size and shape of the produced e-MNPs at the end of each step of the synthesis. In particular, a JEM1010 microscope (JEOL, Peabody, USA) operating at 100 kV was used, preparing the samples by dropping a diluted aqueous solution of nanoparticles on opportune carbon coated copper grids. Samples were dried in oven at 50°C before measuring; this method could lead to the presence of aggregates of MNPs in the TEM picture produced during the drying, which are not necessarily an indicator of aggregation in the original aqueous solutions.

TEM pictures of the goethite precursors obtained at the end of step (i) of the synthesis are reported in Fig. 5.4b, together with the size distributions of the major and minor axis of the needles. Slit-shaped nanopores and highly oriented crystallites, typical of goethite, are clearly visible in the TEM pictures, parallelly distributed along the major axis of the needles. The statistical analysis of the size was performed by means of ImageJ, an open source image processing program, averaging over ∼600 e-MNPs. The distributions were fitted with a Log-Normal function, according to Eq. 1.13, to get the mean value and standard deviation of the size of the goethite precursors both along the major axis (length, L_{TEM}) and the minor axis (width, W_{TEM}). Results are shown in Table 5.1. Differently from the quantities reported by Pozas et al. [188] for the synthesis of similar particles, a molar ratio CO_3^{2-}/Fe(II) = 12 allowed to obtain e-MNPs with $L_{TEM} = 100$ nm.

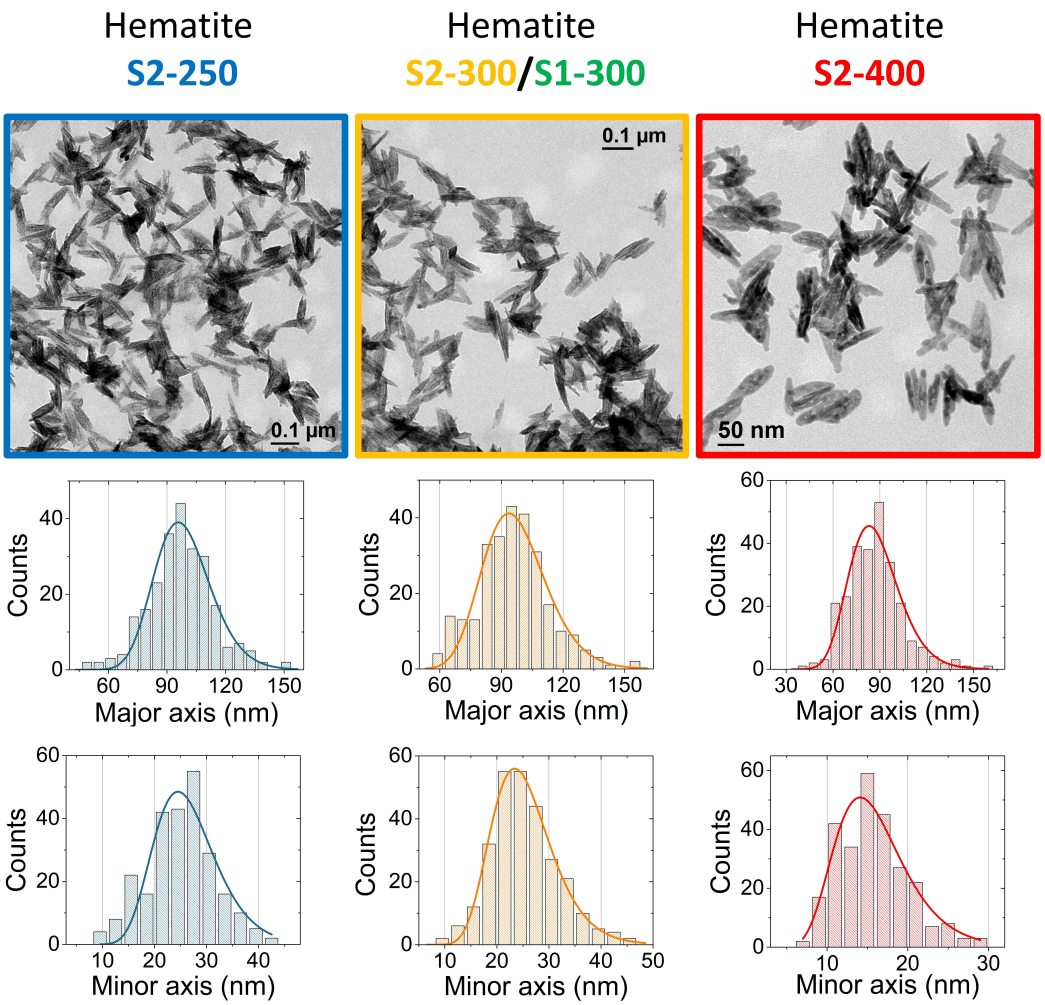

Figure 5.5: TEM pictures and size distributions for the major and minor axes of the elongated nanoparticles in the hematite precursors. It is possible to appreciate the more rounded shape and the larger pores in the e-MNPs of the sample dehydrated at the highest temperature (S2-400).

TEM pictures of the samples dehydrated to hematite at different temperatures (T_d) are shown in Fig. 5.5. From these pictures, the contraction of the particles along the major and minor axes during the dehydration step was evaluated. Results of the statistical analysis performed over $\sim$ 300 e-MNPs are shown in the histograms of Fig. 5.5 (best fits are performed with a Log-Normal distribution) and in Table 5.1. The most relevant changes in the morphological features were observed for the sample S2-400, i.e. the sample dehydrated at the highest temperature. In particular, it shows (i) a greater contraction of the size along both the major and minor axes; (ii) a relevant increase of the aspect ratio compared to the other samples (Table 5.1); (iii) a more rounded shape at the edges of the needles; (iv) the largest observable pores, clearly identifiable in the TEM pictures (Fig. 5.6).

In the final step of the synthesis, samples were totally or partially reduced to

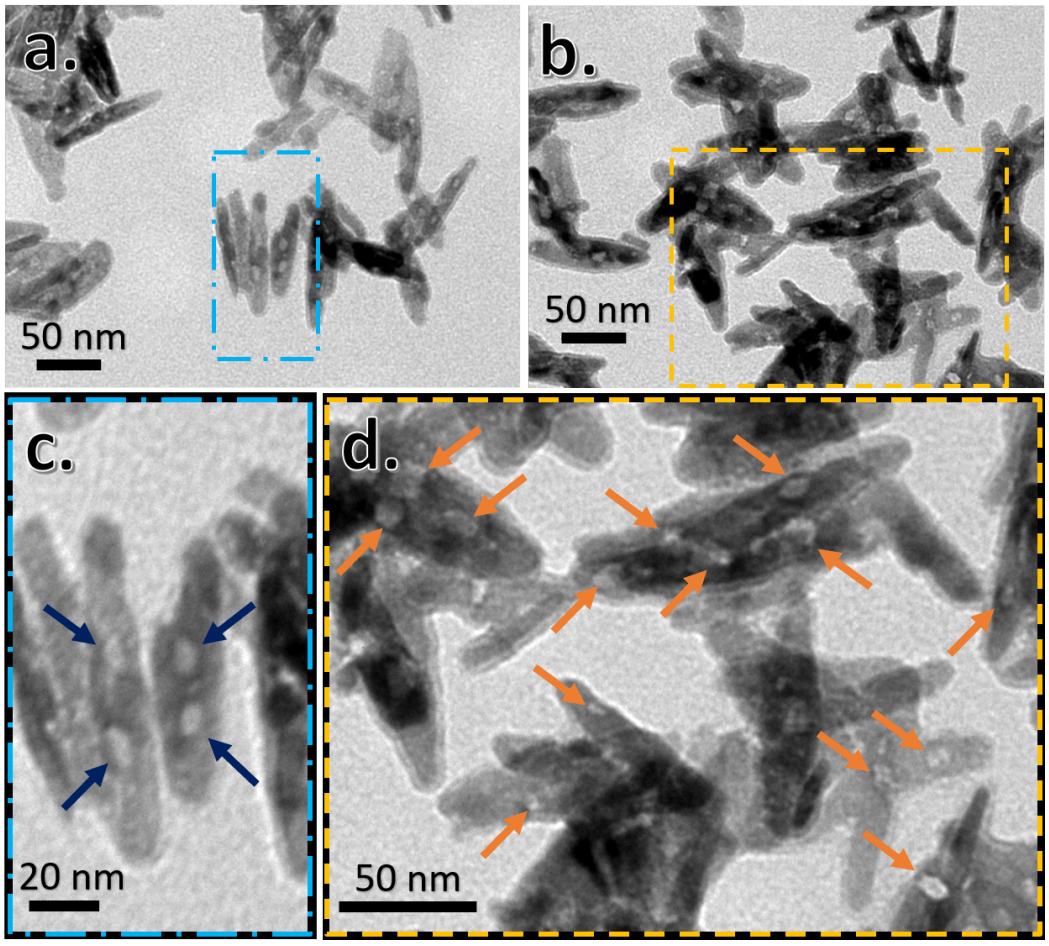

Figure 5.6: TEM images of (a) the hematite precursor S2-400 and (b) the magnetite sample S2-400; (c) detail of the porous structure from (a) and (d) detail of the pores from figure (b). Arrows highlight the most evident pores.

magnetite. The statistical analysis of the size distributions performed on TEM pictures didn't show any relevant change in the size of the e-MNPs compared to that measured on the hematite precursors, therefore the mean values reported in Table 5.1 apply also to the magnetite samples. Moreover, no appreciable differences were observed between the size of the samples totally or partially reduced to magnetite.

It is worth noting that in step (iv) of the synthesis all the samples are heated up to 360°C to allow the transformation of hematite into magnetite. This further heating determines the appearance of larger pores even in the samples previously dehydrated at lower temperatures, i.e. S2-250, S2-300, S1-300, S2-250-P and S2-300-P. However, as it will be shown in the following, the samples maintain memory of their history, and the final porosity in magnetite e-MNPs result to be different depending on T_d.

High-resolution TEM (HRTEM)

To better investigate the porosity of the e-MNPs, one sample (S2-300) was selected for High-resolution TEM (HRTEM) characterization, performed with a JEM-3100 F microscope (JEOL, Peabody, USA) operating at 300 kV.

HRTEM confirmed the presence of the pores (Fig. 5.7a), as already shown on similar samples by Gavilán et al. [128]. Statistical analysis of the pore size counting 300-600 nanoparticles (as for TEM) was not possible because of the few HRTEM images available. However, from the acquired HRTEM pictures the pore size was roughly estimated to be $2-5\times6-10$ nm for sample S2-300.

From TEM images (Figs. 5.5 and 5.6), it was highlighted that the lower the dehydration temperature, the thinner and shorter the pores (resembling more to goethite initial structure); and the higher the dehydration temperature, the broader and longer the pores. The latter is the case of the sample S2-300 analysed by HRTEM (Fig. 5.7b-c), whose e-MNPs present either one or multiple big pores (as evidenced with the green circles) whose direction are along the longest axis of the nanoparticles.

Despite the porosity, HRTEM images also show the monocrystal structure of the e-MNPs. Fourier Transform (FT) of the HRTEM images conducted in a previous work by Gavilán et al. [128] on this kind of e-MNPs has demonstrated patterns typical of a monocrystal structure (clear dots and not arrows).

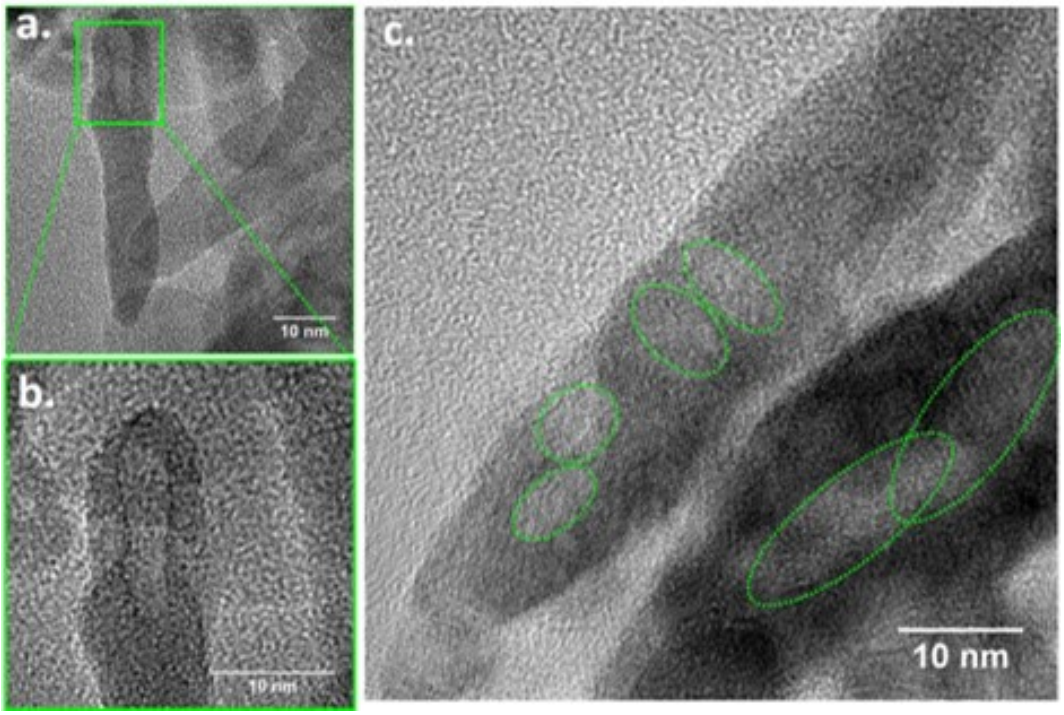

Figure 5.7: HRTEM images of $\alpha-Fe_2O_3$ e-MNPs of sample S2-300. (a) clearly shows the pore direction forming along the longest axis of the nanoparticles. (b) is a detailed HRTEM image showing the crystallinity despite the porosity. (c) shows nanoparticles containing more than one pore, again along the longest axis of the nanoparticle.

5.3.2 XRD and FTIR: analysis of the iron oxide composition

Each iron oxide phase transformation of the synthesis had to be monitored, to check step by step the correctness of the whole synthesis process. Moreover, the successful coating of the particles with silica had also to be verified. For these purposes, X-Rays diffraction analysis (XRD) and Fourier transform infrared spectroscopy (FTIR) are the two most suitable techniques, since both XRD patterns and IR absorption spectra are fingerprints of a given material. In particular, the position of the Bragg peaks in the XRD pattern gives information about the features of the crystal lattice characterizing the material, and the broadness of the diffraction peaks informs about the crystallinity of the sample (small crystals broaden the lines). IR absorption spectra are instead determined by the interactions between the photons of the incident infrared light and the molecules of the investigated material. These interactions could cause excitations of rotations or vibrations of the molecules in their ground state, which are linked to stretching and bending deformations of the interatomic bonds and interbond angles, respectively [23].

For XRD measurements, a Bruker D8 Advance diffractometer was used, equipped with a graphite monochromator and employing CuKα radiation ($\lambda =$ 1.5406 Å) and collecting the pattern in 2θ over the range from 10° to 80° at steps of 0.03°. A Bruker IFS 66V/S apparatus was instead used for the FTIR analysis, working in the wavenumber range of 4000-200 cm^{-1}. Dried nanoparticles were compressed with powders of KBr to obtain a pellet disc for the measurement.

Goethite precursor

The goethite composition of the precursor synthesized in step (i) was confirmed by both XRD and IR analysis, whose results are shown in Fig. 5.8. XRD pattern presents Bragg peaks at 2θ angles typical of goethite, so as maximum absorption is measured in the IR spectrum at the wave numbers expected for goethite [23].

The highest peak in the XRD pattern was used to quantify the crystallinity of the particles by fitting the peak with the Scherrer equation, i.e.:

$$\tau = \frac{K\lambda}{\beta \cos\theta} \tag{5.1}$$

where τ is the mean size of the ordered crystalline domains, K is a shape factor, θ is the Bragg angle and β is the full width half maximum (FWHM) obtained after subtracting the instrumental line broadening. This analysis was performed by means of *APD* software. It is worth noting that the size of the crystals depends on the peak chosen for the analysis, since each peak refers to specific planes of the crystal lattice.

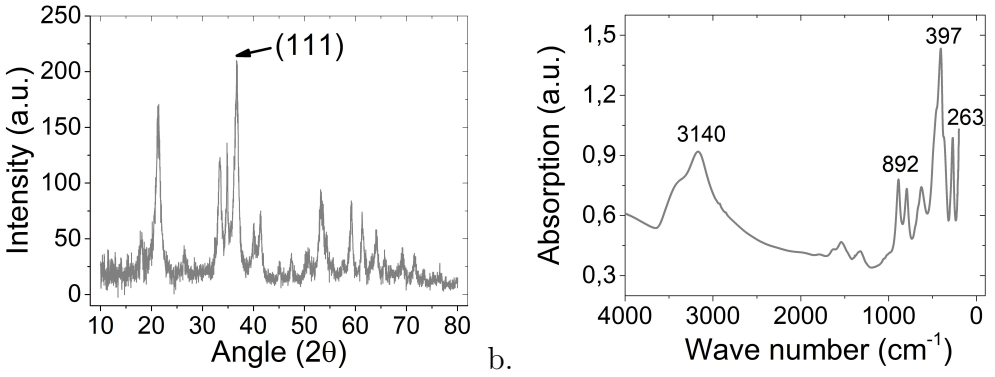

Figure 5.8: (a) XRD pattern and (b) IR absorption spectrum of the goethite precursor nanoparticles.

The crystal size of goethite e-MNPs obtained by fitting the (111) peak of the XRD pattern with the Scherrer equation is reported in Table 5.2. It is equal to 9.9 nm for all the samples since the precursor batch was the same in all cases. For a correct comparison between the crystallinity and the particles size, it is important to note that the major axis of the needles lies along the [100] axis of goethite, therefore a good crystallinity of the precursor has been obtained.

Hematite precursors

After the dehydration of goethite to hematite (step (iii)), the correct transformation between the two iron oxides was verified by both XRD (Fig. 5.9a, blue line on the bottom) and IR (Fig. 5.10a) analysis for all three temperatures selected for the synthesis of the precursors. Crystal size analysis with the Scherrer equation was performed by fitting the (110) peak of the XRD pattern; the crystal size is reported in Table 5.2. Considering that the major axis of the needles is oriented along the [010] axis of hematite (i.e. the crystal size was evaluated along the direction at 45° compared to the longest axis of the e-MNPs), the crystallinity value is compatible with a monocrystalline structure.

Depending on the strategy applied for the synthesis, S1 or S2, the presence of the silica coating around the particles needs to be verified. The easiest way for this check is to apply again IR spectroscopy. It is indeed well known that silica is characterized by a large peak at wave numbers from 1250 to 1000 cm^{-1}, which is a fingerprint of the silica network vibrations. IR absorption spectra of the hematite particles before the coating with silica (blue line on the bottom of Fig. 5.10a) and after the silica coating are reported in Fig. 5.10a. The characteristic peak of silica is clearly recognizable in all the precursors; moreover, the silica coating is also detectable in the TEM pictures as a light grey shadow with uniform thickness around the particles.

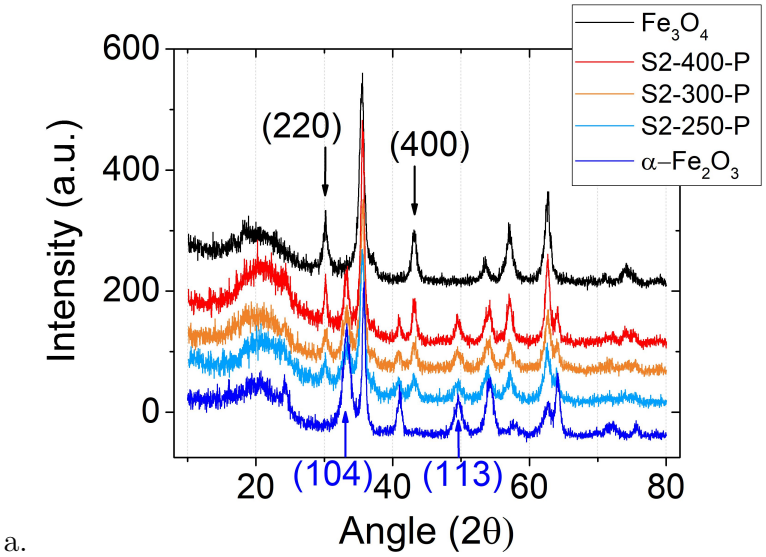

a.

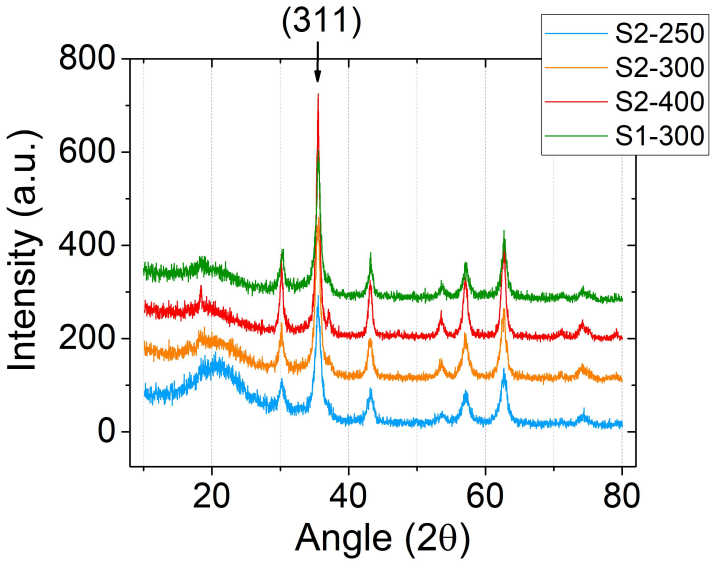

b.

Figure 5.9: XRD patterns of the four samples partially reduced (a) and of the four samples totally reduced (b) to magnetite. In (a) the XRD patterns of pure magnetite (black line) and hematite (blue line) are reported for comparison. Partially reduced samples present characteristic peaks of both hematite and magnetite, confirming the partial reduction. Peaks fitted with the Scherrer equation for the crystal size analysis are indicated by arrows (blue for hematite, black for magnetite).

Totally reduced samples

The complete transformation of hematite into magnetite in the totally reduced samples was also confirmed by XRD (Fig. 5.9c) and IR (Fig. 5.10c) analysis. The XRD pattern indeed shows only diffraction peaks at characteristic Bragg angles of magnetite, as IR maximum absorption is observed at the wave numbers expected for magnetite [23].

Table 5.2: Crystal size of the goethite (second column) and hematite (third column) precursors and of magnetite (fourth column) in the totally reduced samples, as obtained from the XRD pattern analysis. For the sample prepared with the strategy 1 (S1), particles were coated with silica before being dehydrated to hematite; therefore the hematite pattern is dominated by that of silica.

Sample	α-FeOOH (111) (nm)	$\alpha - Fe_2O_3$ (110) (nm)	Fe_3O_4 (311) (nm)
S2-250	9.9 ± 1.5	19.0 ± 2.9	8.9 ± 1.4
S2-300	9.9 ± 1.5	18.3 ± 2.8	10.4 ± 1.6
S2-400	9.9 ± 1.5	21.1 ± 3.2	15.0 ± 2.3
S1-300	9.9 ± 1.5	/	10.5 ± 1.6

Table 5.3: Crystal size of the partially reduced samples obtained from the XRD pattern analysis. Fitting with the Scherrer equation was performed on peaks exclusive of hematite or maghemite, excluding superimposed peaks as the (311) of magnetite and the (110) of hematite.

Sample	$\alpha - Fe_2O_3$ (104) (nm)	$\alpha - Fe_2O_3$ (113) (nm)	Fe_3O_4 (400) (nm)	Fe_3O_4 (220) (nm)
S2-250-P	5.8 ± 0.9	8.3 ± 1.3	9.7 ± 1.5	13.0 ± 2.0
S2-300-P	7.4 ± 1.1	7.8 ± 1.2	12.3 ± 1.9	12.1 ± 1.8
S2-400-P	12.1 ± 1.8	11.8 ± 1.8	14.6 ± 2.2	24.9 ± 3.8

The (311) peak of the XRD pattern was used to evaluate the crystallinity of the particles, whose major axis is oriented along the [100] axis of magnetite (i.e. the crystal size was evaluated along the direction at 30° compared to the longest axis of the e-MNPs). From the values reported in Table 5.2, it can be observed that samples heated at increasing temperatures present increasing values of the crystal size. This behaviour could be related to the different porosity of the samples, as it will be discussed in the next section about the surface area measurements. At high temperatures the micropores typical of goethite indeed coalesce in larger mesopores, leading to a more crystalline structure (it is possible to suppose for each particle a configuration with a large number of small pores and small crystals at low dehydration temperatures, and a configuration with few large pores and large crystals at high dehydration temperatures).

Partially reduced samples

Finally, as regards the three samples partially reduced to magnetite, the presence of both iron oxide phases was confirmed by the observed convolution of the characteristic diffraction peaks of hematite and magnetite in the XRD

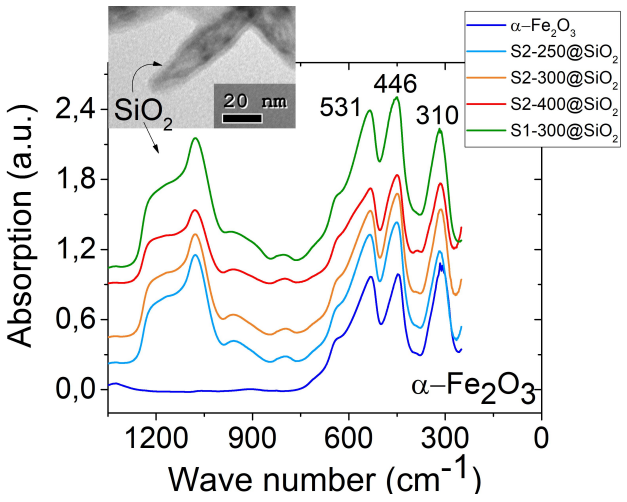

a.

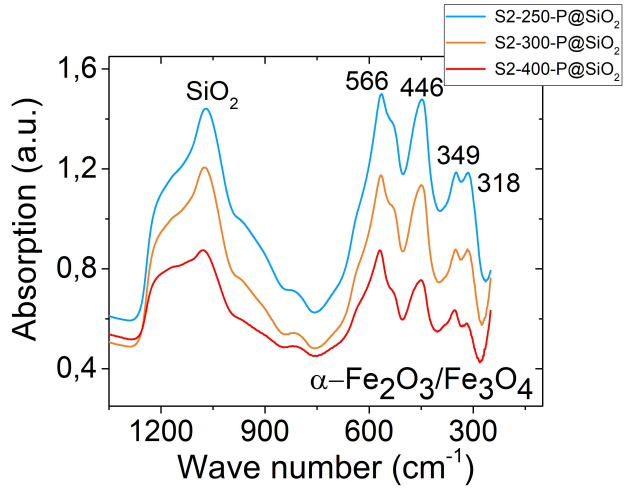

b.

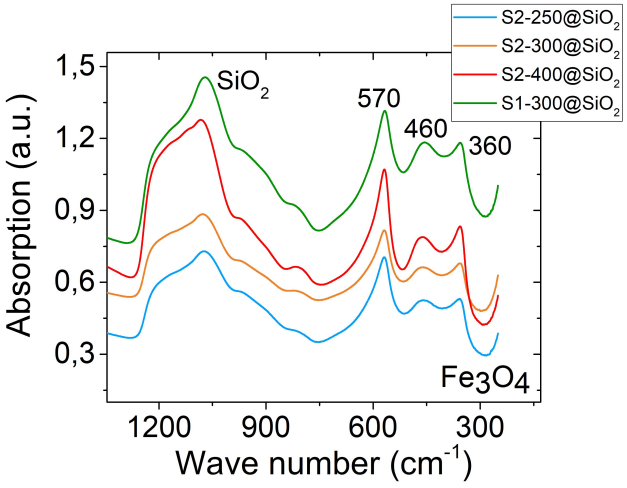

c.

Figure 5.10: (a) IR absorption spectra of the hematite precursors, uncoated (blue line) and coated with silica. The presence of the silica coating is evinced by a large peak at wave numbers from 1250 to 1000 cm^{-1}, as well as by a light grey shadow with uniform thickness in the TEM picture. (b) IR absorption spectra of the three samples partially reduced to magnetite, showing a convolution of the characteristic absorption peaks of pure magnetite and hematite. (c) IR absorption spectra of the four samples totally reduced to magnetite.

spectrum (Fig. 5.9b), as well as by that of the absorption peaks of hematite and magnetite in the IR spectrum (Fig. 5.10c).

Table 5.3 shows the crystal size of both hematite and magnetite, as obtained from the fits of selected diffraction peaks with the Scherrer equation. Only the peaks exclusive of magnetite ((400), (220)) or hematite ((104), (103)) were indeed considered, discarding the overlapping peaks. As for the totally reduced samples, also for the partially reduced samples an increasing crystal size with increasing dehydration temperature is observed, and the sample S2-400-P turns out to be the one with the largest crystals.

Some further considerations can be made regarding the data presented in Table 5.3. First, the size of the hematite crystals measured in the plane (113) results to be larger than that measured in the plane (104) only for the sample S2-250-P, while comparable crystals sizes are measured in both planes for the other samples. The size of magnetite crystals is instead larger in the plane (220) compared to the plane (400) for the sample S2-400-P and, although less marked, for the sample S2-250-P, while no relevant differences are observed for the sample S2-300-P.

5.3.3 Surface area measurements with the BET method

The BET (Brunauer, Emmett and Teller) method was applied for the textural analysis of the samples, by means of a Micromeritics Flowsorb II 2300 apparatus. Measurements were performed by technicians of the Institute of Material Science of Madrid (ICMM).

The BET method allows to determine the Specific Surface Area, i.e. the surface area of a unit mass of material (m^2/g), by measuring the extent of adsorption of nitrogen molecules (N_2) on its surface. The measurement is performed at the boiling temperature of liquid nitrogen (77 K) on a sample of material that has been previously outgassed in order to remove any other molecule (typically water) adsorbed on its surface. The N_2 adsorption is commonly measured as a function of the relative pressure p/p_0, i.e. the ratio between the partial pressure of N_2 (the adsorbate), p, and its equilibrium vapour pressure, p_0. The BET one-point method implies the measurement of the N_2 adsorption at only one value of p/p_0. The surface area of the material is finally calculated by multiplying the number of adsorbed molecules by the area occupied by one molecule of N_2, i.e. 0.162 nm^2 per molecule.

For the sample preparation, nanoparticles were first dried and then degassed at 423 K under an inert gas stream to remove adsorbed water. Measurements were performed on a small amount of MNPs ($\sim$ 50 mg) by nitrogen adsorption at 77 K by the one-point method. A maximum uncertainty of about 10% can be assumed considering both the uncertainties on weighing the MNPs and those on the nitrogen adsorption. Indeed, the small amount of MNPs used for the measurements does not allow to assume lower values for the uncertainty. Results of both adsorption and desorption of N_2 of samples dehydrated at different temperatures are reported in Table 5.4.

Table 5.4: Specific Surface Area of the samples of e-MNPs dehydrated at different temperatures, evaluated with the BET method.

Sample	Adsorption m^2/g	Desorption m^2/g
S2-250	73.4 ± 7.3	71.2 ± 7.1
S2-300	76.3 ± 7.6	72.3 ± 7.2
S2-400	32.9 ± 3.3	27.9 ± 2.8
S1-300	91.9 ± 9.2	85.3 ± 8.5
S2-300-P	69.1 ± 6.9	68.2 ± 6.8

It is worth noting that the reduction of hematite into magnetite occurred at 360°C, and this second heating of the samples (after the one performed during the dehydration of goethite at different T_d) determined a further evolution of the e-MNPs structure, in particular of the porosity. For this reason, the evaluation of the surface area have been performed only after step (iv) of the synthesis. However, despite the common heating at 360°C, the overall porosity maintains a record of the e-MNPs history, i.e. of the dehydration at different T_d, as can be seen from Table 5.4.

Totally reduced samples

Results presented in Table 5.4 show that the e-MNPs of the sample S2-400 are characterized by the smallest surface area, which can be explained by the presence of larger pores (for the same total pore volume) compared to the other samples. The larger the pores volume, indeed, the smaller the surface.

The e-MNPs of the samples S2-250 and S2-300 present compatible values of surface area, a result that can be interpreted as a clear sign of similar porosity. Moreover, the porosity of the samples heated at 250°C and 300°C could be reasonably associated with pores of smaller size than those of the sample S2-400, since their surface area is more than twice the value of the latter. It can be concluded that no significant differences in surface area are induced by a slightly higher dehydration temperature, as is $T_d = 300$°C compared to $T_d = 250$°C.

Finally, although the size measured by TEM is very similar for the sample S1-300 and S2-300 (Table 5.1), the two sample show a difference of about 20% in their surface area (Table 5.4). It is therefore reasonable to hypothesize that the presence of the rigid silica coating during the dehydration process (strategy S1) could cause a different evolution of the internal structure of the particles, compared to the dehydration performed on uncoated particles (strategy S2). As a result, silica leads to pores of different sizes in the final product.

To support the latter analysis, it is worth to remember that the fitting of the XRD patterns (Table 5.2) showed the presence of larger magnetite crystals in the particles of the sample S2-400 compared to the samples S2-250 and S2-

300. It was supposed that the size of the crystals could be related to the size of the pores, therefore larger crystals were expected for the sample presenting the largest pores. This hypothesis is confirmed by the smaller surface area and the larger crystal size of the sample S2-400 compared to the other samples.

As regards the samples synthesized with the strategy S2, there seems to be a positive correlation between the crystals size and the pores size. This observation does not apply to the samples S1-300 and S2-300, whose particles have crystals of identical dimensions (Table 5.2) but variable porosity (Table 5.4). However, this different behaviour is likely due to the morphological transformations induced (or not) by the silica coating in the two synthesis strategies S1 and S2.

Partially reduced samples

The surface area of the partially reduced samples was measured with the BET method only for the sample S2-300-P (Table 5.4): since its surface area resulted to be very similar to that of the corresponding totally reduced sample S2-300, it was possible to conclude that no differences in porosity were induced by different reduction times.

5.3.4 DLS and colloidal properties of the samples

The hydrodynamic size and the colloidal stability of the e-MNPs coated with both silica and dextran were determined by Dynamic Light Scattering (DLS) on very diluted aqueous suspensions of nanoparticles at pH = 7 and at room temperature, using a Zetasizer Nano S (Malvern Instruments, U.K.).

Negative values of the Z-potential ($\sim$ -26 mV) confirmed the stabilization of the magnetic nano-needles via electrostatic repulsion, and along with the values of the hydrodynamic size reported in Table 5.5, which do not differ too much from the size of a single particle as seen by TEM, attested a good colloidal stability of the samples.

Table 5.5 reports the hydrodynamic size of the e-MNPs according to the intensity, the volume and the number peaks of the scattered light. All these three values are commonly reported for DLS measurements, since samples with high colloidal stability should present similar results for all the three different estimations of the hydrodynamic size. However, it must be underlined that only the intensity peak is an assessment of the hydrodynamic size directly obtained from the scattered light, and indeed it is typically considered the most reliable one. In this case, the spectrum is given by a series of peaks corresponding to particles with different sizes and with intensity proportional to the amount of light scattered from each particle, which is approximately proportional to the sixth power of its diameter.

Differently from the intensity peak, the volume and the number peaks are estimations of the hydrodynamic size obtained by manipulating the scattering

Table 5.5: Hydrodynamic size (number, volume and intensity peaks) of the e-MNPs totally and partially reduced, coated with both silica and dextran, as obtained from DLS analysis.

Sample	Intensity peak (nm) L_{DLS}	Number peak (nm)	Volume peak (nm)
S2-250	118 ± 4	115 ± 7	118 ± 7
S2-300	122 ± 6	118 ± 7	122 ± 8
S2-400	156 ± 7	154 ± 10	159 ± 10
S1-300	101 ± 17	89 ± 17	97 ± 21
S2-250-P	110 ± 20	96 ± 19	105 ± 23
S2-300-P	131 ± 17	124 ± 21	131 ± 23
S2-400-P	122 ± 12	119 ± 17	122 ± 17

data. For the volume peak, particles are assumed as spherical and with homogeneous and known optical properties (i.e. refractive index), so the spectrum is represented with peaks of intensities proportional to the volume of the particles. On the contrary, the number peak is an estimation of the size obtained from the volume peak through a further data processing, that leads to a spectrum whose peaks intensity is proportional to the number of particles with a given size inside the sample [195].

As it can be easily understood, the volume and number peaks are highly susceptible to errors, which propagate from the light intensity distribution, and therefore they are rarely reported. This consideration is probably even more pronounced for the samples of this thesis, being e-MNPs not spherical. The anisotropic shape make the volume and number peaks not really reliable, and also the intensity peak could be affected by the asymmetrical shape of the particles.

Despite the previous considerations, all the values returned by the instrument are reported in Table 5.5. However, only the intensity peak is marked as L_{DLS}, since it will be considered as the reference DLS value in the following of the thesis. The intensity, volume and number peaks result to be most of the times in excellent agreement among them and with the sizes seen by TEM (Table 5.1), excluding the presence of pronounced aggregation within the samples ($L_{TEM} \sim L_{DLS}$).

The sample S2-400 is the only exception for which $L_{TEM} \ll L_{DLS}$, being $L_{TEM} \simeq 87$ nm (Table 5.1) and $L_{DLS} \simeq 156$ nm (Table 5.5). As will be discussed in the next section, this sample exhibits a very high saturation magnetization (Table 5.6), near to the value of bulk magnetite, which commonly leads to a higher probability of dipolar interactions between the particles, probably seen by DLS.

5.4 Magnetic characterization of the samples

Hystheresis loops, M_S and H_C

The main magnetic characterization of the samples was carried out in a MLVSM9, MagLab 9T (Oxford Instruments, U.K.) Vibrating-Sample Magnetometer (VSM), by acquiring the hysteresis loops $M(\mu_0 H)$ at $T = 290$ K, in the field range from -1 T to 1 T, and at $T = 5$ K, from -3 T to 3 T. Measurements were performed by saturating the magnetization of the samples in a 5 T field, and subsequently changing the field at a rate of 0.3 T/min. For the sample preparation, 25 μL of e-MNPs suspension in water were dropped on a small cotton swab, dried in a oven at 50°C and finally sealed in a polycarbonate capsule. The exact amount of e-MNPs in each sample was determined by measuring the Fe concentration (about 2-3 mg/mL) in each suspension by means of inductively coupled plasma mass spectrometry (ICP-MS) performed with an Optima 2100 DV PerkinElmer Optical Emission Spectrometer. For the latter measurement, 25 μL of each suspension of e-MNPs were diluted in 1 mL of aqua regia to dissolve the particles, and subsequently in 24 mL of distilled water.

The hysteresis loops acquired on the totally reduced samples at $T = 290$ K and $T = 5$ K are reported in Fig. 5.11, while the loops acquired at the same temperatures on the partially reduced samples are shown in Fig. 5.12. The Langevin function was fitted to the curves at high fields to extrapolate the value of the saturation magnetization M_S of the samples. The coercive field $\mu_0 H_C$ was instead determined by looking at the opening of the hysteresis loops at low fields, reported in the insets of Figs. 5.11 and 5.12. The results of this analysis, i.e. the main magnetic parameters of the samples, are shown in Table 5.6.

From the values of M_S reported in Table 5.6 it is possible to see that for both totally and partially reduced samples the saturation magnetization increases with the dehydration temperature T_d, providing the maximum values for the samples S2-400 and S2-400-P, respectively. This behaviour can be explained by recalling what described in Section 5.3: high T_d values lead to larger pores and larger magnetite crystals, which are reasonably correlated with the higher M_S values here found. In e-MNPs with larger crystals and lower surface area, it could be indeed possible to align more efficiently the electronic spins along the direction of the external magnetic field, thanks to (i) the stronger exchange interactions among the magnetic moments within the same (larger) magnetic domain and (ii) the lower contribution of the spin disorder on the particles and on the pores surfaces. As regards point (ii), it is well-known that the breaking of the crystal structure on the surface determines a major spin disorder compared to the bulk [125,196], and it plays an important role in determining the magnetic properties of MNPs (in particular the smallest ones, with a higher surface to volume ratio) [158].

Opposingly, low dehydration temperatures are linked to smaller crystals and pores sizes (i.e. greater surface area for the same total pore volume), thus

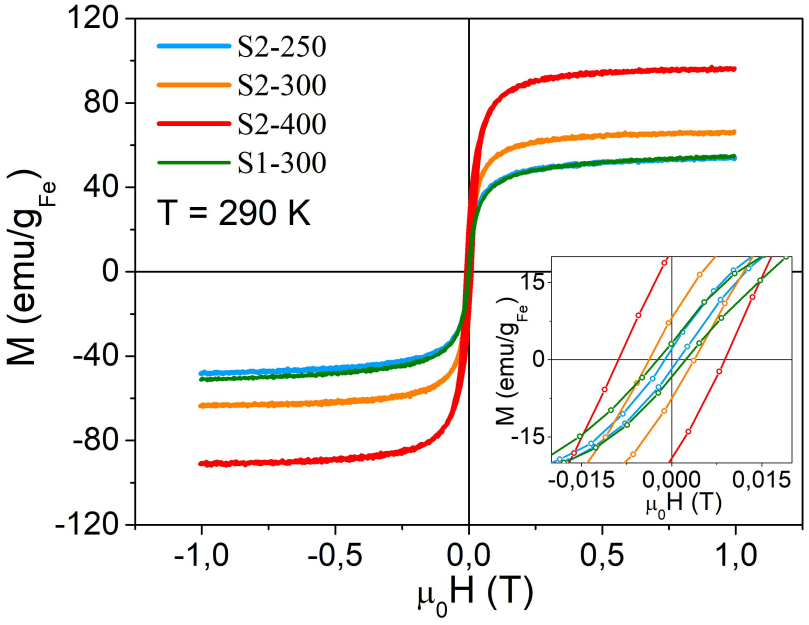

a.

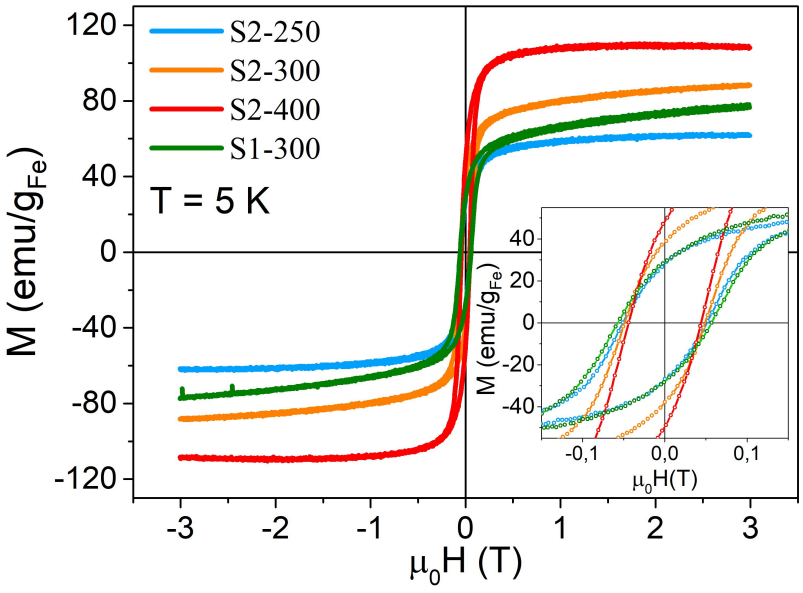

b.

Figure 5.11: Hysteresis loops at T = 290 K (a) and T = 5 K (b) of the four totally reduced samples. In the insets a detail of the loops at low fields allows to determine the coercive field and the remanence magnetization of each sample.

providing lower values of M_S.

Values of Table 5.6 also show a clear difference between the saturation magnetizations of the totally and partially reduced samples, being the M_S of the partially reduced samples much lower (about -40%) than that of the totally reduced samples. This result is in agreement with the antiferromagnetic nature of hematite. Moreover, as expected, the values of M_S at $T = 5$ K are

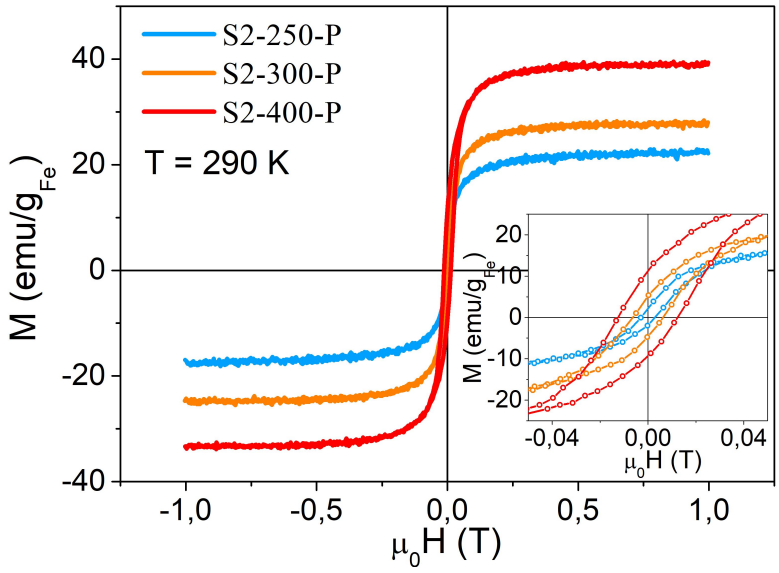

a.

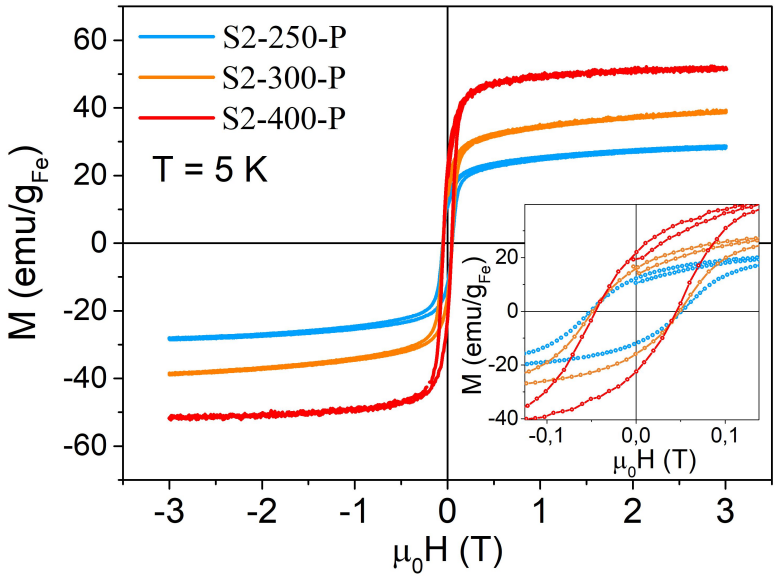

b.

Figure 5.12: Hysteresis loops at T = 290 K (a) and T = 5 K (b) of the three partially reduced samples. In the insets a detail of the loops at low fields allows to determine the coercive field and the remanence magnetization of each sample.

higher than those measured at $T = 290$ K for all the samples, since at low temperatures the thermal agitation of the spins is lower and a better orientation along the direction of the external field is obtained. The maximum value is achieved for the sample S2-400 at $T = 5$ K, whose M_S is slightly lower than that of bulk magnetite (about 125 emu/g$_{Fe}$) [24].

The low values of the coercive field $\mu_0 H_C$ at $T = 290$ K (as can be seen in the insets of Figs. 5.11a and 5.12a, the hysteresis loops are almost closed at room temperature) suggest a superparamagnetic behaviour of the e-MNPs,

Table 5.6: Saturation magnetization M_S and coercive field $\mu_0 H_C$ of the totally and partially reduced samples as evaluated from the VSM measurements.

Sample	M_S [290 K] (emu/g_{Fe})	$\mu_0 H_C$ [290 K] (mT)	M_S [5 K] (emu/g_{Fe})	$\mu_0 H_C$ [5 K] (mT)
S2-250	55.5 ± 2.8	1.80 ± 0.09	63.7 ± 3.2	51.0 ± 2.5
S2-300	66.6 ± 3.3	3.74 ± 0.19	94.9 ± 4.7	49.0 ± 2.5
S2-400	97.1 ± 4.9	8.82 ± 0.44	105.9 ± 5.3	44.0 ± 2.3
S1-300	57.8 ± 2.9	2.33 ± 0.11	88.1 ± 4.4	57.1 ± 2.9
S2-250-P	22.8 ± 1.1	2.93 ± 0.15	29.6 ± 1.5	51.1 ± 2.5
S2-300-P	27.7 ± 1.4	6.35 ± 0.31	42.6 ± 2.1	49.0 ± 2.5
S2-400-P	39.2 ± 2.0	12.4 ± 0.6	50.8 ± 2.5	45.6 ± 2.3

at least at high temperatures. As expected, indeed, superparamagnetism disappears at $T = 5$ K (Figs. 5.11b and 5.12b), that is lower than the blocking temperature, and $\mu_0 H_C$ values increase (Table 5.6). Furthermore, a trend similar to that of M_S can be identified for the $\mu_0 H_C$ values as a function of the dehydration temperature T_d: as shown in Table 5.6, $\mu_0 H_C$ increases with T_d for both totally and partially reduced samples, being higher for the samples S2-400 and S2-400-P, respectively. However, the coercive field of each partially reduced sample results to be greater than that of the corresponding totally reduced sample at room temperature, possibly due to dipolar interactions occurring between the totally reduced particles. This possibility is less likely to regards partially reduced e-MNPs, due to their lower saturation magnetization arising from their smaller magnetic cores dispersed in a non-magnetic hematite matrix that keeps them apart [172].

At low temperature ($T = 5$ K), the differences in $\mu_0 H_C$ between the totally and partially reduced samples are no longer observed, and a similar loop opening is recorded for all the couples of samples (totally and partially reduced) dehydrated at the same temperature.

Finally, some interesting considerations need to be discussed regarding the magnetic properties of the samples S2-300 and S1-300, i.e. the two samples prepared with the two different synthesis strategies S1 and S2. First, Table 5.6 show that both at high and low temperatures the saturation magnetization of the sample S2-300 results to be slightly higher than that of the sample S1-300. No relevant differences are instead observed in the coercive field of the two samples. The different M_S of the samples S2-300 and S1-300 could be interpreted as a direct consequence of the morphological differences reported in Section 5.3, in particular the different surface area. It was indeed shown (Table 5.4) that the presence of the silica coating during the dehydration step of the strategy S1 influences the evolution of the porosity, determining a higher surface area for the sample S1-300 compared to the sample S2-300. As already

discussed, increasing surface area easily means rising spin disorder in MNPs, and lower M_S values.

ZFC-FC curves

A SQUID Quantum Design MPMS magnetometer was used to acquire the Zero-Field-Cooled and Field-Cooled (ZFC–FC) curves of the samples under the action of a 5 mT magnetic field. Measurements were performed directly on the aqueous suspension of e-MNPs, sealed in small capsules of polycarbonate and kept frozen at $T \leq 260$ K during the whole experiment. The weak signal coming from the polycarbonate capsule and the sample holder was measured separately and subtracted to the measurements.

In Fig. 5.13 only one exemplary ZFC-FC curve (the one of the sample S2-250) is reported. All the samples indeed gave analogous curve shapes. In all cases no maxima were recorded in the ZFC curves up to 260 K, a clear sign of a blocked state of the e-MNPs. Moreover, considering the size of the particles ($\sim$ 100 nm), it is not unreasonable to hypothesize a blocked state even at room temperature.

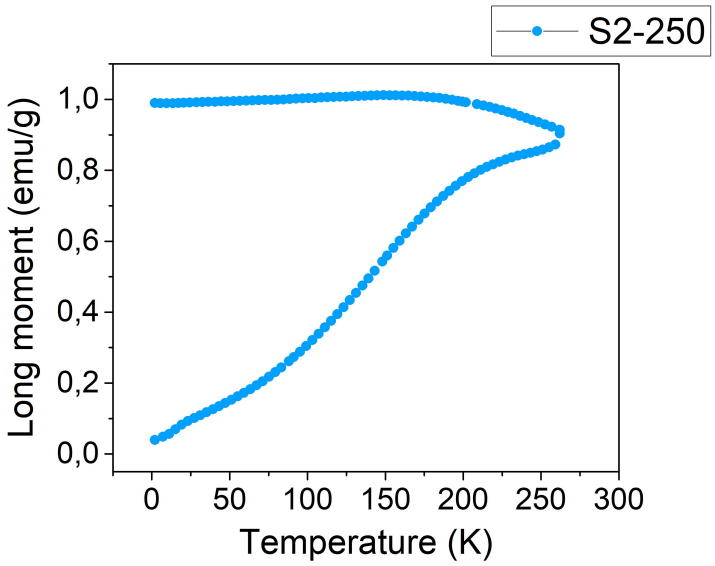

Figure 5.13: Exemplary ZFC-FC curves acquired on a frozen sample of S2-250 (T $\leq$ 260 K) under the action of a small magnetic field ($H = 50$ Oe). All the samples showed similar ZFC-FC curves. The absence of any maximum in the ZFC curve suggests that e-MNPs are blocked at temperatures up to 260 K (probably even at room temperature).

5.5 Considerations about the partially reduced samples

The interest towards elongated nanoparticles has been widely explained in the introduction of this Chapter. However, the samples described in the previous

sections present peculiar features other than the elongated shape, as for example the mixed composition of hematite and magnetite of the partially reduced samples. In this section, the reasons for the interest towards the partially reduced samples is explained.

First, it must be remembered that Rebolledo et al. [173] synthesized samples of e-MNPs quite similar to the partially reduced samples of this thesis. In particular, in Ref. [173] authors studied nanorods characterized by nanosized clusters of magnetite embedded in a hematite matrix, and doped with Mn, Ni, Cu or Sn. Apart from the use of dopants to enrich the magnetic properties of the iron oxides, already discussed in the introduction of this Chapter (Section 5.1), one main difference is recognizable between the synthetic routes described in Ref. [173] and in Section 5.2: in Ref. [173] the reduction of hematite to magnetite was performed by exploiting a stream of H_2 ($\sim$ 20 L/h) through the sample, while the samples of this thesis were reduced under a static atmosphere of H_2 (1 atm). This difference does not allow to hypothesize any similarity between the samples here presented and those in Ref. [173]. Moreover, the structure of the particles in Ref. [173] was studied by high-resolution TEM measurements; unfortunately, it was not possible to perform the same measurements on the partially reduced samples of this thesis.

As a consequence, it is worth noting that it is not possible to assume any particular structure for the partially reduced samples, and all the possibilities must be considered. Since the reduction of hematite to magnetite starts from the surface of the particles, where hydrogen activates the process, in principle both the outer surface of the needles and the inner surface of the pores could be the starting point of the reduction. It means that nanosized clusters of magnetite in a hematite matrix, as in Ref. [173], but also a magnetite shell surrounding a hematite core, or a mixed and not well-organized structure of magnetite and hematite, are all equivalent hypotheses for the partially reduced samples of this thesis.

Despite the lack of a clear description of the partially reduced samples, the interest in studying these samples arises from the large size of the needles. The particles here presented are indeed much larger than particles commonly used for MFH applications [46], since particles with a mean diameter between 12 and 20 nm generally show the highest heating efficiency. As discussed in Chapter 2, the spin dynamics responsible of the heating in MFH changes drastically with the particle size, showing superparamagnetic or ferromagnetic behaviour. Once the frequency of the alternating magnetic field is fixed, superparamagnetic nanoparticles show the maximum heating when their spin dynamics have characteristic times that match the frequency of the field. In the case of ferromagnetic nanoparticles, the most important parameter is instead the amplitude of the magnetic field, which must be sufficiently high to flip the magnetization exceeding the coercive field. For these reasons, it is not possible to determine *a priori* which of the totally or partially reduced samples could be the most efficient sample for MFH. The partially reduced samples

may indeed consist of small magnetite clusters embedded in a hematite matrix, with magnetic properties perhaps more similar to those of superparamagnets and therefore more suitable to heat efficiently, compared to the large totally reduced e-MNPs which are closer to the ferromagnetic regime.

Similarly, even for MRI it is not obvious to assume *a priori* which sample could have the highest contrast efficiency, since as shown by Rebolledo et al. [173] the porosity of the samples allows water molecules to enter the particles, and high transversal relaxivity values could be obtained even for partially reduced samples.

Finally, being the hematite an antiferromagnetic material, the magnetic properties of the particles with a mixed composition of hematite and magnetite could be more attractive in terms of safety conditions for clinical applications. Indeed, as shown in Section 5.4, partially reduced samples have lower values of M_S, which could lower the risk of particles aggregation within the body, and their side effects.

For all the presented reasons, partially reduced samples must be considered in principle as interesting as those totally reduced.

5.6 ^{1}H Nuclear Magnetic Resonance: measurements and results

5.6.1 NMR measurements: methods

For the evaluation of the e-MNPs efficiency for application in MRI, the longitudinal (T_1) and transversal (T_2) relaxation times of hydrogen nuclei (^{1}H) in aqueous suspensions of e-MNPs were measured. Measurements were performed at room temperature on 1 mL of diluted suspensions of e-MNPs, with mean iron molar concentration $C = [\text{Fe}] \simeq 0.2$ mM. The relaxation curves were collected by progressively increasing the static magnetic field, i.e. at different proton Larmor frequencies ($\omega_L = 2\pi\nu_L = \gamma B_0$), from 10 kHz to 56.7 MHz. This procedure allowed to reconstruct the NMRD profiles of each sample.

A Stelar SMARtracer relaxometer was used to collect the NMR signal at low Larmor frequencies, i.e. from 10 kHz to 7.2 MHz, applying the fast-field cycling technique [79]. A Stelar Spinmaster Fourier transform nuclear magnetic resonance (FT-NMR) spectrometer was instead used for the measurements at high frequencies, from 7.2 MHz to 56.7 MHz.

As regards the sequences used to collect the relaxation curves, a Saturation Recovery (SR) pulse sequence was applied for the measurements of T_1, both at low and high Larmor frequencies, although using pre-polarized sequences at $\nu_L \leq 3.7$ MHz and not pre-polarized sequences at $\nu_L \geq 3.7$ MHz. For the measurements of T_2, a standard CPMG pulse sequence was applied at $\nu_L \geq 3.7$ MHz, while at lower frequencies only a classical spin-echo sequence could be used. However, as discussed in Chapter 2.3.2, spin-echo sequences are susceptible of erroneous estimation of the transversal relaxation time due

to diffusion effects and field inhomogeneities. For the samples of this thesis, T_2 values measured at $\nu_L = 3.7$ MHz with not pre-polarized CPMG pulse sequences were observed to differ consistently from those measured at the same Larmor frequency but applying pre-polarized spin-echo sequences. As a result, only T_2 values measured with the CPMG were considered reliable, and T_2 values at $\nu_L < 3.7$ MHz are not reported.

The relaxation curves obtained from NMR measurements were fitted with an exponential function in order to extract the characteristic relaxation times T_1 and T_2 at each Larmor frequency. It is worth noting that in all the measurements performed on the samples of this thesis a perfect mono-exponential recovery/decay of the magnetization vs time curves was observed. This occurrence is not obvious when working with porous materials as the e-MNPs here presented. Theoretically, it is indeed known that a porous material could lead to multiexponential recovery/decay curves, due to the different relaxation times characterizing portions of hydrogen nuclei distributed in bulk water and inside the pores.

For the porous e-MNPs of this Chapter, several reasonable explanations can be formulated about the observed mono-exponential behaviour of the relaxation curves. First, the volume of water enclosed into the pores is much smaller than the volume of bulk water, therefore the observed mono-exponential recovery/decay probably refers to the water protons in the bulk component (dominant). In this regard, it must be remembered that samples for NMR measurements were highly diluted: from the iron molar concentration, it is possible to estimate that less than the 0.3% of the total volume of water was enclosed within the pores. Moreover, the size distribution of the pores within the particles is not known and probably large, therefore different relaxation times would be expected for hydrogen nuclei confined in pores with different sizes. Finally, it must be added that the accessibility of the pores to water and the exchange time between the water molecules inside the pores and the bulk water cannot be easily evaluated. In principle, the permeability of the dextran and the porous nature of the silica coating should allow water molecules to penetrate the pores. However, the residency time of these molecules within the pores is not known.

Once the relaxation times T_1 and T_2 were determined by the fits, the e-MNPs contrast efficiency was evaluated by means of the longitudinal (r_1) and transversal (r_2) relaxivity values, computed according to Eq. 2.27. To apply Eq. 2.27, the diamagnetic contribution of water was subtracted by measuring the relaxation times of the pure solvent. Uncertainty on relaxivity values was propagated from that on the iron molar concentration C and those on the relaxation times $T_{i_{obs}}$ and $T_{i_{diam}}$, giving a value of about 8%. This value includes also the uncertainty coming from the field inhomogeneities.

5.6.2 NMR on hematite precursors

The longitudinal and transversal relaxivities of the three hematite precursors dehydrated at different T_d (250°C, 300°C and 400°C) were measured in order to distinguish between the magnetite and hematite contributions in the partially reduced samples. It is worth noting that hematite is an antiferromagnetic material, therefore a low contrast efficiency was expected. The only magnetization that could shorten the relaxation times of the hydrogen nuclei is the hematite unbalanced sublattice electronic magnetization, particularly near to the pores and at the edges of the needles, where the shape is less regular and the crystal structure is abruptly interrupted. These conditions could lead to hyperfine field fluctuations experienced by water protons.

Measurements were performed on samples more concentrated (i.e. $C = [\mathrm{Fe}] \simeq 10$ mM) than those used for the reduced samples, in order to shorten the relaxation times enough to discern the hematite contribution. In Fig. 5.14 the results for the transversal and longitudinal relaxivities of the three hematite precursors prepared with the strategy S2 at different T_d are shown.

First, it is immediately observed from the results that the expectations about the antiferromagnetic nature of hematite have been confirmed, since both the longitudinal and transversal relaxivities do not overcome $1\,\mathrm{mM^{-1}s^{-1}}$ at the investigated Larmor frequencies.

Moreover, two additional observation can be drawn from Fig. 5.14: (i) r_1 and r_2 converge to the same value at low Larmor frequencies, as predicted by the theory, and this is a clear sign of the absence of aggregation phenomena within the samples (as expected for antiferromagnetic materials); (ii) the relaxivity values, although small, rescale with the dehydration temperature T_d. r_2 values at $\nu_L = 56.7$ MHz can be reported to exemplify the latter observation: a maximum value $r_2 = 0.90\,\mathrm{mM^{-1}s^{-1}}$ is reached by the sample S2-250, an intermediate value $r_2 = 0.80\,\mathrm{mM^{-1}s^{-1}}$ characterizes the sample S2-300, and finally a minor value $r_2 = 0.54\,\mathrm{mM^{-1}s^{-1}}$ is shown by the sample S2-400. The slight different porosity, aspect-ratio and shape (more rounded at the edges of the needles for the sample S2-400) of the three precursors could justify these differences.

In conclusion of this section, it must be noted that due to the very small relaxivity values shown by the hematite precursors, the contribution of hematite to the relaxivity of the partially reduced samples will be considered negligible in the next section.

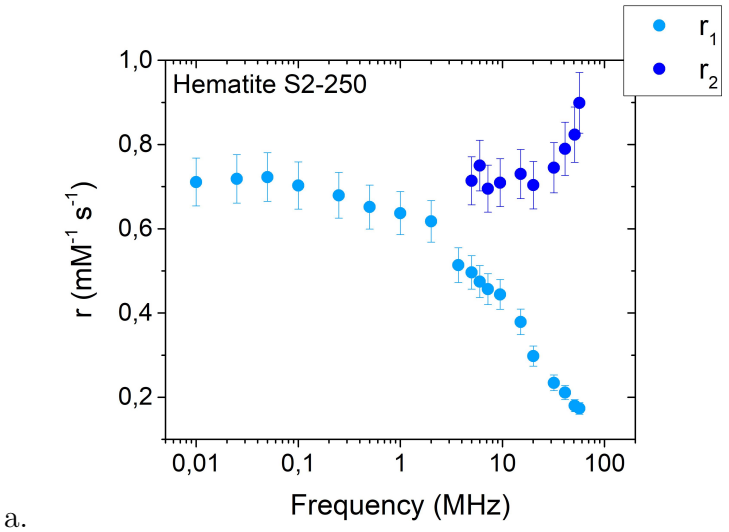

a.

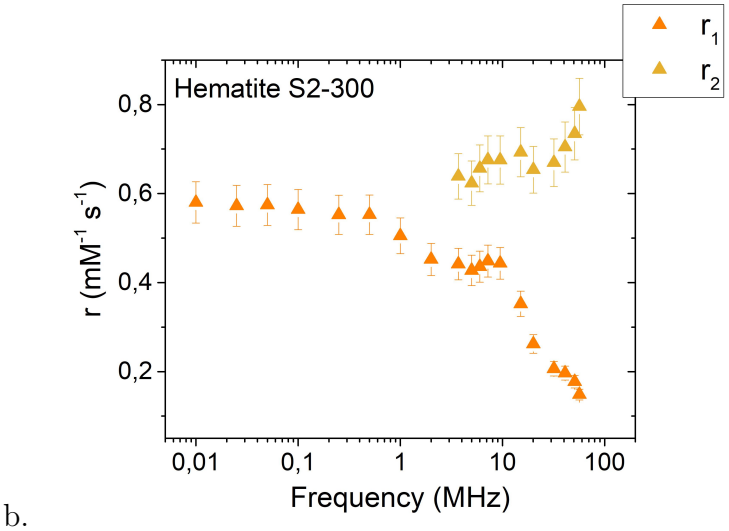

b.

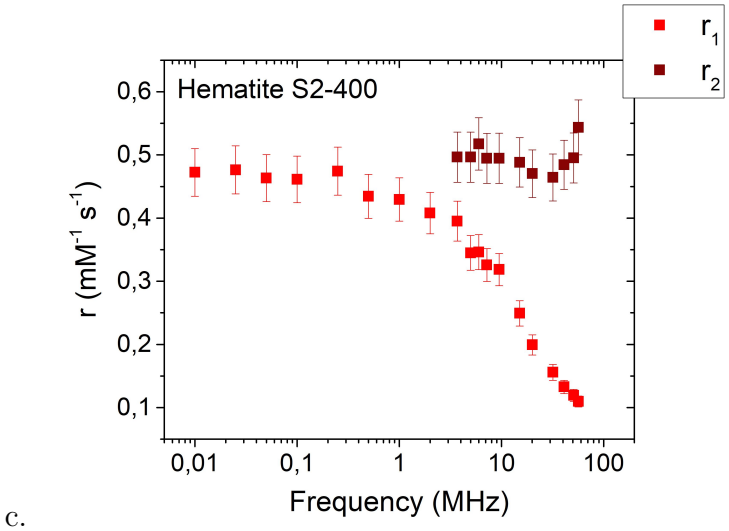

c.

Figure 5.14: . Longitudinal r_1 and transversal r_2 NMRD profiles of the hematite precursors dehydrated at different temperatures: S2-250 (a), S2-300 (b) and S2-400 (c). Relaxivity values were collected at room temperature in the Larmor frequency range 0.01 MHz $\leq \nu_L \leq$ 56.7 MHz. r_1 and r_2 decrease with increasing dehydration temperature, being higher for the precursor S2-250.

5.6.3 NMR on totally and partially reduced samples

Totally reduced samples

The experimental NMRD profiles of the totally reduced samples, i.e. the longitudinal (r_1) and transversal (r_2) relaxivities as a function of the proton Larmor frequency ν_L, are shown in Fig. 5.15. It is worth noting that the longitudinal profiles are particularly useful to investigate the properties of the MNPs, since, as shown in Chapter 2.3.2, theoretical models are available in literature that allow to explain the features of the NMRD profiles in terms of the main chemico-physical features of the particles. The transversal NMRD profiles are instead useful as a reference value for the contrast efficiency of MNPs in MRI. It is indeed known that most of the times MNPs works as T_2-contrast agents (or negative contrast agents), although some pioneering application for $T_1 - T_2$ dual MRI is under developing [197].

Starting the analysis from Fig. 5.15a, i.e. from the longitudinal relaxivity, it can be observed that r_1 increases towards low frequencies for all the samples, and no maxima are detectable in the NMRD profiles. From what described in Chapter 2.3.2, the theory (for spherical particles) would predict a flattening of r_1 at low Larmor frequencies for large particles [80], and the observed trend could be justified by considering a dominant contribution to r_1 coming from the crystal's internal anisotropy energy. In this regard, both the size and particularly the shape of the e-MNPs may contribute to determine a high value of the magnetic anisotropy, explaining the increase of r_1 at low ν_L.

Moreover, the absence of any maximum in the NMRD profile is also predicted by the theory for spherical particles larger than about 15 nm [81,83,91]. Unfortunately, theoretical models for the relaxation processes induced by anisometric nanoparticles have not been developed so far, and this limits the possibility of a deeper understanding of the longitudinal NMRD profiles of e-MNPs.

A great effort has been accomplished on the attempt to adapt the existing models for spherical particles [82, 83] or clusters [157] to the e-MNPs of this thesis, but not consistent results were obtained. As regards the Roch's model presented in Chapter 2.3.2, it has been discussed that the three main assumptions of the model limit its validity to small MNPs, with a mean diameter $d < 20$ nm, presenting low anisotropy energy. These conditions do not apply to the e-MNPs of this thesis, therefore it was not possible to fit rigorously the model to the experimental data obtaining meaningful and reliable results. More efforts were therefore spent in the attempt to adapt the Roch's model for cluster of MNPs to the analysed e-MNPs. It must be noted that this model applies to spherical cluster with diameter up to hundreds of nanometers, containing USPIOs embedded in an organic matrix. Again, the description of the cluster does not fit the characteristics of the needles, which are neither spherical nor clusters of individual particles. However, spherical particles of equivalent volume were considered, and the crystals seen by the

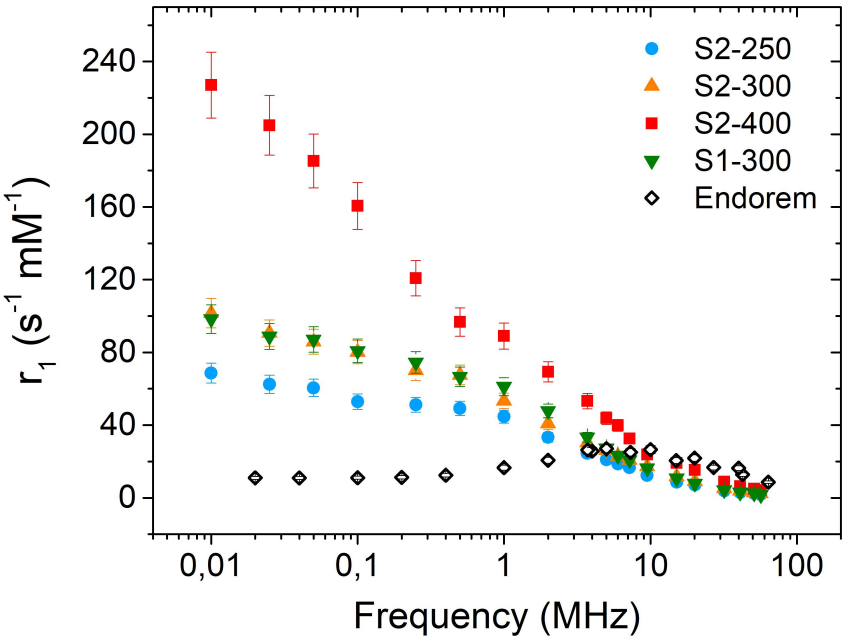

a.

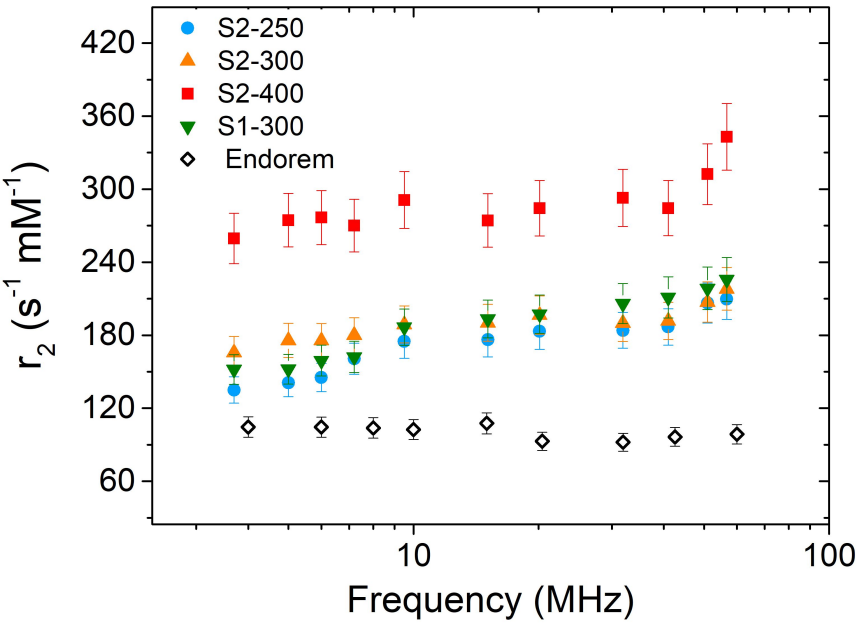

b.

Figure 5.15: (a) Longitudinal r_1 and (b) transversal r_2 NMRD profiles of the four totally reduced samples, collected at room temperature in the Larmor frequency range 0.01 MHz $\leq \nu_L \leq$ 56.7 MHz. The relaxivity values of a commercial MNPs based contrast agent for MRI (Endorem) as reported in Ref. [86] are shown for comparison.

XRD analysis were considered as individual particles within the needles. Despite (or because of) these approximations, the attempts to obtain good fits of the NMRD profiles, returning physically reasonable parameters, were not

successful. Therefore, a different and more theoretical approach, trying to develop a new and dedicated model for e-MNPs, will be necessary to further investigate on the e-MNPs properties starting from the longitudinal NMRD profiles.

The transversal NMRD profiles, shown in Fig. 5.15b, highlight a slight increase of r_2 towards high frequencies, with a similar rate for all the samples. As for r_1, also for r_2 there are not theoretical models available to date to fit the data.

Interesting information can be deduced from the comparison of the relaxivity values of the four totally reduced samples. In particular, rescaling values of r_1 at the same ν_L were registered for samples dehydrated at different temperatures, coherently with the reported differences in the magnetic and morphological characterization of the samples. The sample S2-400, i.e. the one with the largest pores (and smallest surface area), the largest crystals and the highest saturation magnetization, results to be the most efficient, showing the highest values of r_1 and r_2 at all the investigated Larmor frequencies. In particular, at $\nu_L = 56.7$ MHz, near to one of the most common clinical frequencies for MRI (most MRI scanner in clinics works at 1.5 T, i.e. $\nu_L = 63.86$ MHz) it results $r_1 = 4.2\,\mathrm{mM^{-1}s^{-1}}$ and $r_2 = 343\,\mathrm{mM^{-1}s^{-1}}$.

It is worth noting that the contrast efficiency of the sample S2-400, evaluated in terms of r_2, results to be more than three times higher than that of Endorem, a commercial MNPs-based contrast agent for MRI (nowadays it is withdrawn from the market) whose NMRD profiles are reported for comparison in Fig. 5.15. This result highlights the promising properties of this sample for applications with imaging purposes.

As regards the other samples, intermediate values of r_1 were obtained for the sample S2-300, coherently with its intermediate values of M_S; in particular, $r_1 = 2.4\,\mathrm{mM^{-1}s^{-1}}$ at $\nu_L = 56.7$ MHz. The minor r_1 values resulted to be those of the sample S2-250, i.e. the e-MNPs with the smallest pores (and largest surface area), the smallest crystals of magnetite and the lowest M_S, being $r_1 = 1.8\,\mathrm{mM^{-1}s^{-1}}$ at the same frequency.

Comparable values of r_2 were instead obtained for the samples S2-300 and S2-250, both much lower than the r_2 values of the sample S2-400 over the whole investigated Larmor frequency range. In particular, it results $r_2 \simeq 218\,\mathrm{mM^{-1}s^{-1}}$ at $\nu_L = 56.7$ MHz for both samples. Again, these differences between the sample S2-400 and the two samples S2-300 and S2-250 are compatible with the differences reported in the magnetic characterization, being higher M_S commonly associated with higher contrast efficiency.

Finally, the curves reported in Fig. 5.15 allow to investigate also the effects on the nuclear relaxivity produced by the two synthesis strategies S1 and S2, thanks to the comparison between the samples S1-300 and S2-300. Interestingly, NMR does not see any difference between the two synthesis strategies: both r_1 and r_2 values result to be compatible at all the investigated Larmor frequencies. However, this result cannot be easily explained. From the charac-

terization of the e-MNPs of the samples S2-300 and S1-300, it was shown that the sample S2-300 presents a higher saturation magnetization (M_S) than that of the sample S1-300, while the sample S1-300 presents a larger surface area compared to the sample S2-300. From the relaxometric point of view, both the properties could increase the contrast efficiency: high M_S MNPs are commonly more capable to shorten efficiently the nuclear relaxation times, while a large surface area allow a greater number of dipolar interactions between the particle and the water molecules of the solvent. As a result, it is possible to speculate about a compensation of the two effects, which would lead to the same relaxivity values in the two samples.

It is worth noting that also the samples S2-250, S2-300 and S1-300 show higher relaxivity values than those of Endorem, although the differences are less pronounced than those observed for the sample S2-400. However, the increase in r_2 is still important ($r_2[S2-250] \sim 1.5 \cdot r_2[\text{Endorem}]$), therefore also these samples must be considered promising candidates for MRI applications.

Not many data on the relaxometric efficiency of e-MNPs are reported in literature, and the high relaxivity values shown in this Chapter, coupled with the numerous advantages of the e-MNPs reported in the introduction, make quite surprising the lack of interest towards these systems. The only comparison with literature data is possible considering the relaxivity values of the nanorods reported by Nath et al. [198]. In this work, authors prepared magnetite nanorods of about 310 nm × 135 nm (aspect ratio 2.3), coated with dextran, and characterized their transversal nuclear relaxivity in water solution at 0.47 T. Apart from the dextran coating, these nanorods differ for the shape, the size, the aspect ratio and the synthetic route from the e-MNPs of this thesis, therefore a direct comparison is not particularly meaningful. However, the transversal relaxivity of the nanorods reported by Nath et al. ($r_2 \simeq 300\,\text{mM}^{-1}\text{s}^{-1}$) is compatible with that of the sample S2-400 at the same field ($\nu_L = 20$ MHz).

Partially reduced samples

In Fig. 5.16 the NMRD profiles of the three samples partially reduced are reported. Interestingly, the trends of r_1 vs ν_L and r_2 vs ν_L of the samples S2-250-P, S2-300-P and S2-400-P perfectly reproduce those of the totally reduced samples, although translated to lower values. This characteristic reflects two important considerations: (i) r_1 and r_2 values are lower than those of the totally reduced samples because of the presence of the antiferromagnetic hematite, which diminishes their saturation magnetizations (Table 5.6); (ii) the shape of the NMRD profiles is preserved between totally and partially reduced samples (in particular the longitudinal profiles), a result that can be interpreted as inheritance of the morphological properties of the hematite precursors, here included the different porosity. Indeed, it is reasonable to suppose that the type of reduction only affects the amount of magnetite within each sample and consequently its saturation magnetization, but not the other properties.

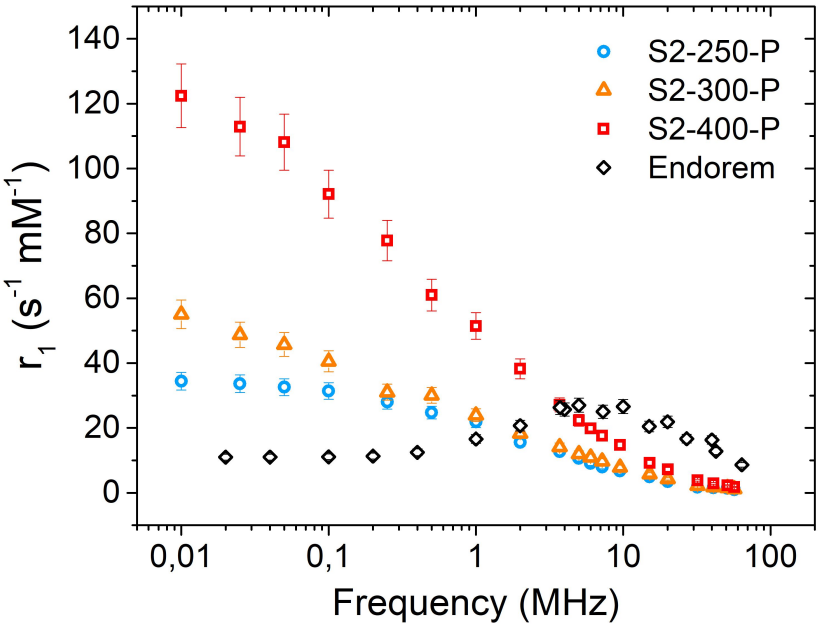

a.

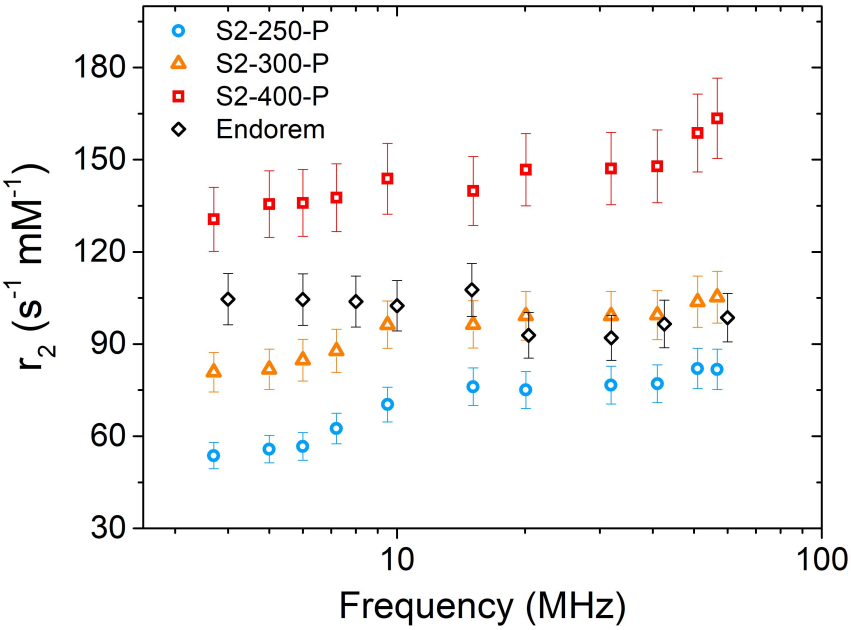

b.

Figure 5.16: (a) Longitudinal r_1 and (b) transversal r_2 NMRD profiles of the three partially reduced samples, collected at room temperature in the Larmor frequency range 0.01 MHz $\leq \nu_L \leq$ 56.7 MHz. The relaxivity values of a commercial MNPs based contrast agent for MRI (Endorem) as reported in Ref. [86] are shown for comparison.

Differently from the totally reduced samples, r_2 rescales in a more pronounced way for the three partially reduced samples, being r_2(S2-250-P) $<$ r_2(S2-300-P) $<$ r_2(S2-400-P). In particular, at the highest Larmor frequency

(ν_L = 56.7 MHz) considered for the measurements, r_2 increases from r_2 = 82 $mM^{-1}s^{-1}$ for the sample S2-250-P, to r_2 = 105 $mM^{-1}s^{-1}$ for the sample S2-300-P, and reaches its maximum value r_2 = 163 $mM^{-1}s^{-1}$ for the sample S2-400-P. Therefore, also for the partially reduced samples, the e-MNPs dehydrated at the highest temperature result to be the most efficient in terms of contrast efficiency.

It is noteworthy that also the partially reduced samples result to be good T_2-contrast agents, being the r_2 values of the samples S2-250-P and S2-300-P roughly compatible with those of Endorem (Fig. 5.16b), and the r_2 of the sample S2-400-P slightly higher. These conclusions apply to all the Larmor frequencies nearby the clinically relevant magnetic fields (1.5 T, 0.5 T and 0.2 T, corresponding to 63.86, 21.28 and 8.51 MHz for ^{1}H-NMR).

However, for both the totally and partially reduced samples, it must be underlined that several parameters other than the absolute value of the nuclear relaxivity should be investigated to identify a good contrast agent for MRI. The particles toxicity, the particles distribution once injected into the body, the risk of blood vessel occlusion and of any other side effects, are only some examples of the parameters typically investigated before moving to the clinical practice. To this aim, a deep *in-vitro* and *in-vivo* study of the samples presented in this thesis is mandatory, and it will be probably carried out in the next future by the group of Prof. Maria del Puerto Morales at ICMM in Madrid. To date, the investigation of the presented needles is limited to their relaxivity values, and so it is the comparison made with FDA and/or EMA approved contrast agent for MRI, as Endorem.

5.7 Magnetic Fluid Hyperthermia: measurements and results

5.7.1 MFH measurements: methods

A 12118-M01 Fives Celes set-up was used for the measurements of Magnetic Fluid Hyperthermia. This system generates alternating magnetic fields (AMFs) at frequencies from 92 kHz to 295 kHz, and maximum amplitude up to 65.7 mT. As the MagneTherm^{TM} previously used in Chapters 3 and 4, also in this system power limitations determine a decrease of the maximum amplitude of the AMF with increasing frequencies. For the measurements of this thesis, two frequencies were chosen, i.e. 109 kHz and 202 kHz, with maximum amplitudes equal to 55.4 mT and 29.9 mT, respectively. The SAR of the samples was therefore studied systematically as a function of the amplitude of the field at both frequencies.

The two frequencies (109 kHz and 202 kHz) were chosen nearby the frequency (100 kHz) used by the Magforce© company (www.magforce.com) for treatments in clinics, with field amplitudes up to 15 kA/m. This maximum field is determined by the safety limit suggested by Brezovich [61] for the safe

application of AMFs to patients: $H \cdot f < 4.85 \cdot 10^8\,\mathrm{Am^{-1}s^{-1}}$. However, it is worth noting again that passionate debate is ongoing in the scientific community to redefine this safety limit in a more objective way, and a limit one order of magnitude higher than that of Brezovich has already been proposed by Hergt et al. ($H \cdot f < 5 \cdot 10^9\,\mathrm{Am^{-1}s^{-1}}$ [133]). In this thesis, the heating efficiency of porous e-MNPs is studied from a physical point of view, therefore no particular interest is devoted to the safety limits for the patients and the SAR is deliberately evaluated also at fields higher than those applicable in the clinics. Of course, this will be considered in the conclusions.

Measurements were performed on water suspensions of e-MNPs with mean iron concentration of about 2-3 mg/mL, measured by means of ICP-MS spectrometry. In details, 1.5 mL of sample were placed into an Eppendorf and then centered within the coil of the Fives Celes set-up thanks to a polystyrene sample holder, that is necessary also to keep the sample as much isolated as possible from the external environment.

A fiber optic temperature transmitter (FTX-100-LUX+ OSENSA Innovations) centered in the Eppendorf was used to register the temperature of the sample as a function of time. The sensitivity of this system is 0.01°C, i.e. much more precise than that of the Optocon$^{\mathrm{TM}}$ system used for the measurements of Chapters 3 and 4. This high sensitivity of the instrument allowed to apply the initial-slope method for the evaluation of the temperature increment rate (i.e. $\Delta T/\Delta t$) in all the measurements, and to perform very quick acquisitions. With this method, indeed, only the $T(t)$ curve acquired during the first 30-40 seconds after the switching on of the AMF is necessary to evaluate the SAR, even at low fields, showing low heating.

Exemplary heating curves acquired on the sample S2-400 at $f = 109$ kHz and field amplitudes from 20 mT to 55 mT are shown in Fig. 5.17. These curves demonstrate the high reliability of the initial-slope method applied to the results of the measurements performed with such a high temperature sensitivity.

It is worth noting that hyperthermia measurements were performed on e-MNPs coated only with silica, i.e. without the dextran coating that was added subsequently to increase the colloidal stability for the NMR measurements. This decision was due to two main considerations: (i) the time required for collecting the data in a MFH measurement was very short, in particular because of the high sensitivity of the temperature transmitter, and the colloidal stability was observed to last for a time ($\sim 2-3$ minutes) longer than that required for precise and repeatable MFH measurements; (ii) the absence of the dextran coating could facilitate a more precise estimation of the SAR, since it allowed to ignore the dextran contribution to the specific heat of the ferrofluid (otherwise difficult to be determined). For the computation of the SAR, indeed, it was already necessary to ignore the contribution of the silica coating, whose mass was unknown. However, looking at the TEM pictures, the thickness of the silica coating was observed to be very thin, therefore the

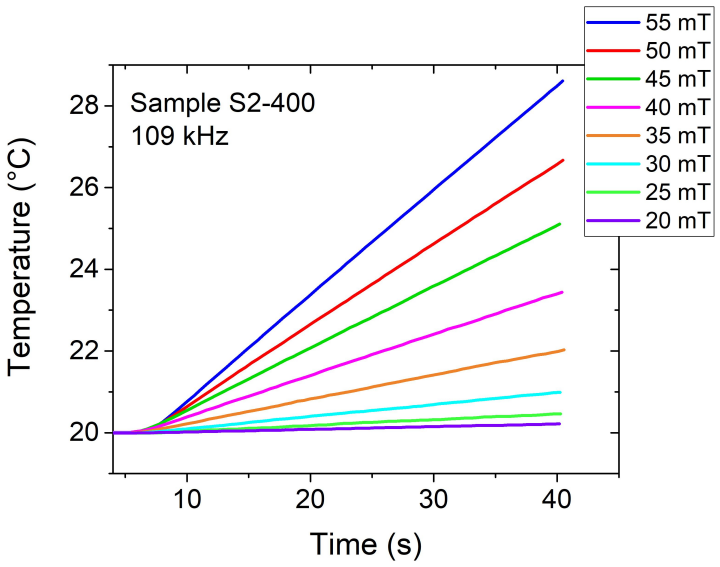

Figure 5.17: Heating curves acquired on the sample S2-400 at $f = 109$ kHz and different maximum amplitudes of the applied field.

mass fraction of the silica compared to that of water was considered negligible while computing the specific heat of the ferrofluids.

Despite the absence of the dextran coating, even a sample as the S2-400 showed a colloidal stability long enough to allow repeatable MFH measurements, showed in Fig. 5.17. According to the DLS measurements (Table 5.5), indeed, it was shown that this sample was the most susceptible to aggregation phenomena, and therefore the most critical with regard to the colloidal stability. However, it must be underlined that to obtain repeatable heating it was necessary (i) to sonicate the sample for some minutes between subsequent MFH measurements, and (ii) to thermalize the sample in the bath with ultrasounds to allow a fast measurement immediately after the introduction of the sample within the coil.

The SAR of the e-MNPs was finally computed by applying the formula:

$$\mathrm{SAR} = \frac{m_{H_2O} c_{H_2O} + m_{\mathrm{Fe}} c_{\mathrm{Fe}}}{m_{\mathrm{Fe}}} \cdot \frac{\Delta T}{\Delta t} \tag{5.2}$$

where $c_{H_2O} = 4.18$ J K^{-1} g^{-1} and m_{H_2O} are the specific heat and the mass of water, respectively, $c_{Fe} = 0.45$ J K^{-1} g^{-1} is the specific heat of iron and m_{Fe} the total mass of iron within the sample [138].

The SAR computed by means of Eq. 5.2 is expressed as a power released per unit mass of iron instead of unit mass of magnetite, because of the presence of the antiferromagnetic hematite in the partially reduced samples. Hematite did not allow to compute the exact amount of magnetite within the samples starting from the iron concentration measured by means of ICP-MS spectrometry, and no other techniques to distinguish the relative amounts of the two iron oxides were available.

The uncertainty on the SAR values was propagated from that on the $\Delta T/\Delta t$ ratio and that on the iron concentration within the sample, giving a value of about 10%.

5.7.2 MFH on totally and partially reduced samples

Totally reduced samples

In Fig. 5.18 the SAR($\mu_0 H$) of the four samples partially reduced at $f = 109$ kHz and $f = 202$ kHz is shown. As expected, the SAR of all the samples increases with the maximum amplitude of the applied field, although different increase rates are observed for samples dehydrated at different temperatures.

Samples S2-250, S2-300 and S1-300 present similar growth of the SAR with the field, with a sharp increase up to ~ 40 mT and subsequently a slight drop of the rate that suggest SAR is achieving saturation. The latter condition is indeed reached when the field amplitude is high enough to induce the maximum opening of the hysteresis loop of the particles, and therefore the maximum power release. Similar heating efficiencies are recorded for these samples at both frequencies up to ~ 30 mT, while at higher fields (reachable only at $f = 109$ kHz) the sample S2-300 shows slightly higher values of SAR, suggesting that strategy S2 leads to more efficient properties for MFH compared to strategy S1. This conclusion is supported by the higher saturation magnetization M_S measured for the sample S2-300 compared to the sample S1-300 (Table 5.6).

Interestingly, a completely different increase rate of the SAR with the field is observed for the sample S2-400: the SAR increases more slowly than the SAR of the other samples up to $\sim 25 - 30$ mT, than a rapid growth is registered up to 55 mT, where the SAR is still increasing fast instead of approaching saturation. As a result, the sample S2-400 (i.e. the sample with the largest pores and crystals and the highest M_S) results to be the least efficient sample at low fields (clinical fields of MFH, $\sim 15 - 20$ mT), where its SAR does not exceed 10 W/g, and the most efficient sample at high fields, with its SAR reaching a very high value, ~ 370 W/g. This behaviour could be explained remembering the largest crystals size observed with the XRD analysis for this sample compared to the others (Tables 5.2 and 5.3): large magnetite crystals probably behave as large magnetic domains, giving the particles ferromagnetic properties, which may require higher field amplitudes to overcome the coercive field and to rotate the spins along the direction of the field, increasing the opening of their hysteresis loops and therefore maximizing the heating.

To summarize, at low fields the sample S2-250, which show SAR ~ 20 W/g, results to be the most efficient one. For clinical applications, this sample would be the best choice between those here investigated. At high fields, instead, a clear rescale of the SAR with the dehydration temperature is observed, being the SAR of the sample S2-250 (~ 190 W/g) the lowest one, the SAR of the sample S2-400 the highest one (~ 370 W/g), and the SAR of the sample S2-300

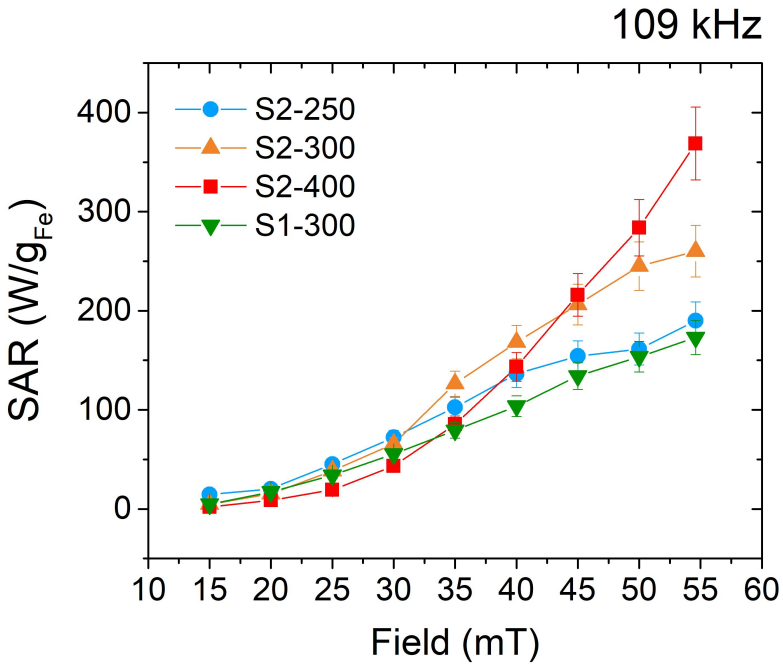

a.

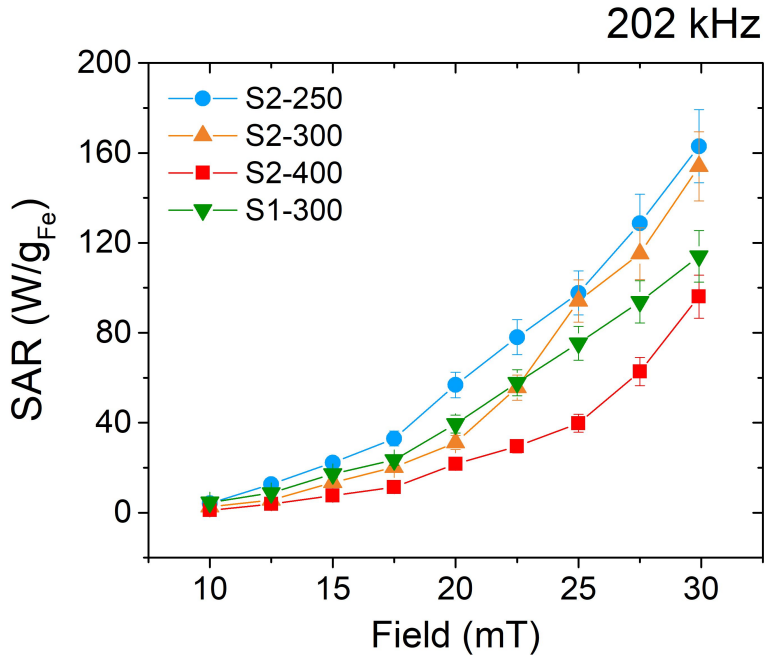

b.

Figure 5.18: SAR of the four totally reduced samples at $f = 109$ kHz (a) and $f = 202$ kHz (b) as a function of the amplitude of the applied alternating magnetic field. The sample S2-400 results to be the most efficient at high field amplitudes but the least efficient at low field amplitudes.

intermediate between the previous ones (~ 260 W/g).

To deepen the study of the increase rate of the SAR with the field amplitude, the theoretical models of MFH were tested on the curves shown in

Fig. 5.18. As described in Chapter 2.2.2, the Linear Response Theory (LRT), which holds for small superparamagnetic nanoparticles, predicts SAR $\propto H^2$, while the Rayleigh model, which holds for large ferromagnetic nanoparticles, predicts SAR $\propto H^3$. The validity conditions of the LRT are not satisfied by the e-MNPs here considered, in particular because of their large size. Moreover, fitting the curves in Fig. 5.18 with a free-exponent function SAR $\propto H^x$ (fits not shown), an exponent much greater than 2 was obtained, i.e. $2.8 \leq x \leq 3.8$ for the samples S2-250, S2-300 and S1-300, and $x \simeq 4.0$ for the sample S2-400. The values of the exponents x just reported therefore describe an increase of the SAR not predicted by any of the theoretical models of MFH developed so far [47], which always refer to spherical and non-porous MNPs.

As regards a general evaluation of the heating efficiency of these particles for clinical applications of MFH, it has already been discussed that the attention should be limited to the first points of Fig. 5.18a, i.e. at fields not exceeding 20 mT at $f = 109$ kHz (for the safety limits), where the SAR ≤ 20 W/g. These values of SAR are much lower than those of other particles reported in literature, however they could still be suitable for efficient MFH treatments. An important parameter in MFH, indeed, is the heat released locally by the particles within the cells, near to fundamental structures as the cell membrane, which could be enough to meet the objectives of MFH even with low SAR MNPs [199]. Of course, low SAR MNPs are less likely to produce high macroscopic temperature increments at the low MNPs concentration typically obtained considering only the MNPs internalized by the cells, but it must be underlined that MNPs are commonly injected at high concentrations within the tumour (the Magforce© company injects 112 mg/mL ferrofluids for treatments), and in these conditions the heating could be high even for low SAR MNPs. One of the main goals of the research in MFH is to find high SAR MNPs to allow performing efficient MFH treatments by administering a lower dose of MNPs to the patient, which is an important objective if considering the non-negligible toxicity of MNPs. Therefore, particles as those here presented are not very promising for MFH, since they probably would not be able to increase the macroscopic temperature of the tumour up to 42°C at low doses. However, *in-vitro* and *in-vivo* studies would be necessary to evaluate the effects of the local heat release within the cells, and nanometric probes [200] would help to evaluate correctly the energy adsorption responsible of the treatment.

Despite the low SAR at low fields, the heating efficiency of the needles studied in this Chapter results to be roughly comparable to that of similar elongated nanoparticles reported in literature. For example, Das et al. [201] investigated the heating efficiency of nanorods with mean length 65 nm and width 5.7 nm, working with ferrofluids at concentrations similar to those used for the measurements of this thesis, i.e. ~ 3 mg/mL. Authors presented an outstanding SAR value of about 500 W/g(Fe_3O_4), but measured at fields much higher than those used in this thesis, i.e. $\mu_0 H = 80$ mT and $f = 310$ kHz, therefore overcoming the safety limits for clinical applications. At clinical

acceptable fields amplitudes (from 10 to 20 mT), but at the same frequency (310 kHz), also the nanorods reported by Das et al. [201] show very low SAR values, i.e. SAR $\leq 25\,\mathrm{W/g}(Fe_3O_4)$. Interestingly, authors studied the heating efficiency dependence by the nanorods aspect ratio, proving that high aspect ratio nanoparticles are more efficient than spherical, cubic and low-aspect ratio MNPs with equivalent volume. This higher efficiency was explained by the high anisotropy of high aspect ratio MNPs and their capability to align along the field direction. However, this SAR dependence on the aspect ratio was limited only to samples at low concentrations (≤ 1 mg/mL), i.e. with negligible dipolar interactions between the particles.

Finally, another example found in literature is the work reported by Geng et al. [202], who characterized e-MNPs with mean length 45 nm and width 10 nm. The SAR of these particles overcame 1000 $\mathrm{W/g}_{Fe}$ when exposed to AMF with maximum amplitude 41.5 mT and frequency $f = 390$ kHz. Again, the high aspect ratio of the particles was identified by the authors as a determinant factor for such a high heating efficiency.

Partially reduced samples

In Figs. 5.19a and 5.19b the SAR of the three partially reduced samples is reported, respectively at 109 kHz and 202 kHz. The main interest towards these samples was to determine if the possible presence of small superparamagnetic clusters of magnetite in a hematite matrix, as described by Rebolledo et al. [173], could increase the heating efficiency of the needles at the clinical fields of MFH.

Comparing the SAR values in Fig. 5.19 with those in Fig. 5.18, it is immediately observed that the SAR of the partially reduced samples is lower than the SAR of the totally reduced samples, in particular at high fields, while compatible values are obtained at low fields. Evidently, the presence of antiferromagnetic hematite in the partially reduced samples, which lower their saturation magnetization M_S (Table 5.6), decreases also their heating efficiency, and a superparamagnetic behaviour of small magnetite clusters embedded within the hematite matrix, if any, does not cause an increment of the SAR.

Interestingly, as for the NMR results, also the SAR($\mu_0 H$) curves of the partially reduced samples follows almost exactly the same trends of the totally reduced samples, although translated to lower SAR values. Therefore, all the considerations done about the totally reduced samples, regarding the comparison between samples dehydrated at different temperatures and the rates of the increment of the SAR($\mu_0 H$) studied with a free exponent function SAR $\propto H^x$, apply also to the partially reduced samples. In particular, also for the SAR of these samples similar trends are observed in the case of samples S2-250-P and S2-300-P, while a rapid rise occurs for the SAR of the sample S2-400-P above 30 mT, where it results to be the most efficient one with SAR $\simeq 204$ W/g at $f = 109$ kHz and $\mu_0 H = 55$ mT.

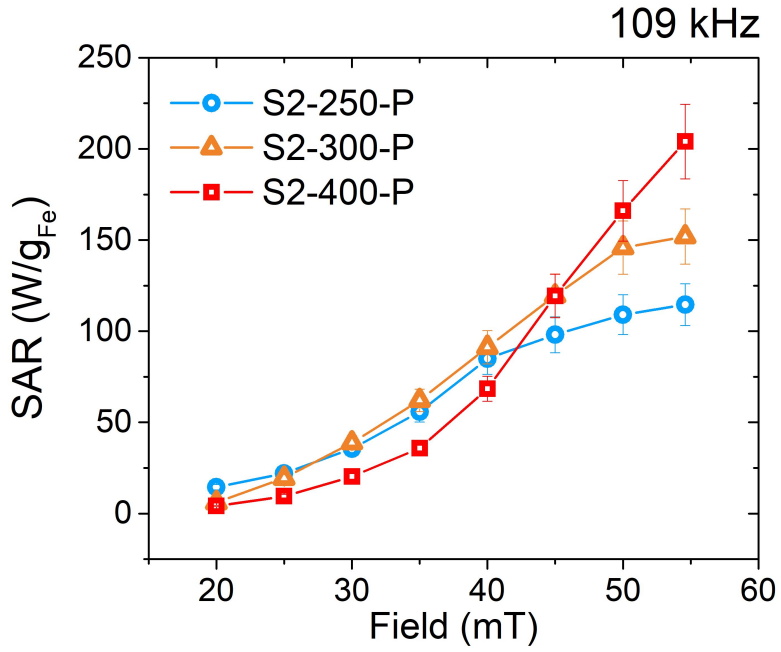

a.

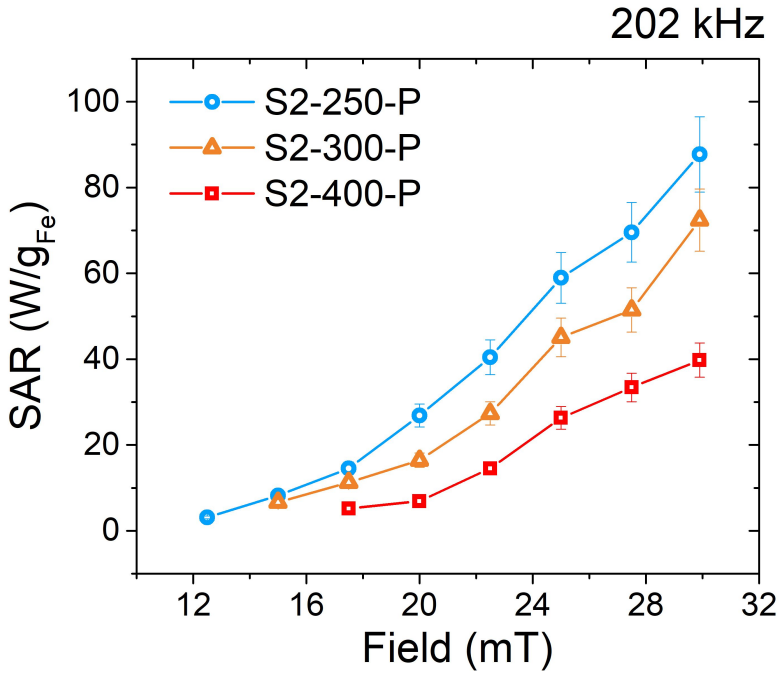

b.

Figure 5.19: SAR of the three partially reduced samples at $f = 109$ kHz (a) and $f = 202$ kHz (b) as a function of the amplitude of the applied alternating magnetic field. The sample S2-400-P results to be the most efficient at high field amplitudes but the least efficient at low field amplitudes.

5.8 Conclusions

In this Chapter, the relaxometric and hyperthermic properties of porous elongated magnetic nanoparticles (e-MNPs), or needles, synthesized through a multistep procedure have been studied.

Goethite precursors were first synthesized through aerial oxidation, and subsequently dehydrated at different temperatures to transform goethite into hematite and to obtain e-MNPs with different porosity. Varying the duration of the following reduction step, both magnetite e-MNPs and e-MNPs with a mixed composition of magnetite and hematite were obtained. All the samples were completely characterized from the chemico-physical, morphological and magnetic points of view by means of TEM, DLS, XRD, IR, and N_2 adsorption (BET method) for the evaluation of the surface area. It was observed a strong correlation between the pores sizes, the crystals sizes and the saturation magnetizations as a function of the synthesis parameters, in particular the dehydration temperature. The higher the dehydration temperature, the larger the pores, the smaller the surface area, the higher the aspect ratio and the higher the saturation magnetization. For the sample dehydrated at the highest temperature (400°C) and totally reduced to magnetite, a saturation magnetization near to the value of bulk magnetite was obtained. The size of the particles resulted to be $\sim$ 100 nm $\times$ 25 nm, with slight differences depending on the dehydration temperature.

The partially reduced samples, i.e. e-MNPs with a mixed composition of hematite and magnetite, were studied in order to verify if the possible occurrence of a structure as that described by Rebolledo et al. [173], with small magnetite clusters embedded in a hematite matrix, could increase the heating and/or the relaxometric efficiencies of the needles. This possibility would be justified by the superparamagnetic behaviour of the small magnetite clusters compared to the nearly ferromagnetic behaviour of the totally reduced samples. However, no information about the real structure of the partially reduced samples were available.

The peculiar differences registered between the samples were observed to have direct consequences on both their relaxometric and hyperthermic efficiencies. Both the SAR in Magnetic Fluid Hyperthermia (MFH) experiments (measured at high fields) and the nuclear relaxivities r_1 and r_2 in the Nuclear Magnetic Resonance (NMR) experiments were indeed shown to rescale with the dehydration temperature, being the samples S2-400 and S2-400-P (i.e. the ones dehydrated at the highest temperature) the most efficient ones among the totally and partially reduced samples, respectively. Moreover, totally reduced samples were proved to be best performing compared to the partially reduced samples, i.e. no particular properties arising from the mixed composition of hematite and magnetite were observed.

NMR measurements showed that all the samples are promising T_2-contrast agents for MRI applications, in particular the totally reduced ones, having transversal relaxivity (r_2) values much higher than those of commercial MNPs-

based contrast agents as Endorem at all the investigated Larmor frequencies (ν_L). In particular, the sample S2-400, having the largest magnetite crystals and the highest saturation magnetization M_S, resulted to be the most efficient one with r_2 values more than three times higher than those of Endorem at the clinically most relevant fields. For example, at $B_0 \simeq 1.33$ T, i.e. at the proton Larmor frequency $\nu_L = 56.7$ MHz, it results $r_2 = 343\,\mathrm{mM^{-1}s^{-1}}$ compared to the value $r_2 \simeq 100\,\mathrm{mM^{-1}s^{-1}}$ of Endorem.

The same promising results for applications were not obtained in MFH experiments, since the SAR of the samples was observed to not exceed 20 W/g at 109 kHz and 15 kA/m, field parameters typically used for clinical applications of MFH (i.e. by the Magforce© company). However, a strong heating was recorded at high field amplitudes, in particular for the sample S2-400, showing SAR = 370 W/g at $f = 109$ kHz and $B_0 = 55$ mT. Moreover, the SAR could not be considered a definitive parameter to evaluate the particles efficiency for MFH, since *in-vitro* and *in-vivo* experiments are necessary to better define their heating performances in the biological medium with a localized heating release near to sensitive structures as the DNA or the cell membrane.

MFH studies on the samples presented in this thesis will probably continue in the next future, in particular particles will be tested in *in-vitro* studies to assess (i) if the elongated shape allows to increase the uptake rate by cells compared to other shapes, as reported in literature, and (ii) the effects of the heating on the cell survival rate. It is worth noting that in-gel MFH measurements, as those reported on spherical particles in Chapter 4, would have been useful to estimate the heating efficiency of the needles in more viscous media as the cytoplasm or, more in general, the tumour tissues. Unfortunately, it was not possible to perform these measurements due to the limited time available at the ICMM in Madrid, where the MFH measurements were carried out.

In conclusion, the investigation performed in this Chapter about the relaxometric and hyperthermic efficiency of e-MNPs showed that all the analysed samples, and particularly the samples with the largest pores, are very promising candidates for MRI applications. On the other hand, MFH results showed that it would be probably necessary to increase the heating efficiency of the samples at low fields, i.e. for MFH applications in the clinical conditions, to make them more attractive in comparison with other best-performing MNPs reported in literature.

The elongated shape of the particles makes them suitable candidates for biomedical applications, due the evidences of increased cellular uptake and favourable flow within the bloodstream reported in literature for anisotropic particles. As an added value, more peculiar biomedical applications could also be envisaged for the e-MNPs presented in this Chapter. For example, the porous structure could suggest more exotic theranostic approaches, for example by filling the pores with opportune drugs and thus using the magnetic nanoparticles as carriers for drug-delivery. As concerns instead the poorly investigated field of magnetic transport, both the elongated shape and the

magnetic properties of the particles could ease their administration to the target, for example by using external magnets to guide the particles through the blood vessels. Finally, rotating magnetic fields can be used to induce a mechanical damage in the region where the particles accumulate, thanks to their motion guided by the external field, which is favoured by their anisotropic shape.

The systems studied in this Chapter are of particular interest since few literature data are available to date on anisotropic magnetic nanoparticles, even showing complex structure as the porous one here presented. Moreover, also from the theoretical point of view the field of high aspect ratio (or, more generally, anisotropic) nanoparticles is quite unexplored. For example, the relaxometric and hyperthermic results of this thesis would require new theoretical modelling to physically explain the observed relaxivity vs ν_L trends in the NMR measurements and the SAR vs H and SAR vs f trends in the hyperthermia experiments. Hopefully, an increasing experimental interest towards these anisotropic systems will stimulate also theoretical research on those topics.

Conclusions and perspectives

In this PhD thesis the effects of some of the most important properties of magnetic nanoparticles (MNPs) for Magnetic Fluid Hyperthermia (MFH) and Magnetic Resonance Imaging (MRI) applications have been investigated. In particular, two main research topics, i.e. the role of the Brownian motion and of the MNPs aspect ratio in MFH and MRI, have been developed.

This study started from a previous investigation on the role of the MNPs size in water solutions in determining the MNPs efficiency for both MFH and MRI. In particular, in Chapter 3 it was shown that spherical MNPs with diameter from 10 nm to 20 nm present an increasing Specific Absorption Rate (SAR) and transversal nuclear relaxivity (r_2) with increasing particles size, and that the laws governing these parameters move gradually from those of superparamagnets to those of ferromagnets.

In Chapter 4, the effects of the electronic correlation times on the heating efficiency of MNPs have been studied. In particular, the role of the Brown relaxation time in MFH has been deepened, compared to the current knowledge reported in literature.

It is known that the particles immobilization in the tumour environment could decrease consistently their Specific Absorption Rate (SAR) with respect to the SAR measured in water suspensions, due to the suppression of the Brownian relaxation. This effect may overestimate the actual heating occurring in the biological medium during MFH treatments on patients. It is therefore necessary to highlight the role of the Brownian motion as a function of all the different parameters concurring in determining the heating efficiency of MNPs.

In this regard, in the thesis the SAR of magnetite spherical nanoparticles has been studied systematically for the first time as a function of: (i) the frequency and the maximum amplitude of the applied alternating magnetic field; (ii) the size of the particles, from superparamagnetic MNPs with $d = 10$ nm up to larger particles ($d = 18$ nm) at the transition between superparamagnetism and the single-domain ferromagnetic regime; (iii) the viscosity of the medium, considering three different dispersant media: water and two agarose gels with different mass fractions (0.5% and 2% w/w).

It has been proved that the immobilization of the particles decreases their

SAR up to 70% but not in the case of small superparamagnetic nanoparticles. The sample with $d = 10$ nm indeed showed the same SAR in all the considered media due to the dominant role of the Néel relaxation time compared to the Brown relaxation time, whose contribution to the heating resulted negligible. Moreover, agarose gels with the lowest mass fraction (0.5%) were already sufficient to immobilize the particles, since no differences were observed between the SAR values measured in the two gels.

As an additional contribution to this experimental study, kinetic Monte Carlo simulations were performed to collect further information about the role of the Brownian motion. Simulations were performed by fixing all the parameters of the particles in the code as those collected during the characterization of the samples used for the experimental measurements. Interestingly, simulations almost perfectly reproduced the decrease of the SAR observed in gel samples compared to water samples, in particular for the sample with $d = 14$ nm. This computational result supports the interpretation of the experimental results as an effect due to the immobilization of the particles in the gels, and not to other effects like for example aggregation phenomena occurring in the gels or chain-like structures formation in the water samples.

As regards the future perspectives in this research field, both the experimental and computational studies could be further developed. For example, the investigation of the effects of the particles immobilization in gel could be extended to particles with different shapes, different core composition and/or different concentration, to add also the effect of dipolar interactions between the particles. The Monte Carlo code could be instead further developed to implement correctly both the Néel and Brown relaxation also for very small magnetic nanoparticles (to date, some validity conditions must be verified before running the simulations), and maybe to add the free movement of the particles in the space (in the current version particles are fixed in their position in the space, and can only rotate without changing their coordinates). It is worth noting that numerical simulations allow to perform several and also very exotic studies, and in this sense the perspective applications of the code are countless. For example, it could be possible to investigate the role of dipolar interactions in rotating and fixing the superspins orientation of MNPs as a function of the MNPs concentration in biological structures as lysosomes.

In Chapter 5, a quite new material has been characterized, i.e. elongated magnetic nanoparticles (e-MNPs), or needles, with a porous structure of pure magnetite or a mixed composition of magnetite and hematite.

The interest towards these systems was justified by several advantages reported in literature for elongated or anisotropic nanoparticles, as for example (i) the increased shape anisotropy, which contributes to their magnetic properties; (ii) the favourable uptake of e-MNPs by cells, thanks to their greater surface area compared to spheres that allow multivalent interactions with the receptors on the cell membrane; (iii) a favourable flow within the bloodstream, thanks to the e-MNPs capability to align to the direction of the flux; and (iv)

the possibility to exploit e-MNPs for a mechanical action aimed to kill cancer cells. Despite all these advantages (and others not cited), a poor interest towards e-MNPs is found in literature, where most of the works published characterize spherical magnetic particles.

A new hydrothermal method has been developed for the synthesis of e-MNPs with mean size of about 100×25 nm and a porous structure. Both the size of the pores and the needles aspect ratio resulted to be tunable properties by changing the chemico-physical parameters of the synthesis. Moreover, the synthesis strategy presented is cheap, environmentally friendly and easy to scale up for the production of very large amounts of e-MNPs, as those required for biomedical applications.

Seven different samples were prepared by changing the two main physical parameters of the synthesis, i.e. the temperature and the time of some steps. The samples had pores with different sizes and cores with different composition: magnetite or a mixture of hematite and magnetite. Interesting correlations were found during the characterization of the e-MNPs between their porous structure, the size of the magnetite crystals within each magnetic core, their magnetic properties and finally their heating and relaxometric efficiencies for MFH and MRI applications. In particular, samples treated at the highest temperature (400°C) presented the largest pores, which were demonstrated to be associated with the largest magnetite crystals and consequently the highest saturation magnetization, causing better heating and relaxometric performances. The samples were indeed characterized in terms of SAR for MFH and in terms of nuclear relaxivity (r_1 and r_2) for MRI.

It has been shown that e-MNPs with a porous structure are promising candidates for MRI applications, and also their heating efficiency for MFH is quite good, although it needs to be improved at low fields.

Unfortunately, it was not possible to deepen the study of the properties of the e-MNPs through the comparison with theoretical models of MFH or MRI, since to date the theoretical investigation on the topic has been limited to spherical particles.

It is worth noting that the future perspectives about e-MNPs are countless, from applications as efficient magnetic carriers to MFH and MRI agents. Moreover, different and more efficient synthesis strategies will be probably developed to produce e-MNPs with different sizes, aspect ratio and composition. As regards the e-MNPs of this thesis, *in-vitro* and *in-vivo* studies will be the next steps to evaluate (i) the particles toxicity, (ii) the particles uptake rate by cells (and, in this regard, to verify if it is really increased thanks to their elongated shape), and (iii) the particles heating and contrast efficiencies in the biological medium. Indeed, several conditions must be verified for any MNPs before moving to the clinical practice; however, the promising physical properties shown in this thesis are a good first step towards the final goal.

Appendix A

Combining MFH and Hadron Therapy: the Hadromag project

The *Hadromag* project is a project that has been being developed since 2016 in collaboration between University of Pavia, University of Milan, University of Florence, University Roma Tre, The National Institute of Tumours (INT - Istituto Nazionale dei Tumori) in Milan and the National Centre for Oncological Hadron therapy (CNAO) in Pavia. It is founded by the Italian National Institute for Nuclear Physics (INFN).

The aim of the project is to study the effect of a combined therapy of Magnetic Fluid Hyperthermia (MFH) and Hadron Therapy (HT) for the treatment of the human pancreatic cancer, a poor prognosis tumour that is particularly deadly because it is rarely detected in its early stages and it spreads rapidly. In its advanced states, a complete surgical removal is not possible and the common treatment with X-Rays (radiotherapy) is compromised by the high risk of inducing damages also to the exquisitely radiosensitive healthy tissues surrounding the pancreas.

Both MFH and HT are novel techniques that may be applied where the classical therapies fail. A combined action of the two therapies has never been studied before, and hopefully may become a new treatment for patients affected by pancreatic cancer.

In this project, the radiotherapy (RT) with X-Rays is considered as a control therapy, to compare the effects of the combined treatments MFH+HT or MFH+RT. To date, *in-vitro* experiments have been performed on BX-PC3 cancer cell line, using magnetite spherical MNPs coated with dimercaptosuccinic acid (DMSA) and with mean diameter from 14 to 19 nm for the MFH experiments. The toxicity of the MNPs have been characterized, as well as the effects of RT, HT and MFH when applied as individual therapies or combined therapies (RT+MFH and HT+MFH). Results are still being collected, however the preliminary results about the combined efficiency of MFH and HT are very promising.

As regard this thesis, author has been involved in the project for all the activities concerning MFH, from the characterization of the SAR of the ferrofluids to the MFH experiments performed *in-vitro* on cancer cells at INT and CNAO. In particular, to carry out experiments on cells the MFH setup had to be improved and the advantages of the new setup have been exploited also for the other measurements presented in this thesis.

In this Appendix, the main tests carried out and the improvements made to the MagneTherm^{TM} setup for MFH are described. Some preliminary results of the Hadromag project are also presented; for further details than those here reported, the reader is invited to refer to a future publication.

A.1 About the Hadromag project

A.1.1 Radiotherapy or Hadron therapy?

One of the most common antitumoral treatment is Radiotherapy, i.e. a therapy carried out by irradiating the tumour with X-Rays. X-Rays belong to the so-called indirectly ionizing radiations, since they transfer their energy to secondary charged particles of the medium (for example electrons) which are subsequently responsible of indirect damages to fundamental structures of the cells like the DNA. DNA can be considered as the main target of the radiations for the sake of simplicity, but it must be specified that several structures of the cells can be damaged by radiations with deadly consequences.

A parameter commonly used to distinguish among different types of radiations is the Linear Energy Transfer (LET), i. e. the energy loss $\mathrm{d}E$ of the radiation while traversing a distance $\mathrm{d}x$ in a medium (LET $= \mathrm{d}E/\mathrm{d}x$). X-Rays are defined as low LET radiation, because they are sparsely ionizing along their track in the medium, causing non-clustered damages as single strand breaks on the DNA (Fig. A.1), which could be repaired by the cells. Moreover, as shown in Fig. A.2, they release most of their energy as soon as they enter the body, and then a decreasing amount of energy as they penetrate in depth tissues. As a result, if a deep tumour has to be treated, RT requires the development of a treatment-plan employing beams with different geometries in order to minimize the energy released to the healthy tissues surrounding the tumour, that however is never negligible.

Hadron therapy (HT) is a more recent technique which employs beams of hadrons, i.e. heavy and charged particles like protons or carbon ions (^{12}C) [205]. These particles belong to the directly ionizing radiations, since they transfer their energy directly to the target (the DNA) by means of electromagnetic interactions (inelastic collisions) or nuclear reactions. Hadrons are high LET particles since they cause clustered damages to the DNA, like double strand breaks, that are difficult to repair by cells and likely to induce cell death.

Moreover, hadron beams have many qualities that are highly appreciated

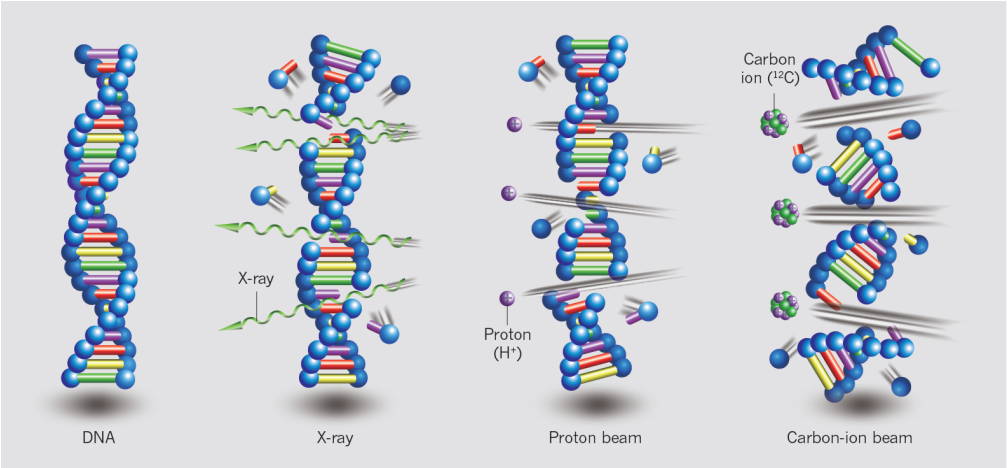

Figure A.1: Schematic representation of the damages produced by different kinds of radiations (X-Rays and Hadrons) on the DNA of cancer cells. Protons are slightly more lethal than X-rays, while carbon ions are about 3 times as damaging as X-rays [203].

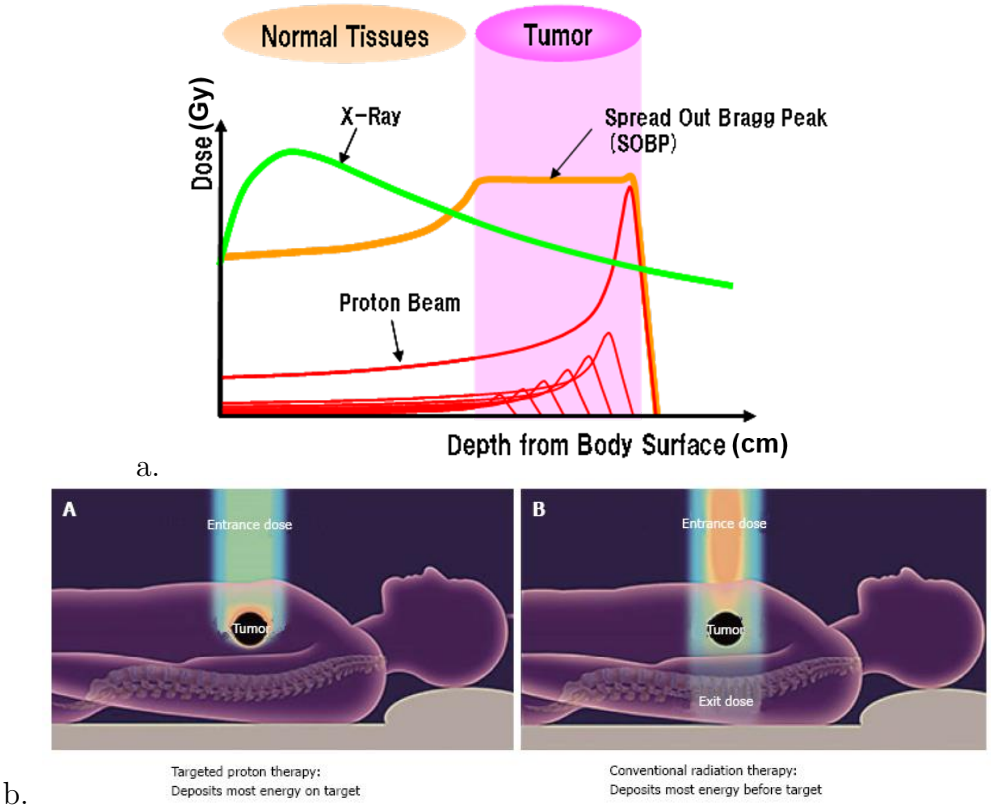

Figure A.2: (a) Dose depth profiles of X-Rays and protons (hadrons), showing the characteristic Bragg peak of hadrons and the Spread Out Bragg Peak (SOBP= for the treatment of extended lesions) [204]. (b) One of the main advantages of hadron therapy (image A) compared to radiotherapy (image B) is that the exit dose beyond the tumour is almost zeroed thanks to the Bragg peak [206] .

in the clinics: they are much more collimated beams compared to X-rays, with much narrower lateral dose profiles, and they release most of their energy just before they stop in the medium, at a depth that depends on their initial energy. The typical depth dose profile of hadrons is shown in Fig. A.2a; the maximum release of energy at high depth is called Bragg peak.

Thanks to the Bragg peak, HT allows a maximum energy deposition on the tumour compared to the surrounding healthy tissues. However, several Bragg peaks with different energies are necessary to treat all the extension of the tumour, leading to the so called Spread Out Bragg Peak (SOBP, Fig. A.2a) and a not negligible energy deposition on the tissues preceding the tumour. Individual well-defined treatment plans are therefore necessary also for irradiation with hadrons.

A last big advantage of HT compared to RT must be cited: the energy deposition beyond the tumour is almost null, apart from a little tail that can be present in the depth energy deposition profile, immediately after the Bragg peak, due to the fragmentation of carbon ions in smaller and more penetrating particles (for example, α-particles).

A.1.2 Combined treatments: rationale and methods

Literature data are available about the efficiency of the combined treatments of radiotherapy and "classical hyperthermia", i.e. hyperthermia realized by means of hot baths, ultrasounds, or other non-magnetic techniques [207–209]. However, very few data are available on the effects of combined hyperthermia and hadron therapy [210]. In this context, the Hadromag project aims to investigate these effect, focusing on hyperthermia realized by means of MNPs (MFH), and using radiotherapy as a control.

To discriminate the effects of each component of the combined treatment, three different modalities have been adopted for the experiments: irradiation alone (RT or HT); MNPs and irradiation (MNP+RT and MNP+HT); MNPs and irradiation and magnetic hyperthermia (MNP+RT+MFH and MNP+HT +MFH). The plating efficiency of the cell line (i.e. the ratio between the number of colonies with more than 50 cells counted with Giemsa staining after two weeks of incubation and the number of cells initially plated) and the mortality induced by the MNPs due to their toxicity were also evaluated as a preliminary effect.

For the experiments with combined therapies, cells were propagated for 4 weeks in order to obtain $\sim$ 2 millions of cells in flasks T25. Cells were then incubated for 48 hours with MNPs at 50 μg/mL within the culture medium; at the end of the uptake process, the medium was renewed in order to remove MNPs neither internalized by cells nor attached to the cell membrane.

Irradiation with photons (RT) or carbon ions (HT - to date experiments with hadrons have been performed only with ^{12}C ions) were carried out positioning the flask T25 in a water phantom at a depth of $\sim$12 cm from the entrance of the beam. In the case of HT, 31 beams with different energies,

ranging from 246 to 312 Mev/u (u is the unit atomic mass), were used to obtain a SOBP of about 6 cm. In the case of RT, the maximum energy of the photons was 6 MeV with a LET of about 0.3-2.5 keV/μm.

Immediately after the irradiation, cells were treated with Trypsin-EDTA to be detached from the flask, centrifuged at 1500 rpm for 10 minutes and resuspended in ∼0.15 mL of culture medium in a small PCR-Eppendorf. This step is necessary because of the size of the coil of the MagneTherm^{TM} used for the subsequent MFH treatment, which is not large enough to host a flask T25.

The obtained "pellet" of cells, i.e. ∼2 millions cells in a small Eppendorf, was then immediately placed within the MagneTherm^{TM} system, thermalized at the physiological temperature of 37°C, for the MFH treatment. The fiber optic temperature probe was placed within a twin pellet positioned near to the first one, that could not be contaminated by the probe (Fig. A.6). An alternating magnetic field at $f = 110$ kHz and $B_{max} = 20.33$ mT was applied to increase the temperature of the cells up to 42°C, that was then maintained for 30 minutes.

At the end of the MFH treatment, cells were immediately seeded at low density within flasks T25 and incubated at 37°C for 2 weeks. Then, they were fixed with ethyl alcohol and coloured with Giemsa to count the colonies (> 50 cells): a cell was indeed considered as survived only if it was able to produce a colony with more than 50 cells in two weeks (a radiobiological standard).

Finally, the plating efficiency (PE) was computed as a function of the dose (D) of radiations, and used to obtain the clonogenic survival (CS) as the ratio between the PE at a certain dose (PE(D)) and the PE of the control (PE(0)), i.e. the sample not treated neither with radiations nor with MFH, and not exposed to MNPs:

$$\mathrm{CS} = \frac{\mathrm{PE(D)}}{\mathrm{PE(0)}}. \tag{A.1}$$

In addition to the clonogenic survival essay, other methodologies are used in the Hadromag project, in particular ICP-MS and imaging techniques involving SEM (Scanning Electron Microscopy), CLSM (Confocal Laser Scanning Microscopy) and radiotracers to study the cellular uptake, the MNPs distribution within the cells, the kinetic of dissolution/release of iron ions in the biological medium and the double strand breaks repair kinetics after irradiation.

A.1.3 Preliminary results

To date, only preliminary results of the Hadromag project can be shown. In Fig. A.3 the clonogenic survival (Eq. A.1) at dose D = 0 Gy is reported for a single experiment (no statistics). Obviously, it results equal to 1 for the control.

The toxicity of the particles resulted to be $\sim 50\%$ in terms of cell survival quantified after two weeks, and $\sim 1 - 2\%$ in terms of cell viability measured after 24 hours. It is worth noting that the toxicity is commonly evaluated in

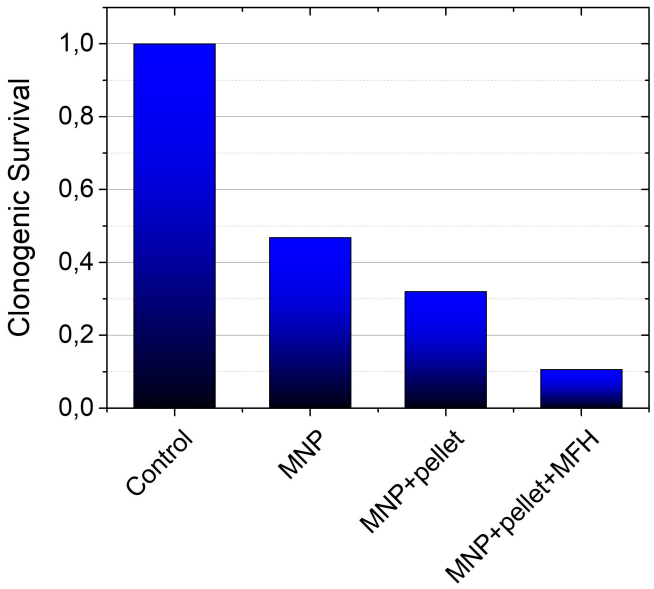

Figure A.3: Clonogenic survival measured in a single experiment at dose D = 0 Gy for a sample of BX-PC3 cells (control), treated with MNPs (MNP), pelletized (MNP+pellet) and exposed to the AMF for the hyperthermia treatment at 42°C for 30 minutes (MNP+pellet+MFH). The clonogenic survival decreases of about the 50% due to the particles toxicity, of about the 30% due to the pelletization step, and finally of about the 65% due to the MFH treatment, proving its high efficiency in causing cell death.

literature with a viability essay, and not with a cell survival essay. However, from a radiobiological point of view, the latter essay gives the most interesting information, since it refers to the cell reproductive ability and not only to the cell state alive/death.

The protocol applied for the experiments required a pelletization step that could be stressing for the cells, and indeed it results to be responsible of a partial cell death. As shown in Fig. A.3, the clonogenic survival decreases of about the 30% due to this step.

Finally, the MFH treatment decreases the clonogenic survival of about the 65%, proving a great efficiency of the heating at 42°C in causing cell death.

In Fig. A.4 the clonogenic survival results of a single experiment performed with carbon ions at CNAO with radiation dose 0 Gy $<$ D $<$ 2 Gy are reported. It is worth noting that averaging over multiple repetitions of the same experiments is necessary (currently under development) to increase the significance of these preliminary results.

Fig. A.4 shows that the clonogenic survival decreases almost linearly in logarithmic scale with increasing dose D, as expected for irradiation with hadrons, being CS(D) $\propto e^{-\alpha D}$ [211]. Moreover, as already discussed for Fig. A.3, the clonogenic survival decreases when combined therapies are performed, being the CS lower for cells treated with MNPs and irradiated with carbon ions compared to cells exposed only to radiation, probably due to the MNPs toxicity, and being the CS even lower when also one MFH treatment (30 minutes

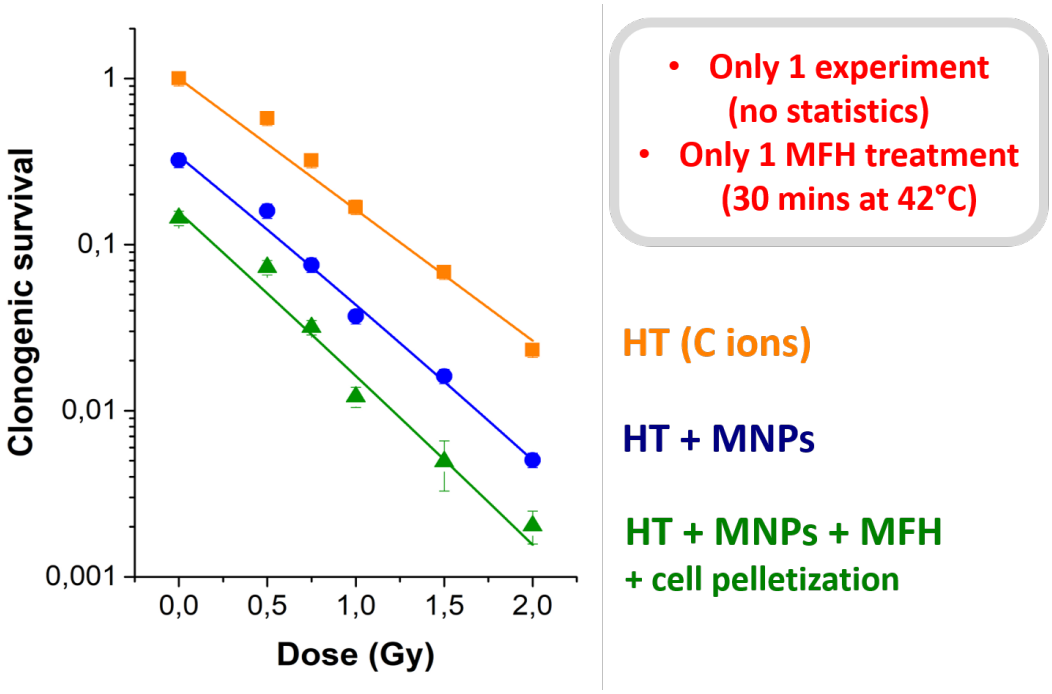

Figure A.4: Clonogenic survival results of a single experiment on BX-PC3 cells performed at CNAO using carbon ions at dose 0 Gy $<$ D $<$ 2 Gy. The experiment was carried out in three different modalities to discriminate the effects of combined therapies: irradiation alone (HT, yellow points); MNPs and irradiation (MNP+HT, blue points); MNPs and irradiation and magnetic hyperthermia (MNP+HT+MFH, green points). Continuous lines represent the best fitting of the clonogenic survival (CS) as a function of the radiation dose (D) according to the law CS(D) $\propto e^{-\alpha D}$ [211]. The green line includes also the effects of the pelletization step required for the hyperthermia treatment at 42°C for 30 minutes with the MagneTherm^{TM} setup. Both a toxicity effect of MNPs and a great combined efficiency of a single MFH experiment (to be quantified by removing the pelletization effect) combined to HT with carbon ions are evidenced.

at 42°) is carried out. However, with regard to the green curve in Fig. A.4, it must be noted that at this stage of the project it includes also the effect of the pelletization step required for the MFH treatment in the MagneTherm^{TM} setup, which is not negligible as shown in Fig. A.3. New experiments are being carried out to better discriminate this effect, also as a function of the radiation dose D. As a result, it is not possible to date to quantify with an exact percentage the efficiency of the combined treatment MNP+HT+MFH, although a great efficiency seems to be predicted by Fig. A.4.

A.2 Optimization of the experimental setup

One of the main activities carried out by the author of this thesis in the frame of the Hadromag project regarded the implementation of the setup for the MFH experiments.

The apparatus used for MFH is the MagneTherm^{TM} setup by NanoTherics,

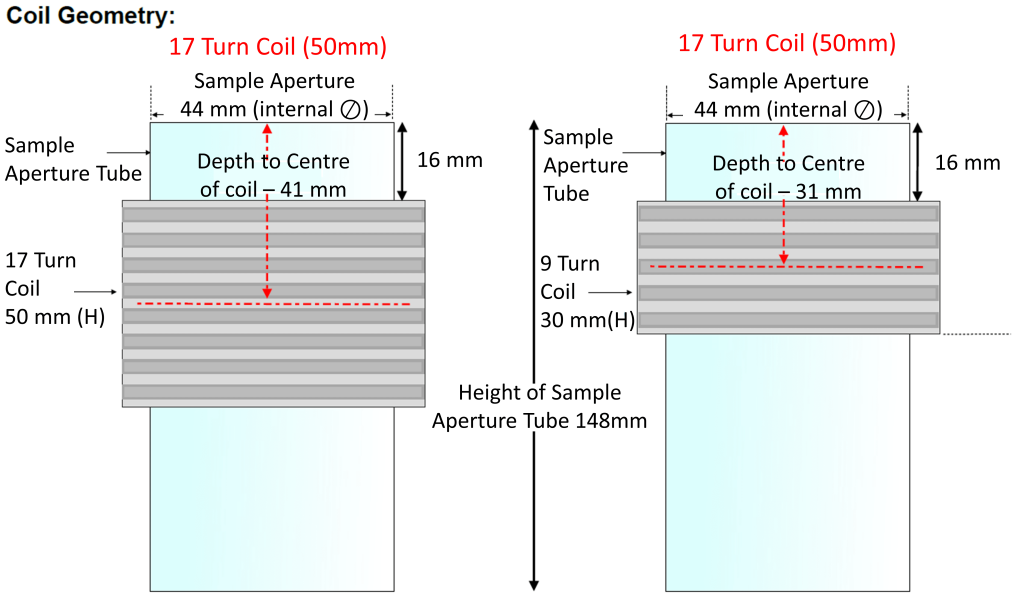

Figure A.5: Illustration of the NanoTherics MagneTherm^{TM} setup for Magnetic Fluid Hyperthermia experiments, with a schematization of the geometry of the two available coils with 17 and 9 turns.

presented Fig. A.5 and already described in Chapter 3. It is equipped with two possible coils, with 9 and 17 turns, and 5 capacitors that allow 10 different combinations for the RLC circuit and, consequently, for the frequencies of the AMF, from about 110 kHz to 990 kHz. The maximum amplitude of the AMF decreases with increasing frequencies due to power limitations of the system, and it is $B_{max} = 20.33$ mT at the lowest frequency.

The homogeneity of the field within the coil has been studied my mapping the maximum amplitude of the field as a function of the radial and vertical positions, using an axial Hall probe. It was found that the region of homogeneity is limited to a cylindrical region of space in the middle of the coil, with $r \simeq 8.5$ mm and $h \simeq 1$ cm in the case of the 17 turns coil, and $r \simeq 8$ mm and $h \simeq 5$ mm in the case of the 9 turns coil.

For the Hadromag project, MFH experiments were carried out using the 17 turns coil ($f = 109.8$ kHz), and the region of homogeneity of the field in

the middle of the coil resulted to be enough to host up to three small PCR-Eppendorf to be treated in parallel.

The development of the MFH setup for the project required the addition of a thermalization system to keep the initial temperature of the cell samples at the physiological value of 37°C. To this aim, a home-made thermalization system was implemented using a Alpha Lauda A thermostat, circulating hot water around the polystyrene sample holder placed in the middle of the coil, as in Fig. A.6. The polystyrene sample holder was useful for centering the sample in the homogenity region of the field and for keeping the samples as much isolated as possible from the external environment, in order to minimize the heat dissipation. Of course, the system is far from being adiabatic, but the losses were limited allowing to reach the 42°C required for the treatment, even when working with very small amount of sample (a minor volume is more susceptible to dissipation effects).

The MagneTherm^{TM} setup is thought to work with sample volumes of about 1 mL, as in the setup A showed in Fig. A.6. However, the Hadromag project required to work in different conditions. First, the "pellet" of cells produced after centrifugation had to be resuspended in no more than 0.1-0.2 mL of culture medium, in order to obtain a concentration of MNPs within the sample high enough to determine a temperature increment of 5°C , from 37°C to 42°C. Then, it was not possible to measure directly the temperature of the sample with the Optocon^{TM} fiber optic probe, since it would have determined a contamination of the sample and an alteration of the clonogenic survival assay. Consequently, a twin sample, prepared with exactly the same procedure, had to be placed near to the first one as in Setup B of Fig. A.6, to monitor the temperature of both samples measuring only the one marked for disposal.

To satisfy the conditions required by the project, the main problem to be solved regarded the limited space available within the coil of the MagneTherm^{TM}, and in particular the small size of the field homogeneity region. The best solution was found by using small PCR-Eppendorf tubes, with maximum volume 0.2 mL, that could be placed into the MagneTherm^{TM} in number up to three. This solution allowed to perform MFH treatments in parallel on two uncontaminated samples, while measuring the temperature of a third one.

However, a characterization of the new MFH system (setup B in Fig. A.6) was mandatory, since, as previously stated, the MagneTherm^{TM} system is thought to work on 1 mL of sample, and the dissipation effects could be much higher when working with only ∼0.2 mL of sample. To investigate this effect, several measurements were performed with both the setups A and B of Fig. A.6, at the AMF used for the Hadromag project (f = 109.9 kHz and H_{max} = 16.1 kA/m), on the 14 nm sample described in Chapter 4 (magnetite MNPs coated with DMSA). MNPs used for the Hadromag project, indeed, were the same (d = 14 nm) described in Chapter 4. Moreover, measurements were performed starting from different initial temperatures (exploiting the just implemented thermalization system) to evaluate (i) the SAR and (ii) the dis-

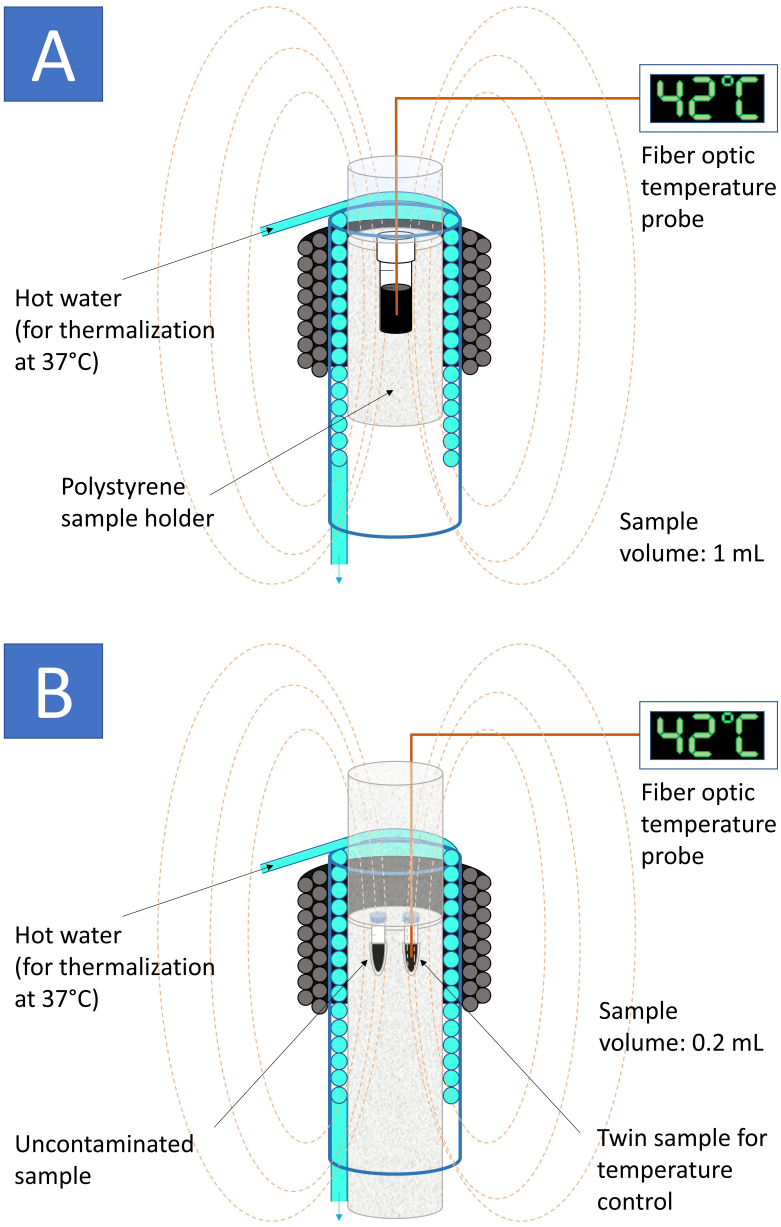

Figure A.6: Schematic representation of the two possible setups for MFH measurements. Setup (A) is just an implementation of the standard setup of the MagneTherm^{TM} with the addition of a thermalization home-made system, which circulate hot water around the sample to fix its initial temperature (for example at 37°C when working with cells). Setup (B) has been implemented for the Hadromag project, which necessitates to perform MFH experiments starting from 37°C on two twin samples of cells and MNPs, one uncontaminated for the further clonogenic survival essay, and one contaminated with a fiber optic probe for the measurement of the temperature.

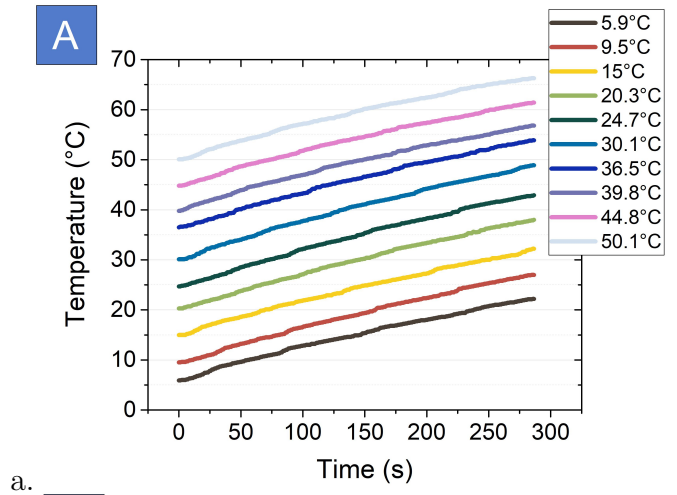

a.

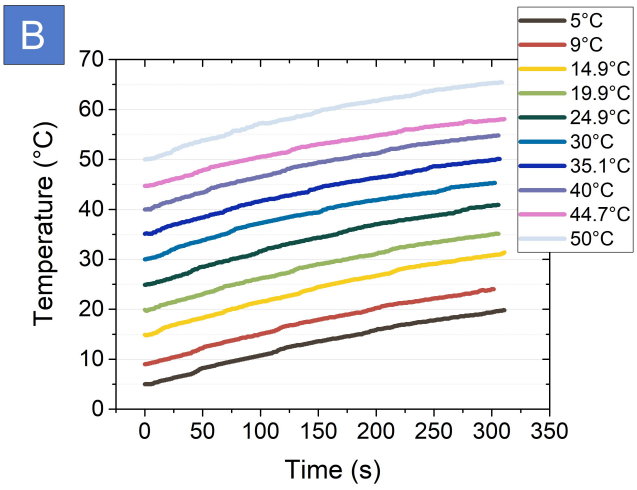

b.

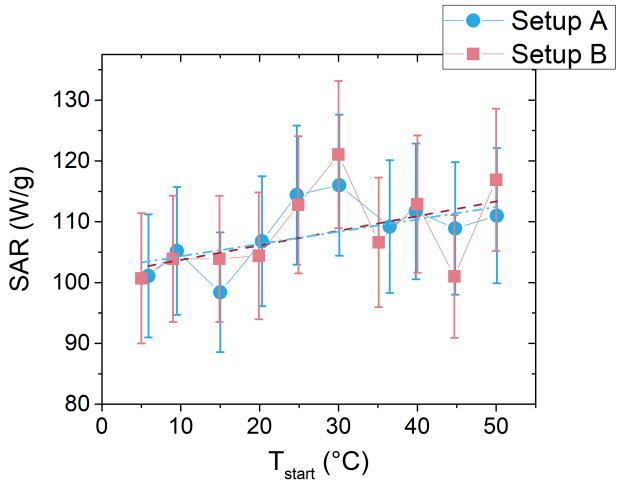

b.

Figure A.7: Temperature vs Time curves acquired during MFH measurements carried out with the setups A (a) and B (b) described in Fig. A.6 on a sample of 14 nm magnetite nanoparticles at 3 mg/mL (in water) under the action of a magnetic field with $f = 109.8$ kHz and $H = 16.1$ kA/m, starting from different initial temperatures in the range 5°C $\leq T \leq$ 50°C. (c) Starting from these measurements, the SAR of the sample was computed and the effect of the initial temperature on the SAR was investigated. An almost constant behaviour of SAR(T_{start}) was found, with a slight increase of 0.25 (W/g)/°C that is not significant considering the error bars on the SAR values.

sipation effects as a function of the initial temperature, in both the setups.

Results are shown in Fig. A.7a-b, where $T(t)$ curves were collected starting from different initial temperatures, from 5°C to 50°C, at steps of about 5°C. The slopes of the curves were then used to compute the SAR with the initial-slope method, according to the procedure described in Chapter 4.

Interestingly, the slope of the curves does not change appreciably while changing the initial temperature. A linear fit performed on the SAR(T_{start}) curves in Fig. A.7c suggests a slight increase of the SAR with the initial temperature, at a rate of only 0.25 (W/g)/°C. However, this trend is not significant, since the variations of the SAR are always largely included within the error bars (10% of the SAR) at all the temperatures. As a consequence, a constant behaviour is also compatible with the SAR(T_{start}) curves, and this allows to measure the SAR of the particles at room temperature even if aimed to be applied for treatments at the physiological temperature. Moreover, this result confirms the capability of Setup B to provide an outcome of the measurement that is perfectly compatible with that of the standard Setup A.

The possibility to work with a very small amount of ferrofluids for their hyperthermic characterization was a big advantage that has been exploited also for measurements of the SAR outside the Hadromag project, as those reported in Chapter 4 of this thesis.

Publications

- **M. Avolio**, H. Gavilán, E. Mazario, F. Brero, P. Arosio, A. Lascialfari & M. Puerto Morales, Elongated magnetic nanoparticles with high-aspect ratio: a nuclear relaxation and specific absorption rate investigation, *Physical Chemistry Chemical Physics*, 21, 18741-18752 (2019).

- **M. Avolio**, C. Innocenti, A. Lascialfari, M. Mariani & C. Sangregorio, Medical Applications of Magnetic Nanoparticles, in *Nanoparticle Magnetism: from Fundamentals to Emerging Applications*, Springer (2019), *submitted*.

- P. Arosio, **M. Avolio**, M. Gargano, F. Orsini, S. Gallo, J. Melada, L. Bonizzoni, N. Ludwig & I. Veronese, Magnetic stimulation of gold fiducial markers used in Image-Guided Radiation Therapy: evidences of hyperthermia effects, *Measurement*, 107242 (2019).

- **M. Avolio**, A. Guerrini, F. Brero, C. Innocenti, C. Sangregorio, M. Cobianchi, M. Mariani, F. Orsini, P. Arosio & A. Lascialfari, In-gel study of the effect of magnetic nanoparticles immobilization on their heating efficiency for application in Magnetic Fluid Hyperthermia, *Journal of Magnetism and Magnetic Materials*, 471, 504-512 (2019).

- M. Basini, A. Guerrini, M. Cobianchi, F. Orsini, D. Bettega, **M. Avolio**, C. Innocenti, C. Sangregorio, A. Lascialfari & P. Arosio, Tailoring the magnetic core of organic-coated iron oxides nanoparticles to influence their contrast efficiency for Magnetic Resonance Imaging, *Journal of Alloys and Compounds*, 770, 58-66 (2018).

- M. Cobianchi, A. Guerrini, **M. Avolio**, C. Innocenti, M. Corti, P. Arosio, F. Orsini, C. Sangregorio & A. Lascialfari, Experimental determination of the frequency and field dependence of Specific Loss Power in Magnetic Fluid Hyperthermia, *Journal of Magnetism and Magnetic Materials*, 444, 154-160 (2017)

- F. Bonutti, **M. Avolio**, G. Magro, A. Cecotti, E. Della Schiava, E. Del Do, F. Longo, M.Y. Herassi, F. Bentayeb, M. Rossi, G. Ferretti, O. Geatti and R. Padovani, Optimization of the image contrast in SPECT-CT bremsstrahlung imaging for Selective Internal Radiation Therapy of liver malignancies with Y-90 microspheres, *arXiv preprint* arXiv:1509.08857.

PCCP

PAPER

Cite this: *Phys. Chem. Chem. Phys.*, 2019, **21**, 18741

Elongated magnetic nanoparticles with high-aspect ratio: a nuclear relaxation and specific absorption rate investigation†

Matteo Avolio,*[a] Helena Gavilán,[b] Eva Mazario,[b] Francesca Brero,[a] Paolo Arosio,[c] Alessandro Lascialfari[c] and M. Puerto Morales[b]

Received 18th June 2019,
Accepted 2nd August 2019

DOI: 10.1039/c9cp03441b

rsc.li/pccp

Medical application of nanotechnology implies the development of nanomaterials capable of being functional in different biological environments. In this sense, elongated nanoparticles (e-MNPs) with high-aspect ratio have demonstrated more effective particle cellular internalization, which is favoured by the increased surface area. This paper makes use of an environmentally friendly hydrothermal method to produce magnetic iron oxide e-MNPs, starting from goethite precursors. At high temperatures (T_d) goethite transforms into hematite, which subsequently reduces to magnetite when exposed to a hydrogen atmosphere for a certain time. It is shown that by adjusting T_d it is possible to obtain Fe_3O_4 e-MNPs with partially controlled specific surface area and magnetic properties, attributed to different porosity of the samples. The particles' efficiencies for diagnostic and therapeutic purposes (in magnetic resonance imaging and magnetic fluid hyperthermia, respectively) are very good in terms of clinical standards, some samples showing transversal proton nuclear relaxivity r_2 (B_0 = 1.33 T) = 340 s^{-1} mM^{-1} and specific absorption rate SAR > 370 W g^{-1} at high field amplitudes (B_0 = 55 mT). Direct correlations between the SAR, relaxivity, magnetic properties and porosity of the samples are found, and the physico-chemical processes underneath these correlations are investigated. Our results open the possibility of using very efficient high-aspect ratio elongated nanoparticles with optimized chemico-physical properties for biomedical applications.

Introduction

Magnetic nanoparticles (MNPs) are being used for several biomedical applications already in clinics and are promising tools to strongly improve diagnostics and cancer therapy in the coming years.[1–4] In particular, MNPs can be utilized as contrast agents in Magnetic Resonance Imaging (MRI), allowing one to obtain higher image contrast and more generally clearer diagnostic information.[5,6] These systems shorten the nuclear relaxation times of the ^{1}H nuclei in the region where they accumulate, thus allowing better tissue contrast. For cancer therapy, instead, MNPs are already used for the treatment of glioblastoma multiforme (see *e.g.* results reported on www.Magforce.com). Such treatment is being developed and extended to prostate cancer, and to some other poor-prognosis tumours,[7] becoming known as Magnetic Fluid Hyperthermia (MFH). MFH is based on the use of MNPs, which are first injected into the tumour and then exposed to an alternating magnetic field (AMF), which allows local heat release that weakens or kills the tumour cells.

The AMF amplitude H and frequency f suitable for application to patients must satisfy the Brezovich criterion, $H{\cdot}f < 4.85 \times 10^8$ A m^{-1} s^{-1}, to avoid any side effects.[8] During the exposure to the AMF, MNPs transfer thermal energy from the field to the tumour due to strong interactions between their magnetic moments and the field.[9–11]

The most widely used MNPs are composed of a magnetic core of iron oxides, typically magnetite (Fe_3O_4) or maghemite (γ-Fe_2O_3), which are preferred due to their high magnetization coming from a ferrimagnetic structure, and their high biocompatibility.[12] Recently, other ferrites that include cobalt, manganese or nickel in their composition were studied for similar applications,[13–15] as such elements provide advantageous magnetic features;[16] however their cytotoxicity is still unclear.[17]

Magnetic cores used in biomedical applications are typically covered by organic moieties, like *e.g.* sugars or polymers, in order to guarantee biocompatibility, to prevent MNPs from aggregation,

[a] *Dipartimento di Fisica, INFN and INSTM, Università degli Studi di Pavia, Via Bassi 6, 27100 Pavia, Italy. E-mail: matteo.avolio01@universitadipavia.it*
[b] *Departamento de Energía, Mediambiente y Salud, Instituto de Ciencia de Materiales de Madrid, ICMM/CSIC, Cantoblanco, 28049 Madrid, Spain*
[c] *Dipartimento di Fisica, INFN and INSTM, Università degli Studi di Milano, Via Celoria 16, 20133 Milano, Italy*

† Electronic supplementary information (ESI) available: Additional information about the synthesis, XRD patterns and crystal size analysis, IR absorption spectra and DLS data, and partially reduced samples with mixed compositions of hematite–magnetite. See DOI: 10.1039/c9cp03441b

Journal of Magnetism and Magnetic Materials 471 (2019) 504–512

Contents lists available at ScienceDirect

Journal of Magnetism and Magnetic Materials

journal homepage: www.elsevier.com/locate/jmmm

Research articles

In-gel study of the effect of magnetic nanoparticles immobilization on their heating efficiency for application in Magnetic Fluid Hyperthermia

Matteo Avolio[a,*], Andrea Guerrini[b], Francesca Brero[a], Claudia Innocenti[b], Claudio Sangregorio[b,c], Marco Cobianchi[a], Manuel Mariani[a], Francesco Orsini[d], Paolo Arosio[d], Alessandro Lascialfari[d]

[a] Dipartimento di Fisica, INFN and INSTM, Università degli Studi di Pavia, Via Bassi 6, 27100 Pavia, Italy
[b] Dipartimento di Chimica and INSTM, Università degli studi di Firenze, Via della Lastruccia 6, Sesto F.no (FI), Italy
[c] ICCOM-CNR, Via della Lastruccia 6, Sesto F.no(FI), Italy
[d] Dipartimento di Fisica, INFN and INSTM, Università degli Studi di Milano, Via Celoria 16, 20133 Milano, Italy

ARTICLE INFO

Keywords:
Magnetic Fluid Hyperthermia
Magnetic nanoparticles
Superparamagnetism
Specific Absorption Rate
Relaxation times
Brownian motion

ABSTRACT

Recent studies on magnetic nanoparticles (MNPs) used for Magnetic Fluid Hyperthermia treatments have shown that Brownian rotation is suppressed when they are confined within a cell. To investigate this effect we conducted a systematic study of the Specific Absorption Rate (*SAR*) of colloidal suspensions of MNPs in water and gels at different agarose concentration. *SAR* measurements were conducted by varying the frequency (f = 110–990 kHz) and amplitude (up to 17 kA/m) of the applied alternating magnetic field (AMF). MNP samples with different diameter (d = 10, 14, and 18 nm) were used. Our results show that Néel relaxation dominates *SAR* with negligible contribution from Brownian motion for smaller MNPs (d = 10 nm). For the largest MNPs (d = 18 nm) we observed a more significant *SAR* decrease in gel suspensions as compared to those in solution. In particular, when applying AMFs as the ones used in a clinical setting (16.2 kA/m at f = 110 kHz), we measured *SAR* value of 67 W/g in solution and 25 W/g in gel. This experimental finding demonstrates that investigation of MNPs properties should be conducted in media with viscosity similar to the one found in mammalian tissues.

1. Introduction

Hyperthermia is an antitumoral therapy consisting in a temperature rise up to 43 °C, with the aim of damaging cancer cells by denaturating their basic molecular structures, such as DNA or enzymes [1,2]. This aim is achieved for instance by the so-called Magnetic Fluid Hyperthermia (MFH), that employs magnetic nanoparticles (MNPs), with the advantage of producing the temperature rise only within the neoplastic region where they are located. In this technique, colloidal solutions of biocompatible MNPs dispersed in physiological liquids and injected e.g., directly inside the tumour, release heat once exposed to an alternating magnetic field (AMF) operating at safe values of frequency and amplitude [3,4].

In most cases, for in vivo applications, MNPs consist of a magnetic core made of iron oxides, known to have a low toxicity [3,5], coated by organic biocompatible moieties. The core size is generally so small (the equivalent diameter typically is less than 20 nm) that the MNPs result to be superparamagnetic [1,6,7]. In the superparamagnetic regime the MNPs magnetization, also called superspin, can fluctuate between the two opposite directions of the easy axis determined by the magnetic anisotropy, with a characteristic relaxation time, τ_N. According to the Néel model for non-interacting particles τ_N depends on the core volume of the particles (V), the anisotropy constant (K_a) and the temperature of the system (T), and its expression is given by the Arrhenius law:

$$\tau_N = \tau_0 e^{K_a V/(k_B T)} \quad (1)$$

In Eq. (1) τ_0 is generally assumed of the order of 10^{-9} s [8,9] and k_B is the Boltzmann constant.

In a solvent the superspin orientation can change also through the physical process of rotation of the entire particle, which occurs in a characteristic time called Brown relaxation time τ_B [10] expressed by:

$$\tau_B = \frac{3\eta V_h}{k_B T} \quad (2)$$

where V_h is the hydrodynamic volume of the particles and η is the local viscosity of the medium. Thus, an effective relaxation time τ that accounts for both Néel and Brown mechanisms can be defined as:

* Corresponding author.
E-mail address: matteo.avolio01@universitadipavia.it (M. Avolio).

https://doi.org/10.1016/j.jmmm.2018.09.111
Received 22 June 2018; Received in revised form 21 September 2018; Accepted 28 September 2018
Available online 29 September 2018
0304-8853/

Measurement 151 (2020) 107242

Contents lists available at ScienceDirect

Measurement

journal homepage: www.elsevier.com/locate/measurement

Magnetic stimulation of gold fiducial markers used in Image-Guided Radiation Therapy: Evidences of hyperthermia effects

Paolo Arosio [a,b,c], Matteo Avolio [c,d,e], Marco Gargano [a], Francesco Orsini [a,b,c], Salvatore Gallo [a,b], Jacopo Melada [a], Letizia Bonizzoni [a], Nicola Ludwig [a,*], Ivan Veronese [a,b,c]

[a] Dipartimento di Fisica, Università degli Studi di Milano, Via Celoria 16, 20133 Milano, Italy
[b] Istituto Nazionale di Fisica Nucleare, Sezione di Milano, Via Celoria 16, 20133 Milano, Italy
[c] Consorzio Interuniversitario Nazionale per la Scienza e Tecnologia dei Materiali, Italy
[d] Dipartimento di Fisica, Università degli Studi di Pavia, Via Bassi 6, 27100 Pavia, Italy
[e] Istituto Nazionale di Fisica Nucleare, Sezione di Pavia, Via Bassi 6, 27100 Pavia, Italy

ARTICLE INFO

Article history:
Received 18 February 2019
Received in revised form 24 September 2019
Accepted 3 November 2019
Available online 6 November 2019

Keywords:
Gold fiducial markers
Magnetic Fluid Hyperthermia
IGRT
Thermography
Hydrogel
Eddy currents

ABSTRACT

A promising approach in oncology consists in combining Radiation Therapy (RT) with Magnetic Fluid Hyperthermia (MFH). Modern day RT takes advantage by imaging techniques able to provide information about the correct patient set-up, target position and movement during the treatments. For these purposes, gold fiducial markers, implanted into the tumors, or in their proximity, are used in the so-called Image-Guided Radiation Therapy (IGRT).

In this study, hyperthermia produced by different gold fiducial markers under the application of an alternating magnetic field in the typical conditions used in Magnetic Fluid Hyperthermia (MFH) clinical trials was investigated. The temperature increase of different types of gold fiducial markers and of tissue mimicking hydrogel phantoms containing the fiducials were measured during the magnetic stimulation by means of a high-resolution thermal camera and a fiber optic temperature sensor.

The results demonstrated that, within few tens of seconds after the start of the magnetic stimulation, the gold fiducial markers might reach temperatures higher than 70 °C. Local increases of the hydrogel temperature to values higher than 45 °C were also measured. These evidences highlight the need to evaluate carefully the presence and location of gold fiducial markers in patients undergoing combined IGRT and MFH treatments in order to prevent any thermal ablation of health tissues surrounding the markers.

1. Introduction

Current treatment strategies for several oncological pathologies are based on the synergic combination of different techniques. Radiation therapy (RT) is one of the most widely used approach. Indeed, more than 14 million new cancer patients are diagnosed globally each year and approximately half of them can benefit from RT treatment at least once during the course of their disease [1].

Modern RT increasingly uses conformal delivery techniques, which require an accurate patient positioning and tumor targeting. This aspect is even more important in the case of irradiation of moving organs, e.g. organs influenced by breathing. The most used imaging techniques in the so-called Image Guided Radiation Therapy (IGRT) are those based on X-rays [2].

In such case, millimetric or sub-millimetric radiopaque metallic fiducial markers can be implanted into the lesions, or in their close proximity. These markers are easily visible by X-ray imaging and allow target localization and patient set up verification [3,4]. Gold markers are more commonly used, as they provide high levels of image contrast. It is worth noting that fiducial markers based on nanostructured gold particles are also being developed to be used in various diagnostic and therapeutic procedures requiring image-guided approaches [5–7].

Meanwhile, Magnetic Fluid Hyperthermia (MFH) in combination with RT is recently gaining importance in oncology [8]. In MFH technique, magnetic nanomaterials (normally iron oxides nanoparticles) directly implanted in the tumour mass at high doses (approximately 50 mg/cm^3), under the action of an externally applied alternating magnetic field (AMF), can generate a certain amount of local heat depending on the frequency f and the amplitude H of field. The success of MFH was recently demonstrated on glioblastoma multiform and prostate cancers in clinical trials, that

* Corresponding author at: Università degli Studi di Milano, via Giovanni Celoria 16 - 20133 Milano, Italy.
E-mail address: nicola.ludwig@unimi.it (N. Ludwig).

https://doi.org/10.1016/j.measurement.2019.107242
0263-2241/

Journal of Alloys and Compounds 770 (2019) 58–66

Contents lists available at ScienceDirect

Journal of Alloys and Compounds

journal homepage: http://www.elsevier.com/locate/jalcom

Review

Tailoring the magnetic core of organic-coated iron oxides nanoparticles to influence their contrast efficiency for Magnetic Resonance Imaging

M. Basini [a], A. Guerrini [b], M. Cobianchi [c], F. Orsini [a], D. Bettega [a], M. Avolio [c], C. Innocenti [b], C. Sangregorio [d, b], A. Lascialfari [a], P. Arosio [a, *]

[a] Dipartimento di Fisica and INSTM, Università degli Studi di Milano, Via Celoria 16, 20133, Milano, Italy
[b] INSTM and Department of Chemistry "U. Schiff", Università di Firenze, Via della Lastruccia 3-13, Sesto Fiorentino, I-50019, Firenze, Italy
[c] Dipartimento di Fisica and INSTM, Università degli Studi di Pavia, Via Bassi 6, 27100, Pavia, Italy
[d] C.N.R. – I.C.C.O.M., Via Madonna del Piano 10, I-50019, Sesto Fiorentino, Italy

ARTICLE INFO

Article history:
Received 8 May 2018
Received in revised form
31 July 2018
Accepted 14 August 2018
Available online 16 August 2018

Keywords:
Magnetic nanoparticles
Nanomagnetism
Nuclear magnetic resonance
Magnetic resonance imaging

ABSTRACT

An experimental ^{1}H NMR relaxometry investigation on iron oxide nanoparticles with different magnetic core size and coated with PolyAcrylic Acid (PAA), is presented. A full structural, morphodimensional and magnetic characterization of the nanoparticles has been performed by means of X-ray diffraction, Dynamic Light Scattering, Transmission Electron Microscopy, Atomic Force Microscopy and SQUID DC magnetometry. The application of a heuristic model for the field dependence of the NMR relaxivity curves allowed us to evaluate the distance of minimum approach of the solvent molecules from the magnetic centers, and to conclude that the local correlation times, namely the Neél time τ_N and the diffusion time τ_D related to the magnetization reversal and to the diffusion process respectively, depend strongly on the core size. A preliminary evaluation of their r_2 efficiency as Magnetic Resonance Imaging (MRI) contrast agents is also performed by means of a universal scaling law model. The results of our experimental investigation should allow to tailor the physical properties of the nanoparticles for obtaining systems with a resultant contrast efficiency optimized for the in-vivo application of MRI at pre-clinical and clinical level.

Contents

* Corresponding author.
E-mail address: paolo.arosio@unimi.it (P. Arosio).

https://doi.org/10.1016/j.jallcom.2018.08.120
0925-8388/

Journal of Magnetism and Magnetic Materials 444 (2017) 154–160

Contents lists available at ScienceDirect

Journal of Magnetism and Magnetic Materials

journal homepage: www.elsevier.com/locate/jmmm

Research articles

Experimental determination of the frequency and field dependence of Specific Loss Power in Magnetic Fluid Hyperthermia

M. Cobianchi [a,*], A. Guerrini [b], M. Avolio [a], C. Innocenti [b], M. Corti [a], P. Arosio [d], F. Orsini [d], C. Sangregorio [c], A. Lascialfari [d,a]

[a] Dipartimento di Fisica and INSTM, Università degli Studi di Pavia, Via Bassi 6, 27100 Pavia, Italy
[b] Dipartimento di Chimica, Università degli studi di Firenze, Via della Lastruccia 3, Sesto F.no (FI), Italy
[c] CNR-ICCOM, Via della Lastruccia 3, Sesto F.no (FI), Italy
[d] Dipartimento di Fisica and INSTM, Università degli Studi di Milano, Via Celoria 16, 20133 Milano, Italy

ARTICLE INFO

Article history:
Received 4 July 2017
Received in revised form 31 July 2017
Accepted 4 August 2017
Available online 4 August 2017

Keywords:
Magnetic Fluid Hyperthermia
Magnetic nanoparticles
Superparamagnetism
Specific Loss Power

ABSTRACT

Magnetic nanoparticles are promising systems for biomedical applications and in particular for Magnetic Fluid Hyperthermia, a therapy that utilizes the heat released by such systems to damage tumor cells. We present an experimental study of the physical properties that influences the capability of heat release, i.e. the Specific Loss Power, *SLP*, of three biocompatible ferrofluid samples having a magnetic core of maghemite with different diameter d = 10.2, 14.6 and 19.7 nm. The *SLP* was measured as a function of frequency f and intensity H of the applied alternating magnetic field, and it turned out to depend on the core diameter, as expected. The results allowed us to highlight experimentally that the physical mechanism responsible for the heating is size-dependent and to establish, at applied constant frequency, the phenomenological functional relationship $SLP = c \cdot H^{x}$, with $2 \leq x < 3$ for all samples. The x-value depends on sample size and field frequency, here chosen in the typical range of operating magnetic hyperthermia devices. For the smallest sample, the effective relaxation time $\tau_{eff} \approx 19.5$ ns obtained from *SLP* data is in agreement with the value estimated from magnetization data, thus confirming the validity of the Linear Response Theory model for this system at properly chosen field intensity and frequency.

1. Introduction

Magnetic nanoparticles are promising tools in biomedical applications against cancer, and suitable systems for diagnostics by e.g. Magnetic Resonance Imaging and innovative therapies, like drug delivery and Magnetic Fluid Hyperthermia (MFH) [1–11]. The MFH is a recently developed anti-cancer locally acting technique which aims to reduce the side effects of the traditional techniques as chemo- or radio-therapies [12]. This technique makes use of the capability of magnetic nanoparticles (MNPs) to release heat when exposed to an alternating magnetic field (AMF), as a therapeutic treatment to selectively destroy tumor cells within the human body. In MFH treatments, the AMF application is strictly limited to a safety range of frequency f and intensity H due to medical and technical restrictions, as established by the Brezovich criterion which requires $H \cdot f < 4.85 \cdot 10^{8}$ Am^{-1} s^{-1} [13]. The amount of magnetic field energy converted into heat (and subsequently absorbed by tissues) is given by the energy losses occurring during the MNP magnetization reversal, according to the dynamic regime determined by the MNPs physico-chemical properties (size, shape, kind of magnetic core, etc.) as well as by the external field and temperature [14–18]. Magnetization reversal can be produced by a rigid rotation of the particles (Brown process) or by a coherent reorientation of the electronic spins inside the particles (Néel process) [19–22]. The characteristic times τ_B and τ_N for Brown and Néel processes, respectively are $\tau_B = 3\eta V_H / k_B T$, where η is the viscosity of the environmental fluid, V_H the hydrodynamic volume of the particle, k_B the Boltzmann constant and T the temperature of the system, and $\tau_N = \tau_0 exp(KV/K_B T)$, where K is the uniaxial magnetic anisotropy constant of the crystalline core, V the volume of the magnetic core and τ_0 the attempt time typically assumed to be 10^{-9} s [3,23,24]. It is noticed that, when a large ac and/or DC magnetic field is applied and the condition $\zeta = (mB/k_B T) \ll 1$ is no more verified, the expressions of τ_B and τ_N assume different analytical forms [25,26].

The parameter that describes the MNPs capacity to release heat to the surrounding environment when exposed to an AMF is the Specific Loss Power (*SLP*). In Fig. 1 the most common empirical models used to evaluate the *SLP* are reported in their intervals of

* Corresponding author.
E-mail address: marco.cobianchi01@universitadipavia.it (M. Cobianchi).

http://dx.doi.org/10.1016/j.jmmm.2017.08.014
0304-8853/

Acknowledgements

I want to acknowledge the University of Pavia for granting my PhD and the related research activity, even included the grant I received for a the three-months mobility period at the ICMM in Madrid, where I had the possibility to synthesise some of the samples presented in this thesis.

A special thank to Prof. Maria Francesca Casula (Università degli Studi di Cagliari) and Prof. Florence Gazeau (Université Paris Diderot) who kindly accepted to review this thesis, giving precious advices for improving its quality.

I want to thank also the COST actions TD1402, *RADIOMAG*, and CA15209, *EURELAX*, for granting me the participation to several international conferences and training schools, and a two-months *Short Term Scientific Mission* (STSM) in Toulouse for a training on kinetic Monte-Carlo simulations.

After institutional acknowledgements, I want to thank all the people who followed my work and collaborated with me during the three years of my PhD.

First, a special thanks to my advisor Alessandro Lascialfari for his constant help, availability and precious suggestions, and similarly to my advisors Manuel Mariani and Maurizio Corti.

A very big thank to Paolo Arosio and Francesco Orsini, for their experimental and human support, and to my colleagues Marco Cobianchi, Martina Basini and Francesca Brero, with which I shared the best moments in the lab.

A special thank to Maria del Puerto Morales, for her availability in hosting me for three months at the ICMM in Madrid, and to all the people who patiently helped me in her laboratory, in particular Helena Gavilán and Eva Mazario. Similarly, a big thank to Julian Carrey, who kindly accepted to give me a training on how to perform Monte Carlo simulations in a two months stay at INSA Toulose.

I want to thank also all the people involved in the *Hadromag* project, and in particular Paola Calzolari, Daniela Bettega and Ivan Veronese in Milan and Claudio Sangregorio, Claudia Innocenti and Andrea Guerrini in Florence.

Finally, I cannot omit to thank my family: Mamma, Papà, Elisa, and Daniele. Although they are not familiar with physics, their contribution can be found in each page of this thesis. Grazie per esserci e per condividere con me i miei successi come se fossero vostri. In fondo, lo sono davvero.

Bibliography

[1] Blundell S., Magnetism in Condensed Matter, OXFORD University Press, 2003.

[2] Kittel, C., McEuen, P., & McEuen, P., Introduction to Solid State Physics, Eight Edition, New York: Wiley, 1976.

[3] Varadan, V. K., Chen, L., & Xie, J., Nanomedicine. Design and Applications of Magnetic Nanomaterials, Nanosensors and Nanosystems, John Wiley & Sons.

[4] Burrows, F., A Model of Magnetic Hyperthermia, The University of York, Department of Physics, March 2012.

[5] Jiles, D. C., Introduction to Magnetism and Magnetic Materials, Chapman and Hall, 1994.

[6] Leslie-Pelecky, D. L., & Rieke, R. D., Magnetic properties of nanostructured materials. *Chemistry of Materials*, 8(8), 1770-1783, 1996.

[7] Papaefthymiou, G. C., Nanoparticle magnetism. *Nano Today*, 4(5), 438-447, 2009.

[8] Rosensweig, R.E., Heating magnetic fluid with alternating magnetic field, *Journal of Magnetism and Magnetic Materials*, 252, 370-374, 2002.

[9] Batlle, X., & Labarta, A., Finite-size effects in fine particles: magnetic and transport properties. *Journal of Physics D: Applied Physics*, 35, R15, 2002.

[10] Respaud, M., Broto, J. M., Rakoto, H., Fert, A. R., Thomas, L., Barbara, B., Verelst, M., Snoeck, E., Lecante, P., Mosset, A., Osuna, J., Ould Ely, T., Amiens, C., & Chaudret, B., Surface effects on the magnetic properties of ultrafine cobalt particles, *Physical Review B*, 57(5), 2925, 1998.

[11] Gambardella, P., Rusponi, S., Veronese, M., Dhesi, S. S., Grazioli, C., Dallmeyer, A., Cabria, I., Zeller, R., Dederichs, P.H., Kern, K., Carbone,

C., & Brune, H., Giant magnetic anisotropy of single cobalt atoms and nanoparticles, *Science*, 300(5622), 1130-1133, 2003.

[12] Perez, N., Guardia, P., Roca, A. G., Morales, M. D. P., Serna, C. J., Iglesias, O., Bartolomé, F., García, L. M., Battle, X., & Labarta, A., Surface anisotropy broadening of the energy barrier distribution in magnetic nanoparticles, *Nanotechnology*, 19(47), 475704, 2008.

[13] Bødker, F., Mørup, S., & Linderoth, S., Surface effects in metallic iron nanoparticles, *Physical Review Letters*, 72(2), 282, 1994.

[14] Gazeau, F., Bacri, J. C., Gendron, F., Perzynski, R., Raikher, Y. L., Stepanov, V. I., & Dubois, E., Magnetic resonance of ferrite nanoparticles: evidence of surface effects, *Journal of Magnetism and Magnetic Materials*, 186(1-2), 175-187, 1998.

[15] Laurent, S., Dutz, S., Häfeli, U. O., & Mahmoudi, M., Magnetic fluid hyperthermia: focus on superparamagnetic iron oxide nanoparticles, *Advances in Colloid and Interface Science*, 166(1-2), 8-23, 2011.

[16] Gittleman, J. I., B. Abeles, and S. Bozowski, Superparamagnetism and relaxation effects in granular $Ni - SiO_2$ and $Ni - Al_2O_3$ films, *Physical Review B*, 9(9), 3891, 1974.

[17] Hergt, R., Dutz, S., & Röder, M., Effects of size distribution on hysteresis losses of magnetic nanoparticles for hyperthermia, *Journal of Physics: Condensed Matter*, 20(38), 385214, 2008.

[18] El-Hilo, M., De Witte, A. M., O'Grady, K., & Chantrell, R. W., The sweep rate dependence of coercivity in recording media. *Journal of Magnetism and Magnetic Materials*, 117(3), L307-L310, 1992.

[19] Dutz, S., & Hergt, R., Magnetic particle hyperthermia - a promising tumour therapy?, *Nanotechnology*, 25(45), 452001, 2014.

[20] Eberbeck, D., & Trahms, L., Experimental investigation of dipolar interaction in suspensions of magnetic nanoparticles, *Journal of Magnetism and Magnetic Materials*, 323(10), 1228-1232, 2011.

[21] Serantes, D., Baldomir, D., Martinez-Boubeta, C., Simeonidis, K., Angelakeris, M., Natividad, E., Castro, M., Mediano, A., Chen, D. X., Sanchez, A., Balcells, L. I., & Martìnez, B., Influence of dipolar interactions on hyperthermia properties of ferromagnetic particles, *Journal of Applied Physics*, 108(7), 073918, 2010.

[22] Phan, M. H., Alonso, J., Khurshid, H., Lampen-Kelley, P., Chandra, S., Stojak Repa, K., Nemati, Z., Das, R., Iglesias, O., & Srikanth, H., Exchange bias effects in iron oxide-based nanoparticle systems, *Nanomaterials*, 6(11), 221, 2016.

[23] Cornell, R. M., & Schwertmann, U., The iron oxides: structure, properties, reactions, occurrences and uses, John Wiley & Sons, 2003.

[24] Cullity, B.D., & Graham, C.D., Introduction to Magnetic Materials, 2nd ed., Wiley-IEEE Press: Hoboken, NJ, USA, 2009.

[25] Verwey, E. J. W., Electronic conduction of magnetite (Fe 3 O 4) and its transition point at low temperatures, *Nature*, 144(3642), 327, 1939.

[26] Walz, F., The Verwey transition-a topical review, *Journal of Physics: Condensed Matter*, 14(12), R285, 2002.

[27] Goya, G. F., Berquo, T. S., Fonseca, F. C., & Morales, M. P., Static and dynamic magnetic properties of spherical magnetite nanoparticles, *Journal of Applied Physics*, 94(5), 3520-3528, 2003.

[28] Tartaj, P., del Puerto Morales, M., Veintemillas-Verdaguer, S., González-Carreno, T., & Serna, C. J., The preparation of magnetic nanoparticles for applications in biomedicine, *Journal of physics D: Applied Physics*, 36(13), R182, 2003.

[29] Blanco-Andujar, C., Walter, A., Cotin, G., Bordeianu, C., Mertz, D., Felder-Flesch, D., & Begin-Colin, S., Design of iron oxide-based nanoparticles for MRI and magnetic hyperthermia, *Nanomedicine*, 11(14), 1889-1910, 2016.

[30] Laurent, S., Forge, D., Port, M., Roch, A., Robic, C., Vander Elst, L., & Muller, R. N., Magnetic iron oxide nanoparticles: synthesis, stabilization, vectorization, physicochemical characterizations, and biological applications, *Chemical Reviews*, 108(6), 2064-2110, 2008.

[31] Chertok, B., Moffat, B. A., David, A. E., Yu, F., Bergemann, C., Ross, B. D., & Yang, V. C., Iron oxide nanoparticles as a drug delivery vehicle for MRI monitored magnetic targeting of brain tumors, *Biomaterials*, 29(4), 487-496, 2008.

[32] Gupta, A. K., & Gupta, M., Synthesis and surface engineering of iron oxide nanoparticles for biomedical applications, *Biomaterials*, 26(18), 3995-4021, 2005.

[33] Yan, F., Wang, Y., He, S., Ku, S., Gu, W., & Ye, L., Transferrin-conjugated, fluorescein-loaded magnetic nanoparticles for targeted delivery across the blood–brain barrier, *Journal of Materials Science: Materials in Medicine*, 24(10), 2371-2379, 2013.

[34] Lee, S. W., Lee, S. H., & Biswal, S., Magnetic resonance reporter gene imaging, *Theranostics*, 2(4), 403, 2012.

[35] Wu, W., Wu, Z., Yu, T., Jiang, C., & Kim, W. S., Recent progress on magnetic iron oxide nanoparticles: synthesis, surface functional strategies and biomedical applications, *Science and Technology of Advanced Materials*, 16(2), 023501, 2015.

[36] Kumar, C. S., & Mohammad, F., Magnetic nanomaterials for hyperthermia-based therapy and controlled drug delivery, *Advanced Drug Delivery Reviews*, 63(9), 789-808, 2011.

[37] Jain, T. K., Morales, M. A., Sahoo, S. K., Leslie-Pelecky, D. L., & Labhasetwar, V., Iron oxide nanoparticles for sustained delivery of anticancer agents, *Molecular Pharmaceutics*, 2(3), 194-205, 2005.

[38] Pankhurst, Q. A., Thanh, N. T. K., Jones, S. K., & Dobson, J., Progress in applications of magnetic nanoparticles in biomedicine, *Journal of Physics D: Applied Physics*, 42(22), 224001, 2009.

[39] Roca, A. G., Costo, R., Rebolledo, A. F., Veintemillas-Verdaguer, S., Tartaj, P., Gonzalez-Carreno, T., Morales, M. P., & Serna, C. J., Progress in the preparation of magnetic nanoparticles for applications in biomedicine, *Journal of Physics D: Applied Physics*, 42(22), 224002, 2009.

[40] Pankhurst, Q. A., Connolly, J., Jones, S. K., & Dobson, J., Applications of magnetic nanoparticles in biomedicine, *Journal of Physics D: Applied Physics*, 36(13), R167, 2003.

[41] Berry, C. C., Progress in functionalization of magnetic nanoparticles for applications in biomedicine, *Journal of Physics D: Applied Physics*, 42(22), 224003, 2009.

[42] Yavuz, C. T., Mayo, J. T., William, W. Y., Prakash, A., Falkner, J. C., Yean, S., Cong, L., Shipley, H. J., Kan, A., Tomson, M., Natelson, D., & Colvin, V. L., Low-field magnetic separation of monodisperse Fe3O4 nanocrystals, *Science*, 314(5801), 964-967, 2006.

[43] Berry, C. C., & Curtis, A. S., Functionalisation of magnetic nanoparticles for applications in biomedicine, *Journal of Physics D: Applied Physics*, 36(13), R198, 2003.

[44] Haun, J. B., Yoon, T. J., Lee, H., & Weissleder, R., Magnetic nanoparticle biosensors, *Wiley Interdisciplinary Reviews: Nanomedicine and Nanobiotechnology*, 2(3), 291-304, 2010.

[45] Ortega, D., & Pankhurst, Q. A., Magnetic hyperthermia, *Nanoscience*, 1(60), e88, 2013.

[46] Périgo, E. A., Hemery, G., Sandre, O., Ortega, D., Garaio, E., Plazaola, F., & Teran, F. J., Fundamentals and advances in magnetic hyperthermia, *Applied Physics Reviews*, 2(4), 041302, 2015.

[47] Carrey, J., Mehdaoui, B., & Respaud, M., Simple models for dynamic hysteresis loop calculations of magnetic single-domain nanoparticles: Application to magnetic hyperthermia optimization, *Journal of Applied Physics*, 109(8), 083921, 2011.

[48] De la Presa, P., Luengo, Y., Multigner, M., Costo, R., Morales, M. P., Rivero, G., & Hernando, A., Study of heating efficiency as a function of concentration, size, and applied field in $\gamma - Fe_2O_3$ nanoparticles, *The Journal of Physical Chemistry C*, 116(48), 25602-25610, 2012.

[49] Mehdaoui, B., Meffre, A., Carrey, J., Lachaize, S., Lacroix, L. M., Gougeon, M., Chudret, B., & Respaud, M., Optimal size of nanoparticles for magnetic hyperthermia: a combined theoretical and experimental study, *Advanced Functional Materials*, 21(23), 4573-4581, 2011.

[50] Jordan, A., MagForce©Nanotherapy: with tumor-specific nanoparticles against cancer, VDI BERICHTE 1920 (2005): 111.

[51] Duan, X., Li, Y., Physicochemical characteristics of nanoparticles affect circulation, biodistribution, cellular internalization, and trafficking, *Small*, 9(9-10), 1521-1532, 2013.

[52] Toy, R., Peiris, P. M., Ghaghada, K. B., & Karathanasis, E., Shaping cancer nanomedicine: the effect of particle shape on the in vivo journey of nanoparticles, *Nanomedicine*, 9(1), 121-134, 2014.

[53] Champion, J. A., Katare, Y. K., & Mitragotri, S., Particle shape: a new design parameter for micro-and nanoscale drug delivery carriers, *Journal of Controlled Release*, 121(1-2), 3-9, 2007.

Salatin Salatin, S., Maleki Dizaj, S., & Yari Khosroushahi, A., Effect of the surface modification, size, and shape on cellular uptake of nanoparticles, *Cell Biology International*, 39(8), 881-890, 2015.

[54] Wilhelm, C., Billotey, C., Roger, J., Pons, J. N., Bacri, J. C., & Gazeau, F., Intracellular uptake of anionic superparamagnetic nanoparticles as a function of their surface coating, *Biomaterials*, 24(6), 1001-1011, 2003.

[55] Agarwal, R., Singh, V., Jurney, P., Shi, L., Sreenivasan, S., & Roy, K., Mammalian cells preferentially internalize hydrogel nanodiscs over nanorods and use shape-specific uptake mechanisms, *Proceedings of the National Academy of Sciences*, 110(43), 17247-17252, 2013.

[56] Lascialfari, A., Filibian, M., Sangregorio, C., & Carretta, P., In vivo biomedical applications of magnetic resonance and magnetic materials, *Riv. Nuovo Cimento*, 36, 211-271, 2013.

[57] Chertok, B., Moffat, B. A., David, A. E., Yu, F., Bergemann, C., Ross, B. D., & Yang, V. C., Iron oxide nanoparticles as a drug delivery vehicle for MRI monitored magnetic targeting of brain tumors, *Biomaterials*, 29(4), 487-496, 2008.

[58] Lascialfari A. & Sangregorio C., Magnetic Nanoparticles in Biomedicine: Recent Advances, *Chemistry Today*, 29 (2), 20-23, 2011

[59] Johannsen, M., Gneveckow, U., Thiesen, B., Taymoorian, K., Cho, C. H., Waldofner, N., Scholz R., Jordan A., Loening S. A., & Wust, P., Thermotherapy of prostate cancer using magnetic nanoparticles: feasibility, imaging, and three-dimensional temperature distribution, *European Urology*, 52(6), 1653-1662, 2007.

[60] https://www.magforce.com/home/

[61] Brezovich, I. A., Low frequency hyperthermia: capacitive and ferromagnetic thermoseed methods, *Medical Physics Monograph*, 16, 82-111, 1988.

[62] Hergt, R., Dutz, S., & Zeisberger, M., Validity limits of the Néel relaxation model of magnetic nanoparticles for hyperthermia, *Nanotechnology*, 21(1), 015706, 2009.

[63] Chikazumi, S., & Graham, C. D., Physics of Ferromagnetism, 2e (Vol. 94), Oxford University Press on Demand, 2009.

[64] Cobianchi, M., Guerrini, A., Avolio, M., Innocenti, C., Corti, M., Arosio, P., Orsini, F., Sangregorio, C., & Lascialfari, A., Experimental determination of the frequency and field dependence of Specific Loss Power in Magnetic Fluid Hyperthermia, *Journal of Magnetism and Magnetic Materials*, 444, 154-160, 2017.

[65] Bloch, F., Nuclear induction, *Physical Review*, 70(7-8), 460, 1946.

[66] Purcell, E. M., Torrey, H. C., & Pound, R. V., Resonance absorption by nuclear magnetic moments in a solid, *Physical Review*, 69(1-2), 37, 1946.

[67] Slichter, C. P., Principles of Magnetic Resonance, Springer-Verlag, Berlin, 1996.

[68] Abragam, A., The Principles of Nuclear Magnetism, Oxford University Press, Oxford, 1961.

[69] Haacke, E. M., Brown, R. W., Thompson, M. R., & Venkatesan, R., Magnetic resonance imaging: physical principles and sequence design, Vol. 82, New York: Wiley-Liss, 1999.

[70] Eidmann, G., Savelsberg, R., Blümler, P., & Blümich, B., The NMR MOUSE, a mobile universal surface explorer, *Journal of Magnetic Resonance*, 122, 104-109, 1996.

[71] Hills, B., Food processing: an MRI perspective, *Trends in Food Science & Technology*, 6(4), 111-117, 1995.

[72] Viggiani, L., & Morelli, M. A. C., Characterization of wines by nuclear magnetic resonance: a work study on wines from the Basilicata region in Italy, *Journal of Agricultural and Food Chemistry*, 56(18), 8273-8279, 2008.

[73] Godefroy, S., Korb, J. P., Fleury, M., & Bryant, R. G., Surface nuclear magnetic relaxation and dynamics of water and oil in macroporous media, *Physical Review E*, 64(2), 021605, 2001.

[74] Lauterbur, P. C., Image formation by induced local interactions: examples employing nuclear magnetic resonance, 1973.

[75] Guy, C., & Ffytche, D., An introduction to the principles of medical imaging, pp. 267-294, London: Imperial College Press, 2005.

[76] Morris, P. G., & Mansfield, P., NMR Imaging in Biomedicine, Academic Press, New York, 1986.

[77] Corti, M., & Lascialfari, A., in NMR-MRI, μSR and Möss-bauer Spectroscopies in Molecular Magnets, pp. 89-110, ed. by Carretta, P. & Lascialfari, A., Springer-Verlag, Milan, 2007.

[78] Muller, R. N., Laurent, S., Vander Elst, L. & Roch, A., in NMR-MRI, μSR and Möss-bauer Spectroscopies in Molecular Magnets, pp. 71-87, ed. by Carretta, P., & Lascialfari, A., Springer-Verlag, Milan, 2007.

[79] Conte, P., & Alonzo, G., Environmental NMR: Fast-field-cycling Relaxometry, *EMagRes*, 389-398, 2007.

[80] Muller, R. N., Encyclopedia of Nuclear Magnetic Resonance, p. 1438, J. Wiley, New York, 1996.

[81] Vuong, Q. L., Gillis, P., Roch, A., & Gossuin, Y., Magnetic resonance relaxation induced by superparamagnetic particles used as contrast agents in magnetic resonance imaging: a theoretical review, *Wiley Interdisciplinary Reviews: Nanomedicine and Nanobiotechnology*, 9(6), e1468, 2017.

[82] Roch, A., Muller, R. N., & Gillis, P., Theory of proton relaxation induced by superparamagnetic particles, *The Journal of Chemical Physics*, 110(11), 5403-5411, 1999.

[83] Lévy, M., Gazeau, F., Wilhelm, C., Neveu, S., Devaud, M., & Levitz, P., Revisiting MRI contrast properties of nanoparticles: beyond the superparamagnetic regime, *The Journal of Physical Chemistry C*, 117(29), 15369-15374, 2013.

[84] Douvalis, A. P., Zboril, R., Bourlinos, A. B., Tucek, J., Spyridi, S., & Bakas, T., A facile synthetic route toward air-stable magnetic nanoalloys with Fe-Ni/Fe-Co core and iron oxide shell, *Journal of Nanoparticle Research*, 14(9), 1130, 2012.

[85] Orlando, T., Albino, M., Orsini, F., Innocenti, C., Basini, M., Arosio, P., Sangregorio, C., Corti, M., & Lascialfari, A., On the magnetic anisotropy and nuclear relaxivity effects of Co and Ni doping in iron oxide nanoparticles, *Journal of Applied Physics*, 119(13), 134301, 2016.

[86] Basini, M., Guerrini, A., Cobianchi, M., Orsini, F., Bettega, D., Avolio, M., Innocenti, C., Sangregorio, C., Lascialfari, A., & Arosio, P., Tailoring the magnetic core of organic-coated iron oxides nanoparticles to influence their contrast efficiency for Magnetic Resonance Imaging, *Journal of Alloys and Compounds*, 770, 58-66, 2019.

[87] Basini, M., Orlando, T., Arosio, P., Casula, M. F., Espa, D., Murgia, S., Sangregorio, C., Innocenti, C., & Lascialfari, A., Local spin dynamics of iron oxide magnetic nanoparticles dispersed in different solvents with variable size and shape: A 1H NMR study, *The Journal of Chemical Physics*, 146(3), 034703, 2017.

[88] Bordonali, L., Kalaivani, T., Sabareesh, K. P. V., Innocenti, C., Fantechi, E., Sangregorio, C., Casula, M. F., Lartigue, L., Larionova, J., Guari, Y., Corti, M., Arosio, P., & Lascialfari, A., NMR-D study of the local spin dynamics and magnetic anisotropy in different nearly monodispersed ferrite nanoparticles, *Journal of Physics: Condensed Matter*, 25(6), 066008, 2013.

[89] Wijaya, A., Brown, K. A., Alper, J. D., & Hamad-Schifferli, K., Magnetic field heating study of Fe-doped Au nanoparticles, *Journal of Magnetism and Magnetic Materials*, 309(1), 15-19, 2007.

[90] Mahmoudi, M., Hosseinkhani, H., Hosseinkhani, M., Boutry, S., Simchi, A., Journeay, W. S., Subramani, K., & Laurent, S., Magnetic resonance imaging tracking of stem cells in vivo using iron oxide nanoparticles as a tool for the advancement of clinical regenerative medicine, *Chemical Reviews*, 111(2), 253-280, 2010.

[91] Gossuin, Y., Orlando, T., Basini, M., Henrard, D., Lascialfari, A., Mattea, C., Stapf, S., & Vuong, Q. L., NMR relaxation induced by iron oxide particles: testing theoretical models, *Nanotechnology*, 27(15), 155706, 2016.

[92] Vuong, Q. L., Berret, J. F., Fresnais, J., Gossuin, Y., & Sandre, O., A universal scaling law to predict the efficiency of magnetic nanoparticles as MRI T2-contrast agents, *Advanced Healthcare Materials*, 1(4), 502-512, 2012.

[93] Brooks, R. A., Moiny, F., & Gillis, P., On T2-shortening by weakly magnetized particles: the chemical exchange model, *Magnetic Resonance in Medicine: An Official Journal of the International Society for Magnetic Resonance in Medicine*, 45(6), 1014-1020, 2001.

[94] Gillis, P., Moiny, F., & Brooks, R. A., On T2-shortening by strongly magnetized spheres: a partial refocusing model, *Magnetic Resonance in Medicine: An Official Journal of the International Society for Magnetic Resonance in Medicine*, 47(2), 257-263, 2002.

[95] Branquinho, L. C., Carriao, M. S., Costa, A. S., Zufelato, N., Sousa, M. H., Miotto, R., Ivkov, R., & Bakuzis, A. F., Effect of magnetic dipolar interactions on nanoparticle heating efficiency: Implications for cancer hyperthermia, *Scientific Reports*, 3, 2887, 2013.

[96] Serantes, D., Simeonidis, K., Angelakeris, M., Chubykalo-Fesenko, O., Marciello, M., Morales, M. D. P., Baldomir, D., & Martinez-Boubeta, C., Multiplying magnetic hyperthermia response by nanoparticle assembling, *The Journal of Physical Chemistry C*, 118(11), 5927-5934, 2014.

[97] Di Corato, R., Espinosa, A., Lartigue, L., Tharaud, M., Chat, S., Pellegrino, T., Ménager, C., Gazeau, F., & Wilhelm, C., Magnetic hyperthermia efficiency in the cellular environment for different nanoparticle designs, *Biomaterials*, 35(24), 6400-6411, 2014.

[98] Soukup, D., Moise, S., Céspedes, E., Dobson, J., & Telling, N. D., In situ measurement of magnetization relaxation of internalized nanoparticles in live cells, *ACS Nano*, 9(1), 231-240, 2015.

[99] Moise, S., Céspedes, E., Soukup, D., Byrne, J. M., El Haj, A. J., & Telling, N. D., The cellular magnetic response and biocompatibility of biogenic zinc- and cobalt-doped magnetite nanoparticles, *Scientific Reports*, 7, 39922, 2017.

[100] Kalambur, V. S., Han, B., Hammer, B. E., Shield, T. W., & Bischof, J. C., In vitro characterization of movement, heating and visualization of magnetic nanoparticles for biomedical applications, *Nanotechnology*, 16(8), 1221, 2005.

[101] Dutz, S., Kettering, M., Hilger, I., Müller, R., & Zeisberger, M., Magnetic multicore nanoparticles for hyperthermia - influence of particle immobilization in tumour tissue on magnetic properties, *Nanotechnology*, 22(26), 265102, 2011.

[102] De la Presa, P., Luengo, Y., Multigner, M., Costo, R., Morales, M. P., Rivero, G., & Hernando, A., Study of heating efficiency as a function of concentration, size, and applied field in $\gamma - Fe_2O_3$ nanoparticles, *The Journal of Physical Chemistry C*, 116(48), 25602-25610, 2012.

[103] Jeun, M., Kim, Y. J., Park, K. H., Paek, S. H., & Bae, S., Physical contribution of Néel and Brown relaxation to interpreting intracellular hyperthermia characteristics using superparamagnetic nanofluids, *Journal of Nanoscience and Nanotechnology*, 13(8), 5719-5725, 2013.

[104] Tan, R. P., Carrey, J., & Respaud, M., Magnetic hyperthermia properties of nanoparticles inside lysosomes using kinetic Monte Carlo simulations: Influence of key parameters and dipolar interactions, and evidence for strong spatial variation of heating power, *Physical Review B*, 90(21), 214421, 2014.

[105] Sanchez, C., El Hajj Diab, D., Connord, V., Clerc, P., Meunier, E., Pipy, B., Payré, B., Tan, R. P., Gougeon, M., Carrey, J., Gigoux, V., & Fourmy, D., Targeting a G-protein-coupled receptor overexpressed in endocrine tumors by magnetic nanoparticles to induce cell death, *ACS Nano*, 8(2), 1350-1363, 2014.

[106] Domenech, M., Marrero-Berrios, I., Torres-Lugo, M., & Rinaldi, C., Lysosomal membrane permeabilization by targeted magnetic nanoparticles in alternating magnetic fields, *ACS Nano*, 7(6), 5091-5101, 2013.

[107] Creixell, M., Bohorquez, A. C., Torres-Lugo, M., & Rinaldi, C., EGFR-targeted magnetic nanoparticle heaters kill cancer cells without a perceptible temperature rise, *ACS Nano*, 5(9), 7124-7129, 2011.

[108] Marcos-Campos, I., Asin, L., Torres, T. E., Marquina, C., Tres, A., Ibarra, M. R., & Goya, G. F., Cell death induced by the application of alternating magnetic fields to nanoparticle-loaded dendritic cells, *Nanotechnology*, 22(20), 205101, 2011.

[109] Grazú, V., Silber, A. M., Moros, M., Asin, L., Torres, T. E., Marquina, C., Ibarra, M. R., & Goya, G. F., Application of magnetically induced hyperthermia in the model protozoan Crithidia fasciculata as a potential therapy against parasitic infections, *International Journal of Nanomedicine*, 7, 5351, 2012.

[110] Asin, L., Ibarra, M. R., Tres, A., & Goya, G. F., Controlled cell death by magnetic hyperthermia: effects of exposure time, field amplitude, and nanoparticle concentration, *Pharmaceutical Research*, 29(5), 1319-1327, 2012.

[111] Villanueva, A., De La Presa, P., Alonso, J. M., Rueda, T., Martinez, A., Crespo, P., Morales, M. P., Gonzalez-Fernandez, M. A., Valdés, J., & Rivero, G., Hyperthermia HeLa cell treatment with silica-coated manganese oxide nanoparticles, *The Journal of Physical Chemistry C*, 114(5), 1976-1981, 2010.

[112] Asin, L., Goya, G. F., Tres, A., & Ibarra, M. R., Induced cell toxicity originates dendritic cell death following magnetic hyperthermia treatment, *Cell Death & Disease*, 4(4), e596, 2013.

[113] Salas, G., Camarero, J., Cabrera, D., Takacs, H., Varela, M., Ludwig, R., Dähring, H., Hilger, I., Miranda, R., Morales, M. P., & Teran, F. J., Modulation of magnetic heating via dipolar magnetic interactions in monodisperse and crystalline iron oxide nanoparticles, *The Journal of Physical Chemistry C*, 118(34), 19985-19994, 2014.

[114] Pineiro, Y., Vargas-Osorio, Z., Banobre-López, M., Kolen'ko, Y. V., López-Quintela, M. A., & Rivas, J., Relevant parameters for magnetic hyperthermia in biological applications: Agglomeration, concentration, and viscosity, *IEEE Transactions on Magnetics*, 52(7), 1-4, 2016.

[115] Culjat, M. O., Goldenberg, D., Tewari, P., & Singh, R. S., A review of tissue substitutes for ultrasound imaging, *Ultrasound in Medicine & Biology*, 36(6), 861-873, 2010.

[116] Fortin, J. P., Wilhelm, C., Servais, J., Ménager, C., Bacri, J. C., & Gazeau, F., Size-sorted anionic iron oxide nanomagnets as colloidal mediators for magnetic hyperthermia, *Journal of the American Chemical Society*, 129(9), 2628-2635, 2007.

[117] Avolio, M., Guerrini, A., Brero, F., Innocenti, C., Sangregorio, C., Cobianchi, M., Mariani, M., Orsini, F., Arosio, P., Lascialfari, A., In-gel study of the effect of magnetic nanoparticles immobilization on their heating efficiency for application in Magnetic Fluid Hyperthermia, *Journal of Magnetism and Magnetic Materials*, 471, 504-512, 2019.

[118] Kossatz, S., Ludwig, R., Dähring, H., Ettelt, V., Rimkus, G., Marciello, M., Salas, G., Patel, V.,Teran, F. J., Hilger, I., High therapeutic efficiency of magnetic hyperthermia in xenograft models achieved with moderate temperature dosages in the tumor area, *Pharmaceutical Research*, 31(12), 3274-3288, 2014.

[119] Moore, T. L., Rodriguez-Lorenzo, L., Hirsch, V., Balog, S., Urban, D., Jud, C., Rothen-Rutishauser, B., Lattuada, M., Petri-Fink, A., Nanoparticle colloidal stability in cell culture media and impact on cellular interactions, *Chemical Society Reviews*, 44(17), 6287-6305, 2015.

[120] Pawley, G. S., Unit-cell refinement from powder diffraction scans, *Journal of Applied Crystallography*, 14(6), 357-361, 1981.

[121] Coelho A. A., Topas, General profile and structure analysis software for powder diffraction Data, *Bruker AXS*, 2005.

[122] Dormann, J. L., Bessais, L., & Fiorani, D., A dynamic study of small interacting particles: superparamagnetic model and spin-glass laws, *Journal of Physics C: Solid State Physics*, 21(10), 2015, 1988.

[123] Dormann, J. L., Fiorani, D., & Tronc, E., On the models for interparticle interactions in nanoparticle assemblies: comparison with experimental results, *Journal of Magnetism and Magnetic Materials*, 202(1), 251-267, 1999.

[124] Soeya, S., Hayakawa, J., Takahashi, H., Ito, K., Yamamoto, C., Kida, A., Asano, H., & Matsui, M., Development of half-metallic ultrathin Fe 3 O 4 films for spin-transport devices, *Applied Physics Letters*, 80(5), 823-825, 2002.

[125] Fiorani, D. (Ed.), Surface effects in magnetic nanoparticles, *Springer Science & Business Media*, 2005.

[126] Kolhatkar, A., Jamison, A., Litvinov, D., Willson, R., & Lee, T., Tuning the magnetic properties of nanoparticles, *International Journal of Molecular Sciences*, 14(8), 15977-16009, 2013.

[127] Aragón, R., Buttrey, D. J., Shepherd, J. P., & Honig, J. M., Influence of nonstoichiometry on the Verwey transition, *Physical Review B*, 31(1), 430, 1985.

[128] Gavilán, H., Posth, O., Bogart, L. K., Steinhoff, U., Gutiérrez, L., & Morales, M. P., How shape and internal structure affect the magnetic properties of anisometric magnetite nanoparticles, *Acta Materialia*, 125, 416-424, 2017.

[129] Salloum, M., Ma, R. H., Weeks, D., & Zhu, L., Controlling nanoparticle delivery in magnetic nanoparticle hyperthermia for cancer treatment: experimental study in agarose gel, *International Journal of Hyperthermia*, 24(4), 337-345, 2008.

[130] Fernández, E., López, D., Mijangos, C., Duskova-Smrckova, M., Ilavsky, M., & Dusek, K., Rheological and thermal properties of agarose aqueous solutions and hydrogels, *Journal of Polymer Science Part B: Polymer Physics*, 46(3), 322-328, 2008.

[131] Lahrech, K., Safouane, A., & Peyrellasse, J., Sol state formation and melting of agar gels rheological study, *Physica A: Statistical Mechanics and its Applications*, 358(1), 205-211, 2005.

[132] Gossuin, Y., Burtea, C., Monseux, A., Toubeau, G., Roch, A., Muller, R. N., & Gillis, P., Ferritin-induced relaxation in tissues: an in vitro study, *Journal of Magnetic Resonance Imaging: An Official Journal of the International Society for Magnetic Resonance in Medicine*, 20(4), 690-696, 2004.

[133] Hergt, R., & Dutz, S., Magnetic particle hyperthermia-biophysical limitations of a visionary tumour therapy, *Journal of Magnetism and Magnetic Materials*, 311(1), 187-192, 2007.

[134] Zhang, M., Che, Z., Chen, J., Zhao, H., Yang, L., Zhong, Z., & Lu, J., Experimental Determination of Thermal Conductivity of Water - Agar Gel at Different Concentrations and Temperatures, *Journal of Chemical & Engineering Data*, 56(4), 859-864, 2010.

[135] Box, G. E., & Lucas, H. L., Design of experiments in non-linear situations, *Biometrika*, 46(1/2), 77-90, 1959.

[136] Blanco-Andujar, C., Ortega, D., Southern, P., Pankhurst, Q. A., & Thanh, N. T. K., High performance multi-core iron oxide nanoparticles for magnetic hyperthermia: microwave synthesis, and the role of core-to-core interactions, *Nanoscale*, 7(5), 1768-1775, 2015.

[137] Landi, G. T., Simple models for the heating curve in magnetic hyperthermia experiments, *Journal of Magnetism and Magnetic Materials*, 326, 14-21, 2013.

[138] Cervadoro, A., Giverso, C., Pande, R., Sarangi, S., Preziosi, L., Wosik, J., Brazdeikis, A., & Decuzzi, P., Design maps for the hyperthermic treatment of tumors with superparamagnetic nanoparticles, *PLOS ONE*, 8(2), e57332, 2013.

[139] Mehdaoui, B., Tan, R. P., Meffre, A., Carrey, J., Lachaize, S., Chaudret, B., & Respaud, M., Increase of magnetic hyperthermia efficiency due to dipolar interactions in low-anisotropy magnetic nanoparticles: Theoretical and experimental results, *Physical Review B*, 87(17), 174419, 2013.

[140] Urtizberea, A., Natividad, E., Arizaga, A., Castro, M., & Mediano, A., Specific absorption rates and magnetic properties of ferrofluids with interaction effects at low concentrations, *The Journal of Physical Chemistry C*, 114(11), 4916-4922, 2010.

[141] Martens, M. A., Deissler, R. J., Wu, Y., Bauer, L., Yao, Z., Brown, R., & Griswold, M., Modeling the Brownian relaxation of nanoparticle ferrofluids: Comparison with experiment, *Medical Physics*, 40(2), 022303, 2013.

[142] Glöckl, G., Hergt, R., Zeisberger, M., Dutz, S., Nagel, S., & Weitschies, W., The effect of field parameters, nanoparticle properties and immobilization on the specific heating power in magnetic particle hyperthermia, *Journal of Physics: Condensed Matter*, 18(38), S2935, 2006.

[143] Hergt, R., Dutz, S., Müller, R., & Zeisberger, M., Magnetic particle hyperthermia: nanoparticle magnetism and materials development for cancer therapy, *Journal of Physics: Condensed Matter*, 18(38), S2919, 2006.

[144] Lima, E., De Biasi, E., Zysler, R. D., Mansilla, M. V., Mojica-Pisciotti, M. L., Torres, T. E., Calatayud, M. P., Marquina, C., Ibarra, M. R., & Goya, G. F., Relaxation time diagram for identifying heat generation mechanisms in magnetic fluid hyperthermia, *Journal of Nanoparticle Research*, 16(12), 2791, 2014.

[145] Perreard, I. M., Reeves, D. B., Zhang, X., Kuehlert, E., Forauer, E. R., & Weaver, J. B., Temperature of the magnetic nanoparticle microenvironment: estimation from relaxation times, *Physics in Medicine & Biology*, 59(5), 1109, 2014.

[146] Haase, C., & Nowak, U., Role of dipole-dipole interactions for hyperthermia heating of magnetic nanoparticle ensembles, *Physical Review B*, 85(4), 045435, 2012.

[147] Dutz, S., Hergt, R., The role of interactions in systems of single domain ferrimagnetic iron oxide nanoparticles, *Journal of Nano and Electronic Physics*, 4, 2012.

[148] Reeves, D. B., & Weaver, J. B., Simulations of magnetic nanoparticle Brownian motion, *Journal of Applied Physics*, 112(12), 124311, 2012.

[149] Raikher, Y. L., & Stepanov, V. I., Absorption of AC field energy in a suspension of magnetic dipoles, *Journal of Magnetism and Magnetic Materials*, 320(21), 2692-2695, 2008.

[150] Usov, N. A., & Liubimov, B. Y., Dynamics of magnetic nanoparticle in a viscous liquid: Application to magnetic nanoparticle hyperthermia, *Journal of Applied Physics*, 112(2), 023901, 2012.

[151] Mamiya, H., & Jeyadevan, B., Hyperthermic effects of dissipative structures of magnetic nanoparticles in large alternating magnetic fields, *Scientific Reports*, 1, 157, 2011.

[152] Boni, A., Marinone, M., Innocenti, C., Sangregorio, C., Corti, M., Lascialfari, A., Mariani, M., Orsini, F., Poletti, G., & Casula, M. F., Magnetic and relaxometric properties of Mn ferrites, *Journal of Physics D: Applied Physics*, 41(13), 134021, 2008.

[153] Fantechi, E., Campo, G., Carta, D., Corrias, A., de Julián Fernández, C., Gatteschi, D., Innocenti, C., Pineider, F., Rugi, F., & Sangregorio, C., Exploring the effect of Co doping in fine maghemite nanoparticles, *The Journal of Physical Chemistry C*, 116(14), 8261-8270, 2012.

[154] Zhang, G., Du, R., Zhang, L., Cai, D., Sun, X., Zhou, Y., Qian, J., Zhong, K., Zheng, K., Kaigler, D., Liu, W., Zhang, X., Zou, D., & Wu, Z., Gadolinium-Doped Iron Oxide Nanoprobe as Multifunctional Bioimaging Agent and Drug Delivery System, *Advanced Functional Materials*, 25(38), 6101-6111, 2015.

[155] Atabaev, T. S., PEG-coated superparamagnetic dysprosium-doped Fe 3 O 4 nanoparticles for potential MRI imaging, *BioNanoScience*, 8(1), 299-303, 2018.

[156] Ho, D., Sun, X., & Sun, S., Monodisperse magnetic nanoparticles for theranostic applications, *Accounts of Chemical Research*, 44(10), 875-882, 2011.

[157] Roch, A., Gossuin, Y., Muller, R. N., & Gillis, P., Superparamagnetic colloid suspensions: water magnetic relaxation and clustering, *Journal of Magnetism and Magnetic Materials*, 293(1), 532-539, 2005.

[158] Bonanni, V., Basini, M., Peddis, D., Lascialfari, A., Rossi, G., & Torelli, P., X-ray magnetic circular dichroism discloses surface spins correlation in maghemite hollow nanoparticles, *Applied Physics Letters*, 112(2), 022404, 2018.

[159] Hao, R., Xing, R., Xu, Z., Hou, Y., Gao, S., & Sun, S,. Synthesis, functionalization, and biomedical applications of multifunctional magnetic nanoparticles, *Advanced Materials*, 22(25), 2729-2742, 2010.

[160] Bogren, S., Fornara, A., Ludwig, F., del Puerto Morales, M., Steinhoff, U., Hansen, M., Kazakova, O., & Johansson, C., Classification of magnetic nanoparticle systems - synthesis, standardization and analysis methods in the nanomag project, *International Journal of Molecular Sciences*, 16(9), 20308-20325, 2015.

[161] Chithrani, B. D., Ghazani, A. A., & Chan, W. C., Determining the size and shape dependence of gold nanoparticle uptake into mammalian cells, *Nano Letters*, 6(4), 662-668, 2006.

[162] Huang, X., Teng, X., Chen, D., Tang, F., & He, J., The effect of the shape of mesoporous silica nanoparticles on cellular uptake and cell function, *Biomaterials*, 31(3), 438-448, 2010.

[163] Chithrani, B. D., & Chan, W. C., Elucidating the mechanism of cellular uptake and removal of protein-coated gold nanoparticles of different sizes and shapes, *Nano Letters*, 7(6), 1542-1550, 2007.

[164] Albanese, A., Tang, P. S., & Chan, W. C., The effect of nanoparticle size, shape, and surface chemistry on biological systems, *Annual Review of Biomedical Engineering*, 14, 1-16, 2012.

[165] Dasgupta, S., Auth, T., & Gompper, G., Shape and orientation matter for the cellular uptake of nonspherical particles, *Nano Letters*, 14(2), 687-693, 2014.

[166] Truong, N. P., Whittaker, M. R., Mak, C. W., & Davis, T. P., The importance of nanoparticle shape in cancer drug delivery, *Expert Opinion on Drug Delivery*, 12(1), 129-142, 2015.

[167] Burda, C., Chen, X., Narayanan, R., & El-Sayed, M. A., Chemistry and properties of nanocrystals of different shapes, *Chemical Reviews*, 105(4), 1025-1102, 2005.

[168] Song, Q., & Zhang, Z. J., Shape control and associated magnetic properties of spinel cobalt ferrite nanocrystals, *Journal of the American Chemical Society*, 126(19), 6164-6168, 2004.

[169] Salazar-Alvarez, G., Qin, J., Sepelak, V., Bergmann, I., Vasilakaki, M., Trohidou, K. N., Ardisson, J. D., Macedo, W. A. A., Mikhaylova, M., Muhammed, M., Baro, M. D., & Nogués, J., Cubic versus spherical magnetic nanoparticles: the role of surface anisotropy, *Journal of the American Chemical Society*, 130(40), 13234-13239, 2008.

[170] Salas, G., Veintemillas-Verdaguer, S., & Morales, M. D. P., Relationship between physico-chemical properties of magnetic fluids and their heating capacity, *International Journal of Hyperthermia*, 29(8), 768-776, 2013.

[171] Guardia, P., Di Corato, R., Lartigue, L., Wilhelm, C., Espinosa, A., Garcia-Hernandez, M., Gazeau, F., Manna, L., & Pellegrino, T., Water-soluble iron oxide nanocubes with high values of specific absorption rate for cancer cell hyperthermia treatment, *ACS Nano*, 6(4), 3080-3091, 2012.

[172] Rebolledo, A. F., Bomatí-Miguel, O., Marco, J. F., & Tartaj, P., A facile synthetic route for the preparation of superparamagnetic iron oxide nanorods and nanorices with tunable surface functionality, *Advanced Materials*, 20(9), 1760-1765, 2008.

[173] Rebolledo, A. F., Laurent, S., Calero, M., Villanueva, A., Knobel, M., Marco, J. F., & Tartaj, P., Iron oxide nanosized clusters embedded in porous nanorods: a new colloidal design to enhance capabilities of MRI contrast agents, *ACS Nano*, 4(4), 2095-2103, 2010.

[174] Kostopoulou, A., Velu, S. K., Thangavel, K., Orsini, F., Brintakis, K., Psycharakis, S., Ranella, A., Bordonali, L., Lappas, A., & Lascialfari, A., Colloidal assemblies of oriented maghemite nanocrystals and their NMR relaxometric properties, *Dalton Transactions*, 43(22), 8395-8404, 2014.

[175] Sakellari, D., Brintakis, K., Kostopoulou, A., Myrovali, E., Simeonidis, K., Lappas, A., & Angelakeris, M., Ferrimagnetic nanocrystal assemblies as versatile magnetic particle hyperthermia mediators, *Materials Science and Engineering: C*, 58, 187-193, 2016.

[176] Gavilán, H., Kowalski, A., Heinke, D., Sugunan, A., Sommertune, J., Varón, M., Bogart, L. K., Posth, O., González-Alonso, D., Balceris, C., Fock, J., Wetterskog, E., Frandsen, C., Gehrke, N., Grüttner, C., Fornare, A., Ludwig, F., Veintemillas-Verdaguer, S., Johansson, C., & Morales, M. P., Colloidal Flower-Shaped Iron Oxide Nanoparticles: Synthesis Strategies and Coatings, *Particle & Particle Systems Characterization*, 34(7), 1700094, 2017.

[177] Gavilán, H., Sánchez, E. H., Brollo, M. E., Asín, L., Moerner, K. K., Frandsen, C., Lázaro, F. J., Serna, C. J., Veintemillas-Verdaguer, S., Morales, M. P., & Gutiérrez, L., Formation Mechanism of Maghemite Nanoflowers Synthesized by a Polyol-Mediated Process, *ACS Omega*, 2(10), 7172-7184, 2017.

[178] Simeonidis, K., Morales, M. P., Marciello, M., Angelakeris, M., de La Presa, P., Lazaro-Carrillo, A., Tabero, A., Villanueva, A., Chubykalo-Fesenko, O., & Serantes, D., In-situ particles reorientation during magnetic hyperthermia application: Shape matters twice, *Scientific Reports*, 6, 38382, 2016.

[179] Toy, R., Peiris, P. M., Ghaghada, K. B., & Karathanasis, E., Shaping cancer nanomedicine: the effect of particle shape on the in vivo journey of nanoparticles, *Nanomedicine*, 9(1), 121-134, 2014.

[180] Duan, X., & Li, Y., Physicochemical characteristics of nanoparticles affect circulation, biodistribution, cellular internalization, and trafficking, *Small*, 9(9-10), 1521-1532, 2013.

[181] Champion, J. A., Katare, Y. K., & Mitragotri, S., Particle shape: a new design parameter for micro-and nanoscale drug delivery carriers, *Journal of Controlled Release*, 121(1-2), 3-9, 2007.

[182] Salatin, S., Maleki Dizaj, S., & Yari Khosroushahi, A., Effect of the surface modification, size, and shape on cellular uptake of nanoparticles, *Cell Biology International*, 39(8), 881-890, 2015.

[183] Gratton, S. E., Ropp, P. A., Pohlhaus, P. D., Luft, J. C., Madden, V. J., Napier, M. E., & DeSimone, J. M., The effect of particle design on cellular internalization pathways, *Proceedings of the National Academy of Sciences*, 105(33), 11613-11618, 2008.

[184] Agarwal, R., Singh, V., Jurney, P., Shi, L., Sreenivasan, S. V., & Roy, K., Mammalian cells preferentially internalize hydrogel nanodiscs over nanorods and use shape-specific uptake mechanisms, *Proceedings of the National Academy of Sciences*, 110(43), 17247-17252, 2013.

[185] Cheng, Y., Muroski, M. E., Petit, D. C., Mansell, R., Vemulkar, T., Morshed, R. A., Han, Y., Balyasnikova, I. V., Horbinski, C. M., Huang,

X., Zhang, L., Cowburn, R. P., & Lesniak, M. S., Rotating magnetic field induced oscillation of magnetic particles for in vivo mechanical destruction of malignant glioma, *Journal of Controlled Release*, 223, 75-84, 2016.

[186] Cheng, D., Li, X., Zhang, G., & Shi, H., Morphological effect of oscillating magnetic nanoparticles in killing tumor cells, *Nanoscale Research Letters*, 9(1), 195, 2014.

[187] Zhen, Z., & Xie, J., Development of manganese-based nanoparticles as contrast probes for magnetic resonance imaging, *Theranostics*, 2(1), 45, 2012.

[188] Pozas, R., Ocana, M., Morales, M. P., & Serna, C. J., Uniform nanosized goethite particles obtained by aerial oxidation in the FeSO4–Na2CO3 system, *Journal of Colloid and Interface Science*, 254(1), 87-94, 2002.

[189] Ohmori, M., & Matijević, E., Preparation and properties of uniform coated inorganic colloidal particles: 8. Silica on iron, *Journal of Colloid and Interface Science*, 160(2), 288-292, 1993.

[190] Liz-Marzán, L. M., Giersig, M., & Mulvaney, P., Synthesis of nanosized gold-silica core-shell particles, *Langmuir*, 12(18), 4329-4335, 1996.

[191] Tassa, C., Shaw, S. Y., & Weissleder, R., Dextran-coated iron oxide nanoparticles: a versatile platform for targeted molecular imaging, molecular diagnostics, and therapy, *Accounts of Chemical Research*, 44(10), 842-852, 2011.

[192] Bulte, J. W., & Modo, M. M., Molecular and cellular MR imaging, *CRC Press*, 2007.

[193] Anselmo, A. C., & Mitragotri, S., Nanoparticles in the clinic, *Bioengineering & Translational Medicine*, 1(1), 10-29, 2016.

[194] Bobo, D., Robinson, K. J., Islam, J., Thurecht, K. J., & Corrie, S. R., Nanoparticle-based medicines: a review of FDA-approved materials and clinical trials to date, *Pharmaceutical Research*, 33(10), 2373-2387, 2016.

[195] Malvern Instruments, Zetasizer nano series user manual, MAN0317, 1, 2004.

[196] Kodama, R. H., Magnetic nanoparticles, *Journal of Magnetism and Magnetic Materials*, 200(1-3), 359-372, 1999.

[197] Yang, H., Zhuang, Y., Sun, Y., Dai, A., Shi, X., Wu, D., Li, F., Hu, H., & Yang, S., Targeted dual-contrast T1-and T2-weighted magnetic resonance imaging of tumors using multifunctional gadolinium-labeled superparamagnetic iron oxide nanoparticles, *Biomaterials*, 32(20), 4584-4593, 2011.

[198] Nath, S., Kaittanis, C., Ramachandran, V., Dalal, N. S., & Perez, J. M., Synthesis, magnetic characterization, and sensing applications of novel dextran-coated iron oxide nanorods, *Chemistry of Materials*, 21(8), 1761-1767, 2009.

[199] Mejías, R., Hernández Flores, P., Talelli, M., Tajada-Herráiz, J. L., Brollo, M. E., Portilla, Y., Morales, M. P., & Barber, D. F.m Cell-Promoted Nanoparticle Aggregation Decreases Nanoparticle-Induced Hyperthermia under an Alternating Magnetic Field Independently of Nanoparticle Coating, Core Size, and Subcellular Localization, *ACS Applied Materials & Interfaces*, 11(1), 340-355, 2018.

[200] Lee, J., & Kotov, N. A., Thermometer design at the nanoscale, *Nano Today*, 2(1), 48-51, 2007.

[201] Das, R., Alonso, J., Nemati Porshokouh, Z., Kalappattil, V., Torres, D., Phan, M. H., Garaio, E., García, J. Á., Llamazares, J. L. S., & Srikanth, H., Tunable high aspect ratio iron oxide nanorods for enhanced hyperthermia, *The Journal of Physical Chemistry C*, 120(18), 10086-10093, 2016.

[202] Geng, S., Yang, H., Ren, X., Liu, Y., He, S., Zhou, J., Su, N., Li, Y., Xu, C., Zhang, X., & Cheng, Z., Anisotropic Magnetite Nanorods for Enhanced Magnetic Hyperthermia, *Chemistry - An Asian Journal*, 11(21), 2996-3000, 2016.

[203] Marx, V., Cancer treatment: Sharp shooters, *Nature Publishing Group*, 133, 2014.

[204] http://www.shi.co.jp/quantum/eng/product/proton/proton.html

[205] Amaldi, U., & Kraft, G., Radiotherapy with beams of carbon ions, *Reports on Progress in Physics*, 68(8), 1861, 2005.

[206] Hitchcock, K. E., Nichols, R. C., Morris, C. G., Bose, D., Hughes, S. J., Stauffer, J. A., Celinski, S. A., Johnson, E. A., Zaiden, R. A., Mendenhall, N. P., & Rutenberg, M. S., Feasibility of pancreatectomy following high-dose proton therapy for unresectable pancreatic cancer, *World Journal of Gastrointestinal Surgery*, 9(4), 103, 2017.

[207] Horsman, M. R., & Overgaard, J., Hyperthermia: a potent enhancer of radiotherapy, *Clinical Oncology*, 19(6), 418-426, 2007.

[208] Kampinga, H. H., Cell biological effects of hyperthermia alone or combined with radiation or drugs: a short introduction to newcomers in the field, *International Journal of Hyperthermia*, 22(3), 191-196, 2006.

[209] Zeng, Z. C., Jiang, G. L., Wang, G. M., Tang, Z. Y., Curran, W. J., & Iliakis, G., DNA-PKcs subunits in radiosensitization by hyperthermia on

hepatocellular carcinoma hepG2 cell line, *World Journal of Gastroenterology*, 8(5), 797, 2002.

[210] Maeda, J., Fujii, Y., Fujisawa, H., Hirakawa, H., Cartwright, I. M., Uesaka, M., Kitamura, H., Fujimori, A., & Kato, T. A., Hyperthermia-induced radiosensitization in CHO wild-type, NHEJ repair mutant and HR repair mutant following proton and carbon-ion exposure, *Oncology Letters*, 10(5), 2828-2834, 2015.

[211] Hall, E. J., & Giaccia, A. J., Radiobiology for the Radiologist, Sixth Edition, LIPPINCOTT WILLIAMS & WILKINS, 2006.